University of West Bohemia
Faculty of Applied Sciences

COMPUTATIONAL MODELLING OF HEMODYNAMICS FOR NON-INVASIVE ASSESSMENT OF ARTERIAL BYPASS GRAFT PATENCY

Ing. Alena Jonášová

Ph.D. thesis
submitted in partial fulfilment of the requirements
for the degree of Doctor of Philosophy in
Applied Mechanics

Supervisor: Assoc. Prof. Ing. Jan Vimmr, Ph.D.
Department of Mechanics

Pilsen 2014

Západočeská univerzita v Plzni
Fakulta aplikovaných věd

VÝPOČTOVÉ MODELOVÁNÍ PROUDĚNÍ KRVE ZA ÚČELEM NEINVAZIVNÍHO POSOUZENÍ ŽIVOTNOSTI BYPASSOVÝCH ŠTĚPŮ

Ing. Alena Jonášová

disertační práce
k získání akademického titulu doktor
v oboru
Aplikovaná mechanika

Školitel: doc. Ing. Jan Vimmr, Ph.D.
Katedra mechaniky

Plzeň 2014

學習是永遠跟隨主人的寶物

"Learning is a treasure that will follow its owner everywhere."

Chinese proverb

Declaration

I declare that this Ph.D. thesis submitted at the University of West Bohemia is my own work, that it has not been submitted before for any degree or examination at any other university, and that all the sources I have used or quoted have been indicated in the bibliography.

Pilsen, 30.9. 2014 Alena Jonášová

The Ph.D. thesis summarises the research work carried out by the author at the University of West Bohemia, which was partially supported by the research project of the Ministry of Education, Youth and Sports of the Czech Republic No. MSM4977751303 (*Failure prediction of heterogeneous materials, components of mechanical and biomechanical systems*) with Prof. Ing. Vladimír Zeman, DrSc. as the principal investigator at the Department of Mechanics and by the European Regional Development Fund (ERDF), project "NTIS – New Technologies for the Information Society", European Centre of Excellence, CZ.1.05/1.1.00/02.0090 as one of the research milestones set for the P3 Research Programme (*Research and modelling of heterogeneous materials and mechanical and biomechanical structures*).

Acknowledgements

First, I would like to express my sincere gratitude to my supervisor, Assoc. Prof. Ing. Jan Vimmr, Ph.D., for his support and guidance during the course of my Ph.D. study at the University of West Bohemia. His encouragement and motivation helped me during my research and the writing process.

I am also thankful to my colleague and co-member of our small research team, Ing. Ondřej Bublík, who provided me with valuable insights, stimulating discussions and help throughout my Ph.D. study.

I would like to give my sincere thanks to the medical doctors from the University Hospital in Pilsen, As. MUDr. Jiří Moláček, Ph.D., As. MUDr. Jan Baxa, Ph.D. and MUDr. Vladimír Mikulenka, for their valuable time, suggestions and clinical data that helped to shape the medical part of this Ph.D. thesis.

I am also grateful to all members of the Department of Mechanics for their endless support and encouragement during my Ph.D. study at the University of West Bohemia.

Last but not the least, I would like to dedicate this Ph.D. thesis to my immediate family, especially my mother. Without them and their unceasing support and patience, I would not be where I am today. Thank you for everything.

Alena Jonášová

Poděkování

Na tomto místě bych ráda vyjádřila poděkování svému školiteli doc. Ing. Janu Vimmrovi, Ph.D. za odborné vedení, cenné rady a podporu, které mi poskytoval během mého doktorského studia a v průběhu psaní této disertační práce. V této souvislosti bych ráda poděkovala i svému kolegovi Ing. Ondřeji Bublíkovi za výbornou spolupráci při řešení společných problémů.

Dále je mou povinností zde poděkovat lékařům z Fakultní nemocnice Plzeň, konkrétně As. MUDr. Jiřímu Moláčkovi, Ph.D., As. MUDr. Janu Baxovi, Ph.D. a MUDr. Vladimíru Mikulenkovi, kteří mi věnovali svůj čas a poskytli mi cenné rady, čímž jistě přispěli ke zkvalitnění této disertační práce po lékařské stránce.

Touto cestou bych rovněž chtěla vyjádřit svůj vděk pracovníkům Katedry mechaniky, Fakulty aplikovaných věd, Západočeské univerzity v Plzni, kteří mi během mého doktorského studia vytvořili vynikající pracovní prostředí a umožnili mi tak se plně věnovat svému studiu a psaní této disertační práce.

Tuto práci bych ráda věnovala své nejbližší rodině, především své mamince. Bez nich a jejich podpory a trpělivosti bych nikdy nemohla být tam, kde jsem dnes. Děkuji.

Alena Jonášová

Abstract

Hemodynamics with its ability to trigger pathological changes in blood vessels plays an important role in the patency and overall performance of implanted arterial bypass grafts. Based on this knowledge, the Ph.D. thesis is aimed at mathematical modelling of blood flow in idealised and patient-specific bypass models with the purpose to offer an alternative (non-clinical) approach to the study of bypass hemodynamics.

The blood is presented as an incompressible viscous fluid that exhibits complex flow properties dependent on various biological and abiological factors including the most important one—the shear rate. With regard to the focus of the Ph.D. thesis, the relevance of hemodynamics-vessel interaction is discussed in relation to graft failure. In most cases, this failure is a consequence of disturbed blood flow and prolonged exposure to abnormal shear stimulation. In the numerical simulations carried out for the purpose of this work, the human blood is assumed to be an incompressible generalised Newtonian fluid, motion of which is governed by the non-linear system of incompressible Navier-Stokes equations. The mathematical model coupled with an appropriate viscosity model for human blood is solved by utilising two different numerical approaches: the coupled method, represented by the artificial compressibility method, and the segregated method, which takes the form of two variations of the projection method. In either case, the spatial discretisation is performed by means of the cell-centred finite volume method formulated for unstructured computational meshes in 3D.

The computational ability of the developed algorithms is demonstrated by steady and pulsatile blood flow simulations aimed at the analysis of non-Newtonian effects and geometry importance in various bypass models, consisting of both proximal and distal anastomoses. All obtained numerical results are analysed and discussed in detail, with particular emphasis placed on the distribution of velocity and hemodynamical wall parameters (wall shear stress, oscillatory shear index), which are commonly used in the assessment of the relative risk of graft failure. Finally, in keeping with the trends of recent years, which show a preference for multiscale blood flow simulations, a lumped parameter model in the form of the three-element Windkessel model is introduced and applied as an outflow boundary condition in order to better approximate the response of a real downstream vascular bed to unsteady flow conditions.

Keywords:
vascular bypass, blood flow, incompressible non-Newtonian fluid, finite volume method, artificial compressibility method, projection method, three-element Windkessel model

Abstrakt

Hemodynamika, resp. proudění krve, jako jeden ze spouštěcích faktorů patologických procesů uvnitř cév, může významným způsobem ovlivnit dlouhodobou životnost a funkčnost implantovaných bypassových štěpů. Záměrem předkládané disertační práce, jež se zabývá matematickým modelováním proudění krve v idealizovaných a reálných modelech cévních bypassů, je poskytnout alternativní (neklinický) náhled na výzkum v této oblasti.

Lidská krev je zde uvažována jako nestlačitelná vazká kapalina, která vykazuje složité tokové vlastnosti závislé na různých biologických a nebiologických faktorech včetně toho nejvýznamnějšího – smykové rychlosti. S ohledem na zaměření práce je význam vzájemného působení hemodynamiky a cévní stěny diskutován v souvislosti s možným selháním implantovaného bypassového štěpu. Toto selhání je v mnoha případech vyvoláno narušeným proudovým polem a dlouhodobým působením abnormálního smykového napětí. Pro numerické simulace prezentované v této práci je proudění lidské krve, modelované jako nestlačitelná zobecněná newtonská kapalina, popsáno nelineárním systémem Navierových-Stokesových rovnic uzavřených vhodným konstitutivním vztahem pro dynamickou viskozitu krve. Matematický model je numericky řešen pomocí dvou různých přístupů: sdružené metody, zastoupené metodou umělé stlačitelnosti, a nesdružené metody, založené na dvou variantách projekční metody. Ve všech případech je pro prostorovou diskretizaci použita „cell-centred“ metoda konečných objemů formulovaná pro nestrukturované výpočetní sítě ve 3D.

Vyvinuté výpočetní algoritmy jsou implementovány pro numerické řešení ustáleného a pulzačního proudění krve v různých modelech cévního bypassu složeného z proximální a distální anastomózy. Získané numerické výsledky jsou detailně analyzovány a diskutovány s ohledem na charakter proudového pole a rozložení významných hemodynamických parametrů (smykové napětí na stěně, oscilační smykový index) běžně používaných pro posouzení rizik možného selhání chirurgicky vytvořeného bypassu. V souladu s nejnovějšími trendy jsou na výstupech reálného modelu aorto-koronárního bypassu aplikovány takové okrajové podmínky, jež jsou schopny aproximovat průtokový odpor reálné oběhové soustavy. Tyto okrajové podmínky jsou získány řešením vhodně nalazených tříprvkových Windkessel modelů.

Klíčová slova:
cévní bypass, proudění krve, nestlačitelná nenewtonská kapalina, metoda konečných objemů, metoda umělé stlačitelnosti, projekční metoda, tříprvkový Windkessel model

Contents

Nomenclature

Symbol	Description
A	outlet area
A_i	mesh node
$\boldsymbol{A}_{\mathrm{NS}},\ \boldsymbol{A}_{\mathrm{Poi}}$	sparse square matrices of order $3N_{CV}$ and N_{CV}
$a,\ b$	parameters of the modified Cross model
$\tilde{a}$	artificial speed of sound
$\boldsymbol{b}_{\mathrm{NS}},\ \boldsymbol{b}_{\mathrm{Poi}}$	right hand-side vectors of order $3N_{CV}$ and N_{CV}
C	vessel compliance, capacitance (Windkessel model)
CFL	constant of the CFL stability condition
$\mathcal{D}$	dissipative operator
D	tube diameter, native artery diameter
$\mathbf{D} = \frac{1}{2}\left(\nabla\boldsymbol{v} + (\nabla\boldsymbol{v})^T\right)$	rate of deformation tensor
D_{II}	second invariant of the rate of deformation tensor $\mathbf{D}$
$D_{ij},\ D_i$	octahedral and pentahedral dual cells
$\lvert D_{ij}\rvert,\ \lvert D_i\rvert$	volume of octahedral and pentahedral dual cells $D_{ij},\ D_i$
d	graft diameter
d_{ij}	components of the rate of deformation tensor $\mathbf{D}$
$\boldsymbol{\mathcal{F}}_m^I,\ \boldsymbol{\mathcal{F}}_m^V$	inviscid and viscous numerical fluxes through the face Γ_i^m
$\boldsymbol{F}_s^I(\boldsymbol{w}),\ \boldsymbol{F}_s^V(\boldsymbol{w})$	vectors of inviscid and viscous fluxes ($s = 1, 2, 3$)
$\tilde{\boldsymbol{F}}_s^I(\boldsymbol{w})$	vector of inviscid fluxes modified in the sense of ACM
$\boldsymbol{f}_m^I,\ \boldsymbol{g}_m^I,\ \boldsymbol{h}_m^I$	Cartesian components of the inviscid numerical flux $\boldsymbol{\mathcal{F}}_m^I$
$\boldsymbol{f}_m^V,\ \boldsymbol{g}_m^V,\ \boldsymbol{h}_m^V$	Cartesian components of the viscous numerical flux $\boldsymbol{\mathcal{F}}_m^V$
$\mathcal{H}$	unstructured hexahedral mesh
$H_i,\ \lvert H_i\rvert$	hexahedral control volume ($H_i \in \mathcal{H}$) and its volume
$\boldsymbol{J}_s(\boldsymbol{w})$	Jacobi matrices of the inviscid fluxes $\tilde{\boldsymbol{F}}_s^I(\boldsymbol{w})$, $s = 1, 2, 3$
$\mathcal{M}$	unstructured tetrahedral mesh
$m,\ n$	parameters of the Carreau-Yasuda model
N_{CV}	total number of control volumes
N_{out}	number of all outlets
$\boldsymbol{n}_{ij},\ \boldsymbol{n}_k^m$	outward unit vectors normal to the face Γ_{ij} or Γ_k^m
p	static pressure
p_d	distal pressure (Windkessel model)
$Q,\ Q_0$	flow rate, average flow rate
$\mathcal{R}$	spatial discretisation operator
$R_d,\ R_p$	distal and proximal resistances (Windkessel model)
Re	Reynolds number
res	relative residuum
$\boldsymbol{S}^m = [S_1^m, S_2^m, S_3^m]^T$	outward surface vector normal to the face Γ_i^m
s	diameter of stenosed native artery

Symbol	**Description**
T	cardiac cycle period, temperature
$t,\ \tilde{t}$	time, fictitious time
V	face-normal velocity
$\boldsymbol{v} = [v_1,\ v_2,\ v_3]^T$	velocity vector
$\hat{\boldsymbol{v}} = [\hat{v}_1,\ \hat{v}_2,\ \hat{v}_3]^T$	intermediate velocity vector
$\boldsymbol{w} = [p, v_1, v_2, v_3]^T$	vector of primitive variables, vector of unknowns
Wo	Womersley number
$\overline{\mathrm{WSS}}$	normalised WSS magnitude
$\boldsymbol{x} = [x_1, x_2, x_3]^T$	spatial coordinate vector
$\boldsymbol{x}_{\mathrm{NS}},\ \boldsymbol{x}_{\mathrm{Poi}}$	column vectors of unknowns of order $3N_{CV}$ and N_{CV}
α	junction angle, under-relaxation parameter
β_2	constant of the Jameson's artificial viscosity
$\Delta t,\ \Delta\tilde{t}$	time step, fictitious time step
$\Delta\mathrm{OSI},\ \Delta\mathrm{WSS}$	OSI/WSS difference between non-Newton. and Newton. values
$\delta\mathrm{OSI}, \delta\mathrm{WSS}$	relative OSI/WSS difference
δ	artificial compressibility
δ_{ij}, δ^i_j	Kronecker delta
$\varepsilon^{(2)}_{im},\ \hat{\varepsilon}_i,\ \hat{\varepsilon}_{[m]}$	coefficients of the Jameson's artificial viscosity
$\eta,\ \eta(\dot{\gamma})$	dynamic viscosity, shear-dependent dynamic viscosity
η_a	apparent dynamic viscosity
$\eta_0,\ \eta_\infty$	limit values of dynamic viscosity for $\dot{\gamma} \to 0$ or $\dot{\gamma} \to \infty$
$\dot{\gamma}$	shear rate
Γ_{ij}	face shared by the control volumes H_i and H_j
$\Gamma^m_i,\ \lvert\Gamma^m_i\rvert$	m-th face of the hexahedral control volume H_i and its length
$\Gamma^m_k,\ \lvert\Gamma^m_k\rvert$	m-th face of the tetrahedral control volume Ω_k and its length
λ	relaxation time (non-Newtonian viscosity models)
λ_{si}	i-th eigenvalue of the Jacobi matrix $\boldsymbol{J}_s(\boldsymbol{w})$
$\Omega,\ \Omega_h$	computational domain and its approximation
$\Omega_k,\ \lvert\Omega_k\rvert$	tetrahedral control volume ($\Omega_k \in \mathcal{M}$) and its volume
Ω_{T}	space-time cylinder
ω	angular frequency
$\partial\Omega,\ \partial\Omega_h$	domain boundaries of Ω and Ω_h
Φ	arbitrary flow quantity
Ψ	pressure correction function
$\varrho,\ \tilde{\varrho}$	fluid density, artificial density
τ_m	wall shear stress of Poiseuille flow
$\boldsymbol{\tau}_W,\ \lvert\boldsymbol{\tau}_W\rvert$	wall shear stress (WSS) vector and its magnitude
$\lvert\overline{\boldsymbol{\tau}_W}\rvert$	cycle-averaged WSS magnitude
τ_0	yield stress

Superscript	**Description**
$*$	dimensionless quantity
$\hat{}$	intermediate quantity
0	initial value, i.e., at the time $t = 0$ or $\tilde{t} = 0$
(A), (CA)	value belonging to aorta or coronary artery
(G), (A)	value belonging to bypass graft or native artery
n	time level
s	inner iteration index
(θ)	fluid index (Newtonian fluid: $\theta = 0$, non-Newtonian fluid: $\theta = 1, 2$)

Subscript	**Description**
I, inlet	inlet boundary, inlet value
i, k	indices of hexahedral and tetrahedral control volumes or values belonging to those control volumes
lm	index of a control volume adjacent to the m-th face of another cell
$[m]$, $[m_{+/-}]$	auxiliary indexing of adjacent control volumes
O, outlet	outlet boundary, outlet value
ref	reference/characteristic value
W, wall	wall boundary, wall value

Abbreviation	**Description**
ACM	artificial compressibility method
C model	modified Cross model ($\theta = 2$)
CABG	coronary artery bypass grafting
CT	computed tomography
CVD	cardiovascular disease
CY model	Carreau-Yasuda model ($\theta = 1$)
ETE anastomosis	end-to-end anastomosis
ETS anastomosis	end-to-side anastomosis
FVM	finite volume method
Hct	hematocrit (volume fraction of blood made up of erythrocytes)
IFH	intimal intracellular hypertrophy
IH	intimal hyperplasia
OSI	oscillatory shear index
PRT	particle residence time
STS anastomosis	side-to-side anastomosis
TTV	thrombotic threshold velocity
vWF	von Willebrand factor, a blood glycoprotein contained in plasma
WSS	wall shear stress
WSSG	wall shear stress gradient

Chapter 1

Introduction

1.1 Motivation

According to the World Health Organisation (WHO) of the United Nations (UN) [117, 197], the disease of the cardiovascular system ranks among the leading causes of premature death in the Western world. In addition to the non-negligible loss of human lives, the cardiovascular disease (CVD) has also a considerable impact on the economy of each country including that of the Czech Republic, which belongs to the most affected states in Europe [131]. In case of severe and life-threatening damage to arteries, often caused by atherosclerosis, implantation of one or several bypass grafts is usually the only way to fully restore blood flow and tissue function. Although more long-term effective than the traditional forms of CVD medical treatment such as the balloon angioplasty, the lifespan of vascular bypasses is not unlimited and has been observed to be (in)directly influenced by the effects of blood flow and wall shear stress [7, 52, 204].

In an attempt to reduce the failure rate of bypass grafts and to improve the quality of health care provided to the CVD patients, increased attention has been paid in the last decades to the research of hemodynamics and its influence on the patency and performance of bypass grafts. Besides the medical research outlined, e.g., in [129], new possibilities and opportunities offered by mathematical modelling and modern computer technology have led to an alternative view of the hemodynamics-vessel interaction, as reported in the review papers [107,122,136]. Although still far from being able to simulate real processes in living organisms, present numerical simulations of bypass hemodynamics are able to provide a valuable source of information and in many cases can be used as useful guides for medical doctors and engineers in search of an optimal graft design [1,153] or ideal synthetic graft [189].

1.2 State of the art

Although the study of bypass hemodynamics is almost as old as the bypass grafting itself, the application of computational fluid dynamics (CFD) as an effective numerical tool for blood flow simulations has become widespread only in the last two decades, as illustrated in the three most recent review papers [107, 122, 136].

Due to unavailability of robust and reliable commercial CFD software that could be used for biofluid simulations, the beginnings of hemodynamical studies in 1980s and 1990s were defined by the development of own in-house software, e.g., [11, 38, 59, 99]. It was only during the last decade or so that the commercial CFD software packages have become more popular in the scientific community. Among the most often used codes, it is possible to mention Fluent (ANSYS Inc., Canonsburg, USA), e.g., [70, 133, 199], and ANSYS CFX (ANSYS Inc., Canonsburg, USA), e.g., [55, 71, 152], based on the finite volume and finite element approaches, respectively. Although quite many

numerical procedures for the solution of the non-linear system of incompressible Navier-Stokes equations are currently available, see [58, 178], the pressure-based methods also denoted as the pressure-correction methods seem to be the most commonly preferred form of numerical solution of flow problems involving blood flow through a complex bypass geometry, e..g, [12, 20, 95]. To be more specific, the majority of published studies on the topic of bypass hemodynamics usually utilise computational algorithms of the SIMPLE class such as the SIMPLE [55, 83], SIMPLEC [70, 99] and PISO [133, 199] algorithms.

Although CFD is currently accepted as an alternative to often expensive and time consuming in vitro and in vivo measurements, the need for software verification and validation of computed results still remains. Thus, besides the purely experimental studies such as [49,63], there are studies, e.g., [12,38,139], that are able to combine both techniques. In other words, they perform numerical simulations as well as experimental measurements and compare the obtained flow characteristics with each other in order to determine the validity of their computations.

Taking into consideration only the most significant studies published on the topic of bypass hemodynamics, the objectives of the works mentioned above can be divided as:

1) study of bypass hemodynamics:

Although the blood flow in large- and middle-sized arteries is always unsteady due to the cyclic nature of the heart pump, several studies showed that some understanding of bypass hemodynamics can be gained from steady flow simulations as well. In this case, it is often the influence of geometry on the blood flow that is of main interest, e.g., [11] (distance of grafting), [83] (stenosis degree) and [84,95] (junction angle), although steady flow conditions are also applied in studies aimed at the analysis of non-Newtonian effects, e.g., [20]. By contrast, pulsatile blood flow is considered in several key studies such as the work by Bonert *et al.* [13], which addresses the issue of side-to-side anastomoses as opposed to the traditional interest in distal end-to-side anastomoses, or by Papaharilaou *et al.* [139], which confirms considerable flow differences between planar and out-of-plane geometries.

During the last decade, the scientific community has become interested in the aorto-coronary bypass—one of the most common types of vascular bypasses [34]. After the idealised geometries, which in fact consist of two tubes (aorta and coronary artery) interconnected with one tube of an appropriate length (graft) [28, 164, 207], recent years have brought a new impulse in the form of patient-specific bypass models reconstructed from CT and/or MRI scans, see, e.g., [43, 162]. In addition to the real geometries, the trend of the last two/three years also indicates that the future of blood flow simulations will belong to multiscale modelling, as apparent from the paper [162], which introduces a lumped parameter (0D) model coupled to a 3D aorto-coronary bypass model.

2) improvement of anastomosis geometry:

Besides the attempts to study bypass hemodynamics, a number of approaches have been used to improve the long-term patency of bypass grafts. Probably the most common improvement is in the form of so-called *cuff and patch anastomotic designs*, which form a new anastomosis geometry by utilising venous cuffs or patches [73]. Selected well-known anastomotic designs are shown in Fig. 1.1 and just as any other bypass geometry have been of main interest in several hemodynamical studies, e.g., [98,99] (Taylor patch)

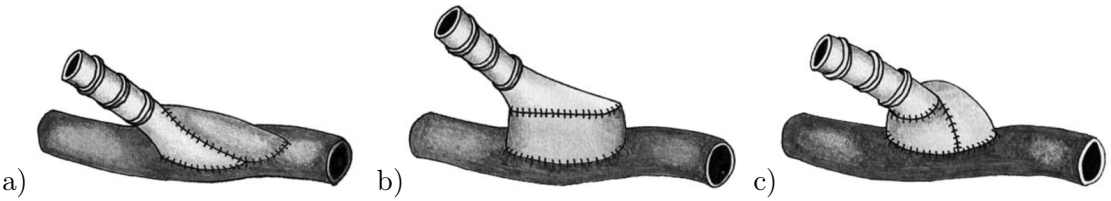

Fig. 1.1. Schematic drawing showing various cuff/patch anastomotic designs [73]: a) Taylor patch, b) Miller cuff, c) vein boot (St. Mary's boot, Tyrrell collar).

and [55, 101, 143] (Miller cuff). Based on clinical trials and numerical studies, the low failure rate of these designs is usually attributed to the gradual transition of compliance at the graft-artery interface and to the improved local hemodynamics [52].

Aside from the commonly used cuff and patch designs, other possible modifications of the anastomosis and/or graft geometries can be found in literature. Although some of these designs are rather of theoretical importance such as the two-way bypass graft introduced by Qiao *et al.* [151, 152], Fig. 1.2a, it is possible to find several original and clinically promising graft designs. For example, there is the called 'y-graft' [133], which essentially replaces the standard end-to-side anastomosis with two end-to-end anastomoses, see Fig. 1.2b, or the helically sinuous vascular prosthesis also known as helical graft, Fig. 1.2c, which has been proposed to enhance the mixing of blood flow and to prevent thrombosis [96, 194]. In recent years, much attention is also paid to the design proposed by Kabine *et al.* [70, 71], which has been developed as a combination of the side-to-side and end-to-side anastomoses, Fig. 1.2d.

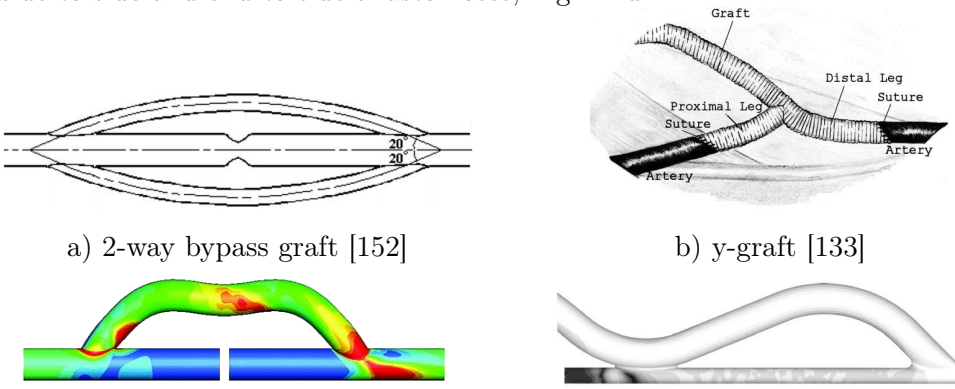

a) 2-way bypass graft [152]

b) y-graft [133]

c) helical graft [194]

d) double anastomosis [70]

Fig. 1.2. Selected new graft and anastomosis designs as proposed in literature.

3) fluid-structure interaction in bypass models:

Despite the fact that venous grafts are known to become rigid after implantation (a process called 'arterialisation'), it is possible to find several studies that solve the fluid-structure interaction (FSI) problem by assuming compliant bypass geometries. Probably the most renowned works are those by Hofer *et al.* [59] and Leuprecht *et al.* [101], which simulate the interaction between pulsatile Newtonian blood flow and a linearly elastic, geometrically non-linear shell structure by means of commercial software ABAQUS coupled to an appropriate CFD solver. According to the observations made in these

two papers, the dissimilar compliances of the graft and native artery (also denoted as *compliance mismatch*) result in very small changes in hemodynamics, but increase the intramural stress and strain at the suture line. One of the more recent studies, which once again models the compliant bypass walls as a linearly elastic, geometrically non-linear shell structure, is the work by Kabine *et al.* [71], which besides FSI also considers blood's non-Newtonian rheology and for the numerical solution utilises the commercial ANSYS Workbench (ANSYS Inc., Canonsburg, USA).

As apparent from the literature review, the mathematical modelling of blood flow has gained popularity in the non-medical community as a result of advances in computer technology and numerical mathematics and, considering the new possibilities offered by the various medical imaging techniques, an increased interest on the part of medical doctors can be expected, as well. Note that a much more extensive overview of studies related to the problem of cardiovascular bypasses can be found in the monograph [C.2] co-authored by the author of this Ph.D. thesis or in the review papers [107, 122, 136].

1.3 Objectives of present work

On the basis of the literature review provided above, the Ph.D. thesis, which is focused on the mathematical modelling of blood flow and the assessment of arterial bypass graft patency, aims to contribute to the research of bypass hemodynamics by pursuing the following main objectives:

- *to use complete bypass models consisting of both proximal and distal anastomoses*

Contrary to the common practice of many authors, who ignore the proximal anastomosis and usually substitute the residual flow through an arterial stenosis with a (not always physiologically accurate) flow rate division between the bypass graft and the native artery (see, e.g., [12,20,199]), only complete bypass models are to be considered. This objective stems from the need to adequately approach the problem of boundary values.

- *to understand the role of geometry in bypass hemodynamics*

Although the literature review showed quite many studies addressing the problem of bypass geometry, it should be noted that there is no work that would provide a comprehensive analysis of different geometrical parameters on one type of bypass models only. Moreover, the geometries of widening and tapered grafts have been so far ignored by the scientific community despite the fact that they may appear in real patients in the form of partially stenosed or reversed venous grafts.

- *to investigate the relevance of non-Newtonian effects*

The objective is to answer the question whether the shear-dependent viscosity of human blood can significantly alter the bypass hemodynamics and affect so the prognosis of graft failure. For this purpose, idealised as well as patient-specific bypass models are to be used with flow conditions corresponding to the type of bypassed native artery.

- *to introduce the three-element Windkessel model as an outflow boundary condition*

As the standard outlet boundary condition is not always able to approximate the response of a real downstream vascular bed to unsteady flow conditions, a lumped (0D) model is to be applied in accordance with recent trends in blood flow modelling, which show a strong preference for multiscale models.

Following the focus of this Ph.D. thesis, *Chapter 2* is organised into sections that describe the liquid and cellular components of the human blood from biological and

biomechanical perspectives. The facts are provided with emphasis placed on physical and flow properties of blood and discussed in accordance with possible blood cell damage arising from non-uniform hemodynamics. Based on these facts, the second half of *Chapter 2* addresses several main factors known to affect blood viscosity such as the hematocrit and temperature and provides an overview of viscosity models commonly used for the description of blood rheology.

At the beginning of *Chapter 3*, a brief introduction into the history and significance of implanted bypass grafts is made in order to understand all the consequences arising out of their failure. For the sake of completeness, main causes of graft failure are mentioned and put in context with disturbed hemodynamics. Consequently, the significance of blood flow is examined with respect to the susceptibility of the vascular wall to pathological changes such as atherosclerosis and intimal hyperplasia. The chapter is concluded by defining several hemodynamical indicators such as the cycle-averaged wall shear stress (WSS) and the oscillatory shear index (OSI), which are also used in the analysis of numerical results presented in this Ph.D. thesis.

The content of *Chapter 4* can be divided into two parts: The first one introduces the blood as an incompressible, homogeneous, generalised Newtonian fluid and describes its motion as a laminar flow governed by the non-linear system of incompressible Navier-Stokes equations. The second, larger, part covers the numerical solution of the aforementioned governing equations by means of the cell-centred finite volume method and two different numerical approaches. The first one based on the artificial compressibility method is characterised by a simultaneous solution of all unknowns, whereas the second approach utilises the principles of segregated methods known as the projection methods, which use a specially derived equation for pressure to correct the computed velocity field.

Chapter 5 is designed to present a detailed analysis and discussion of numerical results obtained with the in-house software, computational algorithms of which are based on the numerical methods described in the previous chapter. The analysis of computed velocity fields and selected hemodynamical wall parameters is organised into three parts according to the studied bypass geometry and prescribed flow conditions. While the first two sections are dedicated to the modelling of blood flow in idealised bypass models, the third one is directed towards simulations in patient-specific geometries reconstructed from CT scans provided by the courtesy of the University Hospital in Pilsen. In accordance with the current trends in blood flow modelling, which include the application of lumped parameter models, *Chapter 5* also presents results of our first attempt at multiscale modelling, which takes the form of several three-element Windkessel models coupled to the 3D bypass models via their coronary artery outlets.

The Ph.D. thesis and its contributions are summarised in *Chapter 6*, which also mentions possible improvements and future perspectives in the field of mathematical modelling of bypass hemodynamics. For the sake of completeness, three appendices are added to the work: *Appendix A* describes the calculation of shear rate, which the non-Newtonian models introduced in *Chapter 2* require to be a known quantity. *Appendix B* contains instructions regarding the implementation of the interpolation method mentioned in Chapter 4. Finally, *Appendix C* addresses the issue of the lumped parameter models in more detail and provides a derivation of the governing equations for the above-mentioned three-element Windkessel model.

Chapter 2

Blood and its flow properties

2.1 Human blood

Similarly to other mammalian blood, human blood is a highly specialised liquid tissue that usually accounts for 6-9% of the human body weight. As an incompressible viscous fluid of red colour and classified as a coarse dispersion, blood exhibits complex flow properties in dependence on various biological and abiological factors. The density of normal blood, which consists of particles (37-54%) suspended in a fluid extracellular matrix known as plasma (46-63%), Fig. 2.1 (left), ranges between 1043 to 1066 $\mathrm{kg\,m^{-3}}$ [36]. This density may strongly differ between each individual depending on various factors such as gender, state of health and physical condition. In addition to other extracellular liquids (lymph, cerebrospinal fluid etc.), the unique composition of blood enables it to perform several functions vital to the living organism:

- *internal respiration* – transport of respiratory gases (O_2, CO_2) from lungs to tissues and vice versa using different partial pressures,
- *maintenance of cellular metabolism* – transport of hormones, vitamins (biocatalysts), nutrients and waste products from and to tissues,
- *maintenance of internal equilibrium (homeostasis)* – pH between $7.35 - 7.45$, constant osmotic pressure of blood around 690 kPa, constant ratio of mineral ions: Na^+, K^+ (sodium-potassium pump), Ca^{2+} (neuromuscular activity), Fe^{2+} (erythrocyte production) etc.,
- *immune system* – defence of the organism against foreign substances and pathogens including production of antibodies,
- *thermoregulation* – maintenance of constant body temperature essential for normal metabolism and the course of enzymatic reactions (warm arterial blood travelling from the body core exchanges heat with the cooler venous blood at the periphery),

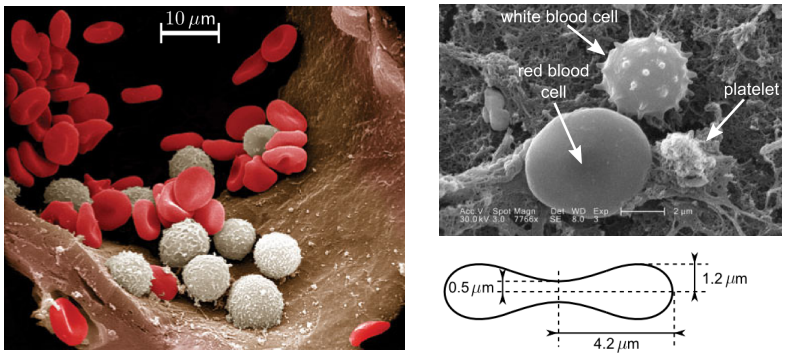

Fig. 2.1. A scanning electron microscope image of blood cells (*left*), size comparison of blood cells (*right top*), average dimensions of a red blood cell (*right bottom*).

- *coagulation* – hemostasis that includes the formation of an insoluble network of fibrin fibres (clot) and promotes the healing responses.

Inadequate blood supply to tissues and organs also known as *ischemia* is often associated with oxygen and nutrient deficiency and accumulation of waste products, which gradually lead to tissue dysfunction and necrosis. Generally, ischemia may be caused by problems with blood composition or circulation. The most common cases of restricted blood supply include stenosed or occluded arteries that are damaged by atherosclerosis and/or blood clots (thrombi and/or emboli).

Blood plasma as the liquid component of blood serves as a transport medium for blood cells and chemical substances such as water, hormones and lipids. Its appearance resembling a transparent liquid with a faint straw color is given by the dissolved bilirubin (yellow breakdown product of normal heme catabolism). The density of blood plasma is mostly around $1025\,\mathrm{kg\,m^{-3}}$ but may change in dependence on actual chemical composition, which is made up of 92% water. The remaining 8% belong mainly to blood proteins and inorganic electrolytes. Some of the plasma proteins and their main functions in human body are listed in Tab. 2.1.

blood proteins	vol pct	main functions
albumins	60%	regulation of osmotic pressure (osmoregulation), transport of chemicals, ability to bind water
globulins	35%	carrier of antibodies (immunoglobulins), transport of lipids and water-insoluble ions
fibrinogen	4%	main element of blood clotting (fibrin fibres)
other proteins	<1%	regulation of biochemical reactions etc.

Tab. 2.1. Blood proteins and their main functions in human body [37]. Here, the abbreviation 'vol pct' stands for volume percent.

Blood cells suspended in plasma, Fig. 2.1, can be divided into three main categories: red blood cells, white blood cells and platelets, Tab. 2.2. The volume fraction of each cell type is to a great extent influenced by gender, state of health and physical condition. Average density of all blood cells, which is strongly dependent on the volume fraction of red blood cells, is stated to be approximately $1125\,\mathrm{kg\,m^{-3}}$.

2.1.1 Erythrocytes (red blood cells, RBCs)

Erythrocytes as the most significant transmitters of respiratory gases[1] in human body are highly specialised, denucleated cells with a typical biconcave shape, Fig. 2.1, and density around $1090 - 1100\,\mathrm{kg\,m^{-3}}$. The cytoplasm of erythrocytes contains the metalloprotein hemoglobin (around $28 - 32 \times 10^{-12}\,\mathrm{g}$ per cell) surrounded by a flexible cell membrane, which enables them to deform in microvessels with inner diameters comparable to the diameter of the blood cell alone. The ability to transport respiratory gases is granted

[1] Around 97% of oxygen is transported via the erythrocytes in dependence on partial pressure (total saturation with oxygen occurs at $p(\mathrm{O_2}) = 20\,\mathrm{kPa}$ [175]), the remaining 3% are physically dissolved in plasma.

blood cells		vol pct	size [μm]	quantity [cells/mm^3]
red blood cells		95%	see Fig. 2.1	male: $4.3 - 5.3 \times 10^6$ female: $3.8 - 4.7 \times 10^6$
white blood cells	neutrophils	0.13%	$10 - 12$	$3\,000 - 6\,000$
	eosinophils		$13 - 14$	$50 - 250$
	basophils		$9 - 10$	$0 - 100$
	lymphocytes		$6 - 8$	$1\,500 - 3\,000$
	monocytes		$15 - 25$	$300 - 500$
platelets		4.9%	$2 - 4$	$1.5 - 3.5 \times 10^5$

Tab. 2.2. Volume fraction and average dimensions of blood particles [175, 192].

by the biomolecule hemoglobin, whose heme groups with iron atoms Fe^{2+} can bind and release gas molecules in dependence on their partial pressure in lungs and tissues.

Due to their biconcave shape and their ability to deform, the erythrocytes are perfectly adapted for maximum gas saturation and passage through microvessels such as capillaries, Fig. 2.2. According to [175], an erythrocyte of normal shape is capable to go through a capillary with inner diameter smaller than $3\,\mu$m without change of volume or surface area. Moreover, the surface area of an average erythrocyte with volume about $87\,\mu$m^3 is 40% bigger compared to that of a spherical cell with the same volume ($163\,\mu$m^2 vs. $95\,\mu$m^2) [18], providing for an efficient gas exchange in tissues and lungs. However, if an erythrocyte is damaged or undergoes pathological structure/shape changes, its ability to deform and the amount of transported gases are the first to be affected. Shape disorders such as the ones shown in Fig. 2.3 (spherocytosis, eliptocytosis etc.) may be caused by hemoglobin disorders or lack of the structural protein spectrin in cytoskeleton and cell membrane [127]. It is proven that all erythrocytes with abnormal shapes exhibit reduced deformability, enhanced resistance to repeated capillary passage and reduced osmotic resistance promoting membrane damage and cell destruction.

Fragility and enhanced membrane permeability of erythrocytes is often associated with *hemolysis* – hemoglobin release or destruction of the whole red blood cell. In addition to the factors mentioned above, the membrane of erythrocytes is also sensitive to physical factors such as low or high temperatures and abnormal values of fluid shear stress. According to [175], permanent erythrocyte damage may be observed at temper-

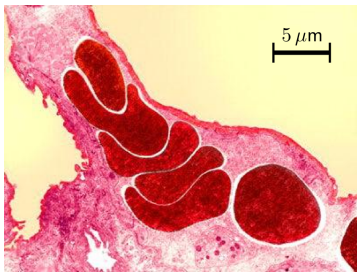

Fig. 2.2. Deformation of erythrocytes in a capillary.

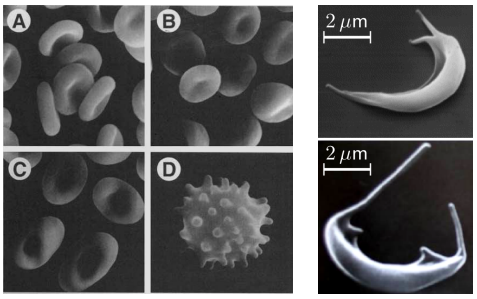

Fig. 2.3. Pathological changes in erythrocyte shape [127], sickle cell anemia.

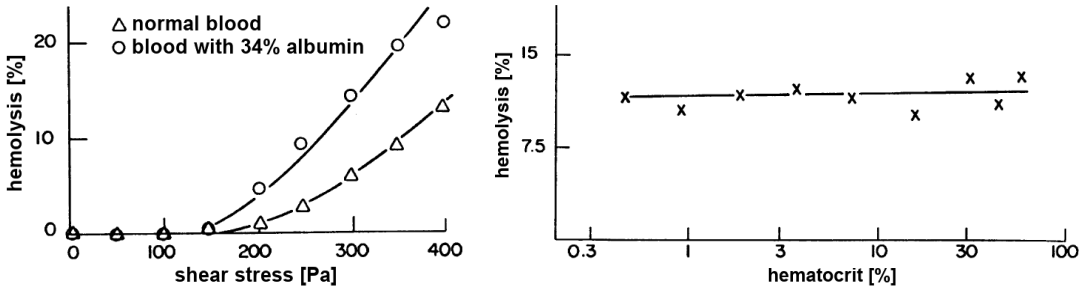

Fig. 2.4. Influence of shear stress (*left*) and hematocrit (*right*) on the hemolysis of erythrocytes in a rotational viscometer [103].

atures greater than 47°C or when reaching critical shear stress (150 Pa for long-time loads or 10^3 Pa for very short-time loads, see Fig. 2.9). The threshold value of 150 Pa is also mentioned in [103], where it is shown that the hemolysis is a function of time and shear stress, but is not influenced by the number of interacting cells, Fig. 2.4 (right). In the last years, the investigation of hemolysis and irreversible damage of erythrocytes has found many applications in the field of artificial prostheses such as prosthetic heart valves, see the value ranges listed in Tab. 2.3. Nowadays, much attention is also given to the mechanical damage of erythrocytes resulting in the loss of their membrane elasticity. This cell damage is commonly known as *pre-hemolytic injury*, and compared to the much higher hemolytic shear stress (150 – 400 Pa), occurs at values around 30 Pa [97].

Among the many parameters associated with erythrocytes, there is one that particularly stands out – the *hematocrit* (Hct). This parameter expresses the (percentage) volume fraction of blood which is made up of erythrocytes, Fig. 2.5. The hematocrit value is known to be influenced by many factors such as gender (male: 39-49%, female: 35-46%), age (premature infants: 65-75%, newborn infants: 50-60%) or partial pressure of oxygen (adults living at very high altitudes: 60%) [175]. In addition to these factors, it is important to take into account the fact that even in an individual, the hematocrit may not remain constant and behaves more like a dynamic parameter, especially if the individual is exposed to stress situations or suffers from pathological or psychosomatic disorders [6].

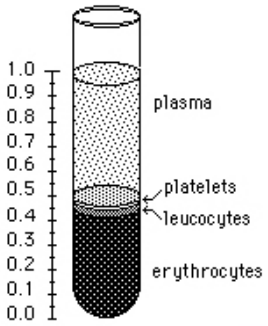

Fig. 2.5. Hematocrit

2.1.2 Leukocytes (white blood cells, WBCs)

Compared to the red erythrocytes, the leukocytes are colourless, nucleated cells, whose main function in the human body is the defence against foreign substances and pathogens by phagocythosis or by producing proteins called antibodies. To the leukocytes, blood serves only as a transport medium that they can leave and return to at any time. In a healthy human, leukocytes can be divided into five main categories according to their size and internal structure: neutrophils, eosinophils, monocytes, lymphocytes and basophiles. Similarly to the hematocrit in the case of erythrocytes, the (percentage) volume fraction of leukocytes present in the blood stream is expressed by a special parameter known

	shear rate $\dot{\gamma}$ [s^{-1}]	shear stress τ [Pa]
large- and middle-sized arteries	300−1 000	1−4
arterioles	500−1 600	2−6
veins	20−250	0.1−1
stenosed artery	5 000−12 000	20−50
prosthetic heart valve	200−200 000	1−1 000

Tab. 2.3. Overview of shear rate and shear stress ranges in vessels and vascular prostheses [88, 97].

leukocyte	pct	main functions
neutrophil	50-70%	phagocytosis of bacteria
eosinophil	2-4%	defence against parasites, modulation of inflammatory processes
monocyte	2-8%	production of macrophages
lymphocyte	20-30%	killing of tumor cells and cells infected by a virus, production of antibodies
basophil	<1%	release of histamin and other inflammatory mediators

Tab. 2.4. Leukocytes and their main functions in human body [37].

as *leukocrit* (Lct). It is also worth mentioning that that the sum of hematocrit and leukocrit values remains roughly constant in each individual, even if he suffers from hyperleukocytosis (a form of leukemia with Lct above $25 - 30\%$) [175].

Because each group of leukocytes is adapted to cause a different immune reaction, Tab. 2.4, their relevant densities may vary according to their internal structure. For example, [175] mentions the density of lymphocytes and monocytes between $1055 - 1070\,\mathrm{kg\,m^{-3}}$ and for neutrophils and eosinophils between $1075 - 1085\,\mathrm{kg\,m^{-3}}$. Compared to erythrocytes, the leukocytes are less deformable [21,104]. On the other hand, their deformability may drastically change after their activation during inflammatory processes, when they go through many biochemical and morphological changes that significantly affect their mechanical properties (they usually become more rigid) [6]. Because of their low numbers and limited deformability, the hemodynamical importance of leukocytes becomes apparent only in microvessels, where they contribute to the non-uniform distribution of blood particles [21]. According to [6], leukocytes may often be the cause of temporary capillary blockage, Fig. 2.6, especially if the cell is larger than the capillary lumen or is in its activated and more rigid form. In general, the entering of a leukocyte in to a capillary is 1-2×10^3-times longer than that of a deformable erythrocyte [175].

2.1.3 Thrombocytes (platelets)

Thrombocytes are cell fragments with density around $1030\,\mathrm{kg\,m^{-3}}$. In appearance, they are similar to irregular discs, whose main function in the human body is the transport of enzymes and other chemical substances necessary for the process of *coagulation*. The

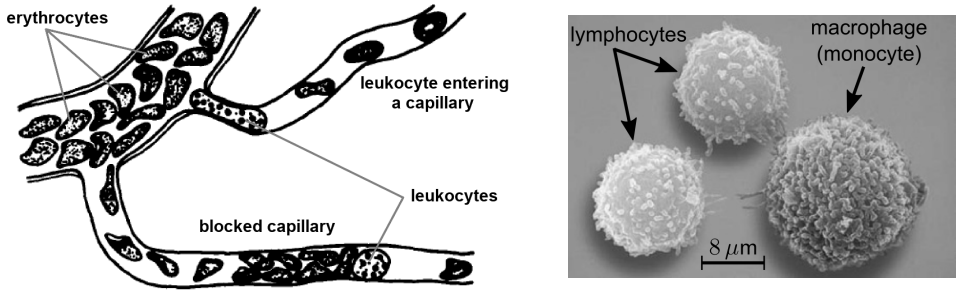

Fig. 2.6. Schematic drawing showing possible reasons for increase/decrease of local hematocrit in relation to leukocytes [150]. Size comparison of white blood cells.

thrombocytes contribute to the maintenance of the inner equilibrium (homeostasis) by creating a temporary blood clot/plug at the site of vessel injury. This process of clot formation can be divided into four phases that may occur simultaneously and have multiple interactions [198]:

1) *adhesion* – triggering of thrombosis by a thrombogenic surface (artificial surfaces, subendothelial and medial layers of blood vessels etc.), thrombocytes adhere to the surface/site of injury,
2) *activation* – thrombocytes undergo morphological and biochemical changes to increase the strength of adhesion and produce biologically active substances,
3) *aggregation* – other activated thrombocytes aggregate to the site of injury, where they connect to the present thrombocytes,
4) *coagulation* – triggering of the coagulation cascade leading to fibrin coagulation that results in the formation of insoluble network of fibrin fibres.

The process of coagulation itself is very complex and influenced by many coagulation and anti-coagulation factors so as to prevent its spontaneous triggering. Currently there are several mathematical models describing the formation of blood clots by respecting the influence of biochemical, physiological and rheological factors, see, for example, [3].

An essential part of the whole coagulation process is the activation of thrombocytes, which takes place when the thrombocyte comes into contact with an exposed collagen of the vessel wall or with the thrombin (an activated form of the coagulation factor known as prothrombin) [14]. A distinctive feature of thrombocyte activation is the change of its shape from a disc-like to an amorphous/stellate one, Fig. 2.7 (left). One of the many important factors involved in the coagulation process is the von Willebrand factor (vWF), a blood glycoprotein synthesised in endothelium and contained in blood plasma. At the site of injury, the vWF promotes adhesion and aggregation of thrombocytes by binding to the exposed wall collagen and to the membrane receptors GP-Ib of the thrombocytes [88] enabling so the formation of a primary blood clot (*white thrombus*). After the activation of the coagulation cascade, the plasma protein fibrinogen is transformed into dissoluble fibrin fibres resulting in a fibrin network with captured blood cells, Fig. 2.7 (middle). This final form of the blood clot is commonly known as the *red thrombus*.

Besides the physiological and biochemical factors, the behaviour of thrombocytes and the coagulation are also affected by the hemodynamical and rheological factors, especially by the values of shear rate and shear stress [61]. Moreover, the presence and number

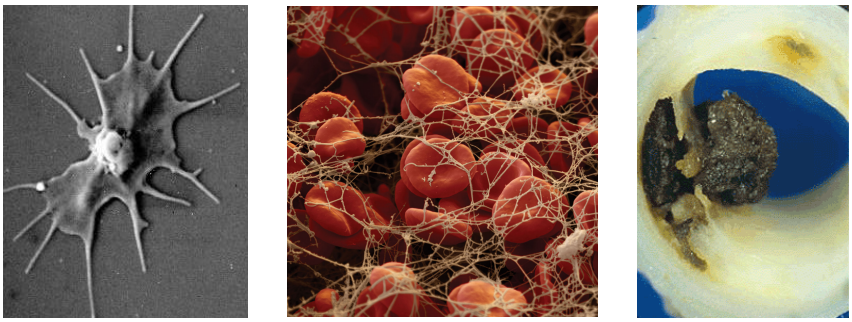

Fig. 2.7. Activated thrombocyte (*left*), a blood clot with fibrin fibres and captured erythrocytes (*middle*), thrombus as a result of atherosclerotic plaque rupture (*right*).

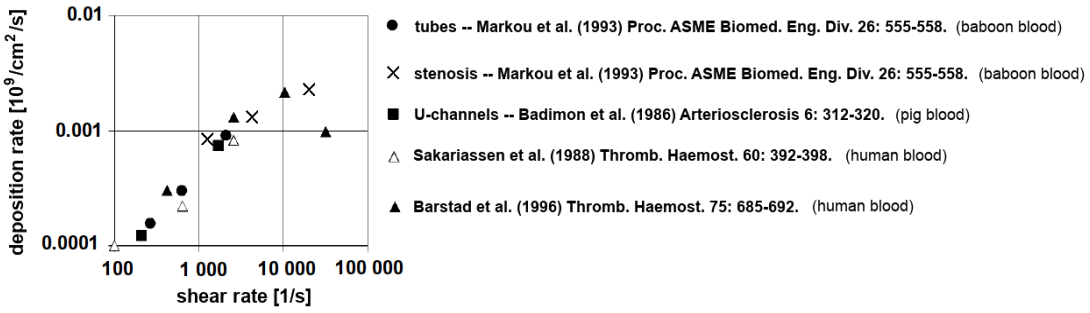

Fig. 2.8. Accumulation of thrombocytes as a function of shear rate according to several selected ex vivo measurements [198].

of erythrocytes is known to positively influence the transport of thrombocytes to the injury site. On the one hand, the thrombocytes are pre-stimulated by a non-zero shear stress originating in their interaction with the erythrocytes, and on the other hand, they are also coordinated in the direction of the vessel wall. In other words, the erythrocytes with their tendency to move near the centre line [6, 137], force the smaller thrombocytes to the vessel wall, where they may accumulate. The concentration of thrombocytes is a function of hematocrit Hct, shear rate and number of thrombocytes. For example, in a 3 mm diameter tube and for blood with Hct = 40% and average number of thrombocytes ($2.5 \times 10^5/\text{mm}^3$), thrombocyte concentration near the walls has been observed to increase two- to four-times if the shear rate increased from $240\,\text{s}^{-1}$ to $1\,200\,\text{s}^{-1}$ [198].

It has been also noted that the behaviour of thrombocytes in relation to their adhesion and accumulation on the exposed collagen in the vessel wall may be stimulated by the local shear rate [198]. According to the experimental results shown in Fig. 2.8, the thrombocytes are not overly affected if the shear rate is smaller than $100\,\text{s}^{-1}$, but they proportionally increase their accumulation for shear rates between $100 - 10\,000\,\text{s}^{-1}$. According to [4], the accumulation decline observed for values higher than $10\,000\,\text{s}^{-1}$ is caused by the destruction of the cell membrane. The tendency of thrombocytes to adhere themselves to the exposed collagen at high shear rates has been proven by clinical studies in stenosed arteries, while a completely opposite behaviour (the thrombocyte adhesion is suppressed even at high shear rates) has been observed in the case of smooth synthetic materials.

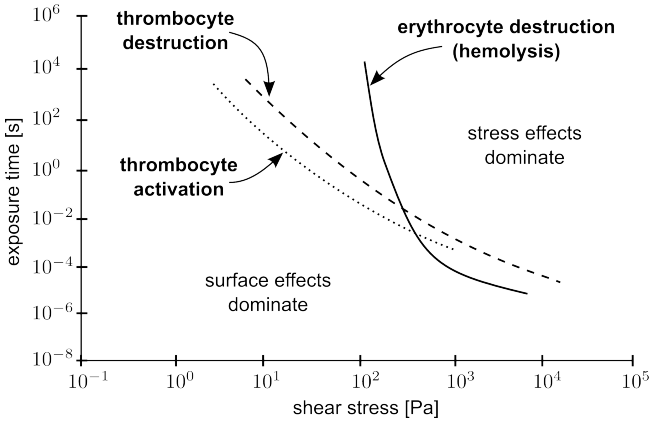

Fig. 2.9. Influence of shear stress and exposure time on the behaviour of thrombocytes and erythrocytes [18]. The graph shows thresholds for hemolysis and thrombocyte activation and destruction.

In addition to chemical stimuli, the thrombocytes may be also activated by prolonged exposure to high shear stress or rapid increases in shear stress, see Fig. 2.9. Their first morphological and biochemical changes have been observed with shear stress magnitudes of $5-10$ Pa [62], while values above 25 Pa have been usually sufficient for the destruction of the whole thrombocyte (*platelet lysis*) [88]. In this case, it is important to note that the time of exposure is also crucial for the determination of the 'destructive' shear stress. According to [4], a platelet-rich plasma shows signs of platelet lysis if it is exposed to shear stresses above 16 Pa for 5 min, while for the 30 s exposure time, shear stresses higher than 60 Pa are required.

Similarly to the adhesion and activation phases, the aggregation of thrombocytes is to a certain degree influenced by the hemodynamics. For example, the shear stress is involved in the formation of bindings between the thrombus components and indirectly determines the binding glycoprotein [65]. For shear stress values below 1.2 Pa, the aggregation has been observed to proceed on the fibrinogen basis using thrombocyte membrane receptors. The main disadvantage of such thrombi is their instability because they disintegrate after an exposure to shear stresses greater than 6.8 Pa. The second type of thrombocyte aggregation, which employs the vWF instead of the fibrinogen, Fig. 2.10, is considerably more stable but does not occur for shear stresses below 8 Pa [88].

Disorders associated with the thrombocytes can be divided into two categories. The first one includes disorders that are induced by an abnormal number of thrombocytes and that are known to trigger hemophilia or thrombosis accompanied by ischemia. The disorders of the second category are a result of thrombocyte dysfunction such as limited adhesion or aggregation. Due to their considerable importance during the coagulation, the thrombocytes play a crucial role in several cardiovascular diseases such as myocardial infarction, brain stroke and venous thrombosis. In most cases, the aggregation of activated thrombocytes in the form of thrombi or emboli is the main reason for ischemia or vessel blockage.

The formation of a thrombus inside a blood vessel resulting in its partial or complete blockage, Fig. 2.7 (right), is commonly called *thrombosis*. Aside from the risk arising from

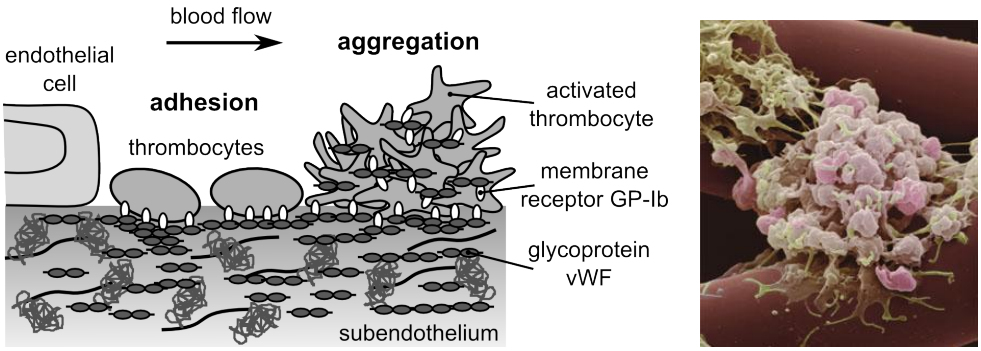

Fig. 2.10. Schematic drawing showing adhesion and aggregation of thrombocytes via vWF (*left*), aggregation of activated thrombocytes at an injury site (*right*).

the blockage of vital vessels, there is also the risk of a released thrombus (also known as embolus), which may travel within the blood stream and clog a major organ inducing its total collapse (brain stroke, pulmonary embolism etc.). The thrombosis is usually triggered by a ruptured atherosclerotic plaque, see Fig. 2.7 (right), turbulent blood flow causing endothelial damage or flow stagnation characterised by extremely low Reynolds numbers ($\mathrm{Re} < 17$ [175]).

The risk of thrombosis is often associated with the hemodynamic parameter known as *particle residence time* (PRT) [16]. It helps to determine how much the particle has to interact with reactive elements in the local environment and if it may trigger possible pathological changes. In the case of recirculation zones, the probability of thrombus formation increases due to the high cell concentration and their inter-particle collisions, which in turn may negatively stimulate the thrombocytes. It is also interesting to note that the particle residence time in the case of stenotic arteries does not correlate with the degree of stenosis, i.e, a serious stenosis does not shield the particles from being washed away better than does a mild stenosis [10]. According to the experiments, the oscillation of blood flow, expressed with the Womersley number Wo, appears to be more important for the thrombus formation.

In artificial valves and synthetic vascular prostheses, where the shear values have been observed to be particularly high, see Tab. 2.3, the thrombus formation is assumed to be a result of so-called *platelet sensitisation*. It is assumed that the short-time exposure to extremely high shear stress leads to a partial activation of the thrombocytes, which then demonstrate an enhanced sensitivity to the local hemodynamics. In other words, the thrombocytes may be fully activated at much lower shear stress values than the non-affected ones. According to [168], the limit shear stress necessary for the platelet sensitisation lies between $200 - 240\,\mathrm{Pa}$.

2.2 Blood rheology

The flow properties of blood particles suspended in plasma in macroscopic, microscopic and submicroscopic dimensions are investigated by *hemorheology*, a science that also studies the interaction of blood and its components with vasculature and foreign materials such as vascular prostheses and medicaments [167]. Most of our current knowledge

about basic blood rheology comes from early experimental studies carried out in the 60s and 70s of the last century. Among the many of the studies originating from this time period, it is possible to mention, for example, the works of Merrill and Wells [118, 120, 193] or Lichtman [104].

Based on the experimental results presented in the studies mentioned above, the human blood is known to behave as a non-Newtonian fluid with complex flow properties. Next to the Newtonian fluids, which demonstrate simple rheological behaviour dependent on one scalar parameter—the dynamic viscosity η, the non-Newtonian fluids and their motion are influenced by various factors from shear rate to history of previous deformations. Thus, for certain experimental conditions (shear rate, temperature ...), the rheological measurements of the non-Newtonian fluids determine only their *apparent viscosity*

$$\eta_a = \tau(\dot{\gamma})/\dot{\gamma}\,, \tag{2.1}$$

where $\tau(\dot{\gamma})$ is the shear stress measured at a given shear rate $\dot{\gamma}$. The dependence of shear stress τ or dynamic viscosity η on shear rate $\dot{\gamma}$ can be graphically expressed in the form of a flow curve. For illustration, Fig. 2.11 shows the flow curves of selected Newtonian and non-Newtonian fluids.

On the basis of the facts mentioned in Section 2.1, it is somewhat understandable that the flow properties of human blood are to some degree dependent on the chemical composition of blood plasma and on the hematocrit. Besides these two factors, which may significantly affect the apparent viscosity, there is also the inner diameter of the vessels also known as vessel lumen. Its influence on blood viscosity becomes apparent by comparing the blood flow in capillaries, where the size of the blood cells is comparable to the vessel lumen, and large-sized arteries such as the aorta. An overview of blood's rheological properties at the macro- and micro-levels is listed in Tab. 2.5.

For the mathematical modelling of hemodynamics, the whole human blood may be considered to be either an isotropic, homogeneous, incompressible fluid or a multiphase fluid with viscoelastic properties depending on the modelling scale. Although the model transition from the homogeneous fluid to the multiphase one can not be uniquely determined, the literature mentions several approximate threshold lumen values. For example, the authors of [167] claim that in large vessels with inner diameters around $1 - 3\,\mathrm{cm}$,

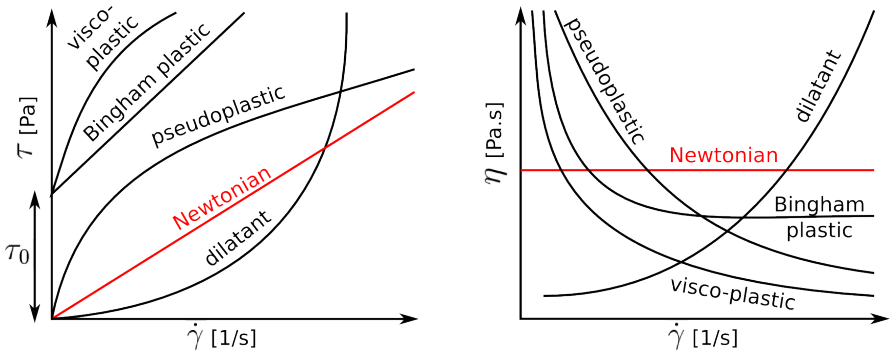

Fig. 2.11. Flow curves of Newtonian and time-independent non-Newtonian fluids – shear stress τ vs. shear rate $\dot{\gamma}$ (*left*) and dynamic viscosity η vs. shear rate $\dot{\gamma}$ (*right*).

bulk properties factors			→ flow resistance in large vessels
blood viscosity			hematocrit plasma viscosity erythrocytes aggregation erythrocytes deformation
cell properties factors			→ resistance to capillary entry and obstruction of microvessels
erythrocytes	deformability adhesiveness		intrinsic structure plasma factors
leukocytes	deformability adhesiveness		intrinsic structure functional state (activation) plasma factors

Tab. 2.5. Rheological properties of blood and their major determining factors [130]

the blood may be assumed to behave as a homogeneous Newtonian fluid, whereas in smaller vessels (lumen between $0.2 - 1\,\mathrm{cm}$), blood exhibits remarkable non-Newtonian properties such as shear-thinning viscosity and viscoelasticity. A different opinion can be found in [175], where the limit for the homogeneous non-Newtonian fluid is stated to be the vessel lumen of $500\,\mu\mathrm{m}$. Below this diameter ($50 - 100\,\mu\mathrm{m}$), the blood behaviour corresponds to that of a two-phase fluid because of the presence of a cell-free plasma layer near the vessel walls, see the Fåhræus-Lindqvist effect described in Section 2.2.2.

Regardless of the threshold diameters mentioned above, the dominant factor that influences the blood flow in large- and medium-sized vessels is known to be the dynamic viscosity [100]. Therefore, for the mathematical modelling of blood flow in such vessels, it is commonly acceptable to use one of the well-known macroscopic non-Newtonian models [144]. The parameters appearing in these viscosity models (some of them are described in Section 2.3) are commonly determined on the basis of experimental measurements with viscometers. In contrast to the viscometry of abiological fluids, the measurement of blood viscosity is much more complex and requires systematic preparation to avoid unwanted changes in the measured blood sample. One of changes to be avoided is the coagulation of the sample, which is initiated after the blood removal from the body. To delay the overall degradation of the blood sample, anticoagulants such as heparin, sequestrate or citrate in isotonic concentrations are usually added. In this context, it is somewhat disputable whether the altered blood sample will have the same rheological properties as the one before the addition of anticoagulants. On the other hand, the authors of [120] claim that the key rheological features of human blood with or without the anticoagulants remain relatively unchanged if the measurement is completed within 8 hours after the blood collection.

Besides the problems with blood degradation, the reliability of the measured data is also dependent on the accuracy of the used viscometer. In other words, broader ranges ($100 - 1\,000\,\mathrm{mPa\,s}$) usually come at the sacrifice of accuracy. Thus, for the clinical measurement of blood and plasma viscosities, viscometers with a linear response from approximately 1 to $10\,\mathrm{mPa\,s}$ are the most suitable ones [161]. The main advantages and disadvantages of several viscometers known to be often used for the measurement of

blood viscosity can be summarised as follows:

- **Capillary viscometers** (diameter of the constricted part has to be $\geq 300\,\mu$m [47])
  The main advantage of this type of viscometers is the short amount of time necessary for the measurement completion, which in the case of blood helps to avoid its excessive degradation [161]. Among the known disadvantages, it is possible to mention the problem with keeping a constant shear rate $\dot{\gamma}$ in the whole blood sample (high $\dot{\gamma}$ at the walls and very low $\dot{\gamma}$ around the capillary centre line [6]) or the difficulty with low shear rate measurements (sedimentation of blood cells and their non-uniform distribution within the sample [118]).
- **Rotational viscometers** (coaxial cylinders, cone-plate, plate-plate etc.)
  Next to the capillary viscometers, the rotational ones are one of the most often used devices for the measurement of blood and plasma viscosities in clinical practice [161]. The most commonly used type of the rotational viscometers is the configuration known as 'cone-plate' [6], whose main advantage in relation to blood's shear-dependent viscosity is its property to maintain constant shear rate within the measured sample.
- **Falling body viscometers**
  This type of viscometers is known to be able to perform reliable short-time measurements at very low shear rates due to its ability to minimally disturb the internal structure of the measured blood sample. For illustration, Fig. 2.12 shows the comparison between the viscosities measured with a falling ball viscometer and cone-plate viscometer for shear rate values in the range of $0.1 - 100\,\mathrm{s}^{-1}$ [35].

Note that the basic principles of the viscometers mentioned above are addressed in the monograph [C.2] co-authored by the author of this Ph.D. thesis. For more details on the topic of viscometry and rheology, it is also possible to refer, for example, to [67,112,166].

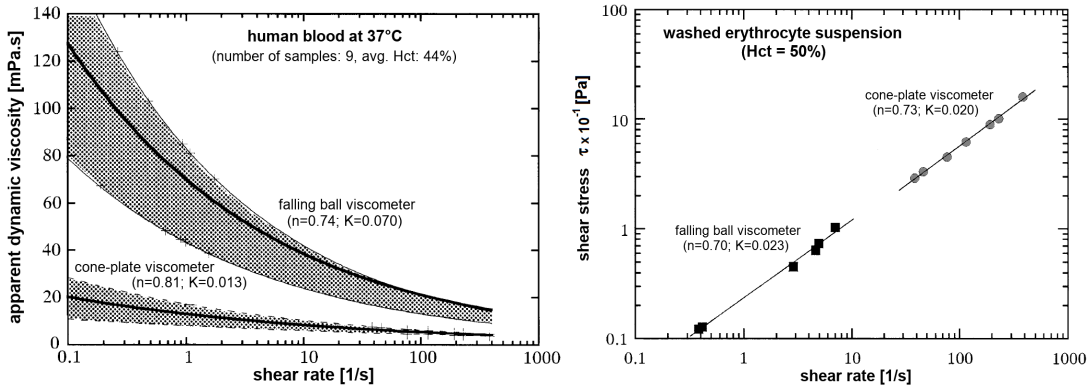

Fig. 2.12. Flow curves obtained with a falling ball and cone-plate viscometer [35]: apparent dynamic viscosity of human blood vs. shear rate for normal human blood (*left*) and shear stress vs. shear rate for washed suspension of erythrocytes (*right*). Parameters n and K represent the rheologic constants of the power law model $\tau = K\dot{\gamma}^n$.

2.2.1 Plasma viscosity

The blood plasma devoid of cells and enriched with anticoagulants demonstrates the flow properties of a Newtonian fluid. For a healthy human, the dynamic viscosity of the plasma is stated to be $1.1 - 1.35\,\mathrm{mPa\,s}$ at the temperature of 37°C [6] or $1.5 - 1.72\,\mathrm{mPa\,s}$ at 25°C [130]. Despite the initial uncertainty regarding the presence of non-Newtonian effects in the early viscometric measurements of the plasma [200], the majority of experts currently inclines to the model of the Newtonian fluid. According to [118], the rather contradictory viscometric results of the past can be explained by the presence of a thin surface film between the plasma and air resulting in the fluctuation of the measured quantities at low shear rates.

In addition to the influence of age, gender and physical condition [47], the plasma viscosity is strongly dependent on the volume fraction of proteins dissolved in it. According to [130], the main plasma proteins – albumins, globulins and fibrinogen influence the final viscosity out of 36%, 41% and 22%, respectively. In most cases, the viscosity increase is often caused by the elevated fibrinogen level. Although the actual increase of plasma viscosity may be eventually small, the role of fibrinogen during the coagulation process and its final influence on the viscosity of the whole blood may not be so negligible, see Section 2.2.2. Another factor affecting the plasma viscosity is the temperature. According to [192], an increase of 1°C leads to a viscosity increase of 2-3% assuming the temperature range of $25 - 37$°C. An empirical formula describing this dependence can be found, for example, in [200]

$$\eta_p(T) = \eta_p^{37^\circ\mathrm{C}} \cdot e^{\,0.021\,(37-T)}\,, \tag{2.2}$$

where T is the temperature in °C and $\eta_p^{37^\circ\mathrm{C}}$ is the reference value of plasma viscosity at 37°C. The function given by Eq. (2.2) is shown in Fig. 2.13 for three different reference values corresponding to an average and two limit values of plasma viscosity in accordance with [6] and [200].

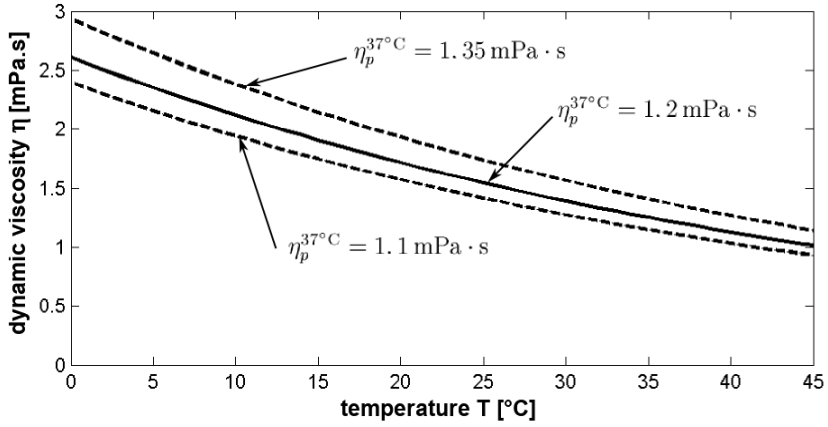

Fig. 2.13. Dynamic viscosity of plasma $\eta_p\,(T)$ as a function of temperature T according to Eq. (2.2). The curves are plotted for three reference values of plasma viscosity $\eta_p^{37^\circ\mathrm{C}}$ at 37°C.

In clinical practice, the plasma viscosity serves as a non-specific indicator of pathological phenomena. A profound viscosity increase is often associated with the presence of pathogens in the human body and is caused by elevated levels of special plasma proteins commonly called acute-phase proteins (APP), which are part of the organism defence and are particularly active during inflammatory processes and tumour growth [170]. For example, the disease known as paraproteinemia (the presence of paraproteins in the blood indicates leukemia) is characterised by an increase of plasma viscosity up to values of $5 - 6\,\mathrm{mPa\,s}$ [6]. Enhanced viscosity has been also observed by patients with diagnosed ischemic heart disease [69]. Tab. 2.6 contains a small overview of physiological and pathological values of plasma viscosity at the temperatures of 25°C and 37°C.

plasma viscosity	$\eta\,[\mathrm{mPa\,s}]$		occurrence, disease indication
	$T = 25°\mathrm{C}$	$T = 37°\mathrm{C}$	
low	<1.40	<1.05	found in infants under 3 years old and patients with low immunoglobulin and fibrinogen levels
normal	1.40–1.75	1.05–1.30	healthy adult
high	1.75–2.00	1.30–1.46	chronic disorders (infection, vascular diseases), autoimmune diseases (lupus ...)
very high	2.01–3.00	1.47–2.18	high concentration of paraproteins, multiple myeloma (leukemia)
extremely high	>3.00	>2.18	Waldenström's macroglobulinaemia (a rare form of leukemia)

Tab. 2.6. Physiological and pathological values of plasma viscosity [9].

2.2.2 Blood viscosity

As mentioned earlier in Section 2.2, the human blood generally behaves as a non-Newtonian fluid with viscosity that may be influenced by various biological and abiological factors (cholesterol level, physical condition, gender etc.). Normal blood with 45% hematocrit is known to have a non-zero yield stress and to exhibit a non-linear flow curve, Fig. 2.14. Because of these flow properties, the blood is often assumed to be a visco-plastic fluid with constitutive equation in the form of the Casson equation, see, for example, [46, 120, 193]. However, it is important to mention that the experts in hemorheology are not united regarding the existence and significance of the yield stress τ_0 [47]. Even though many hemorheological studies tend to the opinion that blood is a visco-plastic fluid, the yield stress remains even now a very controversial topic because of its difficult determination. Part of this controversy is probably caused by inaccurate experimental results at extremely low shear rates ($10^{-3}\,\mathrm{s}^{-1}$), which may lead to underestimation of the measured yield stress [145]. The importance of the used viscometer is also supported by the experimental results presented in [35], where the authors compare the measuring abilities of falling body and rotational viscometers, see Fig. 2.12.

The non-Newtonian behaviour of the blood is predetermined by the large amount of erythrocytes contained in it. The specific properties of erythrocytes are, in this case, crucial because their tendency to aggregate or to deform under the acting forces signif-

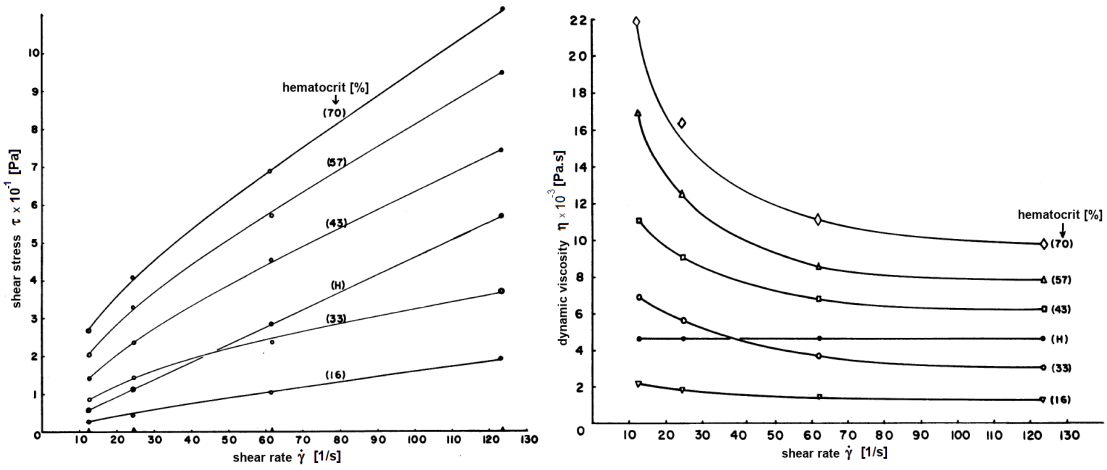

Fig. 2.14. Influence of shear rate $\dot{\gamma}$ on shear stress τ (*left*) and dynamic viscosity η (*right*) for different values of hematocrit Hct at a temperature of 37°C [193]. The sample labelled with the letter H represents measurements obtained for the Bureau of Standards calibration oil with constant dynamic viscosity $\eta_H = 4.69\,\mathrm{mPa\,s}$ at 37°C.

icantly influences the flow properties of the whole blood [6]. Fig. 2.15 shows the flow curves for normal blood and specially modified erythrocyte solutions with or without the ability to deform or aggregate. Besides their deformability and tendency to aggregate, the erythrocytes also demonstrate viscoelastic behaviour, especially in pulsatile blood flow at low shear rates and in microvessels [23, 167].

The erythrocyte aggregation with the consequent increase of blood viscosity for shear rates lower than $10\,\mathrm{s}^{-1}$ is closely connected with the formation of certain structures that

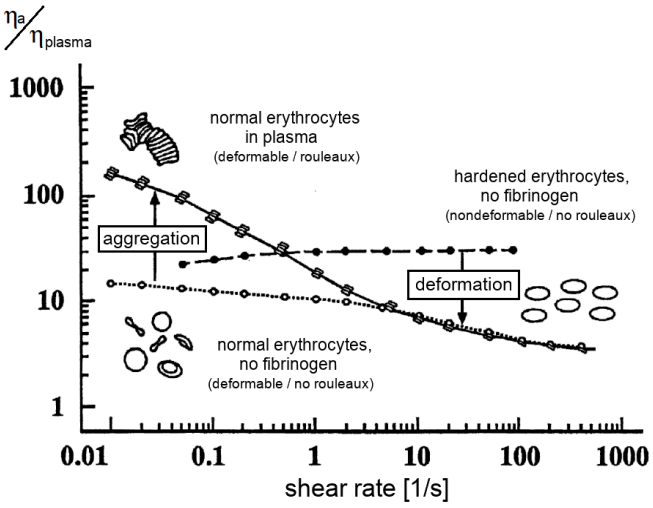

Fig. 2.15. Relative viscosity of blood as a function of shear rate for three different types of erythrocytes ($T = 310\,\mathrm{K}$, Hct = 45%, $\eta_{plasma} = 1.2\,\mathrm{mPa\,s}$) [44].

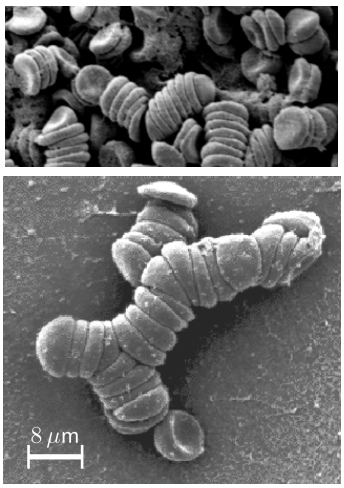

Fig. 2.16. Erythrocyte aggregation and formation of rouleaux at low shear rates.

are commonly called *rouleaux* (rouleau structures), Fig. 2.16. With further decrease of shear rate below $1\,s^{-1}$, the complexity of these structures increases resulting in a large spatial cluster similar to a net. The presence of such clusters within the blood is the main reason for the sudden increase of dynamic viscosity. An opposite effect connected with the rouleaux breakdown can be observed with increasing shear rate. According to [200], the limit shear rate value at which individual cells exist is around $50\,s^{-1}$. With $\dot{\gamma} > 100\,s^{-1}$, the erythrocytes exist as individual cells, stretch and line up with the plasma streamlines, decreasing so the flow resistance [46]. During this 'deformation' phase, the whole blood behaves as a Newtonian fluid with an apparent constant viscosity. Because the rouleaux formation takes time (up to 10 s [144]), it is also possible to classify the blood as a time-dependent non-Newtonian fluid with thixotropic properties [200].

The influence of erythrocyte membrane and its flexibility on the flow properties of the whole blood has been proven by many rheological measurements, whose selected results are shown in Fig. 2.17. From both graphs, it is very well apparent that the flexibility of the particles has a considerable impact on the dynamic viscosity of the whole suspension, which is the lowest in the case of the normal blood with hematocrit around 45%. By contrast, the sickle shaped erythrocytes (Fig. 2.3) known for their reduced deformability show behaviour similar to that of rigid particles, Fig. 2.17 (right).

Because of experimental measurements, we are currently aware of many factors that to some degree are able to affect the flow properties of the whole blood. Besides the effect of shear rate $\dot{\gamma}$, which will be discussed later, the blood viscosity is often associated with plasma proteins, temperature, hematocrit and vessel diameter (lumen). The importance of each of these factors will be addressed in the remainder of this section.

A) Influence of hematocrit

The hematocrit (Hct), as a volume fraction of erythrocytes in the whole blood, has a very strong influence on the final blood viscosity. The non-linear relation between the dynamic viscosity and hematocrit becomes very well apparent at low shear rates because

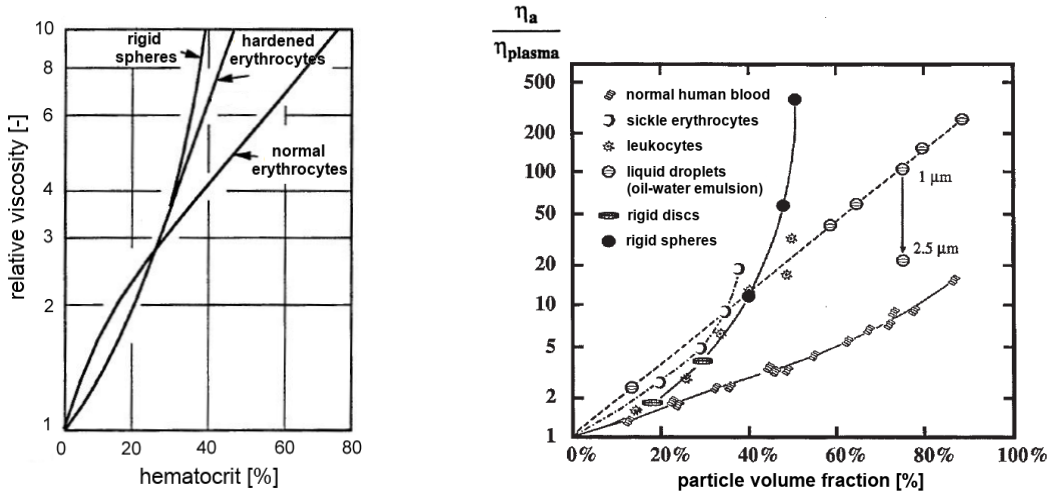

Fig. 2.17. Relative viscosity as a function of hematocrit and particle volume fraction for various suspended particles – [192] (*left*), [44] (*right*). Measured at the temperature of 298 K and for shear rates $\dot{\gamma} > 100\,s^{-1}$.

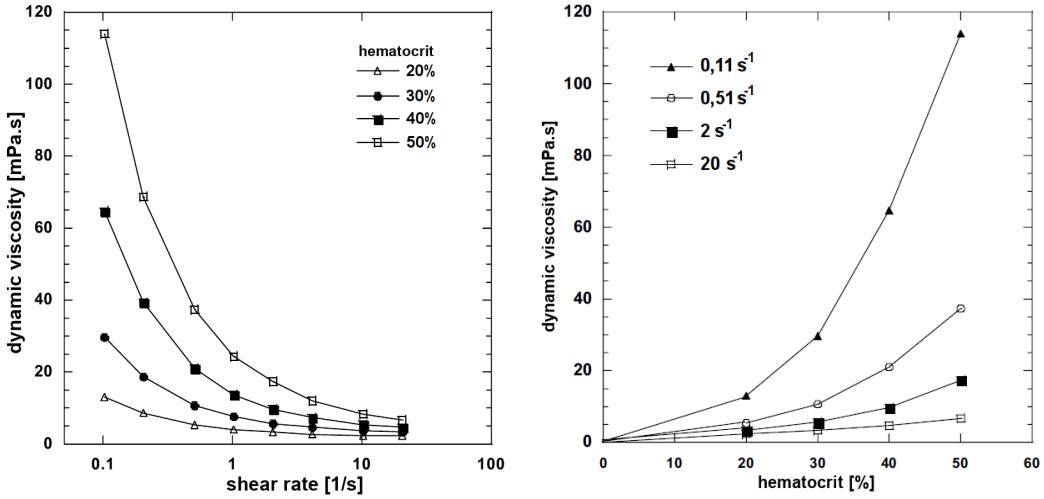

Fig. 2.18. Blood viscosity as a function of shear rate and hematocrit [56].

of the number of blood cells involved in the rouleaux formation, Fig. 2.18. According to [47], the blood's shear-thinning property vanishes for hematocrit values smaller than 13%, confirming so the assumption that the non-Newtonian behaviour is primarily caused by the presence of erythrocytes and their tendency to aggregate at low shear rates.

Despite the fact that the hematocrit is a dynamic quantity dependent on many factors such as age and gender[2], its physiological value usually ranges between 40 to 50%. This interval is a result of delicate balance between the amount of transported oxygen and the frictional resistance at the vessel wall [22]. In other words, the hematocrit is optimal if the number of erythrocytes is high enough to ensure adequate oxygen supply to the tissues and at the same time the cells contained in the blood do not increase the viscosity overmuch. In this regard, it has been proven that the oxygen amount is directly proportional to the number of erythrocytes to a certain critical hematocrit. After the exceeding of this value, the amount of oxygen brought to the tissues decreases due to the decreasing blood perfusion, which is a result of increasing blood viscosity and vessel resistance [6]. According to [23], a hematocrit increase of 10% will lead to viscosity increase of approximately 26%.

One of the well-known viscosity models, which besides the shear rate $\dot{\gamma}$ considers also the influence of hematocrit Hct, is the *2-parameter Wallburn-Schneck model* [47] based on the power law model

$$\eta(\dot{\gamma}, \mathrm{Hct}) = p_1 \, e^{p_2 \mathrm{Hct}} \, \dot{\gamma}^{(p_3 - p_4 \mathrm{Hct} - 1)} \,, \tag{2.3}$$

where $p_1 = 0.00148\,\mathrm{Pa\,s}^n$, $p_2 = 0.0512$, $p_3 = 1$ and $p_4 = 0.00499$. This model is valid for shear rates between 23.28 to $232.8\,\mathrm{s}^{-1}$ and $35 - 50\%$ hematocrit at 37°C.

Yield stress τ_0 is a sensitive index of blood fluidity, i.e., the acting shear stress has to be equal or greater than this critical shear stress value for the blood to flow ($\tau \geq \tau_0$). Considering the importance of the hematocrit and the plasma protein fibrinogen during

[2]Females have lower hematocrit and, thus, lower blood viscosity by approx. 14% than males [23].

the erythrocyte aggregation, it is only natural that they both influence the value of the yield stress [125, 146]. See, for example, Fig. 2.19. As for the temperature of the environment, it does not seem to affect the value of the yield stress in any significant way [119].

The yield stress of blood is derived by extrapolation from experimental data using suitable constitutional relationships, see, for example, [126, 146]. In general, the determination of the yield stress is difficult and strongly dependent on the accuracy of low shear rate measurements. The inaccuracies may arise from undesirable interaction between the blood cells and the viscometer walls or from blood slipping at the walls. With this in mind, it is, therefore, understandable that the literature offers many values of the yield stress at a broad shear rate range ($0.0002 - 0.04\,\mathrm{Pa}$ [47]) and for various exposure times.

For the sake of completeness, it would be appropriate to mention several selected empirical relationships that are currently used for the description of yield stress τ_0 [Pa] as a function of hematocrit and/or fibrinogen concentration. The first of the relationships is based on rheological measurements carried out for blood samples with $53 - 95\%$ hematocrit (Hct) and $\dot{\gamma} = 0.001 - 10\,\mathrm{s}^{-1}$ [146]

$$\tau_0 = A \cdot \mathrm{Hct}^3 \times 10^{-6}\,, \tag{2.4}$$

where $A = 0.02687\,\mathrm{Pa}$. Wider validity with critical hematocrit Hct_{crit} [%] around $5 - 8\%$ is achieved in the following two equations:

$$\sqrt[3]{\tau_0} = A\,(\mathrm{Hct} - \mathrm{Hct}_{crit}) \times 10^{-2}\,, \tag{2.5}$$

where $A = 0.0843 - 0.1\,\sqrt[3]{\mathrm{Pa}}$ [119], and

$$\begin{aligned} \tau_0 &= 0 && \text{for } \mathrm{Hct} < \mathrm{Hct}_{crit}\,, \\ \tau_0 &= 0.08\,(\mathrm{Hct} - \mathrm{Hct}_{crit})^3 \times 10^{-6} && \text{for } \mathrm{Hct} \geq \mathrm{Hct}_{crit}\,. \end{aligned} \tag{2.6}$$

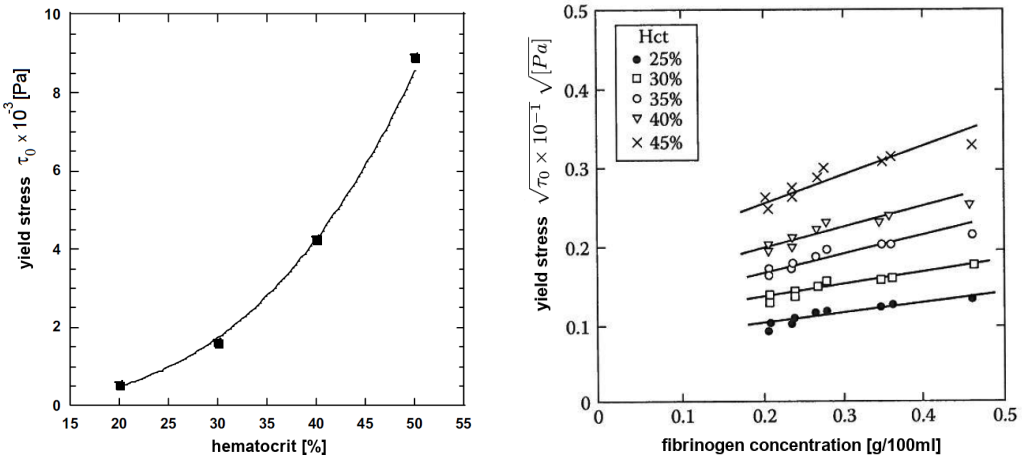

Fig. 2.19. *(Left)* Yield stress τ_0 as a function of hematocrit [5]. *(Right)* Effect of fibrinogen concentration on yield stress τ_0 for selected values of hematocrit Hct [192].

Lastly, the role of fibrinogen during erythrocyte aggregation at low shear rates and its influence on the yield stress is taken into consideration in the following relationship [192]

$$\sqrt{\tau_0} = (\mathrm{Hct} - 10)(C_F + 0.5) \cdot 10^{-\frac{3}{2}}\,, \tag{2.7}$$

where Hct [%] is the hematocrit and C_F [g/100 ml] is the fibrinogen concentration. The validity of Eq. (2.7) is limited to Hct $> 10\%$ and $C_F = 0.21 - 0.46\,\mathrm{g}/100\,\mathrm{ml}$. Further relationships for the calculation of the yield stress can be found, for example, in [200].

B) Influence of plasma proteins

In relation to blood viscosity, the concentrations of albumins, globulins and fibrinogen gain in importance at low shear rates when they begin to affect the erythrocyte aggregation and the yield stress [121]. Fig. 2.20 shows the flow curves for normal blood and isotonic suspensions containing physiological concentrations of each of the three plasma proteins. On the basis of these flow curves, the globulins seem to increase the blood viscosity, whereas the albumins moderate it so that the resulting blood viscosity is lower than that of the globulin suspension. By contrast, the isotonic suspension with fibrinogen, whose physiological concentration in a healthy human is around 4 g/l, shows no so significant changes in the blood viscosity. Considering the volume fraction of the three plasma proteins in the whole blood (Tab. 2.1), the dominant effect of globulins and albumins on the blood viscosity is understandable.

The graph in Fig. 2.21 offers a different perspective on the role of plasma proteins in viscosity increase at low shear rates. Compared to the results displayed in Fig. 2.20, the flow curves in Fig. 2.21 are plotted for isotonic suspensions containing blood cells. The data make it possible to assess the effect of fibrinogen on erythrocyte aggregation or to observe the viscosity change in the absence of all plasma proteins (washed cells in

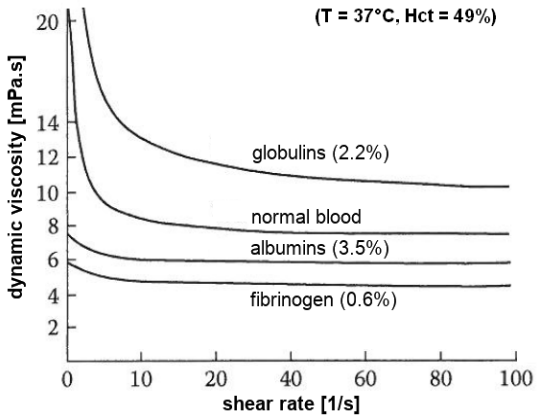

Fig. 2.20. Dynamic viscosity–shear rate relationships for normal blood and isotonic suspensions containing selected plasma proteins at 37°C [192].

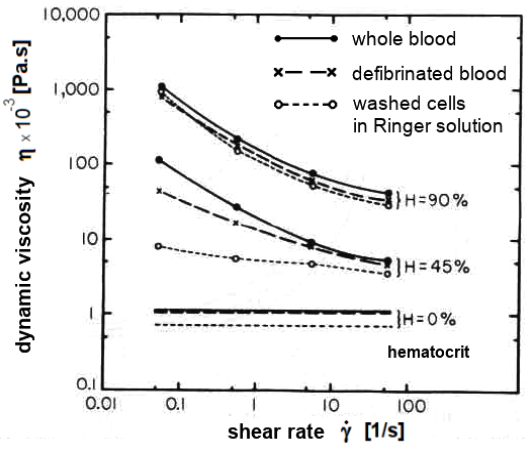

Fig. 2.21. Dynamic viscosity as a function of shear rate for three different values of hematocrit and erythrocyte suspensions [46].

Ringer's solution[3]).

One of the well-known empirical relationships, describing the blood viscosity as a function of shear rate, hematocrit and plasma protein concentration, is the *3-parameter Wallburn-Schneck model* based on the power law model

$$\eta(\dot\gamma, \mathrm{Hct}, \mathrm{TPMA}) = p_1\, e^{\left(p_2 \mathrm{Hct} + p_5 \frac{\mathrm{TPMA}}{\mathrm{Hct}^2}\right)}\, \dot\gamma^{\,(p_3 - p_4 \mathrm{Hct} - 1)}\,, \tag{2.8}$$

where Hct [−] is the hematocrit and TPMA [g/l] is the globulin concentration ('total protein minus albumin'), which in a healthy human ranges from 19 to 34 g/l. According to [200], the remaining parameters are following: $p_1 = 0.00797\,\mathrm{Pa\,s}^n$, $p_2 = 0.0608$, $p_3 = 1$, $p_4 = 0.00499$, $p_5 = 14.585\,\mathrm{l/g}$.

C) Influence of temperature

Just like the viscosity of other fluids, the viscosity of blood may be significantly affected by the temperature of the environment. Namely, a temperature decrease will result in an increase of blood viscosity, Fig. 2.22. Although the body temperature of a healthy human is usually around 37°C, distinctive changes in temperature may occur if the peripheral parts of the body are suddenly exposed to a much colder environment. In this case, the observed reduced blood perfusion of the tissues is often the result not only of constricted vessels, but also of higher blood viscosity. This behaviour is nowadays used during surgery of vital organs such as the heart when an controlled hypothermia is induced to permit temporary cessation of the blood circulation.

Similarly to the case of plasma viscosity described in Section 2.2.1, the influence of temperature on blood viscosity may be expressed by empirical relationships that are based on dynamic viscosities measured at a certain temperature and shear rate. In this

[3]The Ringer's solution is an infusion solution used as a substitution of the extracellular fluid. Its chemical composition includes ions of chlorine, sodium and potassium, making it similar to blood plasma.

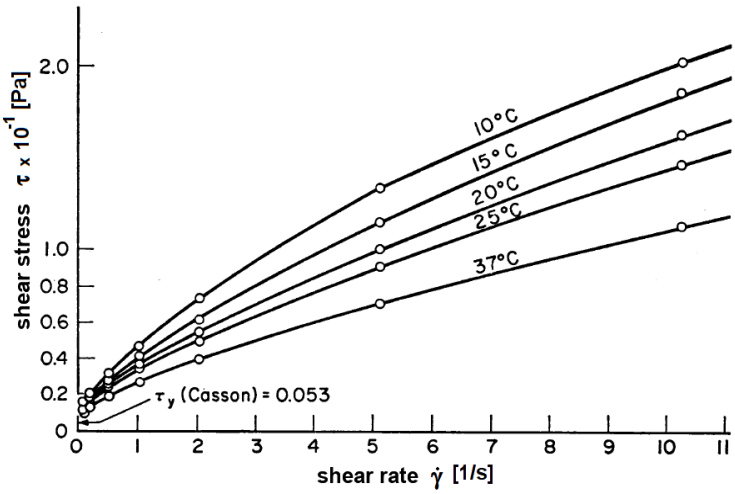

Fig. 2.22. Shear stress–shear rate relationships measured at various temperatures (hematocrit Hct = 44.8%, yield stress $\tau_0 = 0.0053\,\mathrm{Pa}$) [120].

regard, it is possible to mention the work of Merill et al. [120], where the authors derived a function in the following form:

$$\eta(\dot{\gamma}, T) = \eta(\dot{\gamma}, T_0) \cdot e^{-\frac{E_a}{R}\left(\frac{T_0 - T}{T\,T_0}\right)}, \tag{2.9}$$

where $E_a\,[\mathrm{cal\,mol^{-1}}]$ is the activation energy, $R = 1.985\,\mathrm{cal\,mol^{-1}\,K^{-1}}$ is the molar gas constant, T_0 [K] is the temperature with a known reference dynamic viscosity $\eta(\dot{\gamma}, T_0)$ and T [K] is the temperature for which the dynamic viscosity is sought. According to [173], the ratio $\frac{E_a}{R}$ should be chosen in the range from 1 080 to 2 040 K. The graph of the function given by Eq. (2.9) is shown in Fig. 2.23 for an average and two limit values of the reference dynamic viscosity $\eta(\dot{\gamma}, T_0)$ at $T_0 = 37°\mathrm{C}$ and $\dot{\gamma} \approx 100\,\mathrm{s^{-1}}$. Eq. (2.9) is valid for temperatures ranging from 283 to 313 K (10 − 40°C) and shear rates $\dot{\gamma}$ within the interval of $1 - 100\,\mathrm{s^{-1}}$ [47, 120].

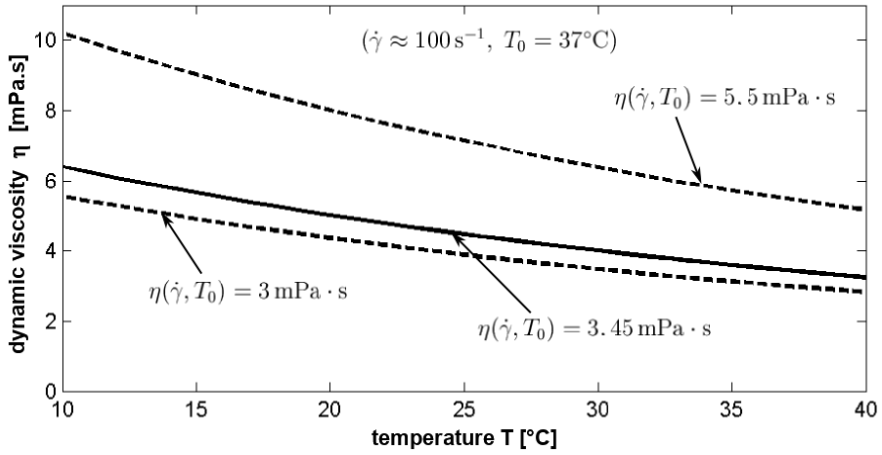

Fig. 2.23. Dynamic viscosity of blood $\eta(\dot{\gamma}, T)$ as a function of temperature T according to Eq. (2.9) for $\frac{E_a}{R} = 2010\,\mathrm{K}$ and three reference values of $\eta(\dot{\gamma}, T_0)$ at $T_0 = 37°\mathrm{C}$ and $\dot{\gamma} \approx 100\,\mathrm{s^{-1}}$.

D) Influence of vessel diameter

The inner diameter of vessels also known as lumen is a rheological factor, whose influence on the blood viscosity is particularly noticeable in microvessels such as the capillaries [147, 149]. The correlation between the lumen and the blood viscosity, which has been observed in vessels with inner diameter smaller than 300 μm [132], is commonly called the *Fåhræus-Lindqvist effect*. This effect, which gains importance when the vessel lumen exceeds the critical values of 1 mm [46], is characterised by a gradual viscosity decrease with decreasing lumen down to approximately 10 μm, Fig. 2.24. For diameters below 10 μm, the blood viscosity sharply increases because the vessel lumen becomes comparable to the diameter of the erythrocytes and leukocytes (see Tab. 2.2).

The existence of the Fåhræus-Lindqvist effect in the vasculature is caused by the blood composition and the diameters of the cells contained in the blood. In principle, the observed viscosity decrease in the microvessels is a result of cell accumulation around the centre line and the existence of a plasma cell-free layer near the vessel walls,

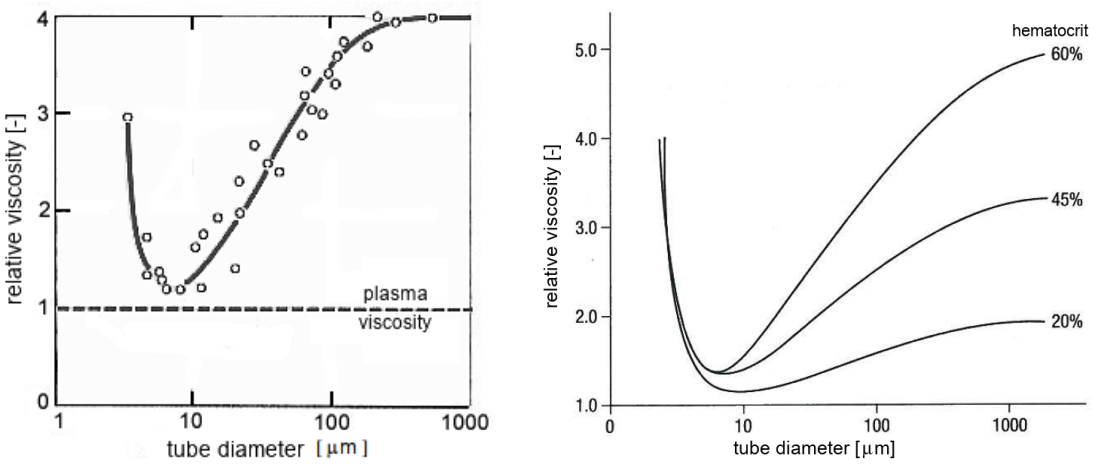

Fig. 2.24. Influence of tube diameter on relative viscosity of blood [44, 132].

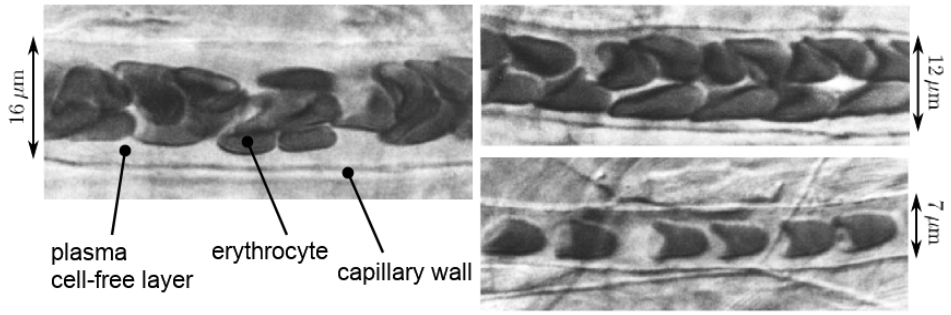

Fig. 2.25. Blood flow through microvessels in the rat mesentery with inner diameters 7 μm, 12 μm and 16 μm [148]. The arrangement of erythrocytes near the centre of the capillary results in the formation of a plasma cell-free layer near the wall.

Fig. 2.25. Until recently, it was assumed that the thickness of the less viscous plasma layer is constant in all vessels of the human body ($\sim 4\,\mu$m) so that its presence becomes apparent only in small-sized vessels. Nowadays this concept is being questioned due to new observations, which indicate that the thickness of the plasma layer is not constant, but varies in dependence on the vessel diameter and time. For example, in $10 - 50\,\mu$m vessels, the thickness has been stated to vary between 0.8 to 3.1 μm [79].

Another effect that is known to affect the blood viscosity in microvessels is the *Fåhræus effect*. The concept of this effect is based on the hematocrit, whose value decreases as vessel lumen decreases. In other words, the hematocrit (also called dynamic hematocrit) may drop from 45% to 25% in vessels with $D < 15\,\mu$m. The reason for this decrease is the accumulation of erythrocytes near the centre line, Fig. 2.25, where they can move faster than the plasma adhering to the vessel walls [175]. In addition to this hemodynamical cell separation, the dynamical hematocrit is also influenced by *plasma skimming* [142], a phenomenon in which small lateral capillaries are filled only with blood plasma because the 'large' erythrocytes are unable to enter them. Local hematocrit change may also occur if a leukocyte causes a temporary capillary blockage [150], as illustrated in Fig. 2.6.

For the human body, the Fåhræus-Lindqvist effect provides several important advantages. The most important one is the fact that lower viscosity of the blood incurs lower vessel resistance and lower perfusion and transmural pressures [132]. If the blood were to behave as a Newtonian fluid even in the capillaries, the perfusion and transmural pressures would be much higher requiring larger heart to adequately perfuse the tissues.

One of the mathematical models describing the Fåhræus-Lindqvist effect is the *cell-free marginal layer model* [18]. It assumes laminar flow in a tube of constant cross-section that is divided into a core region and a cell-free plasma region near the wall, both with different dynamic viscosities. The apparent viscosity of the whole blood determined by this model is given as

$$\eta_a = \eta_p \left[1 - \left(1 - \frac{\delta}{R} \right)^4 \left(1 - \frac{\eta_p}{\eta_c} \right) \right]^{-1}, \tag{2.10}$$

where R is the tube diameter, δ is the thickness of the cell-free plasma layer and η_p and η_c are the dynamic viscosities near the wall and at the tube centre, respectively. As apparent from Fig. 2.26, the size of the cell-free plasma layer grows with decreasing tube diameter to the detriment of the core region occupied by the erythrocytes.

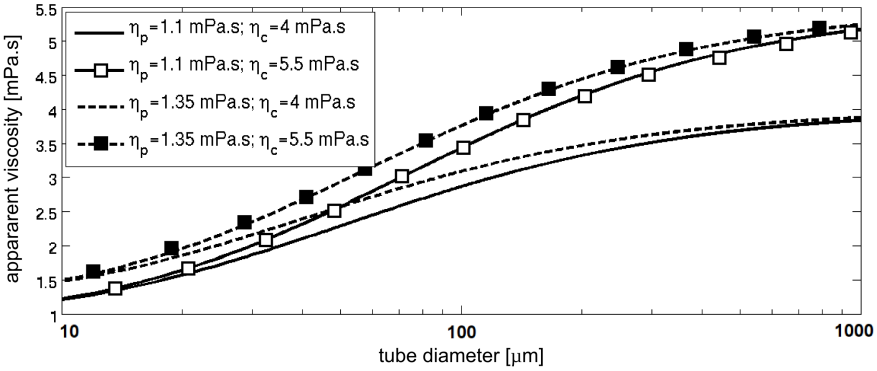

Fig. 2.26. Apparent viscosity $\eta_a\,(R)$ as a function of tube diameter R according to Eq. (2.10) for $\delta = 4\,\mu$m and selected values of η_p and η_c.

2.3 Viscosity models for blood

In large- and middle-sized arteries, where the size of all blood particles is negligible compared to the vessel lumen, the human blood may be assumed to be a homogeneous viscous fluid. For the description of its viscosity, it is possible to use one of the well-known constitutive models, which according to [200] can be divided into two main categories – the Newtonian and non-Newtonian viscosity models. The applicability of the first category is defined by the shear rate range, in which the blood behaves as a Newtonian fluid with apparent constant viscosity. The threshold between the Newtonian to non-Newtonian ranges is usually specified by a critical shear rate $\dot{\gamma}_{crit}$, which according to literature is not unique and may significantly vary depending on the hematocrit and chemical composition of the blood plasma ($50\,\mathrm{s}^{-1}$ [200], $100\,\mathrm{s}^{-1}$ [68, 80] or $200\,\mathrm{s}^{-1}$ [23]).

The second category of viscosity models includes constitutive models describing the influence of various biological and abiological factors on the blood viscosity. Note that the majority of these models is mainly a function of shear rate due to its dominant role.

2.3.1 Newtonian viscosity models

For shear rate values higher than $\dot{\gamma}_{krit}$, the normal blood may be approximated by a Newtonian fluid with average dynamic viscosity between 3.45 and 3.5 mPa s ($33-45\%$ hematocrit) [23]. In this context, it is important to note that this viscosity range is not constant and may change depending on the actual cell concentration (hematocrit), plasma viscosity and other factors such as the ability of erythrocytes to deform, as discussed previously. The Newtonian viscosity models, which are also known as *concentration-dependent models* [200], try to incorporate some of the above mentioned factors. Besides their application to special flow problems, they are used for the determination of limit values η_0 and η_∞ [47], which are an important part of the non-Newtonian viscosity models, see Section 2.3.2.

Note that some of the concentration-dependent models were modified to be non-Newtonian models by taking some of the model parameters as shear dependent variables. This is the case of the Quemada model, whose derivation described in [154–156] is based on the following equation:

$$\eta = \eta_{plazma}\left(1-\frac{1}{2}\,k_Q H\right)^{-2}, \tag{2.11}$$

where $H = \frac{\mathrm{Hct}}{100}\,[-]$ is the volume fraction of the erythrocytes in the blood and the parameter k_Q is known as the intrinsic viscosity of erythrocytes [115]

$$k_Q = \frac{k_0 + k_\infty\sqrt{\dot{\gamma}_r}}{1+\sqrt{\dot{\gamma}_r}} \tag{2.12}$$

where $\dot{\gamma}_r = \dot{\gamma}/\dot{\gamma}_c$ is the relative shear rate and $\dot{\gamma}_c$ is the characteristic rate of rouleaux formation/degradation. The remaining parameters k_0 and k_∞ appearing in Eq. (2.12) express the maximum volume fraction of erythrocytes for zero ($\dot{\gamma} \to 0$) and infinite ($\dot{\gamma} \to \infty$) shear rates, respectively.

2.3.2 Non-Newtonian viscosity models

Besides the factors discussed in Section 2.2.2, the blood viscosity is known to be strongly affected by the shear rate $\dot{\gamma}$, which in the human body may range from 0.1 to 100 000 s^{-1} [80]. If the shear rate is taken as the only factor influencing the blood viscosity, then, the blood can be seen as a *generalised Newtonian fluid* with the following flow equation:

$$\tau = \eta(\dot{\gamma})\cdot\dot{\gamma}\,, \tag{2.13}$$

where τ is the shear stress and $\eta(\dot{\gamma})$ is the shear-dependent dynamic viscosity given by a suitable constitutive model. In the case of the blood, a constitutive model should be able to capture the blood's behaviour at various shear rates in accordance with the rheological results published, e.g., in [104, 118, 120, 193]. In other words, a suitable non-Newtonian model for the description of blood viscosity should exhibit several crucial properties:

1. **pseudoplasticity** – the dynamic viscosity $\eta(\dot{\gamma})$ should increase with decreasing shear rate $\dot{\gamma}$ and vice versa (this property is a result of erythrocyte aggregation/deformation, see Fig. 2.15),
2. **critical shear rate** $\dot{\gamma}_{crit}$ – after its exceeding the fluid should behave as a Newtonian fluid, i.e., $\eta(\dot{\gamma}) = \eta_\infty$ for $\dot{\gamma} \geq \dot{\gamma}_{crit}$,
3. **yield stress** τ_0 – because of its difficult determination (see Section 2.2.2), it may be neglected and replaced with a finite viscosity value, i.e., $\eta(\dot{\gamma}) = \eta_0$ for $\dot{\gamma} \to 0$.

According to [206], the constitutive models usually used for the description of blood's non-Newtonian behaviour can be divided into two main categories:

1. models based on the Casson equation: $\sqrt{\tau} = \sqrt{\tau_0} + \sqrt{\eta\dot{\gamma}}$,
2. models based on the power law model and having the following general form [47]: $\eta(\dot{\gamma}) = \eta_\infty + (\eta_0 - \eta_\infty)\, f(\dot{\gamma})$, where η_0 and η_∞ are the threshold limit values of dynamic viscosity, Fig. 2.27, defined as

$$\eta_0 = \lim_{\dot{\gamma}\to 0} \eta(\dot{\gamma})\,, \qquad \eta_\infty = \lim_{\dot{\gamma}\to \infty} \eta(\dot{\gamma})\,. \tag{2.14}$$

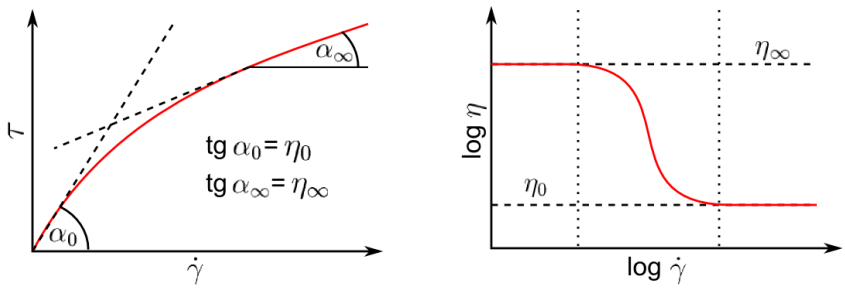

Fig. 2.27. Shear stress–shear rate (*left*) and dynamic viscosity–shear rate (*right*) relationships with threshold limit values η_0 and η_∞ (yield stress is not considered).

Some of the well-known time-independent non-Newtonian models commonly used for the human blood are listed in Tab. 2.7. Note that besides the non-Newtonian models mentioned in Tab. 2.7, the literature offers other models such as the K-L model, Weaver model or Ree-Eyring model, see [115, 200].

According to the results and observations mentioned, for example, in [16, 23, 47, 68, 80, 200, 206], the applicability and limitations of several selected non-Newtonian models from Tab. 2.7 can be summarised as follows:

- **power law model**: This model is able to describe the pseudoplastic behaviour of blood in the shear rate range of 1 to 100 s^{-1}. Outside this range, it is known to have difficulties because it cannot capture the blood's transition to the lower and upper asymptotic viscosity values. Because of its simple form, the power law model is usually applied to simple flow problems, for which an analytical solution is sought or which serves as a test problem for the analysis of numerical algorithms, e.g., [19,123]. The difficulties of the power law model at low shear rates are avoided in its extended form known as the **Herschel-Bulkley model**. Compared to the standard model, the Herschel-Bulkley model introduces a non-zero yield stress.

- **Wallburn-Schneck model**: This model is valid for the shear rate range of 0.03 to $120\,\mathrm{s}^{-1}$ and the blood with $35-50\%$ hematocrit. Because it is based on the standard power law model, it has similar difficulties outside the validity range. Compared to the other basic non-Newtonian models, it considers blood viscosity to be also a function of hematocrit and plasma proteins (total protein minus albumin, TPMA). This ability is mainly used for the modelling of the Fåhræus-Lindqvist effect described in Section 2.2.2.
- **generalised power law model (Ballyk model)**: At low shear rates, this model behaves as the standard power law model and at higher shear rates, exhibits the properties of a Newtonian fluid. Compared to other non-Newtonian models, it is known to give more accurate values of wall shear stress (WSS).
- **Casson model**: Although its validity range is wider compared to the standard power law model (applicable for $\dot{\gamma} > 10\,\mathrm{s}^{-1}$), the discontinuity at low shear rates ($\dot{\gamma} < 20\,\mathrm{s}^{-1}$) has been observed to cause problems for the numerical computation. Because of the difficult determination of the yield stress τ_0, the approximation $k_1 \approx \tau_0$ is often employed. Besides the standard model, there is also the **modified Casson model** (or known as the Quemada model in Casson form), which considers the influence of the hematocrit, as well.
- **Quemada model**: For a given hematocrit value, this model is valid in a very broad range ($0.0001-1\,000\,\mathrm{s}^{-1}$) and shows very good agreement with the published rheological results. Compared to the Casson model, it introduces a finite zero-shear viscosity η_0 instead of the yield stress τ_0, avoiding so the low shear rate problems.
- **Bi-exponent model**: The behaviour of this model is similar to the Quemada model with the exception that its parameters can be more easily associated with each phase of the flow curve, e.g., η_A and η_D denote the blood viscosity during erythrocyte aggregation (A) and deformation (D), respectively, with relaxation times t_A and t_D.

The selection of a suitable non-Newtonian model for the description of blood viscosity depends on the modelled flow problem, i.e., on the geometry, considered flow conditions and expected shear rate range. At high shear rates, most of the models mentioned above or listed in Tab. 2.7 show very similar behaviour that begins to differ as the shear rate decreases. In accordance with [200], it can be said that the models are qualitatively but not quantitatively similar.

In large recirculation zones, where the residual time of erythrocytes to re-aggregate is usually substantial, the blood has been observed to exhibit thixotropic behaviour, i.e., its apparent viscosity decreases even at constant shear rate. Although not so common as the time-independent non-Newtonian models, there are several well-known constitutive equations that may be used for the description of blood's time-dependent viscosity, e.g., the Weltman model or the Rosen model [200].

All of the non-Newtonian models mentioned above are commonly referred to as the inelastic models. An overview of the viscoelastic models used for human blood can be found, for example, in [47, 167] or [200].

Tab. 2.7: Selected rheological models used in the past for human blood modelled as a generalised Newtonian fluid.

rheological model		**source**	**parameters**
power law model:	$\eta(\dot\gamma) = K \cdot \dot\gamma^{n-1}$	[80]	$K = 11.01\,\mathrm{mPa\,s}^n$, $n = 0.7073$
	$\tau = K \cdot \dot\gamma^{n}$	[167]	$K = 42\,\mathrm{mPa\,s}^n$, $n = 0.61$
modified power law model:	$\eta(\dot\gamma) = \begin{cases} K \cdot \dot\gamma_0^{n-1} & \text{for } \dot\gamma < \dot\gamma_0 \\ K \cdot \dot\gamma^{n-1} & \text{for } \dot\gamma_0 \le \dot\gamma \le \dot\gamma_\infty \\ K \cdot \dot\gamma_\infty^{n-1} & \text{for } \dot\gamma < \dot\gamma_\infty \end{cases}$	[201]	$K = 25.6\,\mathrm{mPa\,s}^n$, $n = 0.615$, $\dot\gamma_0 = 0.130\,\mathrm{s}^{-1}$, $\dot\gamma_\infty = 182\,\mathrm{s}^{-1}$
generalised power law model: (also known as Ballyk model)	$\eta(\dot\gamma) = K(\dot\gamma) \cdot \dot\gamma^{n(\dot\gamma)-1}$, where $\begin{cases} K(\dot\gamma) = K_\infty + \Delta K \cdot e^{\left[-\left(1+\frac{\lvert\dot\gamma\rvert}{p_1}\right)\cdot e^{-(p_2/\lvert\dot\gamma\rvert)}\right]} \\ n(\dot\gamma) = n_\infty - \Delta n \cdot e^{\left[-\left(1+\frac{\lvert\dot\gamma\rvert}{p_3}\right)\cdot e^{-(p_4/\lvert\dot\gamma\rvert)}\right]} \end{cases}$	[200]	$K_\infty = 3.5\,\mathrm{mPa\,s}^{n(\dot\gamma)}$, $n_\infty = 1$, $\Delta K = 25\,\mathrm{mPa\,s}^{n(\dot\gamma)}$, $\Delta n = 0.45$, $p_1 = 35.36\,\mathrm{s}^{-1}$, $p_2 = 2.12\,\mathrm{s}^{-1}$, $p_3 = 35.36\,\mathrm{s}^{-1}$, $p_4 = 2.83\,\mathrm{s}^{-1}$
Cross model:	$\eta(\dot\gamma) = \eta_\infty + \left(\eta_0 - \eta_\infty\right)\left[1 + \left(\lambda\dot\gamma\right)^b\right]^{-1}$	[167]	$\eta_\infty = 3.45\,\mathrm{mPa\,s}$, $\eta_0 = 56\,\mathrm{mPa\,s}$, $\lambda = 1.007\,\mathrm{s}$, $b = 1.028$
simplified Cross model:	$\eta(\dot\gamma) = \eta_\infty + \left(\eta_0 - \eta_\infty\right)\left(1 + \lambda\dot\gamma\right)^{-1}$	[23]	$\eta_\infty = 5\,\mathrm{mPa\,s}$, $\eta_0 = 130\,\mathrm{mPa\,s}$, $\lambda = 8.0\,\mathrm{s}$
modified Cross model:	$\eta(\dot\gamma) = \eta_\infty + \left(\eta_0 - \eta_\infty\right)\left[1 + \left(\lambda\dot\gamma\right)^b\right]^{-a}$	[100]	$\eta_\infty = 3.5\,\mathrm{mPa\,s}$, $\eta_0 = 160\,\mathrm{mPa\,s}$, $\lambda = 8.2\,\mathrm{s}$, $a = 1.23$, $b = 0.64$
Carreau model:	$\eta(\dot\gamma) = \eta_\infty + \left(\eta_0 - \eta_\infty\right)\left[1 + \left(\lambda\dot\gamma\right)^2\right]^{\frac{n-1}{2}}$	[167]	$\eta_\infty = 3.45\,\mathrm{mPa\,s}$, $\eta_0 = 56\,\mathrm{mPa\,s}$, $\lambda = 3.313\,\mathrm{s}$, $n = 0.3568$
Carreau-Yasuda model:	$\eta(\dot\gamma) = \eta_\infty + \left(\eta_0 - \eta_\infty\right)\left[1 + \left(\lambda\dot\gamma\right)^m\right]^{\frac{n-1}{m}}$	[23]	$\eta_\infty = 3.45\,\mathrm{mPa\,s}$, $\eta_0 = 56\,\mathrm{mPa\,s}$, $\lambda = 1.902\,\mathrm{s}$, $m = 1.25$, $n = 0.22$
Powell-Eyring model:	$\eta(\dot\gamma) = \eta_\infty + (\eta_0 - \eta_\infty)\frac{\operatorname{arcsinh}(\lambda\dot\gamma)}{\lambda\dot\gamma}$	[167]	$\eta_\infty = 3.45\,\mathrm{mPa\,s}$, $\eta_0 = 56\,\mathrm{mPa\,s}$, $\lambda = 5.383\,\mathrm{s}$

Continued on the next page

Tab. 2.7 – Continued from previous page

rheological model		**source**	**parameters**
modified Powell-Eyring model:	$\eta(\dot\gamma) = \eta_\infty + (\eta_0 - \eta_\infty)\frac{\ln(\lambda\dot\gamma+1)}{(\lambda\dot\gamma)^m}$	[23]	$\eta_\infty = 3.45\,\mathrm{mPa\,s}$, $\eta_0 = 56\,\mathrm{mPa\,s}$, $\lambda = 2.415\,\mathrm{s}$, $m = 1.089$
		[47]	$\eta_\infty = 0.00493\,\mathrm{Pa\,s}$, $m = 1.16$, $\eta_0 = 0.05746\,\mathrm{Pa\,s}$,$\lambda = 5.97\,\mathrm{s}$
Herschel-Bulkley model:	$\eta(\dot\gamma) = K\,\dot\gamma^{n-1} + \frac{\tau_0}{\dot\gamma}$	[200]	$K = 8.9721\,\mathrm{mPa\,s}^n$, $n = 0.8601$, $\tau_0 = 17.5\,\mathrm{mPa}$
Casson model:	$\eta(\dot\gamma) = (\sqrt{k_1} + \sqrt{k_2\cdot\dot\gamma})^2 \cdot \dot\gamma^{-1}$	[80]	$k_1 = 2.81\,\mathrm{mPa}$, $k_2 = 3.09\,\mathrm{mPa\,s}$
	$\sqrt{\tau} = \sqrt{k_1} + \sqrt{k_2\cdot\dot\gamma}$ for $\lvert\tau\rvert > k_1$, otherwise $\tau = 0$	[23]	$k_1 = 5\,\mathrm{mPa}$, $k_2 = 4\,\mathrm{mPa\,s}$
modified Casson model:	$\eta(\dot\gamma) = \left(\sqrt{\eta_\infty} + \frac{\sqrt{\tau_0}}{\sqrt{\dot\gamma}}\right)^2$, where $\begin{cases}\sqrt{\eta_\infty} = \sqrt{\eta_{plasma}(1-H)^{-\alpha}} \\ \sqrt{\tau_0} = \beta\left[(1-H)^{-\alpha/2} - 1\right]\end{cases}$	[29]	$\alpha = 2$, $\beta = 0.3315\,\mathrm{Pa}^{1/2}$, $H = 0.4$, $\eta_{plasma} = 1.2\,\mathrm{mPa\,s}$
Quemada model:	$\eta(\dot\gamma) = \eta_{plasma}\cdot\left[1 - \frac{1}{2}\left(\frac{k_0 + k_\infty\cdot\sqrt{\dot\gamma/\dot\gamma_c}}{1+\sqrt{\dot\gamma/\dot\gamma_c}}\right)H\right]^{-2}$	[80]	$\eta_{plasma} = 1.4\,\mathrm{mPa\,s}$, $\dot\gamma_c = 2.361\,\mathrm{s}^{-1}$, $H = 0.40$, $k_0 = 4.586$, $k_\infty = 1.292$
Quemada model in Casson form:	$\eta(\dot\gamma) = \left(\sqrt{\eta_\infty} + \frac{\sqrt{\tau_0}}{\sqrt{\lambda}+\sqrt{\dot\gamma}}\right)^2$	[80]	$\eta_\infty = 2.65\,\mathrm{mPa\,s}$, $\tau_0 = 43.2\,\mathrm{mPa}$, $\lambda = 0.0218\,\mathrm{s}$
3-parameter Wallburn-Schneck model:	$\eta(\dot\gamma) = p_1\,e^{\left(p_2\mathrm{Hct} + p_5\frac{\mathrm{TPMA}}{\mathrm{Hct}^2}\right)}\,\dot\gamma^{\,(p_3 - p_4\mathrm{Hct} - 1)}$	[200]	$p_1 = 7.97\,\mathrm{mPa\,s}^n$, $p_2 = 0.0608$, $p_3 = 1$, $p_4 = 0.00499$, $p_5 = 14.585\,\mathrm{l/g}$, $\mathrm{Hct} = 40\%$, $\mathrm{TPMA} = 25.9\,\mathrm{g/l}$
K-L model:	$\tau = \tau_0 + (p_1\dot\gamma + p_2\sqrt{\dot\gamma})\cdot\eta_{plasma}$	[206]	$p_1 = 2.16$, $p_2 = 6.5448\,\mathrm{s}^{-1/2}$
Bi-exponent model:	$\eta(\dot\gamma) = \eta_e + \eta_D\,e^{-(t_D\cdot\dot\gamma)^{\frac{1}{2}}} + \eta_A\,e^{-(t_A\cdot\dot\gamma)^{\frac{1}{2}}}$	[206]	$\eta_e = 4.24\,\mathrm{mPa\,s}$, $\eta_D = 6.996\,\mathrm{mPa\,s}$, $\eta_A = 45.6648\,\mathrm{mPa\,s}$, $t_D = 0.14\,\mathrm{s}$, $t_A = 4.04\,\mathrm{s}$

Chapter 3

Biomechanics of vascular bypasses

3.1 Cardiovascular disease and its treatment

According to the regular statistical findings [197] published by the World Health Organisation (WHO) of the United Nations (UN), the cardiovascular disease (CVD) causes more premature deaths worldwide than any other known disease. A similar devastating effect on the human population has only the malnutrition in countries of the third world [111]. One of the latest statistics [117] shows that more than 31% of the recorded premature deaths, which accounts for approximately 17.3 million deaths per year (heart infarction: 7.3 million, brain stroke: 6.3 million), was caused by CVD. In the industrialised countries, the impact of CVD is particularly noticeable because the number of premature deaths caused by the malnutrition and contagious diseases are not so high. For the European countries, the most recent statistics on cardiovascular disease from the year 2012 [131] indicates that over 4 millions people (47%) die because of cardiac infarction or brain stroke. Besides the non-negligible loss of human lives, CVD has a considerable impact on the economy of each country. To be more specific, the EU member states spend yearly around €196 billion on CVD medical treatment. Almost 54% of the estimated amount is for health care, 22% is for informal care and the remaining 24% comes from lost productivity [131].

Together with other (mostly post-Soviet) states, the Czech Republic belongs to the most affected states in Europe [117, 131]. According to the statistics of the Institute of Health Information and Statistics of the Czech Republic, around 106.8 thousand people died in the year 2010, of which about half due to CVD [187]. Tab. 3.1 lists the leading causes of premature death in the Czech Republic in the years 1990 and 2010 for both genders. The decrease of mortality rate due to CVD within the 20 years is attributed to improved health care and better awareness of the risk factors associated with CVD (smoking, physical inactivity etc.).

causes of premature death	male		female	
	1990	2010	1990	2010
cardiovascular disease	53.3%	45.1%	57.7%	50.7%
tumours	23.1%	28.4%	21.6%	26.8%
respiratory diseases	5.2%	6.3%	3.3%	5.2%
digestive diseases	4.3%	4.8%	3.3%	4.3%
external causes	7.5%	7.9%	6.1%	4.2%
other causes	6.6%	7.5%	8.0%	8.8%

Tab. 3.1. Leading causes of death in the Czech Republic in 1990 and 2010 [187]. The data are expressed in the form of the standardised mortality ratio (SMR).

In about 90% of all cases [174], CVD is primarily caused by a long-term degenerative disease of the arterial wall called *atherosclerosis*, which is associated with increased accumulation of lipid and lipoprotein particles underneath the endothelium surface and gradual reduction of the vessel lumen (stenosis formation), Fig. 3.1. Besides the lumen reduction, the affected artery also experiences a loss of wall elasticity (arterial hardening), which negatively affects the ability of the vessel to regulate its lumen (vasoconstriction and vasodilatation). Because the transport of respiratory gases, nutrients and waste products from and to tissues is vital for the organism, an inadequate blood flow may result in serious health damage or even death.

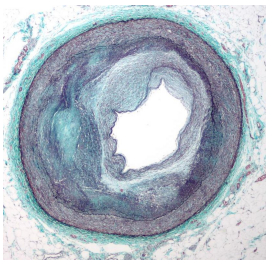

Fig. 3.1. Artery damaged by atherosclerosis.

In the case of the heart, a blockage of one or several coronary arteries is commonly called coronary heart disease (CHD), and if untreated, may lead to myocardial infarction (local necrosis of cardiac tissue due to oxygen deficiency and accumulation of waste products). According to the stenosis degree and its influence on the oxygen delivery to the tissues, the narrowing of vessels can be divided into three main categories:

- *mild stenosis* ($< 50\%$) – hemodynamically insignificant restriction of the vessel lumen (the presence of such stenosis goes mostly unnoticed by the patient);
- *medium stenosis* ($50 - 70\%$) – symptoms such as sudden chest pain and leg cramps occur during exercise (oxygen delivery to the tissues becomes inadequate to support the aerobic metabolism), treatment by drugs or changes of lifestyle;
- *severe stenosis* (70%) – high risk of permanent injury or death due to ischemia and/or tissue necrosis (chest pain and leg cramps occur even at rest), a mechanical intervention is necessary to prevent lasting consequences for the body.

The type of mechanical intervention in the final stages of atherosclerosis is chosen according to the urgency and the extent of the vessel damage. For localised stenoses, it if often the procedure known as the *percutaneous transluminal angioplasty* (PTA), whose principle is based on the dilatation of the narrowed artery segment with an inflated balloon. Although the restoration of blood flow with this approach is usually instantaneous, the forced stretching and flattening accumulation of the atherosclerotic plaque may be also accompanied by wall damage or rupture [2, 40]. Besides the rupture risk, the main disadvantage of PTA is its short-term efficiency (restenosis occurs in approximately 30% of cases within one year [34]). Thus, to prevent or counteract the recurrence of the stenosis within the artery, components from special materials known as *stents* are often used to support the stretched artery.

In the case of moderate to severe atherosclerosis or when the angioplasty shows no long-lasting effect, a surgical intervention is usually the only treatment option [176]. Since the end of the 1960s, the implantation of *bypass grafts* has become a standard surgical treatment [85, 128], whose purpose lies in the bypassing of a damaged artery with an autologous or synthetic graft. The surgically created connections between the native artery and the implanted graft are known as *anastomoses*, of which there are three types, Fig. 3.2:

- *end-to-end* (ETE) – the end of a graft is connected to the end of a vessel (the proximal damaged part of the vessel is completely replaced),
- *end-to-side* (ETS) – the end of a graft is connected to the side of a surgically dissected vessel (blood flow through the proximal damaged part of the vessel is still possible –residual flow through the stenosis),
- *side-to-side* (STS) – the side of a graft is connected to the side of a vessel (parallel and diamond configurations).

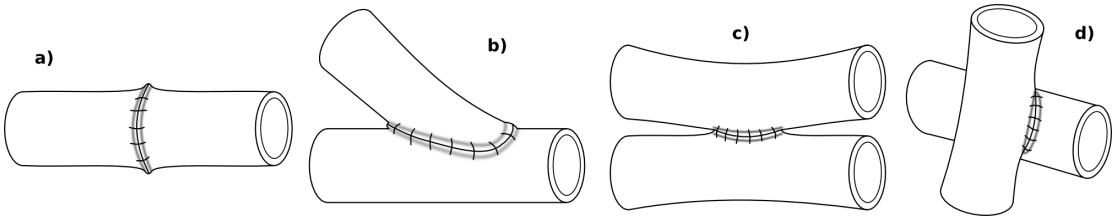

Fig. 3.2. Various types of vascular anastomoses: a) end-to-end, b) end-to-side, c) side-to-side (classic/parallel configuration), d) side-to-side (diamond configuration).

3.2 Vascular bypasses

'Vascular surgery' as a field was first defined by French surgeon Alexis Carrell in 1902 [90], who later unsuccessfully attempted to bypass or replace the coronary arteries of dogs with arterial and venous grafts (1910). The first implantation of an autologous venous graft in a human patient was performed by German surgeon Erich Lexer in the year 1907 when he replaced a damaged part of the axillary artery with an 8 cm long segment of the great saphenous vein from the patient's lower limb [172]. In the following decades, after the development of the cardiopulmonary bypass machine and the angiography technique, first known successful experimental implantations of coronary artery bypass graft in animals were carried out independently by Soviet surgeon Vladimir P. Demikhov (July, 1953) and by Canadian surgeon Gordon Murray (September, 1953), Fig. 3.3 (left). Then, on May 2, 1960, American surgeon Robert Goetz performed the first successful clinical coronary artery bypass operation in a patient by connecting the right internal thoracic artery to the right coronary artery [86]. The first application of venous grafts for coronary surgeries in a patient is attributed to American surgeon David Sabiston, Jr., who in the year 1962 utilised an autologous saphenous vein for the first known human aorto-coronary bypass, Fig. 3.3 (right). Although unsuccessful (the patient died 3 days later due to stroke), the surgery performed by Sabiston is seen as the first step in the development of a reliable coronary artery bypass technique based on the application of venous grafts. A truly successful saphenous vein bypass graft operation was achieved by cardiac surgeons René Favaloro and Donald Effler in May 1967. Since then many surgical techniques including the ones enabling the implantation of multiple bypass grafts have been developed and successfully applied. A detailed overview of historical milestones in the *coronary artery bypass grafting* (CABG) can be found, for example, in [85, 90, 128].

Because of the almost century-long development, there are currently many surgical techniques used for bypass grafting. Three of these techniques meant for peripheral artery

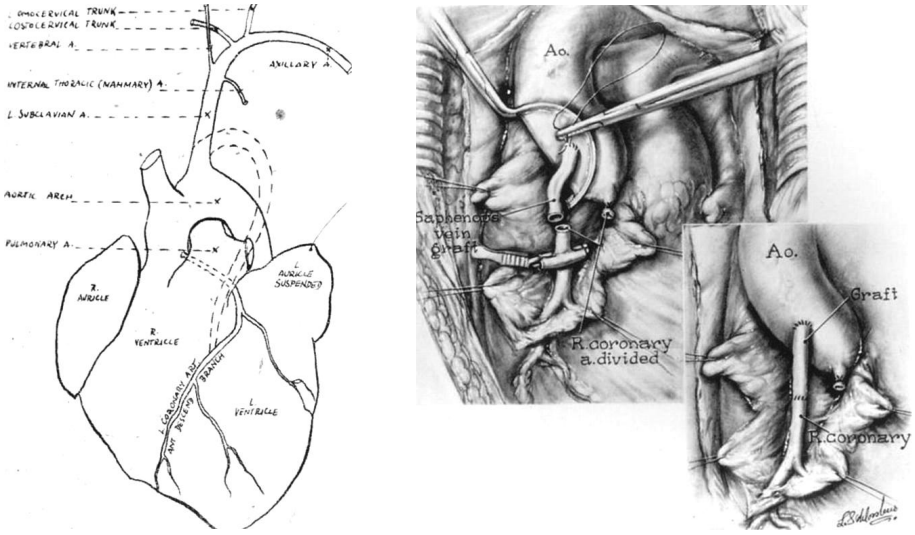

Fig. 3.3. Schematic drawings showing first attempts to bypass a damaged coronary branch: Gordon Murray, 1954 (*left*) – arterial autograft in a mongrel dog; David Sabiston, 1962 (*right*) – saphenous vein-coronary artery bypass with a distal end-to-end anastomosis at the coronary artery (patient died after 3 days due to stroke) [128].

bypass surgery are shown in Fig. 3.4. Other bypass types are described, for example, in [41,106]. For coronary arteries, whose passability is crucial for the cardiac muscle perfusion, the implantation of bypass graft(s) is usually the only long-term solution that may help to reduce the high mortality rate of infarction patients (almost 44% of all diagnosed cardiovascular diseases [197]). Similarly to the peripheral artery bypasses, the bypassing of stenosed or occluded coronary arteries is usually performed using time-proven tech-

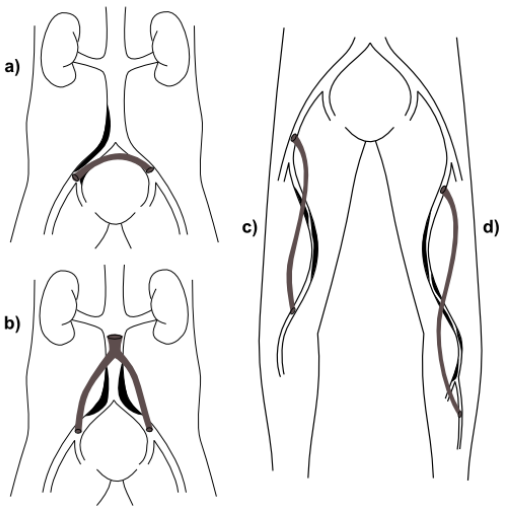

Fig. 3.4. Examples of peripheral bypasses: iliac (a), aorto-bi-iliac (b), femoro-femoral (c), femoro-popliteal (d).

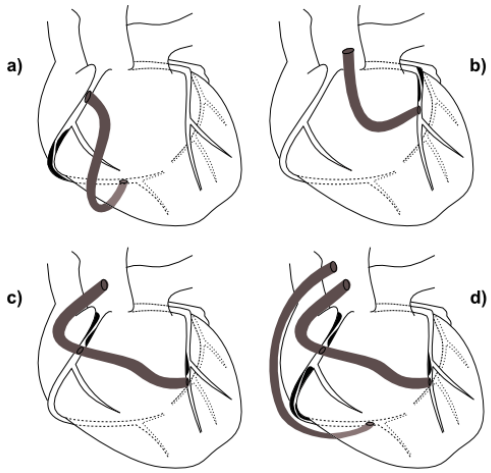

Fig. 3.5. Examples of coronary bypasses: coronaro-coronary (a), aorto-coronary – single (b), double (c), triple (d).

niques, which are chosen according to the extent of the artery damage, the availability of autologous grafts (arterial or venous) and the patient's health condition [34]. Fig. 3.5 shows four different techniques for the coronary bypass if a venous graft is used. Among them, the most common bypass type is the aorto-coronary one, which employs a direct connection between the ascending aorta and the coronary artery downstream from the lumen blockage, Fig. 3.5b-d. A certain disadvantage of aorto-coronary grafting technique is its need for a sufficiently long and un-damaged venous graft, which especially by the elderly patients may be impossible to obtain. In such cases, it is, therefore, usual to create a shorter bypass without an aortic anastomosis, which is also known as the coronaro-coronary bypass, Fig. 3.5a. Besides the simple grafting techniques based on one proximal and one distal end-to-side anastomosis (*individual graft*), Fig. 3.5b, there are also techniques that are able to restore blood circulation in a much larger area. This is achieved, for example, with a *sequential graft* (one graft with two and more distal anastomoses), Fig. 3.5c, or by implanting several grafts at once, Fig. 3.5d. According to the number of anastomoses created during the surgery, the bypasses are often referred to as single, double, triple and so on.

3.2.1 Autologous and synthetic grafts

The long-term patency and efficiency of implanted bypass grafts have been observed to be significantly affected by the surgical technique and the material of the graft. In the clinical vascular surgery, the surgeons commonly use either autologous or synthetic grafts [87] in dependence on the patient's health condition and the type and inner diameter of the bypassed (native) artery. The greatest risk for a newly implanted bypass graft is the thrombosis, which if unrestricted may lead to graft blockage or embolus (thrombus released into the blood stream). The risk of graft failure is particularly high in synthetic prostheses, which cannot be used for CABG due to the small diameter of the coronary arteries (diameters around 3 mm).

A) Autologous grafts

This type of vascular prostheses includes arteries and veins with specific physical properties and necessary dimensions (length, inner diameter ...). Because of possible graft rejection caused by an immunologic attack, the vessels are usually taken from the patient himself prior to the bypass surgery. The most common arteries and veins used as autologous grafts are listed in Fig. 3.6. Compared to the synthetic grafts, the autologous ones satisfy most of the requirements set for a successful graft implantation including the most important one – the biocompatiblity. Although advantageous, the application of the autologous grafts is limited by their availability and overall quality. In $40-50\%$ of cases [106], a suitable graft is not be available because of previous surgeries (graft failure, inadequate revitalisation of the involved tissue ...). By elderly patients, the quality of arterial grafts is also impaired by atherosclerotic lesions ($20-30\%$ of cases [106]).

The graft's mechanical properties are one of the most important factors that may predetermine the success of the whole bypass surgery. In this context, it is, therefore, understandable that the arterial grafts with their structure and properties very similar to those of the native artery, Fig. 3.7, are the best choice that can be made for a bypass graft. Another advantage of the arterial grafts is their ability to respond to hormonal

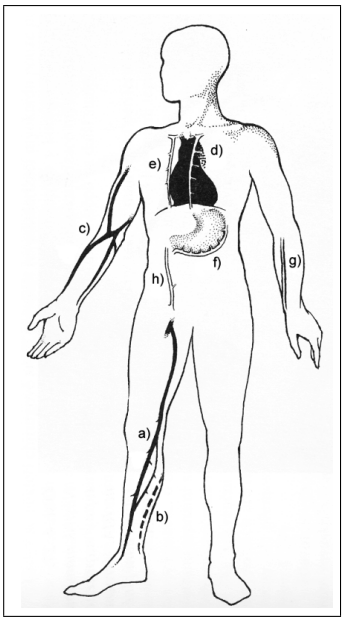

a) *vena saphena magna*
(great saphenous vein)
b) *vena saphena parva*
(small saphenous vein)
c) *vena cephalica*
(cephalic vein)
d) *arteria mamaria interna sinistra*
(left internal mammary artery)
e) *arteria mamaria interna dextra*
(right internal mammary artery)
f) *arteria gastroepiploica dextra*
(right gastroepiploic artery)
g) *arteria radialis*
(radial artery)
h) *arteria epigastrica inferior*
(inferior epigastric artery)

Fig. 3.6. Arteries and veins used as autologous bypass grafts [34].

stimulation and regulate their inner diameter as necessary. Despite their favourable properties, the arterial grafts are used only to a limited extent. One of the reasons for this is that the harvested artery has to be undamaged and free of atherosclerotic lesions, which, especially by elderly patients, is not always the case. A solution to this problem is often the application of one or more venous grafts.

After the implantation into the high-pressure arterial circulation, the venous grafts have been observed to adapt to their new hemodynamical environment by restructuring [61]. This process called *arterialisation* takes place in the first 30 days after the surgery and is a result of overdistension and deendothelisation [165]. Although a vein is known to be more compliant than an artery of similar size, its implantation into a high-pressure environment usually leads to the loss of this mechanical property [33]. Thus, after several weeks, the venous graft resembles nothing more than a stiff tube, which is unable to respond to hormonal stimulation. Another issue that in the case of venous grafts should be taken into consideration, is the presence of venous valves. As a rule, they are either surgically removed or the vein is implanted as a reversed graft (the resulting blood flow is reversed to the one within the venous circulation) [171].

In clinical vascular surgery, the autologous grafts are mainly utilised as a part of coronary bypasses. According to statistics, e.g., [87], their failure rate varies from case to case, but generally confirms the superiority of the arterial grafts. Their patency rate after 10 years has been noted to range between 90 to 95% compared to the $50 - 60\%$ patency rate of the venous grafts [34].

B) Synthetic grafts

The main requirements for synthetic vascular prostheses include a number of specific characteristics such as biocompatiblity, sterility, resistance to kinking and squashing and very low thrombogenicity [50]. On the basis of clinical and experimental studies, it has

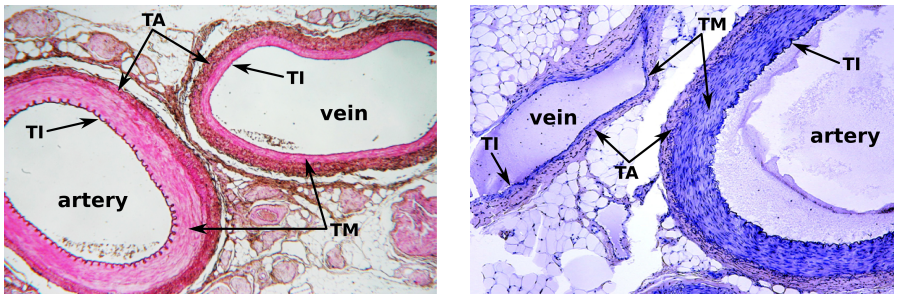

Layers of the vessel wall:

- **Tunica intima** (TI) is the inner most layer of a vessel made up of one layer of endothelial cells and elastic and collagen fibres called internal elastic lamina. This thin layer represents an interface between the blood and the rest of the vessel wall.
- **Tunica media** (TM) is the middle layer of a vessel made up of smooth muscle cells and elastic and collagen fibres in varying amounts:
  - *elastic/conducting arteries* – large-sized arteries near the heart, contain an increased amount of elastic fibres arranged in concentric laminae to better capture the pressure pulsations ('Windkessel effect');
  - *muscular/distributing arteries* – medium-sized arteries, contain a large amount of smooth muscle cells with prominent internal and external elastic laminae, their main function is the transport of blood to organs and tissues.
- **Tunica adventitia/externa** (TA) is the outermost layer of a vessel made up mainly of collagen fibres, its main function is to anchor the vessel to the surrounding tissues and allow the vessel to withstand forces acting on its wall.

Fig. 3.7. Structural differences between middle-sized arteries and veins.

been also proven that the healing process at the native artery and the tissue ingrowth into the graft is dependent on graft's porosity (too small pores elicit inflammatory reactions, while those too large allow excessive seepage of blood [72]). Compared to the autologous grafts, the synthetic prostheses are primarily used for the reconstruction of large-sized vessels such as the aorta or as bypass grafts for peripheral arteries with diameters greater than 6 mm, Fig. 3.8. The main reason for this limitation is the high risk of thrombosis due to low flow rate and the development of atherosclerosis or intimal hyperplasia resulting in stenosis or occlusion [50, 61].

The current synthetic grafts can be divided into three basic categories according to their inner structure and manufacturing method thereof [87, 90]:

- **knitted grafts**

– the most often used synthetic prostheses for vascular reconstruction;
– endothelisation of the luminal graft surface (tissue ingrowth) occurs in the first months after implantation in dependence on material porosity and fibre quality;

- **woven grafts**

– manufactured from low-porosity materials, problems with fraying edges and worsened fibrous healing, prostheses without impregnation;

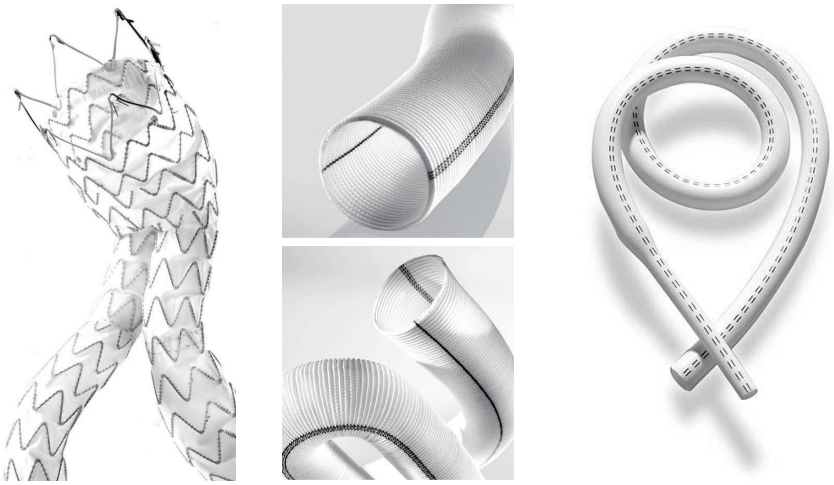

Fig. 3.8. Synthetic vascular prostheses (*from left*: polyester, PET and ePTFE).

– poor handling characteristics and compliance, predominantly used in the repair of the thoracic aorta and ruptured abdominal aortic aneurysms;

• **molten grafts** (from PTFE or expanded PTFE)

– they have complex physical properties (varies between manufacturers);
– resistant to wall dilatations and deformations, may be reinforced with a stent;
– their luminal surface is highly impermeable and non-thrombogenic;

The grafts are manufactured from various polymeric materials [50, 72, 87], e. g.:

• **polyethylene terephthalate (PET)/Dacron:** (since late 1950s and 1960s)
  – structural formula: $[\text{–O–C=O–C}_6\text{H}_6\text{–O–C=O–CH}_2\text{CH}_2\text{–}]_n$
  – tensile modulus: $E = 14\,\text{GPa}$, tensile strength: $R_m = 170 - 180\,\text{MPa}$

Dacron as a type of polyester is used for either woven or knitted grafts, which may be reinforced by coils or external rings to minimise their kinking, Fig. 3.8 (left). Because of their porosity, the knitted Dacron grafts have to be impregnated/coated prior to implementation to ensure their impermeability and lower thrombogenicity. Various physical and biological modifications to the luminal graft surface have been observed to promote greater tissue ingrowth and enhance the formation of a *neointima* – a new intima layer formed by migration and proliferation of cells from the tunica media. The Dacron grafts are mainly used for aortic repairs or as large diameter peripheral bypass grafts ($D > 6\,\text{mm}$). Although non-biodegradable (total resorption by 30 years), the grafts have shown a tendency to dilate over time.

• **polytetrafluorethylene (PTFE)/Teflon:** (since 1970s)
  – structural formula: $[\text{–}(\text{CF}_2\text{–CF}_2)\text{–}]_n$
  – tensile modulus: $E = 0.5\,\text{GPa}$, tensile strength: $R_m = 14\,\text{MPa}$

PTFE was first used for the manufacturing of artificial heart valves, later on in its expanded form (ePTFE) as a material for large diameter peripheral bypass grafts ($D = 7 - 9\,\text{mm}$). In vessels with diameters smaller than 7 mm such as the popliteal and tibial arteries, the patency rate of ePTFE grafts is not so high due to cell adherence to the luminal surface, which often leads to graft occlusion.

- **polypropylene (PP):**
  - structural formula: $[\text{–}(CH_3\text{–}CH)\text{–}CH_2\text{–}]_n$
  - tensile modulus: $E = 2.6\,\text{GPa}$, tensile strength: $R_m = 400\,\text{MPa}$

PP is relatively inert, thermoplastic and resistant to the effects of microorganisms (biostable). Because it does not inhibit arterial regeneration as other polymers do, it is mainly used as a non-resorbable component of synthetic vascular prostheses.

- **polyurethanes (PU):**
  - structural formula: $[\text{–NH–O=C–O–R–}]_n$
  - tensile modulus: $E = 0.005 - 1.15\,\text{GPa}$, tensile strength: $R_m = 20 - 90\,\text{MPa}$

Current experiments and clinical trials indicate PU to be a very promising material for vascular prostheses. PU materials constitute of hard segments, which account for stiffness and rigidity, and soft segments, which ensure flexibility and can be varied (see the aforementioned wide ranges of the tensile modulus and strength).

The patency rate of synthetic grafts is dependent on various factors such as their size and placing in the blood circulation. In general, the large diameter prostheses ($D \geq 6\,\text{mm}$) show high patency rate even several years after implantation, see Fig. 3.9. As for the small diameter grafts, which are used for femoro-popliteal and femoro-tibial bypasses, the percentage is not so high as in the case of the venous grafts, Tab. 3.2. For further details on the topic of synthetic grafts and vascular tissue engineering, see, for example, [C.2] or [50, 72, 165, 189].

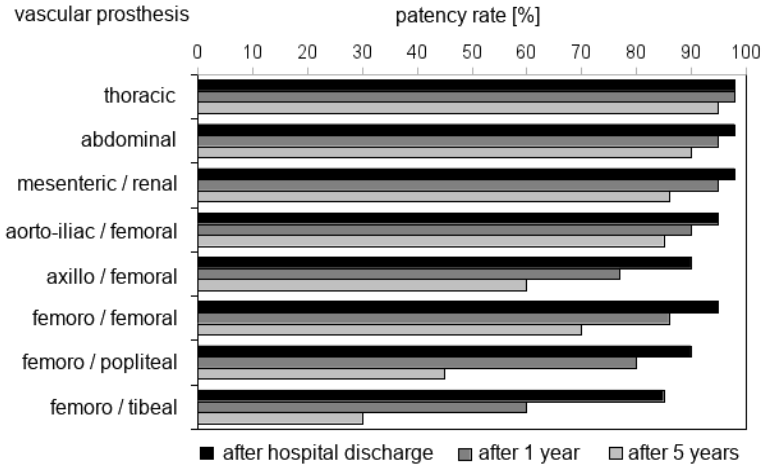

Fig. 3.9. Patency rates of synthetic vascular prostheses [50].

graft type/material	patency rate after		
	2 years	3 years	5 years
autologous – great saphenous vein (*vena saphena magna*, VSM)	$68 - 88\%$	$\approx 73\%$	$62 - 72\%$
synthetic – PET (Dakron)	$45 - 70\%$	$54 - 64\%$	$\approx 46\%$
synthetic – (e)PTFE (Teflon)	$42 - 67\%$	$47 - 61\%$	$29 - 49\%$

Tab. 3.2. Patency rate of selected femoro-popliteal bypass grafts 2, 3 and 5 years after implantation [87].

3.2.2 Graft failures

Similarly to other cardiovascular treatments, the patency and overall performance of bypass grafts is time-limited. It is, however, a fact that their life span is one of the longest provided the graft implantation is successful. For example, compared to the balloon angioplasty, whose effect lasts an average of two years (failure often due to restenosis), only about $40-60\%$ of coronary bypasses usually fail within 10 years after surgery [34]. For peripheral bypasses, the number of failed grafts is much higher (around $40-90\%$ within the first 5 years [90]). The graft performance is dependent on various biological and abiological factors such as the patient's health condition and graft's mechanical properties. With regard to the statistical data mentioned in Section 3.2.1, the most common causes of graft failure include [61, 90, 204]:

- **thrombosis:** (graft failure within one month)

After implantation, the artificial luminal surface of synthetic grafts triggers blood coagulation. The clotting gradually forms a thin layer (called *pseudointimal hyperplasia*), which is devoid of cellular ingrowth and is composed mainly of fibrin, platelet debris, and trapped erythrocytes. In regions with stagnant or low-velocity blood flow, the clotting may become unrestricted resulting in vessel occlusion. Most often the cause for this type of graft failure is technical error during surgery.

- **bacterial infections:**

In clinical vascular surgery, the incidence of bypass graft infection is approximately 2% regardless of aseptic surgical technique, vascular graft production or immunology. Considering all possible complications such as sepsis or toxic shock syndrome, a graft infection is a challenging problem that if untreated, may even endanger the life of the patient[1]. Synthetic grafts are involved in infections four times as often as the autologous venous ones regardless of the graft material. One of the deterioration mechanisms involves a graft contamination at the time of surgery such as the contact of the prosthesis with the patient's skin.

- **neointimal hyperplasia:** (graft failure after several years)

Neointimal hyperplasia is a post-operative process of remodelling and healing, which takes place at anastomoses and which, under certain conditions, may lead to vessel or graft occlusion. This process is characterised by an excessive growth of the tunica intima, Fig. 3.7, in the anastomosis region, which is commonly called *intimal thickening*. Histologically, two forms of intima growth have been described:

1) *intimal fibrocellular hypertrophy*, Fig. 3.10a,
2) *intimal hyperplasia*, Fig. 3.10b.

The intimal fibrocellular hypertrophy (IFH) is basically a normal healing process that takes place on all implanted grafts regardless of their material (autologous or synthetic). As a well-organised, uniformly layered intimal thickening [48], IFH includes both smooth muscle cells and collagen and elastin matrix fibres oriented in a common direction, see Fig. 3.10a. Compared to the intimal hyperplasia, IFH represents a non-stenotic form of intimal thickening. According to clinical observations, IFH can be seen as a form of

[1] The mortality rates vary with the graft location and the aggressiveness of the infecting organism. For femoro-popliteal and aorto-bifemoral bypasses, the reported mortality rate lies between 5 to 10% and 50 to 75%, respectively, [90].

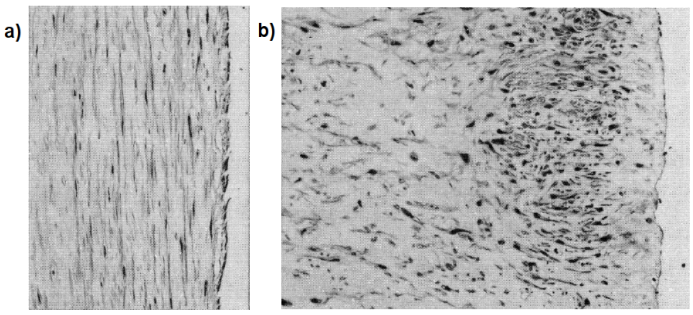

Fig. 3.10. Histological appearance of two different types of intimal thickening: a) intimal fibrocellular hypertrophy, b) intimal hyperplasia [48].

adaptive reaction to the changes in local hemodynamics and wall tension in the anastomosis region. Its main objective is to restore baseline values of wall shear stress and/or wall tensile stress by remodelling and smoothing of the luminal surface [204].

Compared to IFH, the intimal hyperplasia (IH) creates stenotic and occlusive thickening resulting in early graft failure. Histologically, IH is characterised by a chaotic appearance of randomly oriented cells embedded in a extracellular matrix with minimum of collagen and elastin fibres, see Fig. 3.10b. It is, therefore, understandable that the growth of IH is sometimes compared to a tumour-like behaviour [90]. Similarly to IFH, IH is associated with disturbed blood flow and inadequate mechanical stimulation of the vessel wall.

Exact factors that differentiate the occlusive healing in the form of IH from the non-occlusive one (IFH) are not known. It is, however, assumed that one of the major factors that prevent the stabilisation of the intimal thickening into the form of IFH is the hemodynamic shear stress [48]. The following summary diagram illustrates the influence of the wall shear stress (WSS) on the differentiation between both forms of intimal thickening:

$$\text{low WSS} \rightarrow \text{intimal thickening (lumen reduction)} \rightarrow \text{WSS increase} \rightarrow \\ \rightarrow \begin{cases} \text{1. normal WSS} \rightarrow \text{stabilisation (IFH)} \\ \text{2. low WSS} \rightarrow \text{further intimal thickening} \rightarrow \text{stenosis/occlusion (IH)} \end{cases}$$

Because intimal thickening is primarily an adaptive response to hemodynamic forces of subnormal WSS, which may be induced by injury, inflammation and/or hemodynamical changes, both IFH and IH may be found in their isolated 'pure' or hybrid forms [204].

3.3 Significance of hemodynamics in the cardiovascular system

Vessels, particularly arteries, are known for their ability to adapt to changes in hemodynamic forces (blood pressure, wall shear stress etc.) [61, 113]. Besides the aforementioned vessel remodelling, the most common and relatively fast form of adaptation is the regulation of the vessel lumen called either vasoconstriction (lumen reduction) or vasodilatation (lumen increase) [110]. The inner diameter of the vessel as the primary determinant of wall thickness and composition is closely connected with the *transmural*

pressure [181, 204] defined as the difference between the internal (intraluminal) p_i and external p_o pressures, i.e., $p = p_i - p_o$. The extent of the morphological adaptation in relation to blood pressure and/or vessel diameter may be expressed with the help of the *wall tensile stress* (WTS). Assuming the blood vessel to be a thin-walled cylinder, the wall tensile stress may be approximated using the Laplace's law

$$\sigma = \frac{R}{d}\, p\,, \tag{3.1}$$

where p is the transmural pressure, d is the wall thickness, and R is the inner radius of the vessel (for a thin-walled cylinder: $R_{out} \approx R$), see Fig. 3.11 (left). For illustration, some physiological WTS values are summarised in Tab. 3.3 together with other characteristic vessel parameters. According to Eq. (3.1), WTS is directly proportional to the vessel radius and transmural pressure. This correlation is very well apparent in hypertension, when a higher intraluminal pressure stimulates the vessel wall to increase its thickness in order to restore the tensile stress to its normal range. The resulting changes in structure and composition are often accompanied by worsened mechanical properties of the vessel wall [110].

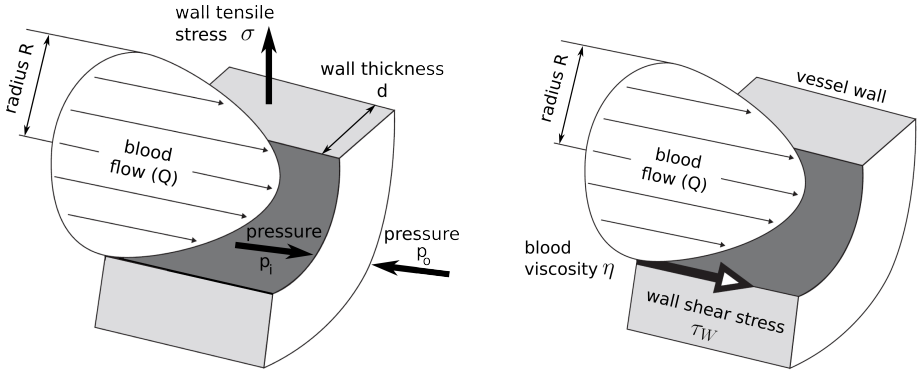

Fig. 3.11. Schematic drawings showing wall tensile stress σ (*left*) and wall shear stress τ_W (*right*) in a vessel.

vessel	pressure p [kPa]	radius R [mm]	WTS σ [Pa]	wall thickness d [mm]
aorta and large arteries	13.3	≤ 13	170	2
small arteries	12	5	60	1
arterioles	8	$0.06 - 0.15$	$1.2 - 0.5$	0.020
capillaries	4	0.004	0.016	0.001
venules	2.6	0.010	0.026	0.002
veins	2	≥ 0.2	0.4	0.5
vena cava	1.33	16	20	1.5

Tab. 3.3. Overview of selected vessel parameters. Note that the values are only approximate and do not take into account the influence of ageing in the form of lumen increase and/or progressive increase in wall thickness [110].

The influence of the transmural pressure and tensile stress on the vessel structure and composition is particularly apparent in arteries changed with ageing [110]. As mentioned earlier, arteries adapt to sudden hemodynamical or mechanical changes by regulating their lumen. By elderly patients, whose arteries may be damaged by atherosclerosis, the ability of the vessels to regulate their lumen becomes significantly impaired. In this case, remodelling of the vessel wall (long-term adaptation) is usually the only option left to restore the normal hemodynamical and mechanical environment.

As mentioned in Section 3.2.2, one of the reasons for graft failure is the thrombosis. In addition to the exposure of blood to a thrombogenic surface, the blood coagulation may be also triggered by insufficiently high flow rate, promoting platelet deposition, accumulation and activation, see Section 2.1.3. According to [61], the risk of thrombosis may be determined with the help of the indicator known as *thrombotic threshold velocity* (TTV) and defined as a material-dependent time-average velocity, for which at least 50% of the graft is covered in thrombus deposits. According to the TTV concept, synthetic grafts cannot be used for vessels with diameters smaller than 4 mm, where the flow rate is low and the graft inner diameter may be further reduced by the growing neointima. Because of this limitation, the synthetic grafts are not used in coronary arteries with diameters around 3.5 mm.

Among all the various hemodynamic factors, there is also the *wall shear stress* (WSS), representing the friction force that blood exerts on a unit area of the vessel wall [140]. Approximating the blood flow in a vessel segment as an isothermal laminar flow of an incompressible Newtonian fluid in a circular tube, the wall shear stress is defined as

$$\tau_W = \frac{4\eta\, Q}{\pi R^3}\,, \tag{3.2}$$

where η is the dynamic viscosity of the fluid, Q is the flow rate and R is the tube inner radius, see Fig. 3.11 (right). Besides the significance of WSS in hemolysis and thrombogenesis, which was described in detail in the previous chapter, WSS is known to influence the structure and composition of the vessel wall and to be involved in the triggering of the cardiovascular disease [32]. Under normal flow conditions, the arteries regulate their diameter to achieve mean WSS in the relatively narrow range of $1 - 2\,\mathrm{Pa}$ [80, 113, 204]. This range is important for optimal endothelium stimulation and subsequent secretion of vessel mediators such as nitric oxide (NO) and endothelin [110]. Low shear stress ($\mathrm{WSS} \leq 0.5\,\mathrm{Pa}$) and inadequate NO secretion often lead to enhanced lipid accumulation and pro-inflammatory processes inside the vessel wall resulting in atherosclerosis [140].

At this point, it is worth noting that the flow conditions affect not only the function of the endothelial cells, but also their morphology. According to [113, 114], the shear stress transforms cobblestone-shaped endothelial cells of random orientation into fusiform endothelial cells aligned in the direction of blood flow, Fig. 3.12. When exposed to turbulent flow, the endothelial cells have shown a tendency to develop a more rounded form than in the laminar flow regime. Moreover, very low turbulent shear stresses ($\leq 0.15\,\mathrm{Pa}$) also seem to promote cell division [61]. Experiments have further indicated that the shape of the endothelial cells is affected not only by the shear stress magnitude, but also by its oscillation. Namely, under oscillatory flow conditions, the endothelial morphology has been observed to resemble the one corresponding to low shear stress exposure [80].

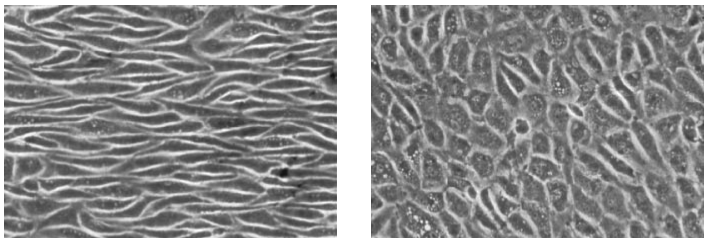

Fig. 3.12. Transformation of endothelial cell morphology by fluid shear stress: $\tau_W > 1.5\,\mathrm{Pa}$ (*left*) and $\tau_W = 0 - 0.4\,\mathrm{Pa}$ (*right*) [113].

Endothelial dysfunction originating from cell damage or destruction, caused, for example, by abnormal hemodynamics, surgical injury or ageing of the organism [110], can have far-reaching consequences for the vessel and the organism itself. With the dysfunctional endothelium, the vessel loses its ability to perceive its immediate hemodynamical environment and to synthesise mediators important for the maintenance of the internal equilibrium (homeostasis). It is, therefore, understandable that during the healing process the vessel tries to restore its tunica intima by forming a new non-thrombogenic layer commonly called *neointima*. In synthetic grafts, the thickness of this new layer, which consists mainly of longitudinally orientated smooth muscle cells migrated from the tunica media, is dependent on the surface roughness [61]. Generally, crimped prostheses have thicker neointima than the non-crimped ones.

3.3.1 Atherosclerosis

The arteriosclerotic vascular disease as the main reason for the development of cardiovascular disease has several phases, each of which can last several years or decades, Fig. 3.13. The process of atherosclerotic plaque growth denoted as atherogenesis begins in the presence of elevated plasma cholesterol and high levels of low density lipoprotein (LDL) oxidation within the tunica intima. The formation of foam cells and their continued accumulation in the intima leads to a lesion called fatty streak. With the continuing effect of endothelial cell injury, high cholesterol level and abnormal hemodynamics, the smooth muscle cells tend to migrate to the subendothelial level. In this phase, the fatty streak is mostly grown into a fibro-fatty lesion with multiple layers of smooth muscle

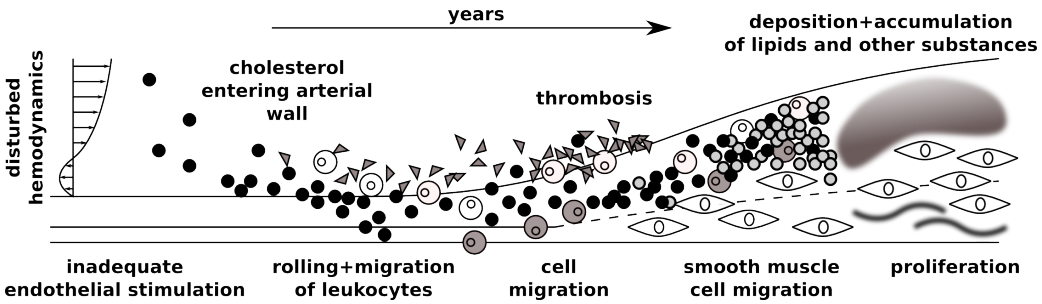

Fig. 3.13. Schematic of atherogenesis as a result of disturbed blood flow and inadequate endothelial stimulation.

cells and connective tissue. After many years of lipid deposition and calcification, the resulting atherosclerotic plaque may consists of several layers and/or lipid cores, see, for example, Fig. 3.1.

On the basis of clinical observations, it has been noted that the occurrence of atherosclerotic plaques is restricted to certain parts of the arterial circulation such as the coronary and carotid bifurcations [174, 181]. In the past, there have been many hypotheses and theories that tried to explain this localised lipid deposition and later on suggested a possible connection between the atherosclerosis and local hemodynamics. Among the many theories, it is possible to mention, for example:

- **low pressure theory** (M. Texon, 1957) [180]:

This theory is based on the hypothesis that at sites of arterial curvature, where the blood is affected by the inertia forces, the pressure at the outer wall is higher than the one at the inner wall of the curvature. Texon postulated that the pressure at the inner wall would significantly decrease to become negative so that it would lead to the detachment of the intima from the media sites, triggering so the disease process. Later, it was shown that the pressure difference between the inner and outer walls in the arteries is very small and that under normal physiological conditions the pressure at the inner wall will not drop to negative values [18]. Although refuted, this theory was one of the first to seek a correlation between atherosclerosis and hemodynamics.

- **high shear stress theory** (D. L. Fry, 1968) [45]:

This theory assumes that elevated shear stress may cause endothelial damage and impair the normal mass transport process within the vessel wall. On the basis of in vivo canine studies, Fry defined the critical shear stress to be $37.9 \pm 8.5\,\mathrm{Pa}$. Similarly to the previous theory, this hypothesis was also refuted because it could not explain the fact that many atherosclerotic lesions occur in low shear stress regions or that some expected high shear stress regions are spared of atherosclerotic lesions [80].

- **safe wall shear stress bandwidth theory** (C. Kleinstreuer et al., 1991) [82]:

This theory postulates that the atherogenesis is initiated by very low, oscillating wall shear and the actual plaque growth is influenced by both high and low shear stresses. Taking these facts into consideration, the authors of this theory set up a safe wall shear stress (WSS) bandwidth with lower and higher limits. When WSS falls outside this safe band, it triggers plaque formation and the WSS magnitude beyond the band limits determines the growth rate of this plaque. According to its authors, the concept of the safe-WSS-bandwidth is applicable to a wide variety of physiological flow problems from aortic and carotid artery bifurcations to bypass configurations. The only known exception is the blood flow in arterial bifurcations, whose input contains a reverse flow phase [80]. In this case, the theory fails.

The limited success of some of the hemodynamic theories, which are discussed in detail in [18,61,80,181], is due to the fact that they neglect the response of endothelium to the changes in hemodynamical environment. At present, the more successful hypotheses are those based on spatial and temporal shear stress variations rather than on the WSS magnitude [80]. One of the most popular hypotheses is the **low and oscillating shear stress model** introduced by Ku et al. in 1985 [91] and later on reformulated in 1996 [54]. It utilises the *oscillatory shear index* (OSI), see Eq. (5.4).

3.3.2 Intimal hyperplasia

As described in Section 3.2.2, the healing process at an anastomosis may have the form of stabilised intimal fibrocellular hypertrophy (IHF) and/or occlusive intimal hyperplasia (IH). The exact factors determining the course of the healing process between both intimal forms remain still unknown, although some hypotheses suggest the endothelial damage and compliance mismatch to be some kind of triggers [7]. On the other hand, it is important to note that intimal thickening can develop only during decreased blood flow and low shear stress and that it does not require surgical wall injury or endothelial damage [204]. Because graft implantation is always associated with significant changes in hemodynamics, vessel lumen and wall tensile stress, the hemodynamical and mechanical factors play a crucial role in the IH formation.

According to the review paper [129], which offers a detailed insight into the complex mechanism of venous graft IH, the thickening of tunica intima can be summarised in five main phases following the graft implantation, Fig. 3.14:

1) endothelium damage resulting in thrombocyte activation,
2) inflammatory processes accompanied by the presence of leukocytes,
3) thrombosis (activation of the coagulation cascade),
4) smooth muscle cell migration into the neointima,
5) intimal thickening due to smooth muscle cell proliferation and extracellular matrix deposition.

In addition to the biological and biochemical viewpoints, there are also first attempts to mathematically describe the complex mechanism of IH formation in dependence on shear stress and time. Although some of these attempts are rather theoretical, e.g., [17, 157], there are some mathematical models based on experimental data obtained from mongrel dogs and rabbits [64, 185].

As mentioned earlier, one of the most common causes of graft failure is the neointimal hyperplasia associated with occlusive intimal thickening in the anastomosis region, Fig. 3.15. The literature such as [34] and [61] addresses this problem mainly in relation with end-to-side anastomoses, since the intimal growth at side-to-side anastomoses is usually not so progressive to cause occlusion. Some of the sites prone to IH, which include the suture line and the arterial wall opposite the distal anastomosis, are shown

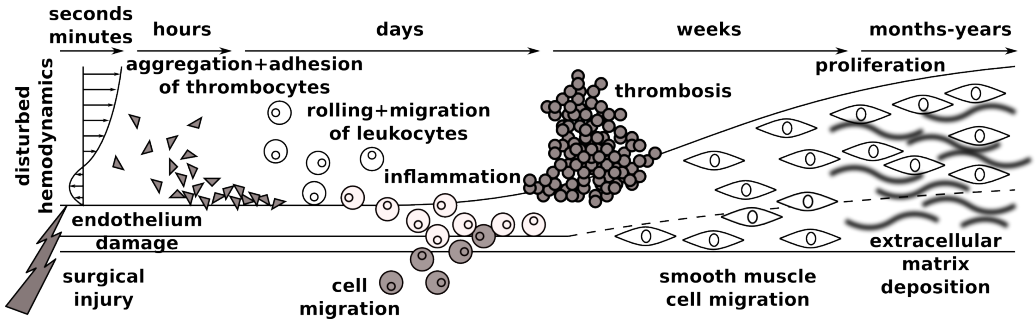

Fig. 3.14. Schematic of IH formation as a result of surgical injury according to [129].

in Fig. 3.16. The terminology used in connection with the localisation of anastomotic intimal hyperplasia is very specific, as apparent from Fig. 3.16, and as such will be used for the analysis and discussion of obtained numerical results in Chapter 5.

Some of the hypotheses attribute the anastomotic intimal hyperplasia to the *compliance mismatch* between the native artery and the bypass graft [52]. The concept of this mismatch is based on the different mechanical properties of both constituent vessels in the suture line region. According to [87], the *compliance* as a quantity has been introduced clinically in order to define the complex physical properties of tissues. It expresses a dimensional change with respect to either force or pressure change. For example, a tissue is denoted as highly compliant if it is easily stretched with minimal force or small luminal pressure increase. For vessels, the compliance is defined as [182]

$$C = \frac{D_{\mathrm{sys}} - D_{\mathrm{dia}}}{D_{\mathrm{dia}}(p_{\mathrm{sys}} - p_{\mathrm{dia}})} \times 10^4 \, [\%/\mathrm{mmHg} \times 10^{-2}] \,, \tag{3.3}$$

where D_{sys} and D_{dia} are the inner diameters of the vessel during the systolic and diastolic phases of the cardiac cycle, respectively, and p_{sys} and p_{dia} are the pressures in mmHg corresponding to the systolic and diastolic phases, respectively. The compliance of several selected autologous and synthetic graft materials is summarised in Tab. 3.4 and shown in Fig. 3.17. At this point, it is also worth mentioning that the compliance is not time-independent. In other words, arterial compliance is known to decrease with advancing age (age-related arterial stiffening) [110] and the compliance of some grafts usually changes after their implantation into the arterial circulation (e.g., 'arterialisation' of venous grafts) [75].

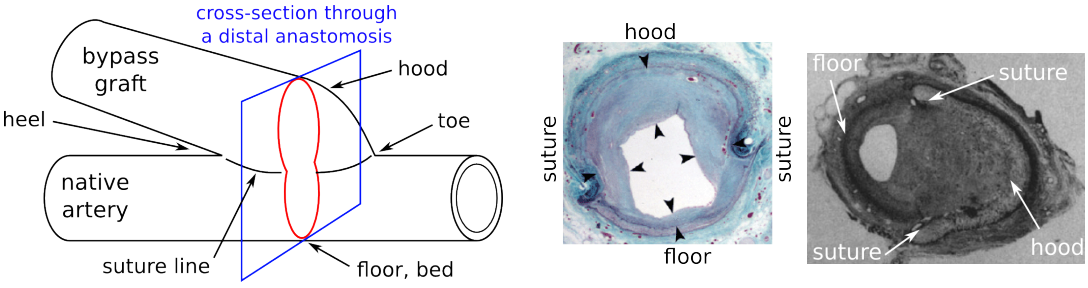

Fig. 3.15. Examples of intimal hyperplasia in an end-to-side anastomosis cross-section [134].

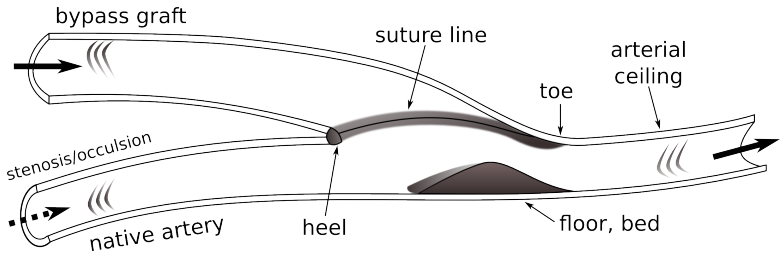

Fig. 3.16. Longitudinal section of a distal end-to-side anastomosis with areas prone to intimal hyperplasia formation, modified from [7].

graft type/material	compliance C
arteries	$5.4 - 7.4$
– femoral artery	6.0
– thoracic aorta	$13.6 - 26.8$
veins	$2.5 - 10$
– great saphenous vein	$4.4 - 4.6$
bovine heterograft[a]	2.6
Dacron (PET)	$1.9 - 3.7$
(e)PTFE	$1.5 - 1.8$
polyurethane (PU)	$8.4 - 8.8$

Tab. 3.4. Compliance of vessels and selected graft materials, [50, 87, 165, 182].

[a]Heterograft is a tissue graft taken from a species different from that of the recipient.

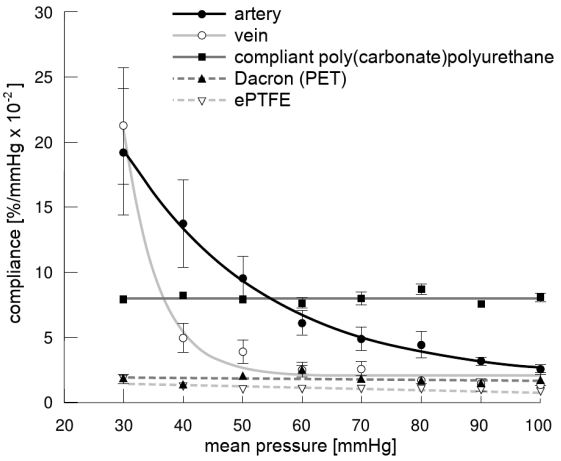

Fig. 3.17. Compliance as a function of mean pressure for various grafts [177].

The different mechanical properties of the native artery and graft predetermine the behaviour of the anastomosis region as apparent from Fig. 3.18, where the suture line response to pressure increase is intermediate between that of its constituent vessels. The impact of the compliance mismatch is also particularly noticeable at the anastomosis and its immediate vicinity ($2 - 4$ mm), where a hypercompliant zone has been observed, Fig. 3.19. According to [53], this zone commonly called *para-anastomotic hypercompliant zone* (PHZ) is characterised by an approximately 50% compliance increase and than around 60% compliance decrease compared to the adjacent reference values. Some hypotheses claim that this phenomenon is caused by the presence of elastic elastin and inelastic collagen fibres [165], whereas others attribute it to the suturing material and suturing technique [182].

According to [181], the effect of compliance mismatch on the development of intimal hyperplasia is amplified by the hemodynamical changes associated with graft implanta-

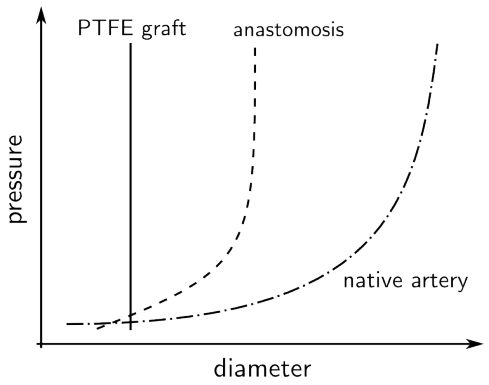

Fig. 3.18. Pressure-diameter relationships according to [165].

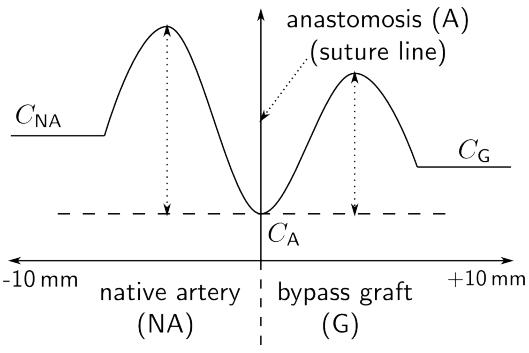

Fig. 3.19. Compliance profile – compliance distribution in the vicinity of suture line [182].

tion. For a vein graft, normal physiological flow conditions include blood pressures in the range of 20 to 30 mmHg ($2.5 - 4.0$ kPa). In general, veins are not exposed to pressures greater than 75 mmHg (10 kPa) [165]. Thus, their implantation into the arterial circulation, where the pressures are mostly around $120 - 130$ mmHg ($16 - 17$ kPa), inevitably leads to overdistension and immediate de-endothelisation. Following this exposure, a venous graft goes through an adaptation process denoted as 'arterialisation' consisting of re-endothelisation and wall thickening accompanied by reduction in wall tension and considerable increase in wall stiffness [183].

The concept of the compliance mismatch is sufficient to explain the presence of the suture line stenosis, but is unable to predict the intimal thickening at the arterial floor, Fig. 3.16, where the tissue remains surgically undamaged. According to [52], the observed pathological changes in the tunica intima are mainly of hemodynamic origin, i.e., triggered by disturbed blood flow and inadequate endothelium stimulation. For illustration, Fig. 3.20 (left) shows the flow pattern in an end-to-side anastomosis with occluded native artery (the only incoming blood flow is the one from the graft). As apparent, the flow field is complex and includes a stagnation point at the arterial floor and a large recirculation zone in the proximal part of the native artery.

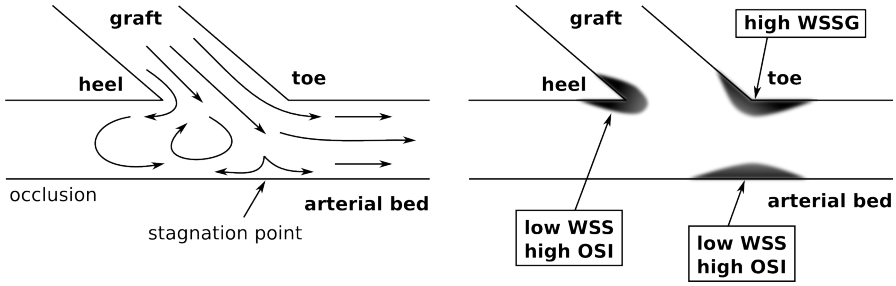

Fig. 3.20. Arterial bypass graft – flow field (*left*) and distribution of hemodynamical wall parameters (*right*) in areas prone to intimal hyperplasia formation [52].

Because the IH formation is very similar to the initial phases of atherosclerosis [61,80], hemodynamical studies often employ theories and hypotheses originally formulated for the atherosclerosis such as the 'safe wall shear stress bandwidth theory' described in Section 3.3.1. In general, it can be said that during the last two decades quite many hemodynamical indicators of areas prone to intimal hyperplasia and atherosclerosis have been defined, for example:

- **wall shear stress** (WSS):
  - WSS has a significant effect on the proper endothelial function and the secretion of vasoactive agents such as nitric oxide (NO) and endothelin [110];
  - after exposure to low and oscillating WSS ($|\boldsymbol{\tau}_W| < 0.5$ Pa [52]), the surface of endothelial cells changes from anti- into a pro-thrombotic surface promoting lipid accumulation and pro-inflammatory processes inside the vessel wall;
  - *instantaneous WSS magnitude*:

$$|\boldsymbol{\tau}_W| = \eta \left| \frac{\partial \boldsymbol{v}}{\partial \boldsymbol{n}} \right| = \eta \sqrt{\left(\frac{\partial v_1}{\partial \boldsymbol{n}} \right)^2 + \left(\frac{\partial v_2}{\partial \boldsymbol{n}} \right)^2 + \left(\frac{\partial v_3}{\partial \boldsymbol{n}} \right)^2}, \tag{3.4}$$

where η is the dynamic viscosity, $\boldsymbol{n}$ is the outward unit vector normal to the wall and $\boldsymbol{v} = [v_1, v_2, v_3]^T$ is the velocity vector;

– *cycle-averaged WSS*:

$$|\overline{\boldsymbol{\tau}_W}| = \frac{1}{T}\int_0^T |\boldsymbol{\tau}_W|\,\mathrm{d}\,t = \frac{1}{T}\int_0^T \eta \left|\frac{\partial \boldsymbol{v}}{\partial \boldsymbol{n}}\right| \mathrm{d}\,t\,, \tag{3.5}$$

where T is the period of the cardiac cycle and $|\boldsymbol{\tau}_W|$ is the WSS magnitude;

– *stagnation point* – a point at the arterial floor characterised by very low WSS magnitude and zero velocity gradient (a result of blood flow division between the proximal and distal parts of the native artery [61]), see Fig. 3.20 (left);

- **wall shear stress gradient** (WSSG):
  – large gradients of WSS induce functional changes in endothelial cells that may trigger morphological remodelling associated with vessel restenosis [52];
  – *spacial wall shear stress gradient* (SWSSG):

$$|\mathrm{SWSSG}| = \left|\frac{\partial \boldsymbol{\tau}_W}{\partial \boldsymbol{n}}\right|, \quad |\overline{\mathrm{SWSSG}}| = \frac{1}{T}\int_0^T |\mathrm{SWSSG}|\,\mathrm{d}\,t\,; \tag{3.6}$$

  – *temporal wall shear stress gradient* (TWSSG):

$$|\mathrm{TWSSG}| = \left|\frac{\partial \boldsymbol{\tau}_W}{\partial t}\right|, \quad |\overline{\mathrm{TWSSG}}| = \frac{1}{T}\int_0^T |\mathrm{TWSSG}|\,\mathrm{d}\,t\,; \tag{3.7}$$

- **oscillatory shear index** (OSI):
  – expresses the extent of the WSS oscillation within one cardiac cycle;
  – introduced by Ku et al. in 1985 [91] and later on reformulated in 1996 [54]:

$$\mathrm{OSI} = \frac{1}{2}\left(1 - \frac{\left|\int_0^T \boldsymbol{\tau}_W\,\mathrm{d}\,t\right|}{\int_0^T |\boldsymbol{\tau}_W|\,\mathrm{d}\,t}\right); \tag{3.8}$$

  – OSI equal to zero indicates an area without any shear stress oscillation, whereas the value 0.5 stands for a highly oscillatory shear stress;

Besides the hemodynamical quantities mentioned above, there are others that may be used as indicators of relative impact and extent of pathological changes occurring in blood vessels, e.g., the near wall residence time (NWRT) used for the quantification of platelet accumulation or the surface reactivity (SR) to determine the surface proneness to thrombus formation [188].

Distribution of hemodynamical wall parameters (WSS and OSI) in an end-to-side anastomosis is illustrated in Fig. 3.20 (right). On the basis of experiments and clinical observations, it has been proven that the formation of intimal hyperplasia at the heel and arterial floor is, among others, caused by low and oscillating WSS [52]. By contrast, the intimal thickening in the toe region is a result of large WSS gradients, especially the temporal ones that have been observed to stimulate cell proliferation [196].

3.3.3 Summary

All the information pertaining to the significance of hemodynamics in the cardiovascular system and the triggering of atherosclerosis and intimal hyperplasia mentioned in this work is summarised in Fig. 3.21, which shows a schematic of the correlation and two-way interaction between 'disturbed' hemodynamics and two arterial disease processes. It should be also noted that the hemodynamical factors together with the abnormal biological processes listed in Fig. 3.21 represent only the triggers, but not the causes of the disease [80]. In other words, the blood flow may set off and accelerate the disease process only if one or several risk factors such as hypertension and high cholesterol levels are present.

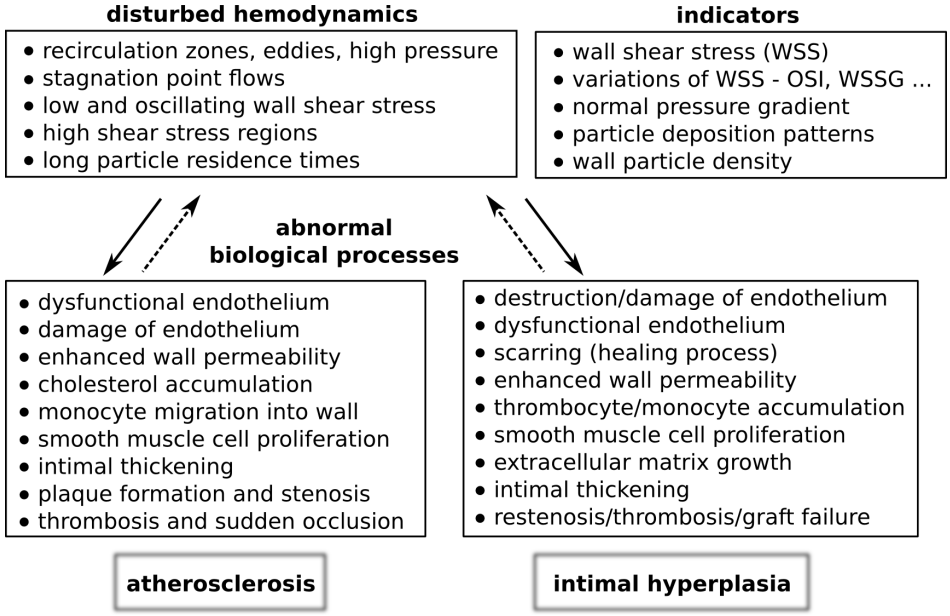

Fig. 3.21. Correlation and interaction between blood flow and vessel wall leading either to atherosclerosis or intimal hyperplasia [80, 81, 105].

Chapter 4

Mathematical modelling of blood flow

As comprehensively discussed, e.g., in [89] or [132], the blood flow in large- and middle-sized arteries is known to be very complex and in some (usually pathological) cases can even involve various flow regimes. Thus, before the introduction of the mathematical model and the description of numerical methods used for its solution, it is appropriate to address the simplifications and general assumptions made in this Ph.D. thesis:

- **blood rheology**

During the discussion carried out in Section 2.2, it was established that human blood as an incompressible fluid exhibits complex flow properties and falls into the category of non-Newtonian fluids. On the other hand, it was also mentioned that under certain conditions, blood's non-Newtonian behaviour does not significantly affect the overall hemodynamics and may be, thus, neglected. In this work, we will consider both possibilities. In other words, the blood will be treated as an incompressible generalised Newtonian fluid and the Newtonian behaviour will be seen as a special case.

- **impermeable and inelastic walls**

As mentioned in Section 3.3.2, saphenous veins used for bypass grafting adapt to high-pressure arterial blood flow by triggering morphological and metabolic changes [33, 75] that often result in gradual wall thickening and overall compliance decrease [61]. Based on this arterialisation process, we adopt the assumption of impermeable and inelastic walls in the remainder of this work. Note that this assumption is also made for the aorta, which can be explained by the fact that patients with coronary artery disease (and bypasses) have abnormally rigid aorta and that the stiffness of the aorta increases with age and in hypertension [92].

- **static bypass models**

All vessels in the human body are exposed to some kind of motion such as the coronary arteries to the motion of the heart. The effect of arterial motion on blood flow is closely addressed in [205], with the result that it does not have any significant effect on the hemodynamics if pulsatile flow conditions are considered. Thus, for the purpose of this Ph.D. thesis and to simplify the flow problems, the beating of the heart is neglected.

- **laminar blood flow**

In this study, we work on the assumption that blood flow in normal pathologically unchanged arteries is always laminar [89]. In the case of the aorta, the largest artery in the human body (see, for example, Section 5.3), there are still some doubts in the scientific community whether the normal flow regime is laminar flow or not. In the past, turbulent flow has been confirmed during exercise, when the Reynolds number for the aorta can increase 10-fold [89], and in some pathological cases, where it is diagnosed as heart murmur and usually associated with aortic stenosis, valve incompetence or artificial heart valves. Because all numerical simulations will be carried out under rest conditions and the CT scans used for model reconstruction in Section 5.3 are from patients with

no diagnosed heart murmur, the assumption of laminar blood flow is adopted in the remainder of this work. Note that this assumption is also motivated by other studies such as [43, 162, 207], where similar modelling approach was chosen.

4.1 Mathematical model of incompressible generalised Newtonian flow

Let us consider a time interval $(0, \mathcal{T})$, $\mathcal{T} > 0$ and a bounded three-dimensional computational domain $\Omega \subset \mathbb{R}^3$ with boundary $\partial\Omega = \partial\Omega_{\mathrm{I}} \cup \partial\Omega_{\mathrm{O}} \cup \partial\Omega_{\mathrm{W}}$. The boundaries $\partial\Omega_I$, $\partial\Omega_O$ and $\partial\Omega_W$ represent the *Inlet*, *Outlet* and *impermeable, inelastic Walls* of the computational domain Ω, respectively. Further, let us introduce the *space-time cylinder* denoted by $\Omega_{\mathrm{T}} = \Omega \times (0, \mathcal{T})$.

According to the assumptions listed above, we consider the blood flow to be an unsteady laminar isothermal flow of an incompressible generalised Newtonian fluid with constant density ϱ and shear-dependent dynamic viscosity $\eta(\dot{\gamma})$, where $\dot{\gamma}$ is the shear rate (see Appendix A). The assumption of isothermal flow is based on the fact that the temperature change of the blood within the computational domain Ω is assumed to be negligible. With regard to Section 2.3, where the blood rheology and the known viscosity models were described in detail, we apply the following viscosity models, Fig. 4.1:

- the Newtonian viscosity model

$$\eta(\dot{\gamma})^{(0)} = \eta_{\infty}^{(0)}\,, \tag{4.1}$$

- the Carreau-Yasuda model [23]

$$\eta(\dot{\gamma})^{(1)} = \eta_{\infty}^{(1)} + \left(\eta_0^{(1)} - \eta_{\infty}^{(1)}\right)\left[1 + \left(\lambda^{(1)}\dot{\gamma}\right)^m\right]^{\frac{n-1}{m}}\,, \tag{4.2}$$

- the modified Cross model [100]

$$\eta(\dot{\gamma})^{(2)} = \eta_{\infty}^{(2)} + \left(\eta_0^{(2)} - \eta_{\infty}^{(2)}\right)\left[1 + \left(\lambda^{(2)}\dot{\gamma}\right)^b\right]^{-a}. \tag{4.3}$$

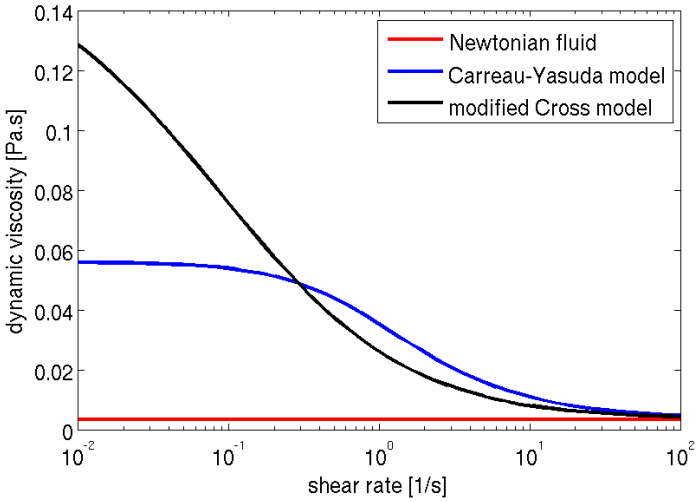

Fig. 4.1. Dynamic viscosity η – shear rate $\dot{\gamma}$ relationships for the three selected viscosity models taken from Tab. 2.7.

The fundamental governing equations describing the motion of blood in large- and middle-sized arteries are derived from the integral form of the conservative laws of mass, momentum and total energy in Eulerian description [57,178]. In the time-space cylinder $\Omega_{\mathrm{T}} = \Omega \times (0, \mathcal{T})$, the resulting equations commonly known as the non-linear system of Navier-Stokes equations in the conservative form [60,190] have the following form:

$$\frac{\partial v_i}{\partial x_i} = 0\,, \tag{4.4}$$

$$\frac{\partial v_i}{\partial t} + \frac{\partial}{\partial x_j}\left(v_i v_j\right) + \frac{1}{\varrho}\frac{\partial p}{\partial x_i} = \frac{1}{\varrho}\frac{\partial}{\partial x_j}\left[\eta(\dot\gamma)^{(\theta)}\left(\frac{\partial v_i}{\partial x_j} + \frac{\partial v_j}{\partial x_i}\right)\right] \equiv \frac{1}{\varrho}\frac{\partial}{\partial x_j}\left(2\eta(\dot\gamma)^{(\theta)} d_{ij}\right) \tag{4.5}$$

for $i, j = 1, 2, 3$, where $t \in (0, \mathcal{T})$ is the time, v_i is the i-th component of the velocity vector $\boldsymbol{v} = [v_1, v_2, v_3]^T$ corresponding to the Cartesian coordinate x_i of the spatial coordinate vector $\boldsymbol{x} = [x_1, x_2, x_3]^T \in \Omega$, p is the pressure, $\eta(\dot\gamma)^{(\theta)}$, $\theta = 0, 1, 2$ denotes the dynamic viscosity of the generalised Newtonian fluid given by Eqs. (4.1)–(4.3), and d_{ij} are the components of the rate of deformation tensor $\mathbf{D} = \frac{1}{2}\left(\nabla\boldsymbol{v} + (\nabla\boldsymbol{v})^T\right)$. Because of the isothermal assumption mentioned above, all of the blood's properties are considered temperature-independent, making it possible to omit the energy equation from the system of equations (4.4) and (4.5). For the modelling purposes in the work, the influence of external volume forces is neglected, as well.

In the Cartesian coordinate system, the non-linear elliptic-parabolic system of partial differential equations (4.4) and (4.5), known as the system of Navier-Stokes equations for the laminar flow of an incompressible generalised Newtonian fluid, has the form

$$\frac{\partial u}{\partial x} + \frac{\partial v}{\partial y} + \frac{\partial w}{\partial z} = 0\,, \tag{4.6}$$

$$\begin{aligned}\frac{\partial u}{\partial t} &+ \frac{\partial}{\partial x}(u^2) + \frac{\partial}{\partial y}(uv) + \frac{\partial}{\partial z}(uw) + \frac{1}{\varrho}\frac{\partial p}{\partial x} = \frac{1}{\varrho}\frac{\partial}{\partial x}\left[2\eta(\dot\gamma)^{(\theta)}\frac{\partial u}{\partial x}\right] + \\ &+ \frac{1}{\varrho}\frac{\partial}{\partial y}\left[\eta(\dot\gamma)^{(\theta)}\left(\frac{\partial u}{\partial y} + \frac{\partial v}{\partial x}\right)\right] + \frac{1}{\varrho}\frac{\partial}{\partial z}\left[\eta(\dot\gamma)^{(\theta)}\left(\frac{\partial u}{\partial z} + \frac{\partial w}{\partial x}\right)\right],\end{aligned} \tag{4.7}$$

$$\begin{aligned}\frac{\partial v}{\partial t} &+ \frac{\partial}{\partial x}(uv) + \frac{\partial}{\partial y}(v^2) + \frac{\partial}{\partial z}(vw) + \frac{1}{\varrho}\frac{\partial p}{\partial y} = \frac{1}{\varrho}\frac{\partial}{\partial x}\left[\eta(\dot\gamma)^{(\theta)}\left(\frac{\partial v}{\partial x} + \frac{\partial u}{\partial y}\right)\right] + \\ &+ \frac{1}{\varrho}\frac{\partial}{\partial y}\left[2\eta(\dot\gamma)^{(\theta)}\frac{\partial v}{\partial y}\right] + \frac{1}{\varrho}\frac{\partial}{\partial z}\left[\eta(\dot\gamma)^{(\theta)}\left(\frac{\partial v}{\partial z} + \frac{\partial w}{\partial y}\right)\right],\end{aligned} \tag{4.8}$$

$$\begin{aligned}\frac{\partial w}{\partial t} &+ \frac{\partial}{\partial x}(uw) + \frac{\partial}{\partial y}(vw) + \frac{\partial}{\partial z}(w^2) + \frac{1}{\varrho}\frac{\partial p}{\partial z} = \frac{1}{\varrho}\frac{\partial}{\partial x}\left[\eta(\dot\gamma)^{(\theta)}\left(\frac{\partial w}{\partial x} + \frac{\partial u}{\partial z}\right)\right] + \\ &+ \frac{1}{\varrho}\frac{\partial}{\partial y}\left[\eta(\dot\gamma)^{(\theta)}\left(\frac{\partial w}{\partial y} + \frac{\partial v}{\partial z}\right)\right] + \frac{1}{\varrho}\frac{\partial}{\partial z}\left[2\eta(\dot\gamma)^{(\theta)}\frac{\partial w}{\partial z}\right],\end{aligned} \tag{4.9}$$

where u, v, w are the components of the velocity vector $\boldsymbol{v}$ corresponding to the Cartesian coordinates x, y, z of the spacial coordinate vector $\boldsymbol{x}$. The system of equations (4.6)–(4.9) written in *primitive variables* p, u, v, w can be transformed into its dimensionless form by dividing all quantities with suitably chosen reference values

$$\begin{aligned}&x^* = \frac{x}{L_{ref}},\ \ y^* = \frac{y}{L_{ref}},\ \ z^* = \frac{z}{L_{ref}},\ \ u^* = \frac{u}{v_{ref}},\ \ v^* = \frac{v}{v_{ref}},\ \ w^* = \frac{w}{v_{ref}},\\ &\varrho^* = \frac{\varrho}{\varrho_{ref}},\ \ p^* = \frac{p}{p_{ref}},\ \ t^* = \frac{t}{t_{ref}},\ \ \eta_0^{*(\theta)} = \frac{\eta_0^{(\theta)}}{\eta_{ref}^{(\theta)}},\ \ \eta_\infty^{*(\theta)} = \frac{\eta_\infty^{(\theta)}}{\eta_{ref}^{(\theta)}},\ \theta = 0, 1, 2.\end{aligned} \tag{4.10}$$

Here, the characteristic length $L_{ref} > 0$, reference velocity $v_{ref} > 0$, reference density ϱ_{ref} and reference dynamic viscosity $\eta_{ref}^{(\theta)}$, $\theta = 0, 1, 2$ are chosen beforehand, whereas the remaining reference values of pressure and time have to be calculated

$$p_{ref} = \varrho_{ref} v_{ref}^2, \qquad t_{ref} = \frac{L_{ref}}{v_{ref}}. \tag{4.11}$$

In this Ph.D. thesis, the values of the reference density ϱ_{ref} and reference dynamic viscosity $\eta_{ref}^{(\theta)}$ are chosen such that the resulting dimensionless variables ϱ^* and $\eta_\infty^{*(\theta)}$ are equal to one, i.e., we set $\varrho_{ref} \equiv \varrho$ and $\eta_{ref}^{(\theta)} \equiv \eta_\infty^{(\theta)}$, $\theta = 0, 1, 2$.

For the non-dimensionalisation of the viscosity models (4.1)–(4.3), we utilise

$$\dot{\gamma} = \frac{v_{ref}}{L_{ref}} \dot{\gamma}^*, \tag{4.12}$$

which results from the substitution of Eq. (4.10) into the formula for shear rate (A.8). In the case of the Newtonian viscosity model ($\theta = 0$) given by Eq. (4.1), we write

$$\eta(\dot{\gamma})^{(0)} = \eta_{ref}^{(0)} \cdot \eta_\infty^{*(0)} \equiv \eta_{ref}^{(0)} \cdot \eta^*(\dot{\gamma}^*)^{(0)}, \tag{4.13}$$

where $\eta^*(\dot{\gamma}^*)^{(0)} = 1$. For the Carreau-Yasuda model ($\theta = 1$) given by Eq. (4.2), the application of Eqs. (4.10)–(4.12) yields

$$\begin{aligned} \eta(\dot{\gamma})^{(1)} &= \eta_{ref}^{(1)} \cdot \eta_\infty^{*(1)} + \frac{\eta_{ref}^{(1)} \cdot \eta_0^{*(1)} - \eta_{ref}^{(1)} \cdot \eta_\infty^{*(1)}}{\left[1 + \left(t_{ref} \cdot \lambda^{*(1)} \cdot \frac{v_{ref}}{L_{ref}} \dot{\gamma}^*\right)^m\right]^{\frac{1-n}{m}}} = \\ &= \eta_{ref}^{(1)} \left\{ 1 + \frac{\eta_0^{*(1)} - 1}{\left[1 + \left(\lambda^{*(1)} \dot{\gamma}^*\right)^m\right]^{\frac{1-n}{m}}} \right\} \equiv \eta_{ref}^{(1)} \cdot \eta^*(\dot{\gamma}^*)^{(1)}, \end{aligned} \tag{4.14}$$

where the dimensionless relaxation time $\lambda^{(\theta)}$, which is present in both considered non-Newtonian models, is given as

$$\lambda^{(\theta)} = t_{ref} \cdot \lambda^{*(\theta)}, \quad \theta = 1, 2. \tag{4.15}$$

Based on Eq. (4.14), the Carreau-Yasuda model can be transformed into the non-dimensional form

$$\eta^*(\dot{\gamma}^*)^{(1)} = 1 + \left(\eta_0^{*(1)} - 1\right) \left[1 + \left(\lambda^{*(1)} \dot{\gamma}^*\right)^m\right]^{\frac{n-1}{m}}. \tag{4.16}$$

Analogously, the non-dimensionalisation of the modified Cross model ($\theta = 2$) given by Eq. (4.3) utilises Eqs. (4.10)–(4.12) and (4.15)

$$\begin{aligned} \eta(\dot{\gamma})^{(2)} &= \eta_{ref}^{(2)} \cdot \eta_\infty^{*(2)} + \frac{\eta_{ref}^{(2)} \cdot \eta_0^{*(2)} - \eta_{ref}^{(2)} \cdot \eta_\infty^{*(2)}}{\left[1 + \left(t_{ref} \cdot \lambda^{*(2)} \cdot \frac{v_{ref}}{L_{ref}} \dot{\gamma}^*\right)^b\right]^a} = \\ &= \eta_{ref}^{(2)} \left\{ 1 + \frac{\eta_0^{*(2)} - 1}{\left[1 + \left(\lambda^{*(2)} \dot{\gamma}^*\right)^b\right]^a} \right\} \equiv \eta_{ref}^{(2)} \cdot \eta^*(\dot{\gamma}^*)^{(2)}, \end{aligned} \tag{4.17}$$

which consequently leads to

$$\eta^*(\dot{\gamma}^*)^{(2)} = 1 + \left(\eta_0^{*\,(2)} - 1\right)\left[1 + \left(\lambda^{*\,(2)}\dot{\gamma}^*\right)^b\right]^{-a}. \tag{4.18}$$

The substitution of Eqs. (4.10), (4.11) and (4.13) or (4.14) or (4.17) into the governing equations (4.6)–(4.9) yields the non-linear system of Navier-Stokes equations in the non-dimensional conservative form

$$\frac{\partial u^*}{\partial x^*} + \frac{\partial v^*}{\partial y^*} + \frac{\partial w^*}{\partial z^*} = 0\,, \tag{4.19}$$

$$\begin{aligned}
\frac{\partial u^*}{\partial t^*} &+ \frac{\partial}{\partial x^*}(u^{*2} + p^*) + \frac{\partial}{\partial y^*}(u^*v^*) + \frac{\partial}{\partial z^*}(u^*w^*) = \\
&= \frac{1}{\mathrm{Re}^{(\theta)}}\left\{\frac{\partial}{\partial x^*}\left[2\eta^*(\dot{\gamma}^*)^{(\theta)}\frac{\partial u^*}{\partial x^*}\right] + \frac{\partial}{\partial y^*}\left[\eta^*(\dot{\gamma}^*)^{(\theta)}\left(\frac{\partial u^*}{\partial y^*} + \frac{\partial v^*}{\partial x^*}\right)\right] + \right. \\
&\left. + \frac{\partial}{\partial z^*}\left[\eta^*(\dot{\gamma}^*)^{(\theta)}\left(\frac{\partial u^*}{\partial z^*} + \frac{\partial w^*}{\partial x^*}\right)\right]\right\},
\end{aligned} \tag{4.20}$$

$$\begin{aligned}
\frac{\partial v^*}{\partial t^*} &+ \frac{\partial}{\partial x^*}(u^*v^*) + \frac{\partial}{\partial y^*}(v^{*2} + p^*) + \frac{\partial}{\partial z^*}(v^*w^*) = \\
&= \frac{1}{\mathrm{Re}^{(\theta)}}\left\{\frac{\partial}{\partial x^*}\left[\eta^*(\dot{\gamma}^*)^{(\theta)}\left(\frac{\partial v^*}{\partial x^*} + \frac{\partial u^*}{\partial y^*}\right)\right] + \frac{\partial}{\partial y^*}\left[2\eta^*(\dot{\gamma}^*)^{(\theta)}\frac{\partial v^*}{\partial y^*}\right] + \right. \\
&\left. + \frac{\partial}{\partial z^*}\left[\eta^*(\dot{\gamma}^*)^{(\theta)}\left(\frac{\partial v^*}{\partial z^*} + \frac{\partial w^*}{\partial y^*}\right)\right]\right\},
\end{aligned} \tag{4.21}$$

$$\begin{aligned}
\frac{\partial w^*}{\partial t^*} &+ \frac{\partial}{\partial x^*}(u^*w^*) + \frac{\partial}{\partial y^*}(v^*w^*) + \frac{\partial}{\partial z^*}(w^{*2} + p^*) = \\
&= \frac{1}{\mathrm{Re}^{(\theta)}}\left\{\frac{\partial}{\partial x^*}\left[\eta^*(\dot{\gamma}^*)^{(\theta)}\left(\frac{\partial w^*}{\partial x^*} + \frac{\partial u^*}{\partial z^*}\right)\right] + \right. \\
&\left. + \frac{\partial}{\partial y^*}\left[\eta^*(\dot{\gamma}^*)^{(\theta)}\left(\frac{\partial w^*}{\partial y^*} + \frac{\partial v^*}{\partial z^*}\right)\right] + \frac{\partial}{\partial z^*}\left[2\eta^*(\dot{\gamma}^*)^{(\theta)}\frac{\partial w^*}{\partial z^*}\right]\right\},
\end{aligned} \tag{4.22}$$

where the formula for the dimensionless dynamic viscosity $\eta^*(\dot{\gamma}^*)^{(\theta)}$ is chosen according to the applied viscosity model, i.e., for the Newtonian fluid ($\theta = 0$), the Carreau-Yasuda model ($\theta = 1$) and the modified Cross model ($\theta = 2$), we use Eqs. (4.13), (4.16) and (4.18), respectively. The reference Reynolds number $\mathrm{Re}^{(\theta)}$, $\theta = 0, 1, 2$ present in the right hand side of Eqs. (4.20)–(4.22) is defined as

$$\mathrm{Re}^{(\theta)} = \frac{\varrho_{ref}\, L_{ref}\, v_{ref}}{\eta_{ref}^{(\theta)}} \equiv \frac{\varrho\, L_{ref}\, v_{ref}}{\eta_{\infty}^{(\theta)}}. \tag{4.23}$$

Before proceeding, it should be mentioned that in the remainder of this Ph.D. thesis, the notation of all dimensionless variables by an asterisk will be dropped and that if not said otherwise, we will assume all variables to be dimensionless. This choice is made in order to avoid complications in notation.

For the defined bounded computational domain $\Omega \subset \mathbb{R}^3$ with boundary $\partial\Omega = \partial\Omega_{\mathrm{I}} \cup \partial\Omega_{\mathrm{O}} \cup \partial\Omega_{\mathrm{W}}$, we introduce the vector of primitive variables (the vector of unknowns)

$$\boldsymbol{w} = [w_1, \ldots, w_4]^T \equiv [p, v_1, v_2, v_3]^T \in \mathbb{R}^4\,, \tag{4.24}$$

where $\boldsymbol{w} = \boldsymbol{w}(\boldsymbol{x},t)$, $\boldsymbol{x} = [x_1, x_2, x_3]^T \in \Omega$ and $t \in (0, \mathcal{T})$. Then, in the time-space cylinder $\Omega_{\mathrm{T}} = \Omega \times (0, \mathcal{T})$, the non-linear system of Navier-Stokes equations (4.19)–(4.22) describing the unsteady incompressible Newtonian flow ($\theta = 0$) can be rewritten into the following compact vector form:

$$\boldsymbol{D}\frac{\partial \boldsymbol{w}}{\partial t} + \sum_{s=1}^{3} \frac{\partial \boldsymbol{F}_s^I(\boldsymbol{w})}{\partial x_s} = \frac{1}{\mathrm{Re}^{(0)}} \sum_{s=1}^{3} \frac{\partial \boldsymbol{F}_s^V(\boldsymbol{w})}{\partial x_s} \equiv \frac{1}{\mathrm{Re}^{(0)}} \nabla^2 \boldsymbol{D}\boldsymbol{w}, \tag{4.25}$$

where $\boldsymbol{D} = \mathrm{diag}\,(0,1,1,1)$, $\nabla^2 = \sum\limits_{s=1}^{3} \frac{\partial^2}{\partial x_s^2}$ is the Laplace operator and the vectors of inviscid $\boldsymbol{F}_s^I(\boldsymbol{w}) \in \mathbb{R}^4$, $s = 1,2,3$ and viscous $\boldsymbol{F}_s^V(\boldsymbol{w}) \in \mathbb{R}^4$, $s = 1,2,3$ fluxes are defined as

$$\boldsymbol{F}_s^I(\boldsymbol{w}) = \left[f_{s1}^I(\boldsymbol{w}), \ldots, f_{s4}^I(\boldsymbol{w})\right]^T \equiv [v_s, v_1 v_s + p\delta_{1s}, v_2 v_s + p\delta_{2s}, v_3 v_s + p\delta_{3s}]^T, \tag{4.26}$$

$$\boldsymbol{F}_s^V(\boldsymbol{w}) = \left[f_{s1}^V(\boldsymbol{w}), \ldots, f_{s4}^V(\boldsymbol{w})\right]^T \equiv \left[0, \frac{\partial v_1}{\partial x_s}, \frac{\partial v_2}{\partial x_s}, \frac{\partial v_3}{\partial x_s}\right]^T. \tag{4.27}$$

where δ_{ij} is the Kronecker delta. Similarly, for the unsteady incompressible non-Newtonian flow ($\theta = 1,2$), the governing equations (4.19)–(4.22) take the compact vector form

$$\boldsymbol{D}\frac{\partial \boldsymbol{w}}{\partial t} + \sum_{s=1}^{N} \frac{\partial \boldsymbol{F}_s^I(\boldsymbol{w})}{\partial x_s} = \frac{1}{\mathrm{Re}^{(\theta)}} \sum_{s=1}^{N} \frac{\partial \boldsymbol{F}_s^V(\boldsymbol{w})}{\partial x_s}, \tag{4.28}$$

where $\boldsymbol{D} = \mathrm{diag}\,(0,1,1,1)$, the vector of inviscid fluxes $\boldsymbol{F}_s^I(\boldsymbol{w}) \in \mathbb{R}^4$, $s = 1,2,3$ is given by Eq. (4.26) and the vector of viscous fluxes $\boldsymbol{F}_s^V(\boldsymbol{w}) \in \mathbb{R}^4$, $s = 1,2,3$ is defined as

$$\begin{aligned} \boldsymbol{F}_s^V(\boldsymbol{w}) &= \left[f_{s1}^V(\boldsymbol{w}), \ldots, f_{s4}^V(\boldsymbol{w})\right]^T \equiv \\ &\equiv \left[0, \eta(\dot{\gamma})^{(\theta)} \left(\frac{\partial v_1}{\partial x_s} + \frac{\partial v_s}{\partial x_1}\right), \ldots, \eta(\dot{\gamma})^{(\theta)} \left(\frac{\partial v_3}{\partial x_s} + \frac{\partial v_s}{\partial x_3}\right)\right]^T. \end{aligned} \tag{4.29}$$

Before we proceed to the description of the numerical methods for the solution of the aforementioned mathematical model in the time-space cylinder $\Omega_{\mathrm{T}} = \Omega \times (0, \mathcal{T})$, it is necessary to complete the system of equations (4.25) or (4.28) with the dimensionless initial condition

$$\boldsymbol{w}(\boldsymbol{x}, 0) = \boldsymbol{w}^0(\boldsymbol{x}),\ \boldsymbol{x} \in \Omega, \tag{4.30}$$

where $\boldsymbol{w}^0 \in \mathbb{R}^4$ is the vector of primitive variables at time $t = t^0 = 0$, and the dimensionless boundary conditions

$$\mathcal{B}(\boldsymbol{w}\,(\boldsymbol{x},t)) = 0 \quad \text{for } (\boldsymbol{x},t) \in \partial\Omega \times (0,\mathcal{T})\,, \tag{4.31}$$

where $\mathcal{B}$ is an appropriate operator. Since the Ph.D. thesis is aimed at the numerical solution of laminar blood flow in selected bypass models, see Chapter 5, the boundary $\partial\Omega$ of the computational domain $\Omega \subset \mathbb{R}^3$ is divided into three main parts:

- *inlet* $\partial\Omega_I$ – a Dirichlet boundary condition for the Cartesian components v_s, $s = 1,2,3$ of the velocity vector $\boldsymbol{v}$: $v_1 = v_{1I}, v_2 = v_{2I}, v_3 = v_{3I}$,
- *outlet* $\partial\Omega_O$ – a Dirichlet boundary condition for the pressure $p = p_O$,
- *impermeable and inelastic wall* $\partial\Omega_W$ – a non-slip boundary condition for the Cartesian components v_s, $s = 1,2,3$ of the velocity vector $\boldsymbol{v}$: $v_1 = 0, v_2 = 0, v_3 = 0$.

4.2 Numerical methods

Compared to the solution approaches commonly employed for the compressible viscous flows, the numerical solution of the non-linear system of incompressible Navier-Stokes equations (4.25) for $\theta = 0$ or (4.28) for $\theta = 1, 2$ requires a completely different strategy in order to overcome the absence of the time-dependent term in the continuity equation (4.19). Depending on this strategy, the numerical methods can be grouped into two main categories [39, 57, 178, 184]:

- *coupled/density-based methods* (e.g., artificial compressibility and dual time methods): In this approach, all primitive variables are treated as simultaneous unknowns. The governing equations are modified in order to support the velocity-pressure coupling and solved using traditional techniques developed for the solution of compressible flows.
- *segregated/sequential/pressure-based/pressure-correction methods* (e.g., SIMPLE and PISO algorithms): The distinguishing feature of this approach is the use of a derived equation to determine the pressure or its changes (usually a Poisson equation). Essentially, the computational algorithms employ a basic iterative procedure between the velocity and pressure fields until a divergence-free velocity field is reached, i.e., a process of velocity/pressure corrections takes place until the continuity equation is satisfied at the given time level.

In this Ph.D. thesis, selected methods from both the aforementioned categories will be addressed in detail and used for the numerical simulation of blood flow in idealised and patient-specific bypass models (Chapter 5).

4.3 Artificial compressibility method

The artificial compressibility method (ACM), as a typical representative of the coupled/density-based methods, was originally introduced by A. J. Chorin in the year 1967 [27]. Since then, the method has been improved many times [15, 24, 158, 160, 186] and is nowadays one of the most often used methods for the numerical solution of incompressible viscous flow problems, see, for example, [8, 74, 108, 190].

As described in the original work by Chorin [27], the artificial compressibility method is based on a slightly modified dimensionless continuity equation, which includes a term representing the artificial compressibility of the fluid, i.e.,

$$\sum_{s=1}^{3} \frac{\partial v_s}{\partial x_s} = 0 \qquad \overset{(ACM)}{\Longrightarrow} \qquad \frac{\partial \tilde{\varrho}}{\partial \tilde{t}} + \sum_{s=1}^{3} \frac{\partial v_s}{\partial x_s} = 0\,, \tag{4.32}$$

where $\tilde{\varrho}$ represents the dimensionless artificial density and $\tilde{t}$ is the dimensionless auxiliary iteration variable also known as the fictitious time, which, in principle, plays a similar role as the real time in the compressible flow case. The artificial density $\tilde{\varrho}$ is connected with the pressure p of the fluid through the dimensionless artificial equation of state

$$p = \frac{\tilde{\varrho}}{\delta}\,, \tag{4.33}$$

where the parameter δ is the artificial compressibility of the fluid. Comparing Eq. (4.33) with the equation of state for low Mach number compressible flows, we obtain the formula

for the dimensionless artificial speed of sound

$$\tilde{a} = \frac{1}{\sqrt{\delta}}\,. \tag{4.34}$$

When the steady state solution is reached, the term representing the artificial compressibility of the fluid vanishes (i.e., $\frac{\partial \tilde{\varrho}}{\partial \tilde{t}} \to 0$) and the modified continuity equation $(4.32)_2$ reduces to its original form given by Eq. $(4.32)_1$.

Taking into consideration Eqs. (4.33) and (4.34), the continuity equation modified in the sense of the artificial compressibility method $(4.32)_2$ can be rewritten as

$$\frac{1}{\tilde{a}^2}\frac{\partial p}{\partial \tilde{t}} + \sum_{s=1}^{3}\frac{\partial v_s}{\partial x_s} = 0\,. \tag{4.35}$$

Then, after replacing the dimensionless time t in Eqs. (4.20)–(4.22) with the fictitious time $\tilde{t}$, we get the modified dimensionless system of Navier-Stokes equations (4.35) and (4.20)–(4.22) written in the compact vector form

$$\frac{\partial \boldsymbol{w}}{\partial \tilde{t}} + \sum_{s=1}^{3}\frac{\partial \tilde{\boldsymbol{F}}_s^I(\boldsymbol{w})}{\partial x_s} = \frac{1}{\mathrm{Re}^{(\theta)}}\sum_{s=1}^{3}\frac{\partial \boldsymbol{F}_s^V(\boldsymbol{w})}{\partial x_s} \tag{4.36}$$

in the space-time cylinder $\Omega_{\mathrm{T}} = \Omega \times (0,\infty)$, where the vector of primitive variables $\boldsymbol{w} \in \mathbb{R}^4$, $\boldsymbol{w} = \boldsymbol{w}(\boldsymbol{x},\tilde{t})$, $\boldsymbol{x} = [x_1, x_2, x_3]^T \in \Omega$, $\tilde{t} \in (0,\infty)$ is given by Eq. (4.24) and the vector of inviscid fluxes $\tilde{\boldsymbol{F}}_s^I(\boldsymbol{w}) \in \mathbb{R}^4$, $s = 1,2,3$ is defined as

$$\tilde{\boldsymbol{F}}_s^I(\boldsymbol{w}) = \left[\tilde{f}_{s1}^I(\boldsymbol{w}),\ldots,\tilde{f}_{s4}^I(\boldsymbol{w})\right]^T \equiv \left[\tilde{a}^2 v_s, v_1 v_s + p\delta_{1s}, v_2 v_s + p\delta_{2s}, v_3 v_s + p\delta_{3s}\right]^T. \tag{4.37}$$

The vector of viscous fluxes $\boldsymbol{F}_s^V(\boldsymbol{w}) \in \mathbb{R}^4$, $s = 1,2,3$ for the Newtonian ($\theta = 0$) and non-Newtonian ($\theta = 1,2$) fluids is given by Eq. (4.27) and (4.29), respectively.

As apparent from above, the artificial compressibility method is based on the modification of the original conservative system of Navier-Stokes equations, which is of elliptic-parabolic type, into a hyperbolic-parabolic system. The main advantage of this approach is the possibility to use one of the standard numerical schemes commonly used for the solution of compressible flow problems, see, for example, [57, 60]. The principle of the artificial compressibility method also indicates that a steady state solution of the modified hyperbolic-parabolic conservative system of Navier-Stokes equations (4.36), (4.24), (4.37) and (4.27) or (4.29) will be independent of the fictitious time $\tilde{t}$ and the artificial compressibility parameter δ [27]. In this case, the role of δ is analogous to that of a relaxation parameter and the fictitious time $\tilde{t}$ serves as an auxiliary iteration variable without any physical meaning. Because of this, the applicability of the original artificial compressibility method is limited to the numerical solution of steady incompressible viscous flows.

Defining the Jacobi matrices $\boldsymbol{J}_s(\boldsymbol{w})$ of the inviscid fluxes $\tilde{\boldsymbol{F}}_s^I(\boldsymbol{w})$, $s = 1,2,3$

$$\boldsymbol{J}_s(\boldsymbol{w}) = \frac{\partial \tilde{\boldsymbol{F}}_s^I(\boldsymbol{w})}{\partial \boldsymbol{w}} = \begin{bmatrix} \dfrac{\partial \tilde{f}_{s1}^I}{\partial w_1} & \cdots & \dfrac{\partial \tilde{f}_{s1}^I}{\partial w_4} \\ \vdots & \ddots & \vdots \\ \dfrac{\partial \tilde{f}_{s4}^I}{\partial w_1} & \cdots & \dfrac{\partial \tilde{f}_{s4}^I}{\partial w_4} \end{bmatrix}, \tag{4.38}$$

which in 3D take the following form:

$$\boldsymbol{J}_1(\boldsymbol{w}) = \begin{bmatrix} 0 & \tilde{a}^2 & 0 & 0 \\ 1 & 2v_1 & 0 & 0 \\ 0 & v_2 & v_1 & 0 \\ 0 & v_3 & 0 & v_1 \end{bmatrix}, \; \boldsymbol{J}_2(\boldsymbol{w}) = \begin{bmatrix} 0 & 0 & \tilde{a}^2 & 0 \\ 0 & v_2 & v_1 & 0 \\ 1 & 0 & 2v_2 & 0 \\ 0 & 0 & v_3 & v_2 \end{bmatrix}, \; \boldsymbol{J}_3(\boldsymbol{w}) = \begin{bmatrix} 0 & 0 & 0 & \tilde{a}^2 \\ 0 & v_3 & 0 & v_1 \\ 0 & 0 & v_3 & v_2 \\ 1 & 0 & 0 & 2v_3 \end{bmatrix}, \quad (4.39)$$

the left-hand side of the conservative system of equations (4.36) can be rewritten as

$$\frac{\partial \boldsymbol{w}}{\partial \tilde{t}} + \sum_{s=1}^{N} \boldsymbol{J}_s(\boldsymbol{w}) \frac{\partial \boldsymbol{w}}{\partial x_s} = \frac{1}{\mathrm{Re}^{(\theta)}} \sum_{s=1}^{N} \frac{\partial \boldsymbol{F}_s^V(\boldsymbol{w})}{\partial x_s} \,. \quad (4.40)$$

The eigenvalues λ_{si}, $i = 1, \ldots, 4$ of the Jacobi matrices $\boldsymbol{J}_s(\boldsymbol{w})$, $s = 1, 2, 3$, determined as the roots of the characteristic polynomial

$$\det\left(\boldsymbol{J}_s(\boldsymbol{w}) - \lambda_s \boldsymbol{I}\right) = 0 \,, \quad (4.41)$$

where $\boldsymbol{I}$ is an identity matrix of order four, are

$$\lambda_{s1} = v_s - \sqrt{v_s^2 + \tilde{a}^2} \,, \quad \lambda_{s2} \equiv \lambda_{s3} = v_s \,, \quad \lambda_{s4} = v_s + \sqrt{v_s^2 + \tilde{a}^2}. \quad (4.42)$$

A crucial point for a successful application of the artificial compressibility method is the value of the artificial compressibility parameter $\tilde{a}$ (aka the dimensionless artificial speed of sound). According to the various numerical experiments published in literature, e.g., in [93], a universal value for $\tilde{a}$ does not exist and the parameter $\tilde{a}$ has to be chosen in dependence on the solved flow problem. In this regard, we follow the recommendation of Louda *et al.* [108], who inclined to the opinion that $\tilde{a}$ should be chosen proportionally to the maximum velocity magnitude achieved by the fluid within the computational domain. In this Ph.D. thesis, the dimensionless value of $\tilde{a}$ is chosen to be constant and equal to 2.5, i.e., a value that approximately corresponds to the maximum velocity magnitude observed for the steady flow in the bypass models analysed in Section 5.1

$$\tilde{a} \approx \max_{\Omega \subset \mathbb{R}^3} \left(\sqrt{v_1^2 + v_2^2 + v_3^2} \right) \,. \quad (4.43)$$

Since 1967 the artificial compressibility method has been numerically tested for various flow problems [8,108,190]. In this work, the conservative hyperbolic-parabolic system of Navier-Stokes equations (4.36), (4.24), (4.37) and (4.27) or (4.29) is solved using the cell-centred finite volume method formulated for unstructured hexahedral meshes and the classical explicit four-stage Runge-Kutta time-stepping scheme of fourth order accuracy in the fictitious time $\tilde{t}$.

4.3.1 Cell-centred finite volume method

Among the many discretisation approaches available, the finite volume method (FVM) is one of the most often used methods in computational fluid dynamics (CFD) [57,102,184]. Because it makes use of the conservation laws in integral form, it is often regarded as

the most natural discretisation method applicable to a wide range of flow problems solved on general non-Cartesian domains. In this section, the FVM variant known as the *cell-centred finite volume method* is used for the spatial discretisation of the system of Navier-Stokes equations (4.36), (4.24), (4.37) and (4.27) or (4.29) modified in the sense of the artificial compressibility method.

Let us divide the bounded computational domain $\Omega \subset \mathbb{R}^3$ into a finite number of small disjoint subdomains $\tilde{\Omega}_i \subset \Omega$, $i = 1, 2, \ldots, N_{CV}$ such that $\Omega_h = \bigcup_{i=1}^{N_{CV}} \tilde{\Omega}_i$, where Ω_h is the approximation of the computational domain Ω with closed convex polyhedrons. In this case, the boundary $\partial\Omega_h = \partial\Omega_{hI} \cup \partial\Omega_{hO} \cup \partial\Omega_{hW}$ is formed by a finite number of convex polygons. For the purpose of this work, we assume the approximation of the subdomains $\tilde{\Omega}_i$, $i = 1, 2, \ldots, N_{CV}$ to be carried out with convex hexahedrons H_i also known as *control volumes*, which form a (generally unstructured) hexahedral computational mesh $\mathcal{H} = \{H_i\}_{i=1}^{N_{CV}}$, where N_{CV} is the total number of hexahedrons. For illustration, Fig. 4.2 shows a control volume $H_i \equiv A_1A_2A_3A_4A_5A_6A_7A_8$, $A_k = [x_{1k}, x_{2k}, x_{3k}]$, $k = 1, \ldots, 8$ with boundary $\partial H_i = \bigcup_{m=1}^{6} \Gamma_i^m$, where Γ_i^m is the m-th planar quadrilateral face of the control volume H_i. In accordance with Fig. 4.2, the six faces are defined as: $\Gamma_i^1 = A_1A_2A_6A_5$, $\Gamma_i^2 = A_6A_2A_3A_7$, $\Gamma_i^3 = A_1A_2A_3A_4$, $\Gamma_i^4 = A_4A_3A_7A_8$, $\Gamma_i^5 = A_5A_1A_4A_8$ and $\Gamma_i^6 = A_5A_6A_7A_8$.

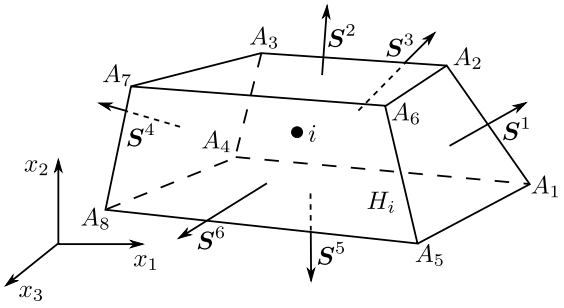

Fig. 4.2. Control volume (hexahedron) H_i of the hexahedral mesh $\mathcal{H}$.

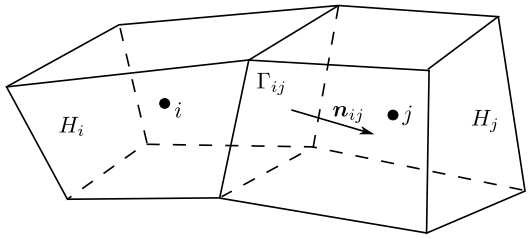

Fig. 4.3. Two adjacent control volumes H_i, $H_j \in \mathcal{H}$ with the common face Γ_{ij}.

Within the computational mesh $\mathcal{H}$, the control volumes H_i, $H_j \in \mathcal{H}$ are defined as being adjacent if $\Gamma_{ij} = \partial H_i \cap \partial H_j = \Gamma_{ji}$, where Γ_{ij} is the quadrilateral face shared by both the control volumes H_i and H_j, Fig. 4.3. In the rest of the work, we will use the following notations: $|H_i|$ is the volume of the hexahedron (control volume) H_i; $|\Gamma_i^m|$ is the area of the quadrilateral Γ_i^m representing the m-th face of the control volume H_i; $\boldsymbol{n}_{ij} = \left[{}^1n_{ij}, {}^2n_{ij}, {}^3n_{ij}\right]^T$ is the outward unit vector normal to the face Γ_{ij} shared by the adjacent control volumes H_i, H_j such that $\boldsymbol{n}_{ij} = -\boldsymbol{n}_{ji}$; and $\mathcal{N}(i) = \{j = 1, 2, \ldots, N_{CV}; j \neq i\}$ is the set of indices j of all hexahedrons $H_j \in \mathcal{H}$ adjacent to the control volume H_i. Then, for the boundary ∂H_i of the inner[1] control volume H_i, we can write $\partial H_i = \bigcup_{m=1}^{6} \Gamma_i^m \equiv \bigcup_{j \in \mathcal{N}(i)} \Gamma_{ij}$.

In accordance with the principles of the cell-centred finite volume method, the vector of primitive variables $\boldsymbol{w}$ of the modified system of Navier-Stokes equations (4.36), (4.24),

[1]The term 'inner control volume' refers to a control volume located inside the computational domain Ω_h, i.e., it is not part of the domain boundary $\partial\Omega_h$.

(4.37) and (4.27) or (4.29) will be determined in the centre of each control volume $H_i \in \mathcal{H}$. First, let us integrate the vector equation (4.36) over each control volume H_i

$$\int_{H_i} \frac{\partial \boldsymbol{w}}{\partial \tilde{t}} \, \mathrm{d}V = -\int_{H_i} \sum_{s=1}^{3} \frac{\partial \tilde{\boldsymbol{F}}_s^I(\boldsymbol{w})}{\partial x_s} \, \mathrm{d}V + \frac{1}{\mathrm{Re}^{(\theta)}} \int_{H_i} \sum_{s=1}^{3} \frac{\partial \boldsymbol{F}_s^V(\boldsymbol{w})}{\partial x_s} \, \mathrm{d}V \tag{4.44}$$

and convert the right-hand side with the help of the Gauss-Ostrogradsky theorem to

$$\int_{H_i} \frac{\partial \boldsymbol{w}}{\partial \tilde{t}} \, \mathrm{d}V = -\oint_{\partial H_i} \sum_{s=1}^{3} \tilde{\boldsymbol{F}}_s^I(\boldsymbol{w}) \, {}^s n_i \, \mathrm{d}S + \frac{1}{\mathrm{Re}^{(\theta)}} \oint_{\partial H_i} \sum_{s=1}^{3} \boldsymbol{F}_s^V(\boldsymbol{w}) \, {}^s n_i \, \mathrm{d}S, \tag{4.45}$$

where ${}^s n_i$ is the s-th component of the outward unit vector $\boldsymbol{n}_i = [{}^1 n_i, {}^2 n_i, {}^3 n_i]^T$ normal to the boundary ∂H_i of the control volume H_i. Then, rewriting the volume integral on the left-hand side of Eq. (4.45)

$$\int_{H_i} \frac{\partial \boldsymbol{w}}{\partial \tilde{t}} \, \mathrm{d}V = \frac{\partial}{\partial \tilde{t}} \int_{H_i} \boldsymbol{w}(\boldsymbol{x}, \tilde{t}) \, \mathrm{d}V \tag{4.46}$$

and introducing the integral average $\boldsymbol{w}_i(\tilde{t})$ of the vector $\boldsymbol{w}(\boldsymbol{x}, \tilde{t}) \in \mathbb{R}^4$ on the control volume H_i

$$\boldsymbol{w}_i(\tilde{t}) = \frac{1}{|H_i|} \int_{H_i} \boldsymbol{w}(\boldsymbol{x}, \tilde{t}) \, \mathrm{d}V, \tag{4.47}$$

where $\boldsymbol{w}_i(\tilde{t})$ is the approximate solution on the control volume H_i at the fictitious time $\tilde{t}$, Eq. (4.45) takes the following form:

$$\frac{\mathrm{d}}{\mathrm{d}\,\tilde{t}} \left[\boldsymbol{w}_i(\tilde{t}) \right] |H_i| = -\oint_{\partial H_i} \sum_{s=1}^{3} \tilde{\boldsymbol{F}}_s^I(\boldsymbol{w}) \, {}^s n_i \, \mathrm{d}S + \frac{1}{\mathrm{Re}^{(\theta)}} \oint_{\partial H_i} \sum_{s=1}^{3} \boldsymbol{F}_s^V(\boldsymbol{w}) \, {}^s n_i \, \mathrm{d}S. \tag{4.48}$$

The surface integrals in Eq. (4.48), which represent the total inviscid and viscous physical fluxes of the quantity $\boldsymbol{w}$ through the boundary $\partial H_i = \bigcup_{m=1}^{6} \Gamma_i^m$ at the fictitious time $\tilde{t}$, can be expressed as a sum of integrals over each face Γ_i^m, $m = 1, \ldots, 6$ of the control volume H_i, Fig. 4.2,

$$\begin{aligned} \frac{\mathrm{d}}{\mathrm{d}\,\tilde{t}} \left[\boldsymbol{w}_i(\tilde{t}) \right] |H_i| \; = \; & -\sum_{m=1}^{6} \int_{\Gamma_i^m} \sum_{s=1}^{3} \tilde{\boldsymbol{F}}_{sm}^I(\boldsymbol{w}) \, {}^s n_i^m \, \mathrm{d}S + \\ & + \frac{1}{\mathrm{Re}^{(\theta)}} \sum_{m=1}^{6} \int_{\Gamma_i^m} \sum_{s=1}^{3} \boldsymbol{F}_{sm}^V(\boldsymbol{w}) \, {}^s n_i^m \, \mathrm{d}S, \end{aligned} \tag{4.49}$$

where ${}^s n_i^m$ is the s-th component of the outward unit vector $\boldsymbol{n}_i^m = [{}^1 n_i^m, {}^2 n_i^m, {}^3 n_i^m]^T$ normal to the m-th face Γ_i^m of the control volume H_i. Approximation of the integrals in Eq. (4.49) using the average values of the inviscid and viscous fluxes, which are also known as **inviscid** $\boldsymbol{\mathcal{F}}_m^I \equiv \boldsymbol{f}_m^I \, {}^1 n_i^m + \boldsymbol{g}_m^I \, {}^2 n_i^m + \boldsymbol{h}_m^I \, {}^3 n_i^m$ and **viscous** $\boldsymbol{\mathcal{F}}_m^V \equiv \boldsymbol{f}_m^V \, {}^1 n_i^m +$

$\boldsymbol{g}_m^V\,{}^2n_i^m + \boldsymbol{h}_m^V\,{}^3n_i^m$ **numerical fluxes** through the m-th face Γ_i^m in the direction of the outward unit normal vector $\boldsymbol{n}_i^m$, yields

$$\boldsymbol{\mathcal{F}}_m^I \equiv \boldsymbol{f}_m^I\,{}^1n_i^m + \boldsymbol{g}_m^I\,{}^2n_i^m + \boldsymbol{h}_m^I\,{}^3n_i^m = \frac{1}{|\Gamma_i^m|}\int\limits_{\Gamma_i^m}\sum_{s=1}^{3}\tilde{\boldsymbol{F}}_{sm}^I(\boldsymbol{w})\;{}^sn_i^m\;\mathrm{d}S, \tag{4.50}$$

$$\boldsymbol{\mathcal{F}}_m^V \equiv \boldsymbol{f}_m^V\,{}^1n_i^m + \boldsymbol{g}_m^V\,{}^2n_i^m + \boldsymbol{h}_m^V\,{}^3n_i^m = \frac{1}{|\Gamma_i^m|}\int\limits_{\Gamma_i^m}\sum_{s=1}^{3}\boldsymbol{F}_{sm}^V(\boldsymbol{w})\;{}^sn_i^m\;\mathrm{d}S. \tag{4.51}$$

Then, taking both Eqs. (4.50) and (4.51) into consideration, Eq. (4.49) becomes

$$\begin{aligned}\frac{\mathrm{d}}{\mathrm{d}\,\tilde{t}}\left[\boldsymbol{w}_i(\tilde{t})\right]|H_i| = -\Bigg[&\sum_{m=1}^{6}\left(\boldsymbol{f}_m^I\,{}^1n_i^m + \boldsymbol{g}_m^I\,{}^2n_i^m + \boldsymbol{h}_m^I\,{}^3n_i^m\right)|\Gamma_i^m| - \\ &- \frac{1}{\mathrm{Re}^{(\theta)}}\sum_{m=1}^{6}\left(\boldsymbol{f}_m^V\,{}^1n_i^m + \boldsymbol{g}_m^V\,{}^2n_i^m + \boldsymbol{h}_m^V\,{}^3n_i^m\right)|\Gamma_i^m|\Bigg],\ H_i\in\mathcal{H}.\end{aligned} \tag{4.52}$$

With the introduction of the surface vector $\boldsymbol{S}^m = [S_1^m, S_2^m, S_3^m]^T$ that has the direction of the outward unit vector $\boldsymbol{n}_i^m$ normal to the face Γ_i^m of the control volume H_i, see Fig. 4.2,

$$\boldsymbol{S}^m = \boldsymbol{n}_i^m\,|\Gamma_i^m|\,,\ m = 1,\ldots,6, \tag{4.53}$$

Eq. (4.52) can be further rewritten as

$$\begin{aligned}\frac{\mathrm{d}}{\mathrm{d}\,\tilde{t}}\left[\boldsymbol{w}_i(\tilde{t})\right]|H_i| = -\Bigg[&\sum_{m=1}^{6}\left(\boldsymbol{f}_m^I\,S_1^m + \boldsymbol{g}_m^I\,S_2^m + \boldsymbol{h}_m^I\,S_3^m\right) - \\ &- \frac{1}{\mathrm{Re}^{(\theta)}}\sum_{m=1}^{6}\left(\boldsymbol{f}_m^V\,S_1^m + \boldsymbol{g}_m^V\,S_2^m + \boldsymbol{h}_m^V\,S_3^m\right)\Bigg].\end{aligned} \tag{4.54}$$

Approximation of the inviscid numerical flux

At the fictitious time $\tilde{t}$, the Cartesian components $\boldsymbol{f}_m^I$, $\boldsymbol{g}_m^I$, $\boldsymbol{h}_m^I$, $m = 1,\ldots,6$ of the inviscid numerical flux $\boldsymbol{\mathcal{F}}^I$ through the m-th face Γ_i^m of the inner control volume H_i are approximated as

$$\begin{aligned}\boldsymbol{f}_m^I &\equiv \boldsymbol{f}^I(\boldsymbol{w}_i(\tilde{t}),\boldsymbol{w}_j(\tilde{t})) \overset{\mathrm{def}}{=} \tfrac{1}{2}\left[\tilde{\boldsymbol{F}}_1^I(\boldsymbol{w}_i(\tilde{t})) + \tilde{\boldsymbol{F}}_1^I(\boldsymbol{w}_j(\tilde{t}))\right],\\ \boldsymbol{g}_m^I &\equiv \boldsymbol{g}^I(\boldsymbol{w}_i(\tilde{t}),\boldsymbol{w}_j(\tilde{t})) \overset{\mathrm{def}}{=} \tfrac{1}{2}\left[\tilde{\boldsymbol{F}}_2^I(\boldsymbol{w}_i(\tilde{t})) + \tilde{\boldsymbol{F}}_2^I(\boldsymbol{w}_j(\tilde{t}))\right],\\ \boldsymbol{h}_m^I &\equiv \boldsymbol{h}^I(\boldsymbol{w}_i(\tilde{t}),\boldsymbol{w}_j(\tilde{t})) \overset{\mathrm{def}}{=} \tfrac{1}{2}\left[\tilde{\boldsymbol{F}}_3^I(\boldsymbol{w}_i(\tilde{t})) + \tilde{\boldsymbol{F}}_3^I(\boldsymbol{w}_j(\tilde{t}))\right],\end{aligned} \tag{4.55}$$

where $\boldsymbol{w}_j(\tilde{t})$ is the integral average of the vector of primitive variables $\boldsymbol{w}(\boldsymbol{x},\tilde{t}) \in \mathbb{R}^4$ on the control volume $H_j \in \mathcal{H}$ adjacent to the control volume $H_i \in \mathcal{H}$ through the face Γ_i^m, Fig. 4.3. When the m-th face Γ_i^m of the control volume H_i is part of the domain boundary $\partial\Omega_h$, i.e., $\Gamma_i^m \subset \partial\Omega_h$, it is necessary to modify Eq. (4.55) accordingly:

- *outlet* $\Gamma_i^m \subset \partial\Omega_{hO}$, e.g., for $m = 1$:

$$\boldsymbol{f}_1^I = \frac{1}{2}\left[\tilde{\boldsymbol{F}}_1^I(\boldsymbol{w}_i(\tilde{t})) + \tilde{\boldsymbol{F}}_1^I(\boldsymbol{w}_{\text{outlet}}(\tilde{t}))\right], \quad \boldsymbol{g}_1^I = \frac{1}{2}\left[\tilde{\boldsymbol{F}}_2^I(\boldsymbol{w}_i(\tilde{t})) + \tilde{\boldsymbol{F}}_2^I(\boldsymbol{w}_{\text{outlet}}(\tilde{t}))\right],$$

$$\boldsymbol{h}_1^I = \frac{1}{2}\left[\tilde{\boldsymbol{F}}_3^I(\boldsymbol{w}_i(\tilde{t})) + \tilde{\boldsymbol{F}}_3^I(\boldsymbol{w}_{\text{outlet}}(\tilde{t}))\right], \tag{4.56}$$

  where $\boldsymbol{w}_{\text{outlet}} = \left[p^{\text{outlet}}, v_1^{\text{outlet}}, v_2^{\text{outlet}}, v_3^{\text{outlet}}\right]^T$ is the vector of primitive variables with p^{outlet} set equal to the prescribed dimensionless outlet pressure p_O. The Cartesian velocity components $v_1^{\text{outlet}}, v_2^{\text{outlet}}, v_3^{\text{outlet}}$ are extrapolated from the flow field.

- *inlet* $\Gamma_i^m \subset \partial\Omega_{hI}$, e.g., for $m = 3$:

$$\boldsymbol{f}_3^I = \frac{1}{2}\left[\tilde{\boldsymbol{F}}_1^I(\boldsymbol{w}_i(\tilde{t})) + \tilde{\boldsymbol{F}}_1^I(\boldsymbol{w}_{\text{inlet}}(\tilde{t}))\right], \quad \boldsymbol{g}_3^I = \frac{1}{2}\left[\tilde{\boldsymbol{F}}_2^I(\boldsymbol{w}_i(\tilde{t})) + \tilde{\boldsymbol{F}}_2^I(\boldsymbol{w}_{\text{inlet}}(\tilde{t}))\right],$$

$$\boldsymbol{h}_3^I = \frac{1}{2}\left[\tilde{\boldsymbol{F}}_3^I(\boldsymbol{w}_i(\tilde{t})) + \tilde{\boldsymbol{F}}_3^I(\boldsymbol{w}_{\text{inlet}}(\tilde{t}))\right], \tag{4.57}$$

  where $\boldsymbol{w}_{\text{inlet}} = \left[p^{\text{inlet}}, v_1^{\text{inlet}}, v_2^{\text{inlet}}, v_3^{\text{inlet}}\right]^T$ is the vector of primitive variables with the Cartesian velocity components $v_1^{\text{inlet}}, v_2^{\text{inlet}}, v_3^{\text{inlet}}$ set equal to the prescribed dimensionless components of the inlet velocity vector $\boldsymbol{v}_I = [v_{1I}, v_{2I}, v_{3I}]^T$. The pressure p^{inlet} is extrapolated from the flow field.

- *impermeable and inelastic wall* $\Gamma_i^m \subset \partial\Omega_{hW}$, e.g., for $m = 4$: Taking the non-slip boundary condition ($\boldsymbol{v}\,|_{\Gamma_i^4} = \boldsymbol{0}$) into consideration, the inviscid numerical flux through the face Γ_i^4 in the direction of the normal vector $\boldsymbol{S}^4$, Fig. 4.2,

$$\boldsymbol{f}_4^I\, S_1^4 + \boldsymbol{g}_4^I\, S_2^4 + \boldsymbol{h}_4^I\, S_3^4 \equiv \tilde{\boldsymbol{F}}_1^I(\boldsymbol{w}(\tilde{t})\Big|_{\Gamma_i^4})\, S_1^4 + \tilde{\boldsymbol{F}}_2^I(\boldsymbol{w}(\tilde{t})\Big|_{\Gamma_i^4})\, S_2^4 + \tilde{\boldsymbol{F}}_3^I(\boldsymbol{w}(\tilde{t})\Big|_{\Gamma_i^4})\, S_3^4 \overset{(4.37)}{=}$$

$$\overset{(4.37)}{=} \begin{bmatrix} \tilde{a}^2 v_1 \\ v_1^2 + p \\ v_1\, v_2 \\ v_1\, v_3 \end{bmatrix}_{\Gamma_i^4} S_1^4 + \begin{bmatrix} \tilde{a}^2 v_2 \\ v_1\, v_2 \\ v_2^2 + p \\ v_2\, v_3 \end{bmatrix}_{\Gamma_i^4} S_2^4 + \begin{bmatrix} \tilde{a}^2 v_3 \\ v_1\, v_3 \\ v_2\, v_3 \\ v_3^2 + p \end{bmatrix}_{\Gamma_i^4} S_3^4 \tag{4.58}$$

  reduces to

$$\boldsymbol{f}_4^I\, S_1^4 + \boldsymbol{g}_4^I\, S_2^4 + \boldsymbol{h}_4^I\, S_3^4 = p\Big|_{\Gamma_i^4}\left[0,\, S_1^4,\, S_2^4,\, S_3^4\right]^T \approx p_i\left[0,\, S_1^4,\, S_2^4,\, S_3^4\right]^T, \tag{4.59}$$

  where the pressure $p\,|_{\Gamma_i^4}$ is approximated with the pressure p_i defined in the centre of the control volume H_i.

Approximation of the viscous numerical flux

At the fictitious time $\tilde{t}$, the Cartesian components $\boldsymbol{f}_m^V$, $\boldsymbol{g}_m^V$, $\boldsymbol{h}_m^V$, $m = 1, \ldots, 6$ of the viscous numerical flux $\boldsymbol{\mathcal{F}}^V$ through the m-th face Γ_i^m of the inner control volume H_i are approximated as

$$\boldsymbol{f}_m^V \equiv \boldsymbol{F}_1^V\left(\boldsymbol{w}(\tilde{t})\Big|_{\Gamma_{ij}}\right), \quad \boldsymbol{g}_m^V \equiv \boldsymbol{F}_2^V\left(\boldsymbol{w}(\tilde{t})\Big|_{\Gamma_{ij}}\right), \quad \boldsymbol{h}_m^V \equiv \boldsymbol{F}_3^V\left(\boldsymbol{w}(\tilde{t})\Big|_{\Gamma_{ij}}\right), \tag{4.60}$$

where $\boldsymbol{F}_s^V\left(\boldsymbol{w}(\tilde{t})|_{\Gamma_{ij}}\right)$, $s = 1,2,3$ is the approximation of the s-th component of the viscous flux vector on the face $\Gamma_i^m \equiv \Gamma_{ij}$ shared by the control volumes $H_i, H_j \in \mathcal{H}$ for $j \in \mathcal{N}(i)$, Fig. 4.3. According to Eq. (4.27) or (4.29), the Cartesian components of the viscous numerical flux $\boldsymbol{\mathcal{F}}^V$ require a calculation of derivatives of velocity components $\frac{\partial v_1}{\partial x_s}$, $\frac{\partial v_2}{\partial x_s}$, $\frac{\partial v_3}{\partial x_s}$, $s = 1,2,3$ on the m-th face $\Gamma_i^m \equiv \Gamma_{ij}$ of the control volume H_i. For this purpose, we introduce an octahedral *dual cell* D_{ij} with boundary ∂D_{ij}, vertices of which are located in the nodes and centres of the two adjacent control volumes H_i, H_j, see Fig. 4.4. With the application of the mean value theorem on the dual cell D_{ij} and the Gauss-Ostrogradsky theorem, the derivatives $\frac{\partial v_1}{\partial x_s}$, $s = 1,2,3$ on the face Γ_{ij} of the control volume H_i, Fig. 4.4, are obtained as

$$\begin{aligned}
\left.\frac{\partial v_1}{\partial x_1}\right|_{\Gamma_{ij}} &\approx \frac{1}{|D_{ij}|}\int\limits_{D_{ij}} \frac{\partial v_1}{\partial x_1}\,\mathrm{d}V = \frac{1}{|D_{ij}|}\oint\limits_{\partial D_{ij}} v_1 \cdot {}^1n_{D_{ij}}\,\mathrm{d}S,\\
\left.\frac{\partial v_1}{\partial x_2}\right|_{\Gamma_{ij}} &\approx \frac{1}{|D_{ij}|}\int\limits_{D_{ij}} \frac{\partial v_1}{\partial x_2}\,\mathrm{d}V = \frac{1}{|D_{ij}|}\oint\limits_{\partial D_{ij}} v_1 \cdot {}^2n_{D_{ij}}\,\mathrm{d}S,\\
\left.\frac{\partial v_1}{\partial x_3}\right|_{\Gamma_{ij}} &\approx \frac{1}{|D_{ij}|}\int\limits_{D_{ij}} \frac{\partial v_1}{\partial x_3}\,\mathrm{d}V = \frac{1}{|D_{ij}|}\oint\limits_{\partial D_{ij}} v_1 \cdot {}^3n_{D_{ij}}\,\mathrm{d}S,
\end{aligned} \tag{4.61}$$

where $|D_{ij}|$ is the volume of the octahedral dual cell D_{ij} and $\boldsymbol{n}_{D_{ij}} = [{}^1n_{D_{ij}}, {}^2n_{D_{ij}}, {}^3n_{D_{ij}}]^T$ is the outer unit vector normal to the dual cell boundary ∂D_{ij}. The surface integrals in Eq. (4.61) are replaced with a sum of integrals over each face $\Gamma_{D_{ij}}^k$, $k = 1,\ldots,8$ of the dual cell D_{ij} as

$$\left.\frac{\partial v_1}{\partial x_1}\right|_{\Gamma_{ij}} \approx \frac{1}{|D_{ij}|}\sum_{k=1}^{8}\int\limits_{\Gamma_{D_{ij}}^k} v_1^k \cdot {}^1n_{D_{ij}}^k\,\mathrm{d}S, \qquad \left.\frac{\partial v_2}{\partial x_2}\right|_{\Gamma_{ij}} \approx \frac{1}{|D_{ij}|}\sum_{k=1}^{8}\int\limits_{\Gamma_{D_{ij}}^k} v_1^k \cdot {}^2n_{D_{ij}}^k\,\mathrm{d}S,$$

$$\left.\frac{\partial v_3}{\partial x_3}\right|_{\Gamma_{ij}} \approx \frac{1}{|D_{ij}|}\sum_{k=1}^{8}\int\limits_{\Gamma_{D_{ij}}^k} v_1^k \cdot {}^3n_{D_{ij}}^k\,\mathrm{d}S, \tag{4.62}$$

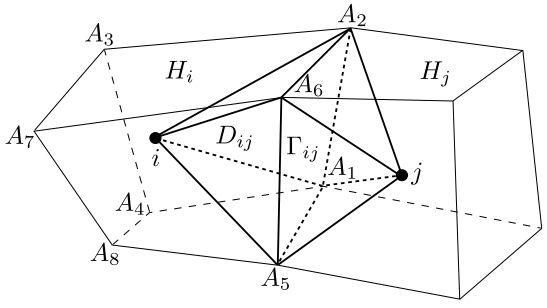

Fig. 4.4. Two adjacent primary cells H_i, H_j sharing an octahedral dual cell D_{ij} through the common face Γ_{ij}.

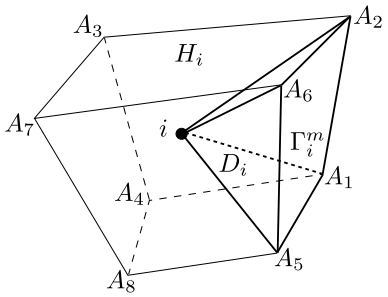

Fig. 4.5. Pyramid dual cell D_i constructed on the border face $\Gamma_i^m \subset \partial\Omega_h$ of the primary cell H_i.

where $\boldsymbol{n}^k_{D_{ij}} = [{}^1n^k_{D_{ij}}, {}^2n^k_{D_{ij}}, {}^3n^k_{D_{ij}}]^T$ is the outer unit vector normal to the k-th face $\Gamma^k_{D_{ij}}$ of the dual cell D_{ij}. The integrals in Eq. (4.62) are calculated with a mean value over each face $\Gamma^k_{D_{ij}}$, $k = 1, \ldots, 8$ of the dual cell D_{ij} as

$$\int\limits_{\Gamma^k_{D_{ij}}} v_1^k \cdot {}^1n^k_{D_{ij}}\,\mathrm{d}S = \overline{v}_1^k \cdot {}^1n^k_{D_{ij}}|\Gamma^k_{D_{ij}}|, \qquad \int\limits_{\Gamma^k_{D_{ij}}} v_1^k \cdot {}^2n^k_{D_{ij}}\,\mathrm{d}S = \overline{v}_1^k \cdot {}^2n^k_{D_{ij}}|\Gamma^k_{D_{ij}}|,$$

$$\int\limits_{\Gamma^k_{D_{ij}}} v_1^k \cdot {}^3n^k_{D_{ij}}\,\mathrm{d}S \;= \overline{v}_1^k \cdot {}^3n^k_{D_{ij}}|\Gamma^k_{D_{ij}}|, \tag{4.63}$$

where $|\Gamma^k_{D_{ij}}|$ is the area of the triangular face $\Gamma^k_{D_{ij}}$ and $\overline{v}_1^k$ is the mean value of the velocity vector component v_1 on $\Gamma^k_{D_{ij}}$ estimated as an average of the three face vertices. For example, for $k = 1$, we use the formula $\overline{v}_1^1 = \frac{1}{3}\left[(v_1)_{A_2} + (v_1)_i + (v_1)_{A_6}\right]$, see Fig. 4.4, where the nodal velocity $(v_1)_{A_2}$ or $(v_1)_{A_6}$ is computed as an average of v_1 defined in the centres of primary cells (control volumes), which are associated with the node A_2 or A_6. With the introduction of the surface vector ${}^{dual}\boldsymbol{S}^k$ that has the direction of the outward unit vector $\boldsymbol{n}^k_{D_{ij}}$ normal to the face $\Gamma^k_{D_{ij}}$ of the dual cell D_{ij}

$${}^{dual}\boldsymbol{S}^k = \boldsymbol{n}^k_{D_{ij}} \cdot |\Gamma^k_{D_{ij}}| = \left[{}^1n^k_{D_{ij}}\,|\Gamma^k_{D_{ij}}|,\, {}^2n^k_{D_{ij}}\,|\Gamma^k_{D_{ij}}|,\, {}^3n^k_{D_{ij}}\,|\Gamma^k_{D_{ij}}|\right]^T \equiv$$

$$\equiv \left[{}^{dual}S^k_1,\, {}^{dual}S^k_2,\, {}^{dual}S^k_3\right]^T,\ k = 1, \ldots, 8, \tag{4.64}$$

the substitution of Eq. (4.63) into Eq. (4.62) yields the following approximations of the derivatives $\frac{\partial v_1}{\partial x_s}$, $s = 1, 2, 3$ on the m-th face $\Gamma^m_i \equiv \Gamma_{ij}$ of the control volume H_i, Fig. 4.4,

$$\left.\frac{\partial v_1}{\partial x_1}\right|_{\Gamma_{ij}} \approx \frac{1}{|D_{ij}|}\sum_{k=1}^{8} \overline{v}_1^k \cdot {}^{dual}S^k_1, \qquad \left.\frac{\partial v_1}{\partial x_2}\right|_{\Gamma_{ij}} \approx \frac{1}{|D_{ij}|}\sum_{k=1}^{8} \overline{v}_1^k \cdot {}^{dual}S^k_2,$$

$$\left.\frac{\partial v_1}{\partial x_3}\right|_{\Gamma_{ij}} \approx \frac{1}{|D_{ij}|}\sum_{k=1}^{8} \overline{v}_1^k \cdot {}^{dual}S^k_3. \tag{4.65}$$

The remaining velocity derivatives on the face $\Gamma^m_i \equiv \Gamma_{ij}$ of the control volume H_i, i.e., $\frac{\partial v_2}{\partial x_s}$, $s = 1, 2, 3$ and $\frac{\partial v_3}{\partial x_s}$, $s = 1, 2, 3$, are computed analogously.

When the m-th quadrilateral face Γ^m_i, $m = 1, \ldots, 6$ of the control volume $H_i \in \mathcal{H}$ is a part of the domain boundary $\partial\Omega_h$, i.e., $\Gamma^m_i \subset \partial\Omega_h$, the velocity derivatives are determined with only half of the dual cell D_{ij}, which, in this case, takes the form of a pentahedron D_i with boundary ∂D_i, Fig. 4.5. Then, the derivatives $\frac{\partial v_1}{\partial x_s}$, $s = 1, 2, 3$ on the m-th face Γ^m_i of the control volume H_i are estimated as

$$\begin{aligned}
\left.\frac{\partial v_1}{\partial x_1}\right|_{\Gamma^m_i} &\approx \frac{1}{|D_i|}\left(\sum_{k=1}^{4} \overline{v}_1^k \cdot {}^{dual}S^k_1 + {}^{\square}\overline{v}_1^m S^m_1\right),\\
\left.\frac{\partial v_1}{\partial x_2}\right|_{\Gamma^m_i} &\approx \frac{1}{|D_i|}\left(\sum_{k=1}^{4} \overline{v}_1^k \cdot {}^{dual}S^k_2 + {}^{\square}\overline{v}_1^m S^m_2\right),\\
\left.\frac{\partial v_1}{\partial x_3}\right|_{\Gamma^m_i} &\approx \frac{1}{|D_i|}\left(\sum_{k=1}^{4} \overline{v}_1^k \cdot {}^{dual}S^k_3 + {}^{\square}\overline{v}_1^m S^m_3\right),
\end{aligned} \tag{4.66}$$

where $|D_i|$ is the volume of the pentahedral dual cell D_i, the surface normal vector ${}^{dual}\boldsymbol{S}^k$ is given by Eq. (4.64) and the surface vector $\boldsymbol{S}^m$ normal to the face Γ_i^m of the control volume H_i is determined with Eq. (4.53). The computation of the mean value ${}^{\square}\overline{v}_1^m$ of the velocity vector component v_1 on the face Γ_i^m is carried out in accordance with Fig. 4.5 as (e.g., for $m = 1$: $\Gamma_i^1 \equiv A_1A_2A_5A_6$) ${}^{\square}\overline{v}_1^1 = \frac{1}{4}\left[(v_1)_{A_1} + (v_1)_{A_2} + (v_1)_{A_5} + (v_1)_{A_6}\right]$. The remaining derivatives $\frac{\partial v_2}{\partial x_s}$, $s = 1, 2, 3$ and $\frac{\partial v_3}{\partial x_s}$, $s = 1, 2, 3$ on the border face $\Gamma_i^m \subset \partial\Omega_h$ are determined analogously.

Taking into consideration the three different boundary types introduced in this Ph.D. thesis, Eq. (4.66) can be further modified, e.g., for $m = 1$ ($\Gamma_i^1 \equiv A_1A_2A_5A_6$, Fig. 4.5):

- *impermeable and inelastic wall* $\Gamma_i^1 \subset \partial\Omega_{hW}$: Because of the non-slip boundary condition, the mean face velocity components ${}^{\square}\overline{v}_1^1$, ${}^{\square}\overline{v}_2^1$ and ${}^{\square}\overline{v}_3^1$ are set equal to zero.
- *outlet* $\Gamma_i^1 \subset \partial\Omega_{hO}$: The condition for this boundary type is known as the traction-free condition

$$\sum_{\beta=1}^{3} \tau_{\alpha\beta} \cdot {}^{\beta}n = 0\,,\ \alpha = 1, 2, 3 \qquad \text{or} \qquad \sum_{\beta=1}^{3} \tau_{\alpha\beta} \cdot S_\beta^m = 0\,,\ \alpha = 1, 2, 3, \tag{4.67}$$

  where $\tau_{\alpha\beta} = \left(\frac{\partial v_\alpha}{\partial x_\beta} + \frac{\partial v_\beta}{\partial x_\alpha}\right)$ is the dimensionless viscous stress tensor for an incompressible Newtonian fluid, n_β is the component of the outer unit vector normal to the boundary $\partial\Omega_{hO}$ and S_β^m is the component of the surface vector $\boldsymbol{S}^m$ given by Eq. (4.53). Then, for the viscous numerical flux through the border face Γ_i^1 in the direction of the normal vector $\boldsymbol{S}^1$, we can write

$$\begin{aligned}
&\boldsymbol{f}_1^V\, S_1^1 + \boldsymbol{g}_1^V\, S_2^1 + \boldsymbol{h}_1^V\, S_3^1 \equiv \tilde{\boldsymbol{F}}_1^V(\boldsymbol{w}(\tilde{t})\big|_{\Gamma_i^1})\, S_1^1 + \tilde{\boldsymbol{F}}_2^V(\boldsymbol{w}(\tilde{t})\big|_{\Gamma_i^1})\, S_2^1 + \tilde{\boldsymbol{F}}_3^V(\boldsymbol{w}(\tilde{t})\big|_{\Gamma_i^1})\, S_3^1 \;= \\
&= \begin{bmatrix} 0 \\ 2\frac{\partial v_1}{\partial x_1} \\ \frac{\partial v_1}{\partial x_2} + \frac{\partial v_2}{\partial x_1} \\ \frac{\partial v_1}{\partial x_3} + \frac{\partial v_3}{\partial x_1} \end{bmatrix}_{\Gamma_i^4} S_1^1 \;+\; \begin{bmatrix} 0 \\ \frac{\partial v_1}{\partial x_2} + \frac{\partial v_2}{\partial x_1} \\ 2\frac{\partial v_2}{\partial x_2} \\ \frac{\partial v_2}{\partial x_3} + \frac{\partial v_3}{\partial x_2} \end{bmatrix}_{\Gamma_i^4} S_2^1 \;+\; \begin{bmatrix} 0 \\ \frac{\partial v_1}{\partial x_3} + \frac{\partial v_3}{\partial x_1} \\ \frac{\partial v_2}{\partial x_3} + \frac{\partial v_3}{\partial x_2} \\ 2\frac{\partial v_3}{\partial x_3} \end{bmatrix}_{\Gamma_i^4} S_3^1 = \begin{bmatrix} 0 \\ 0 \\ 0 \\ 0 \end{bmatrix}.
\end{aligned} \tag{4.68}$$

- *inlet* $\Gamma_i^1 \subset \partial\Omega_{hI}$: Similarly to the outlet, we apply the traction-free condition.

In accordance with the aforementioned principles of the cell-centred finite volume method formulated for the unstructured hexahedral mesh $\mathcal{H}$, the system of Navier-Stokes equations (4.36), (4.24), (4.37) and (4.27) or (4.29) modified in the sense of the artificial compressibility method transforms into a system of ordinary differential equations (4.54) at the fictitious time $\tilde{t}$. By introducing the second-order spatial discretisation operator

$$\begin{aligned}
\mathcal{R}\left(\boldsymbol{w}_i(\tilde{t})\right) \;=\; &\sum_{m=1}^{6} \left(\boldsymbol{f}_m^I\, S_m^x + \boldsymbol{g}_m^I\, S_m^y + \boldsymbol{h}_m^I\, S_m^z\right) - \\
&- \frac{1}{\mathrm{Re}^{(\theta)}} \sum_{m=1}^{6} \left(\boldsymbol{f}_m^V\, S_m^x + \boldsymbol{g}_m^V\, S_m^y + \boldsymbol{h}_m^V\, S_m^z\right),
\end{aligned} \tag{4.69}$$

the obtained system of ordinary differential equations (4.54) can be written as

$$\frac{\mathrm{d}}{\mathrm{d}\,\tilde{t}}\left[\boldsymbol{w}_i(\tilde{t})\right]|H_i| = -\mathcal{R}\left(\boldsymbol{w}_i(\tilde{t})\right). \tag{4.70}$$

As discussed, for example, in [58, 178], the central discretisation of the inviscid numerical flux is known to generate non-physical oscillations in regions containing severe pressure gradients. In the non-linear case, these oscillations have been observed to increase during the iteration process and contribute to the loss of numerical stability. One of the possible ways how to stabilise the numerical solution is to augment the finite volume scheme (4.70) with artificial dissipation terms

$$\frac{\mathrm{d}}{\mathrm{d}\,\tilde{t}}\left[\boldsymbol{w}_i(\tilde{t})\right]|H_i| = -\mathcal{R}\left(\boldsymbol{w}_i(\tilde{t})\right) + \mathcal{D}\left(\boldsymbol{w}_i(\tilde{t})\right), \tag{4.71}$$

where $\mathcal{D}$ is a dissipative operator. Among the various types of artificial damping, the *Jameson's artificial viscosity* [66] is probably one of the most well-known. In its original form, it is based on a blend of second and fourth differences with coefficients depending on the local pressure gradient. In this Ph.D. thesis, we employ a modified form of this artificial viscosity by switching the fourth differences off and damping only the pressure field. This step is taken due to potential over-damping in non-Newtonian flow simulations, where the shear-dependent viscosity of the fluid may help with the suppression of numerically induced oscillations and where an addition of too much artificial viscosity can negatively influence the studied flow field.

Before proceeding to the description of the artificial viscosity as used in this work, let us introduce an auxiliary indexing of control volumes adjacent to the control volume $H_i \in \mathcal{H}$ that follows the numbering of faces shown in Fig. 4.2. Namely, the control volume sharing the face Γ_i^m with the control volume H_i will be in the following text denoted as $H_{[m]}$, making it clear that it adjoins H_i at its m-th face. Obviously, $H_{[m]} \equiv H_j$, $j \in \mathcal{N}(i)$ if $\Gamma_i^m \equiv \Gamma_{ij}$, Fig. 4.3. In the context of the original Jameson's artificial viscosity as described in [66], the new indexing is made to cover the possibility when it is necessary to refer to a control volume located 'behind' $H_{[m]}$ from the perspective of H_i. In this case, we will identify this hexahedron with the indices $[m_+]$ and $[m_-]$, as illustrated in Fig. 4.6 for the faces Γ_i^1 and Γ_i^4 of the control volume H_i.

In accordance with the original work of Jameson [66], the dissipative term $\mathcal{D}\left(\boldsymbol{w}_i(\tilde{t})\right)$ from Eq. (4.71) can be decomposed into the direction of the Cartesian coordinates x_s,

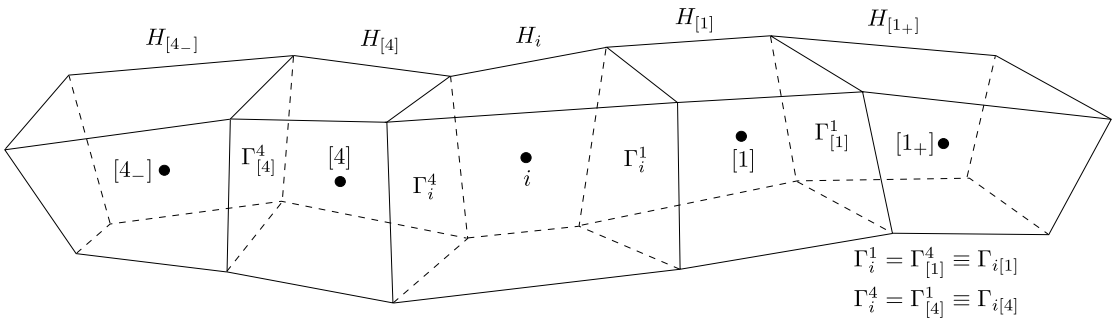

Fig. 4.6. Use of the auxiliary indexing when faces Γ_i^1 and Γ_i^4 are considered.

$s = 1, 2, 3$ as

$$\mathcal{D}\left(\boldsymbol{w}_i(\tilde{t})\right) = \mathcal{D}_1\left(\boldsymbol{w}_i(\tilde{t})\right) + \mathcal{D}_2\left(\boldsymbol{w}_i(\tilde{t})\right) + \mathcal{D}_3\left(\boldsymbol{w}_i(\tilde{t})\right). \tag{4.72}$$

Then, for an inner hexahedral control volume $H_i \in \mathcal{H}$, Fig. 4.2, the dissipation terms at the right-hand side of Eq. (4.72) are computed as

$$\begin{aligned}
\mathcal{D}_1\left(\boldsymbol{w}_i(\tilde{t})\right) &= \overline{\boldsymbol{D}}\left[\frac{|H_i| + |H_{[1]}|}{2\Delta\tilde{t}}\,\varepsilon_{i1}^{(2)}\left(p_{[1]} - p_i\right) - \frac{|H_i| + |H_{[4]}|}{2\Delta\tilde{t}}\,\varepsilon_{i4}^{(2)}\left(p_i - p_{[4]}\right)\right],\\
\mathcal{D}_2\left(\boldsymbol{w}_i(\tilde{t})\right) &= \overline{\boldsymbol{D}}\left[\frac{|Hi| + |H_{[2]}|}{2\Delta\tilde{t}}\,\varepsilon_{i2}^{(2)}\left(p_{[2]} - p_i\right) - \frac{|H_i| + |H_{[5]}|}{2\Delta\tilde{t}}\,\varepsilon_{i5}^{(2)}\left(p_i - p_{[5]}\right)\right],\\
\mathcal{D}_3\left(\boldsymbol{w}_i(\tilde{t})\right) &= \overline{\boldsymbol{D}}\left[\frac{|H_i| + |H_{[3]}|}{2\Delta\tilde{t}}\,\varepsilon_{i3}^{(2)}\left(p_{[3]} - p_i\right) - \frac{|H_{ij}| + |H_{[6]}|}{2\Delta\tilde{t}}\,\varepsilon_{i6}^{(2)}\left(p_i - p_{[6]}\right)\right],
\end{aligned} \tag{4.73}$$

where $\overline{\boldsymbol{D}} = [1, 0, 0, 0]^T$, $\Delta\tilde{t}$ is the fictitious time step, $\frac{|H_i|+|H_{[m]}|}{2}$ is the arithmetic mean of the volumes of the adjacent hexahedrons H_i and $H_{[m]}$ and p_i, $p_{[m]}$ are the pressures defined in the centre of the control volumes H_i and $H_{[m]}$, respectively. For the coefficients $\varepsilon_{im}^{(2)}$, $m = 1, \ldots, 6$ on the faces Γ_i^m of the control volume H_i, we apply

$$\varepsilon_{i1}^{(2)} = \beta_2 \max\left(\hat{\varepsilon}_i, \hat{\varepsilon}_{[1]}\right),\ \hat{\varepsilon}_i = \frac{|p_{[1]} - 2p_i + p_{[4]}|}{|p_{[1]}| + 2|p_i| + |p_{[4]}|},\ \hat{\varepsilon}_{[1]} = \frac{|p_{[1_+]} - 2p_{[1]} + p_i|}{|p_{[1_+]}| + 2|p_{[1]}| + |p_i|}, \tag{4.74}$$

$$\varepsilon_{i2}^{(2)} = \beta_2 \max\left(\hat{\varepsilon}_i, \hat{\varepsilon}_{[2]}\right),\ \hat{\varepsilon}_i = \frac{|p_{[2]} - 2p_i + p_{[5]}|}{|p_{[2]}| + 2|p_i| + |p_{[5]}|},\ \hat{\varepsilon}_{[2]} = \frac{|p_{[2_+]} - 2p_{[2]} + p_i|}{|p_{[2_+]}| + 2|p_{[2]}| + |p_i|}, \tag{4.75}$$

$$\varepsilon_{i3}^{(2)} = \beta_2 \max\left(\hat{\varepsilon}_i, \hat{\varepsilon}_{[3]}\right),\ \hat{\varepsilon}_i = \frac{|p_{[3]} - 2p_i + p_{[6]}|}{|p_{[3]}| + 2|p_i| + |p_{[6]}|},\ \hat{\varepsilon}_{[3]} = \frac{|p_{[3_+]} - 2p_{[3]} + p_i|}{|p_{[3_+]}| + 2|p_{[3]}| + |p_i|}, \tag{4.76}$$

$$\varepsilon_{i4}^{(2)} = \beta_2 \max\left(\hat{\varepsilon}_i, \hat{\varepsilon}_{[4]}\right),\ \hat{\varepsilon}_i = \frac{|p_{[1]} - 2p_i + p_{[4]}|}{|p_{[1]}| + 2|p_i| + |p_{[4]}|},\ \hat{\varepsilon}_{[4]} = \frac{|p_i - 2p_{[4]} + p_{[4_-]}|}{|p_i| + 2|p_{[4]}| + |p_{[4_-]}|}, \tag{4.77}$$

$$\varepsilon_{i5}^{(2)} = \beta_2 \max\left(\hat{\varepsilon}_i, \hat{\varepsilon}_{[5]}\right),\ \hat{\varepsilon}_i = \frac{|p_{[2]} - 2p_i + p_{[5]}|}{|p_{[2]}| + 2|p_i| + |p_{[5]}|},\ \hat{\varepsilon}_{[5]} = \frac{|p_i - 2p_{[5]} + p_{[5_-]}|}{|p_i| + 2|p_{[5]}| + |p_{[5_-]}|}, \tag{4.78}$$

$$\varepsilon_{i6}^{(2)} = \beta_2 \max\left(\hat{\varepsilon}_i, \hat{\varepsilon}_{[6]}\right),\ \hat{\varepsilon}_i = \frac{|p_{[3]} - 2p_i + p_{[6]}|}{|p_{[3]}| + 2|p_i| + |p_{[6]}|},\ \hat{\varepsilon}_{[6]} = \frac{|p_i - 2p_{[6]} + p_{[6_-]}|}{|p_i| + 2|p_{[6]}| + |p_{[6_-]}|}, \tag{4.79}$$

where β_2 is a constant that needs to be determined on the basis of numerical experiments carried out for each solved flow problem independently. When the control volume H_i is part of the domain boundary $\partial\Omega_h$, i.e., $\Gamma_i^m \subset \partial\Omega_h$, Eqs. (4.72)–(4.79) cannot be applied directly, because there are no cells beyond the boundary. To avoid this difficulty, fictitious control volumes are created that in fact mirror the existing hexahedrons H_i and $H_{[m]}$ and utilise the appropriate vectors of unknowns.

As can be noted from [66], the Jameson's artificial viscosity was primarily intended to be used in structured meshes, where it is easy to find two consecutive cells 'before' and 'after' the relevant control volume. Naturally, in unstructured meshes, especially those based on tetrahedrons, this requirement is difficult to achieve. Although not without some inaccuracies, the present work uses the aforementioned artificial viscosity on unstructured hexahedral meshes, which compared to the tetrahedral ones are organised in a manner that to some degree resembles a structured mesh.

4.3.2 Time discretisation

In accordance with the dimensionless initial condition given by Eq. (4.30), the system of ordinary differential equations (4.71) is completed with the following initial condition:

$$\boldsymbol{w}_i^0 \equiv \boldsymbol{w}_i(0) = \frac{1}{|H_i|} \int\limits_{H_i} \boldsymbol{w}(\boldsymbol{x}, 0)\, \mathrm{d}V\,, \tag{4.80}$$

where $\boldsymbol{w}_i^0 = \left[p_i^0, (v_1)_i^0, (v_2)_i^0, (v_3)_i^0\right]^T$ is the vector of primitive variables $\boldsymbol{w}_i(\tilde{t}^0)$ at the fictitious time $\tilde{t}^0 = 0$ defined in the centre of the hexahedral control volume $H_i \in \mathcal{H}$, Fig. 4.2. Let $0 = \tilde{t}^0 < \tilde{t}^1 < \tilde{t}^2 < \ldots < \mathcal{T}$ be a division of the fictitious time interval $(0, \mathcal{T})$ and let $\Delta\tilde{t} = \tilde{t}^{n+1} - \tilde{t}^n$ be the fictitious time step between the fictitious time levels $\tilde{t}^n$ and $\tilde{t}^{n+1}$. By $\boldsymbol{w}_i^n$ we denote the approximation of the function $\boldsymbol{w}_i(\tilde{t}^n)$ on the control volume H_i at the fictitious time $\tilde{t}^n$.

The literature such as [39] and [60] offers various methods for the numerical solution of the initial problem given by Eqs. (4.71) and (4.80). Among the various schemes, the multistage Runge-Kutta methods are probably ones of the most popular. In this Ph.D. thesis, we follow this trend and consider the *classical explicit four-stage Runge-Kutta time-stepping scheme* [66] of fourth order accuracy in the fictitious time $\tilde{t}$

$$\begin{aligned}
\boldsymbol{w}_i^{(0)} &= \boldsymbol{w}_i^n, \\
\boldsymbol{w}_i^{(l)} &= \boldsymbol{w}_i^{(0)} - \alpha_l \frac{\Delta\tilde{t}}{|H_i|} \left[\mathcal{R}(\boldsymbol{w}_i^{(l-1)}) - \mathcal{D}(\boldsymbol{w}_i^{(l-1)})\right] \quad \text{for } l = 1, 2, 3, \\
\boldsymbol{w}_i^{(4)} &= \boldsymbol{w}_i^{(0)} - \frac{1}{6} \frac{\Delta\tilde{t}}{|H_i|} \Big[\mathcal{R}(\boldsymbol{w}_i^{(0)}) - \mathcal{D}(\boldsymbol{w}_i^{(0)}) + 2\left(\mathcal{R}(\boldsymbol{w}_i^{(1)}) - \mathcal{D}(\boldsymbol{w}_i^{(1)})\right) + \\
&\quad + 2\left(\mathcal{R}(\boldsymbol{w}_i^{(2)}) - \mathcal{D}(\boldsymbol{w}_i^{(2)})\right) + \mathcal{R}(\boldsymbol{w}_i^{(3)}) - \mathcal{D}(\boldsymbol{w}_i^{(3)})\Big], \\
\boldsymbol{w}_i^{n+1} &= \boldsymbol{w}_i^{(4)},
\end{aligned} \tag{4.81}$$

where $\alpha_1 = 0.5$, $\alpha_2 = 0.5$, $\alpha_3 = 1$. In principle, the Runge-Kutta scheme (4.81) utilises a weighted average of four solutions over one time interval in order to improve accuracy of the numerical solution at the fictitious time $\tilde{t}$. Because of this approach, the explicit Runge-Kutta schemes, in general, are known to posses better stability criteria than comparable explicit schemes such as the explicit two-step MacCormack scheme [60, 66]. For example, for a model scalar linear hyperbolic partial differential equation in 1D

$$\frac{\partial u}{\partial t} + a\frac{\partial u}{\partial x} = 0\,, \quad x \in \mathbb{R},\, t > 0,\, a \in \mathbb{R}\,, \tag{4.82}$$

where $u(x,t) : \mathbb{R} \times (0, \infty) \to \mathbb{R}$ is the solution of Eq. (4.82) and $u(x,0) = u^0(x)$ is the initial condition, it can be shown that the classical explicit four-stage Runge-Kutta scheme in combination with the second-order central difference approximation of the convective term is stable if $|\sigma| \equiv \left|\frac{a\Delta t}{\Delta x}\right| \leq 2\sqrt{2}$, where σ is the Courant number. By contrast, the stability of the explicit two-step MacCormack scheme is, in this case, limited by the condition $\sigma \leq 1$.

As the stability advantage of the Runge-Kutta methods is gained at the expense of increased computational time, which stems from the necessity to perform several computations (stages) within one time step, there are some tendencies to modify the original

algorithm. For example, in this work, we know from past experience and the recommendations mentioned, e.g., in [66] that the calculation of the dissipative term only once per time level can significantly reduce the computational time. With this in mind, the algorithm of the explicit four-stage Runge-Kutta scheme (4.81) for the numerical solution of the initial problem (4.71) and (4.80) simplifies to

$$\begin{aligned}
\boldsymbol{w}_i^{(0)} &= \boldsymbol{w}_i^n, \\
\boldsymbol{w}_i^{(l)} &= \boldsymbol{w}_i^{(0)} - \alpha_l \frac{\Delta\tilde{t}}{|H_i|}\mathcal{R}(\boldsymbol{w}_i^{(l-1)}) + \alpha_l \frac{\Delta\tilde{t}}{|H_i|}\mathcal{D}(\boldsymbol{w}_i^{(0)}) \text{ for } l = 1,2,3, \\
\boldsymbol{w}_i^{(4)} &= \boldsymbol{w}_i^{(0)} - \frac{1}{6}\frac{\Delta\tilde{t}}{|H_i|}\left[\mathcal{R}(\boldsymbol{w}_i^{(0)}) + 2\mathcal{R}(\boldsymbol{w}_i^{(1)}) + 2\mathcal{R}(\boldsymbol{w}_i^{(2)}) + \mathcal{R}(\boldsymbol{w}_i^{(3)})\right] + \frac{\Delta\tilde{t}}{|H_i|}\mathcal{D}(\boldsymbol{w}_i^{(0)}), \\
\boldsymbol{w}_i^{n+1} &= \boldsymbol{w}_i^{(4)},
\end{aligned} \tag{4.83}$$

where $\alpha_1 = 0.5$, $\alpha_2 = 0.5$, $\alpha_3 = 1$, $\Delta\tilde{t}$ is the fictitious time step, $\mathcal{R}(\boldsymbol{w}_i^{(l_0)})$, $l_0 = 0,\ldots,3$ is computed according to Eq. (4.69) and $\mathcal{D}(\boldsymbol{w}_i^{(0)})$ is the dissipative term with the Jameson's artificial viscosity given by Eqs. (4.72)–(4.79). Similarly to other explicit schemes, the size of the fictitious time step $\Delta\tilde{t}$ of the Runge-Kutta method is restricted by the necessary stability condition [57, 60]. For the explicit four-stage Runge-Kutta scheme (4.83) formulated in the sense of the cell-centred finite volume method for unstructured hexahedral meshes, this stability condition in the non-dimensional form is given as

$$\Delta\tilde{t} \leq \min_i \left[\frac{\mathrm{CFL}}{\Theta_1 + \Theta_2}\right], \tag{4.84}$$

$$\begin{aligned}
\Theta_1 &= \frac{|\lambda(\boldsymbol{J}_1(\boldsymbol{w}_i))|_{\max}}{\Delta(x_1)_i} + \frac{|\lambda(\boldsymbol{J}_2(\boldsymbol{w}_i))|_{\max}}{\Delta(x_2)_i} + \frac{|\lambda(\boldsymbol{J}_3(\boldsymbol{w}_i))|_{\max}}{\Delta(x_3)_i}, \\
\Theta_2 &= \frac{2}{\mathrm{Re}^{(\theta)}}\left(\frac{1}{\Delta(x_1)_i^2} + \frac{1}{\Delta(x_2)_i^2} + \frac{1}{\Delta(x_3)_i^2}\right),
\end{aligned}$$

where $\mathrm{CFL} \in (0, 2\sqrt{2})$, $|\lambda(\boldsymbol{J}_s(\boldsymbol{w}_i))|_{\max} = |(v_s)_i| + \sqrt{(v_s)_i^2 + \tilde{a}^2}$, $s = 1,2,3$ are the maximum absolute values of the eigenvalues (4.42) of the Jacobian matrices (4.39) computed in the centre of the control volume $H_i \in \mathcal{H}$, and $(\Delta x_s)_i$, $s = 1,2,3$ are the approximations of the cell lengths of the control volume H_i determined as

$$(\Delta x_1)_i = \frac{2|H_i|}{|\boldsymbol{S}^1 - \boldsymbol{S}^4|}, \qquad (\Delta x_2)_i = \frac{2|H_i|}{|\boldsymbol{S}^2 - \boldsymbol{S}^5|}, \qquad (\Delta x_3)_i = \frac{2|H_i|}{|\boldsymbol{S}^3 - \boldsymbol{S}^6|}, \tag{4.85}$$

where $\boldsymbol{S}^m$, $m = 1,\ldots,6$ is the surface vector that has the direction of the outward unit vector normal to the face Γ_i^m of the control volume H_i, see Eq. (4.53).

For the purpose of this Ph.D. thesis, the numerical method described above is implemented in the programming language Fortran 90. The convergence process is monitored with a dimensionless relative residuum res computed as a discrete $\mathcal{L}_2$ norm of the time derivative of pressure p

$$res = \sqrt{\frac{\sum_i |H_i| \left(\frac{p_i^{(n+1)} - p_i^{(n)}}{\Delta\tilde{t}}\right)^2}{\sum_i |H_i|}}. \tag{4.86}$$

The convergence criterion is chosen as $res < \varepsilon$, where ε is a small pre-selected value.

4.4 Projection methods

Projection methods [26], also known as fractional step methods [179], constitute a special class of segregated methods suitable for the numerical solution of steady as well as unsteady incompressible flow problems [25,76,78,94,203]. The name 'projection' is derived from the concept that the computed velocity is projected onto a space of divergence-free vector field in order to satisfy the continuity equation (*divergence-free condition*).

Compared to the coupled approach when all unknowns are solved simultaneously, see Section 4.3, the segregated methods solve the velocity and pressure fields in a sequential manner. Because of the iterative procedure between the momentum equations and the Poisson equation for pressure, additional velocity-pressure decoupling is created that in the centrally discretised governing equations, generates non-physical high frequency oscillations and is often the cause of stability issues [58]. In collocated grids, where all the unknowns are stored at the same position (usually in the cell centre), this type of instabilities is called the *odd-even decoupling* [58] or the *chessboard effect* [57] due to the chessboard character of pressure/velocity dependences[2]. The problem can be overcome either by introducing artificial dissipation terms or by using a *staggered grid system* instead of the collocated one, i.e., by storing the pressure and velocity vector components at different positions (e.g., in the cell and face centres, respectively).

Although the staggered grid system is relatively easy to implement on structured orthogonal meshes, it can over-complicate the design of the computational code if unstructured meshes are considered. To avoid these difficulties, we adopt an alternative approach in the form of a *hybrid grid system* [76], which involves the coupling of an interpolation method with the collocated (non-staggered) grid system. According to Kim and Choi, who used this approach for the solution of unsteady incompressible flow problems in 2D [76], the hybrid grid system has two major benefits. First, it prevents the occurrence of non-physical pressure oscillations and second, it can be programmed for 3D flow problems more easily than the staggered grid system.

To demonstrate the suitability of projection methods for unsteady flow simulations, the second part of this chapter is focused on pulsatile blood flow modelling in large- and medium-sized arteries. For this purpose, let us consider a time interval $(0,\mathcal{T})$, $\mathcal{T}>0$ and a bounded three-dimensional computational domain $\Omega\subset\mathbb{R}^3$ with boundary $\partial\Omega=\partial\Omega_{\mathrm{I}}\cup\partial\Omega_{\mathrm{O}}\cup\partial\Omega_{\mathrm{W}}$. The space-time cylinder is denoted by $\Omega_{\mathrm{T}}=\Omega\times(0,\mathcal{T})$. Upholding the assumptions and simplifications mentioned at the beginning of the chapter, the equations governing the pulsatile blood flow modelled as an unsteady laminar isothermal flow of an incompressible generalised Newtonian fluid ($\theta=0,1$) are based on the time-dependent system of incompressible Navier-Stokes equations (4.4)–(4.5) introduced in Section 4.1. In the time-space cylinder $\Omega_{\mathrm{T}}=\Omega\times(0,\mathcal{T})$, the dimensionless mathematical model takes the following form:

$$\frac{\partial v_i}{\partial x_i}=0\,, \tag{4.87}$$

[2]It can be shown that the central discretisation of the governing equations on a structured collocated grid results in velocity-pressure decoupling on even and odd points, i.e., the pressure at even points is not influenced by the velocity components of the same points and in return the velocity components at even points are not affected by the pressure at even points. For more details see, e.g., [58] or [190].

$$\frac{\partial v_i}{\partial t} + \frac{\partial}{\partial x_j}\left(v_i v_j\right) + \frac{\partial p}{\partial x_i} = \frac{1}{\mathrm{Re}^{(\theta)}}\frac{\partial}{\partial x_j}\left[\eta(\dot{\gamma})^{(\theta)}\left(\frac{\partial v_i}{\partial x_j} + \frac{\partial v_j}{\partial x_i}\right)\right],\ i,j = 1,2,3\,, \tag{4.88}$$

where $t \in (0, \mathcal{T})$ is the time, v_i is the i-th component of the velocity vector $\boldsymbol{v} = [v_1, v_2, v_3]^T$ corresponding to the Cartesian component x_i of the space variables vector $\boldsymbol{x} = [x_1, x_2, x_3]^T \in \Omega$, p is the pressure, $\mathrm{Re}^{(\theta)}$ is the reference Reynolds number (4.23), and $\eta(\dot{\gamma})^{(\theta)}$, $\theta = 0, 1$ is the dimensionless dynamic viscosity of the generalised Newtonian fluid computed either with Eq. (4.13) or (4.16). As apparent from above, the blood's shear-thinning behaviour is described only by the Carreau-Yasuda model (4.16). This step is taken due to the fact that the modified Cross model gives qualitatively very similar results to those of the Carreau-Yasuda model, see Section 5.1.

Similarly to Section 4.3.1, let us divide the bounded computational domain $\Omega \subset \mathbb{R}^3$ into a finite number of small disjoint subdomains $\tilde{\Omega}_k \subset \Omega$, $k = 1, 2, \ldots, N_{CV}$ such that $\Omega_h = \bigcup_{k=1}^{N_{CV}} \tilde{\Omega}_k$. In the rest of the chapter, the subdomains $\tilde{\Omega}_k \subset \Omega$, $k = 1, 2, \ldots, N_{CV}$ are approximated with convex tetrahedrons also known as control volumes Ω_k, Fig. 4.7, which form an unstructured computational mesh $\mathcal{M} = \{\Omega_k\}_{k=1}^{N_{CV}}$, where N_{CV} is the total number of tetrahedrons. For illustration, Fig. 4.7 shows a control volume $\Omega_k \equiv A_1A_2A_3A_4$, $A_i = [x_{1i}, x_{2i}, x_{3i}]$, $i = 1, \ldots, 4$ with boundary $\partial\Omega_k = \bigcup_{m=1}^{4} \Gamma_k^m$, where Γ_k^m is the m-th planar triangular face of the control volume Ω_k. In accordance with the notation introduced in Section 4.3.1, we will denote $|\Omega_k|$ as the volume of the tetrahedron (control volume) Ω_k, $|\Gamma_k^m|$ as the area of the triangular face Γ_k^m and $\boldsymbol{n}_k^m = \left[{}^1n_k^m, {}^2n_k^m, {}^3n_k^m\right]^T$ as the outward unit vector normal to the m-th face Γ_k^m of the control volume Ω_k.

Based on the idea of the hybrid grid system introduced in [76], all the primitive variables, i.e., the pressure p and the Cartesian velocity vector components v_i, $i = 1, 2, 3$, are defined in the centre of the control volume Ω_k, Fig. 4.7, while the face-normal velocity V_m is introduced in the middle of the m-th face Γ_k^m of the control volume Ω_k as

$$V_m = v_{im} \cdot {}^in_k^m \equiv v_{1m} \cdot {}^1n_k^m + v_{2m} \cdot {}^2n_k^m + v_{3m} \cdot {}^3n_k^m\,, \tag{4.89}$$

where v_{im}, $i = 1, 2, 3$ are the Cartesian velocity vector components on the face Γ_k^m computed with the help of the interpolation method described in Appendix B.

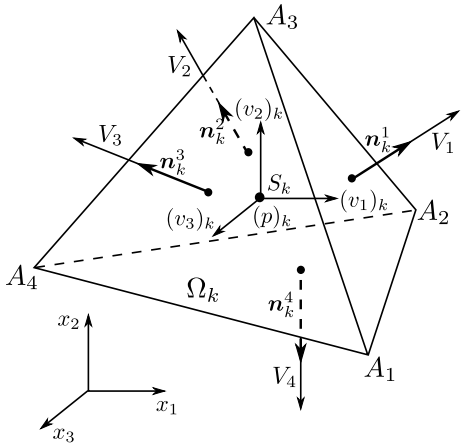

$$\begin{aligned}
\Gamma_k^1 &\equiv \Delta A_1A_2A_3\\
\Gamma_k^2 &\equiv \Delta A_2A_4A_3\\
\Gamma_k^3 &\equiv \Delta A_4A_1A_3\\
\Gamma_k^4 &\equiv \Delta A_1A_2A_4
\end{aligned}$$

Fig. 4.7. Hybrid unstructured computational mesh $\mathcal{M}$ – a tetrahedral control volume $\Omega_k = A_1A_2A_3A_4$ with boundary $\partial\Omega_k = \bigcup_{m=1}^{4} \Gamma_k^m$.

4.4.1 Modified projection method

Since the 1960s, when the first projection/fractional step method was introduced by Chorin [26] and independently by Témam [179], the algorithm of this type of segregated methods has been modified and improved many times [78, 94, 203]. In this section, we focus on a modified variant of the original projection method, which, among others, involves the application of the hybrid grid system [76]. For the sake of simplicity, the blood's non-Newtonian rheology is neglected in the following text, i.e., the numerical solution of the dimensionless time-dependent system of incompressible Navier-Stokes equations (4.87)–(4.88) is carried out for $\theta = 0$ (Newtonian fluid).

The fundamental approach of the segregated methods involves the decoupling of the pressure field from the velocity field [58, 178] in such a way that the pressure is used to correct the velocity field in order to satisfy the continuity equation (4.87) at each computational time level t^n, $n = 0, 1, \ldots, N$. For example, if a first-order explicit time discretisation of Eq. (4.88) is performed

$$\frac{v_i^{n+1} - v_i^n}{\Delta t} + \frac{\partial}{\partial x_j}(v_i^n v_j^n) + \frac{\partial p^n}{\partial x_i} = \frac{1}{\mathrm{Re}^{(0)}} \frac{\partial^2 v_i^n}{\partial x_j \partial x_j}, \quad i, j = 1, 2, 3\,, \tag{4.90}$$

where $\Delta t = t^{n+1} - t^n$ is the time step, then the continuity equation (4.87) is generally not satisfied for the velocity components v_i^{n+1} computed from Eq. (4.90), i.e., $\frac{\partial v_i^{n+1}}{\partial x_i} \neq 0$. In addition, the pressure field p^{n+1} at the time level $(n+1)$ remains unknown. The projection methods eliminate this problem.

They usually operate as a two-stage fractional step scheme that uses multiple calculation steps to determine the velocity components v_i^{n+1} from Eq. (4.90). In the first stage, intermediate velocity components $\hat{v}_i$ that do not satisfy the divergence-free condition (4.87) are explicitly computed from

$$\frac{\hat{v}_i - v_i^n}{\Delta t} + \frac{\partial}{\partial x_j}(v_i^n v_j^n) + \frac{\partial p^n}{\partial x_i} = \frac{1}{\mathrm{Re}^{(0)}} \frac{\partial^2 v_i^n}{\partial x_j \partial x_j}, \quad i, j = 1, 2, 3. \tag{4.91}$$

Note that in contrast to Chorin's original projection method [26], the pressure gradient term at the time level n is not omitted from Eq. (4.91). In the second stage, the pressure is used to project the intermediate velocity vector $\hat{\boldsymbol{v}}$ onto the divergence-free velocity field to obtain the values of velocity and pressure at the next time level $(n+1)$. Hence, the velocity components v_i^{n+1} are computed from

$$\frac{v_i^{n+1} - \hat{v}_i}{\Delta t} + \frac{\partial}{\partial x_i}(p^{n+1} - p^n) = 0 \quad \Longrightarrow \quad v_i^{n+1} = \hat{v}_i - \frac{\partial \Psi}{\partial x_i}\,, \tag{4.92}$$

while a pressure correction function is introduced as

$$\Psi = (p^{n+1} - p^n)\Delta t\,. \tag{4.93}$$

Next, the continuity equation (4.87) is used because it must be satisfied for the computed velocity field v_i^{n+1} at the time level $(n+1)$, i.e., $\frac{\partial v_i^{n+1}}{\partial x_i} = 0$. By taking the divergence of Eq. $(4.92)_2$, we obtain the Poisson equation for the pressure correction function Ψ

$$\frac{\partial v_i^{n+1}}{\partial x_i} = \frac{\partial \hat{v}_i}{\partial x_i} - \frac{\partial^2 \Psi}{\partial x_i \partial x_i} = 0 \quad \Longrightarrow \quad \frac{\partial^2 \Psi}{\partial x_i \partial x_i} = \frac{\partial \hat{v}_i}{\partial x_i}\,. \tag{4.94}$$

In most numerical simulations, an implicit numerical scheme is usually preferred if the time step limit imposed by a CFL stability condition of an explicit scheme is too restrictive. Moreover, rapid variation of flow variables in the vicinity of sharp corners, which are relatively common in many flow geometries, would require grid refinement resulting in the restriction of the computational time step. A fully implicit method overcomes this explicit scheme disadvantage with a trade-off in terms of possible higher operation counts per time step. In this sense, we apply an unconditionally stable implicit Crank-Nicolson scheme of second-order time accuracy to the convective and viscous terms in Eq. (4.91)

$$\frac{\hat{v}_i - v_i^n}{\Delta t} + \frac{1}{2}\frac{\partial}{\partial x_j}(\hat{v}_i\hat{v}_j + v_i^n v_j^n) + \frac{\partial p^n}{\partial x_i} = \frac{1}{2\mathrm{Re}^{(0)}}\frac{\partial^2}{\partial x_j \partial x_j}(\hat{v}_i + v_i^n), \quad i,j = 1,2,3. \tag{4.95}$$

The implicit treatment of the convective and viscous terms eliminates the numerical stability restriction. Further, a linearisation of the non-linear convective term in Eq. (4.95) is performed without losing the overall time accuracy [190] as

$$\hat{v}_i\hat{v}_j = \hat{v}_i v_j^n + v_i^n\hat{v}_j - v_i^n v_j^n + \mathcal{O}(\Delta t^2). \tag{4.96}$$

Finally, by substituting Eq. (4.96) into Eq. (4.95), the whole algorithm of the proposed fractional step method may be written as follows:

$$\frac{\hat{v}_i - v_i^n}{\Delta t} + \frac{1}{2}\frac{\partial}{\partial x_j}(\hat{v}_i v_j^n + v_i^n\hat{v}_j) + \frac{\partial p^n}{\partial x_i} = \frac{1}{2\mathrm{Re}^{(0)}}\frac{\partial^2}{\partial x_j \partial x_j}(\hat{v}_i + v_i^n)\,, \tag{4.97}$$

$$\frac{\partial^2 \Psi}{\partial x_i \partial x_i} = \frac{\partial \hat{v}_i}{\partial x_i}\,, \tag{4.98}$$

$$v_i^{n+1} = \hat{v}_i - \frac{\partial \Psi}{\partial x_i}\,, \tag{4.99}$$

$$p^{n+1} = p^n + \frac{1}{\Delta t}\Psi\,, \tag{4.100}$$

where $i,j = 1,2,3$. Thus, we obtained all the equations necessary for the computation of unknown values of pressure p^{n+1} and velocity components v_i^{n+1} that satisfy the continuity equation (4.87) at the time level $(n+1)$. Note that Eq. (4.97) corresponds to the momentum equations discretised in time, and Eq. (4.98) is the Poisson equation for the pressure correction function Ψ.

For the space discretisation of the system of equations (4.97)–(4.100), we apply the cell-centred finite volume method in accordance with the principles described in Section 4.3.1. Namely, after the integration of Eqs. (4.97)–(4.100) over each tetrahedral control volume $\Omega_k \in \mathcal{M}$, $k = 1,2,\ldots,N_{CV}$ and after the introduction of the integral average for an arbitrary flow quantity Φ over the control volume Ω_k

$$(\Phi)_k = \frac{1}{|\Omega_k|}\int\limits_{\Omega_k} \Phi \mathrm{d}\Omega, \tag{4.101}$$

we convert the volume integrals to surface integrals by means of the Gauss-Ostrogradsky

theorem to

$$(\hat{v}_i)_k - (v_i^n)_k + \frac{\Delta t}{2|\Omega_k|} \oint\limits_{\partial\Omega_k} (\hat{v}_i v_j^n \; + \; v_i^n \hat{v}_j) \cdot {}^j n_k \, \mathrm{d}\Gamma + \frac{\Delta t}{|\Omega_k|} \oint\limits_{\partial\Omega_k} p^n \cdot {}^i n_k \, \mathrm{d}\Gamma =$$

$$= \frac{\Delta t}{2\mathrm{Re}^{(0)}|\Omega_k|} \oint\limits_{\partial\Omega_k} \frac{\partial}{\partial x_j} (\hat{v}_i + v_i^n) \cdot {}^j n_k \, \mathrm{d}\Gamma, \quad (4.102)$$

$$\oint\limits_{\partial\Omega_k} \frac{\partial \Psi}{\partial x_i} \cdot {}^i n_k \, \mathrm{d}\Gamma = \oint\limits_{\partial\Omega_k} \hat{v}_i \cdot {}^i n_k \, \mathrm{d}\Gamma, \quad (4.103)$$

$$(v_i^{n+1})_k = (\hat{v}_i)_k - \frac{1}{|\Omega_k|} \oint\limits_{\partial\Omega_k} \Psi \cdot {}^i n_k \, \mathrm{d}\Gamma, \quad (4.104)$$

$$(p^{n+1})_k = (p^n)_k + \frac{1}{\Delta t}(\Psi)_k, \quad (4.105)$$

where ${}^i n_k$ is the i-th component of the outward unit vector $\boldsymbol{n}_k = [{}^1 n_k, \, {}^2 n_k, \, {}^3 n_k]^T$ normal to the boundary $\partial\Omega_k$ of the tetrahedral control volume Ω_k. By using the identities

$$\oint\limits_{\partial\Omega_k} \frac{\partial}{\partial x_j} (\hat{v}_i + v_i^n) \cdot {}^j n_k \, \mathrm{d}\Gamma = \oint\limits_{\partial\Omega_k} \frac{\partial}{\partial \boldsymbol{n}_k} (\hat{v}_i + v_i^n) \, \mathrm{d}\Gamma,$$

$$\oint\limits_{\partial\Omega_k} \frac{\partial \Psi}{\partial x_i} \cdot {}^i n_k \, \mathrm{d}\Gamma = \oint\limits_{\partial\Omega_k} \frac{\partial \Psi}{\partial \boldsymbol{n}_k} \, \mathrm{d}\Gamma,$$

Eqs. (4.102) and (4.103) can be further modified to

$$(\hat{v}_i)_k - (v_i^n)_k + \frac{\Delta t}{2|\Omega_k|} \oint\limits_{\partial\Omega_k} \left(\hat{v}_i v_j^n \; + \; v_i^n \hat{v}_j\right) \cdot {}^j n_k \, \mathrm{d}\Gamma + \frac{\Delta t}{|\Omega_k|} \oint\limits_{\partial\Omega_k} p^n \cdot {}^i n_k \, \mathrm{d}\Gamma =$$

$$= \frac{\Delta t}{2\mathrm{Re}^{(0)}|\Omega_k|} \oint\limits_{\partial\Omega_k} \frac{\partial}{\partial \boldsymbol{n}_k} (\hat{v}_i + v_i^n) \, \mathrm{d}\Gamma, \quad (4.106)$$

$$\oint\limits_{\partial\Omega_k} \frac{\partial \Psi}{\partial \boldsymbol{n}_k} \, \mathrm{d}\Gamma = \oint\limits_{\partial\Omega_k} \hat{v}_i \cdot {}^i n_k \, \mathrm{d}\Gamma. \quad (4.107)$$

To eliminate potential non-physical high-frequency oscillations within the flow field [58] and to satisfy the continuity equation (4.87), the system of equations (4.104)–(4.107) is completed with

$$V^{n+1} = \hat{V} - \frac{\partial \Psi}{\partial \boldsymbol{n}_k}. \quad (4.108)$$

This equation defines normal velocity V^{n+1} at the time level $(n+1)$ with the direction of the outward unit vector $\boldsymbol{n}_k$ normal to the boundary $\partial\Omega_k$ of the control volume Ω_k. The intermediate normal velocity $\hat{V}$ is given as $\hat{V} = \hat{v}_i \cdot {}^i n_k$ in accordance with Eq. (4.89). By introducing a new variable

$$\delta\hat{v}_i = \hat{v}_i - v_i^n \, , \quad (4.109)$$

the surface integral from the linearised convective term in Eq. (4.106) are modified as

$$\oint_{\partial\Omega_k} \left(\hat{v}_i\, v_j^n + v_i^n \hat{v}_j\right) \cdot {}^j n_k \; \mathrm{d}\Gamma = \oint_{\partial\Omega_k} \left(\hat{v}_i\, v_j^n + v_i^n \hat{v}_j + 2v_i^n v_j^n - 2v_i^n v_j^n\right) \cdot {}^j n_k \, \mathrm{d}\Gamma =$$

$$= \oint_{\partial\Omega_k} \left[\left(\hat{v}_i - v_i^n\right) v_j^n + v_i^n \left(\hat{v}_j - v_j^n\right) + 2v_i^n v_j^n \right] \cdot {}^j n_k \, \mathrm{d}\Gamma =$$

$$= \oint_{\partial\Omega_k} \left(\delta\hat{v}_i\, v_j^n \cdot {}^j n_k + v_i^n \cdot {}^j n_k \;\, \delta\hat{v}_j + 2v_i^n v_j^n \cdot {}^j n_k\right) \mathrm{d}\Gamma. \quad (4.110)$$

Because $V^n = v_j^n \cdot {}^j n_k$, Eq. (4.110) can be further rewritten to

$$\oint_{\partial\Omega_k} \left(\hat{v}_i v_j^n + v_i^n \hat{v}_j\right) \cdot {}^j n_k \, \mathrm{d}\Gamma = \oint_{\partial\Omega_k} \left(\delta\hat{v}_i V^n + v_i^n \cdot {}^j n_k \;\, \delta\hat{v}_j + 2v_i^n V^n\right) \mathrm{d}\Gamma. \quad (4.111)$$

In this way, Eq. (4.108) and the system of equations (4.104)–(4.107) are coupled to eliminate undesirable non-physical oscillations by applying the interpolation formulas (B.1) and (B.2) from Appendix B. Finally, after employing Eq. (4.109), we obtain

$$(\delta\hat{v}_i)_k + \frac{\Delta t}{2|\Omega_k|} \oint_{\partial\Omega_k} \left(\delta\hat{v}_i V^n \;+\; v_i^n \cdot {}^j n_k \;\, \delta\hat{v}_j + 2v_i^n V^n\right) \mathrm{d}\Gamma + \frac{\Delta t}{|\Omega_k|} \oint_{\partial\Omega_k} p^n \cdot {}^i n_k \, \mathrm{d}\Gamma =$$

$$= \frac{\Delta t}{2\mathrm{Re}^{(0)}|\Omega_k|} \oint_{\partial\Omega_k} \frac{\partial}{\partial \boldsymbol{n}_k} \left(\delta\hat{v}_i + 2v_i^n\right) \mathrm{d}\Gamma, \quad (4.112)$$

$$(\hat{v}_i)_k = (v_i^n)_k + (\delta\hat{v}_i)_k, \quad (4.113)$$

$$\oint_{\partial\Omega_k} \frac{\partial\Psi}{\partial \boldsymbol{n}_k} \mathrm{d}\Gamma = \oint_{\partial\Omega_k} \hat{v}_i \cdot {}^i n_k \, \mathrm{d}\Gamma, \quad (4.114)$$

$$(v_i^{n+1})_k = (\hat{v}_i)_k - \frac{1}{|\Omega_k|} \oint_{\partial\Omega_k} \Psi \cdot {}^i n_k \, \mathrm{d}\Gamma, \quad (4.115)$$

$$(p^{n+1})_k = (p^n)_k + \frac{1}{\Delta t}(\Psi)_k, \quad (4.116)$$

$$V^{n+1} = \hat{V} - \frac{\partial\Psi}{\partial \boldsymbol{n}_k}. \quad (4.117)$$

As the next step, we approximate the surface integrals in the system of equations (4.112)–(4.117). First, each integral is replaced by the sum of integrals over each face Γ_k^m of the control volume Ω_k, Fig. 4.7, and then approximated by the midpoint rule

$$\oint_{\partial\Omega_k} \Phi \, \mathrm{d}\Gamma = \sum_{m=1}^{4} \iint_{\Gamma_k^m} \Phi \, \mathrm{d}\Gamma \approx \sum_{m=1}^{4} \Phi_m |\Gamma_k^m|, \quad (4.118)$$

where Φ_m is the value of an arbitrary flow quantity at the integration point on the m-th face Γ_k^m of the control volume Ω_k. The interpolation process required for the determination of Φ_m in described in Appendix B.

The application of Eq. (4.118) to the system of equations (4.112)–(4.117) yields

$$(\delta\hat{v}_i)_k + \frac{\Delta t}{2|\Omega_k|}\sum_{m=1}^{4}\left(\delta\hat{v}_{im}V_m^n \;+\; v_{im}^n\cdot {}^j n_k^m\;\delta\hat{v}_{jm} + 2v_{im}^n V_m^n\right)|\Gamma_k^m| + \\ + \frac{\Delta t}{|\Omega_k|}\sum_{m=1}^{4} p_m^n\cdot {}^i n_k^m\,|\Gamma_k^m| \;=\; \frac{\Delta t}{2\mathrm{Re}^{(0)}|\Omega_k|}\sum_{m=1}^{4}\frac{\partial}{\partial \boldsymbol{n}_k^m}\left(\delta\hat{v}_{im} + 2v_{im}^n\right)|\Gamma_k^m|, \quad (4.119)$$

$$(\hat{v}_i)_k \;=\; (v_i^n)_k + (\delta\hat{v}_i)_k, \quad (4.120)$$

$$\sum_{m=1}^{4}\frac{\partial\Psi}{\partial \boldsymbol{n}_k^m}|\Gamma_k^m| \;=\; \sum_{m=1}^{4}\hat{v}_{im}\cdot {}^i n_k^m\,|\Gamma_k^m| \equiv \sum_{m=1}^{4}\hat{V}_m\,|\Gamma_k^m|, \quad (4.121)$$

$$(v_i^{n+1})_k \;=\; (\hat{v}_i)_k - \frac{1}{|\Omega_k|}\sum_{m=1}^{4}\Psi_m\cdot {}^i n_k^m\,|\Gamma_k^m|, \quad (4.122)$$

$$(p^{n+1})_k \;=\; (p^n)_k + \frac{1}{\Delta t}(\Psi)_k\,, \quad (4.123)$$

$$V_m^{n+1} \;=\; \hat{V}_m - \frac{\partial\Psi}{\partial \boldsymbol{n}_k^m}\,, \quad (4.124)$$

where ${}^i n_k^m$ is the i-th component of the outward unit vector $\boldsymbol{n}_k^m = [{}^1 n_k^m,\, {}^2 n_k^m,\, {}^3 n_k^m]^T$ normal to the m-th face Γ_k^m of the control volume Ω_k, and the intermediate face-normal velocity $\hat{V}_m$ on the face Γ_k^m is defined as $\hat{V}_m = \hat{v}_{im}\cdot {}^i n_k^m$. Note that the values of the face-normal velocity V_m^{n+1} computed with the help of Eq. (4.124) are used as the values of face-normal velocity V_m^n in Eq. (4.119) at the next time level.

To perform numerical computations according to Eqs. (4.119)–(4.124), the values of $\delta\hat{v}_{im}$, v_{im}^n, p_m^n, Ψ_m and derivatives $\frac{\partial\Psi}{\partial \boldsymbol{n}_k^m}$, $\frac{\partial}{\partial \boldsymbol{n}_k^m}\left(\delta\hat{v}_{im} + 2v_{im}^n\right)$ on the m-th face Γ_k^m of the tetrahedral control volume $\Omega_k \in \mathcal{M}$ must be determined. For this purpose, we employ a second-order accurate interpolation method, which is based on the well-known interpolation method proposed by Rhie and Chow [159], see Appendix B.

Taking into consideration the three different boundary types introduced in this Ph.D. thesis, the non-dimensional boundary conditions at the boundary $\partial\Omega_h$ of the computational domain $\Omega_h \subset \mathbb{R}^3$ are implemented as follows:

- *inlet* $\Gamma_k^m \subset \partial\Omega_{hI}$: Dirichlet boundary conditions for the velocity vector components v_{im} and a zero normal derivative of velocity vector components are prescribed

$$v_{im} = v_{iI}, \quad \left.\frac{\partial v_{im}}{\partial \boldsymbol{n}_k^m}\right|_{\Gamma_k^m} = 0. \quad (4.125)$$

  The value of the face-normal velocity V_m^I on the face Γ_k^m is computed as $V_m^I = v_{iI}\cdot {}^i n_k^m$, where v_{iI} are the given dimensionless components of the velocity vector $\boldsymbol{v}_I$. For the normal derivative of the pressure correction function Ψ on the face Γ_k^m, we prescribe

$$\left.\frac{\partial\Psi}{\partial \boldsymbol{n}_k^m}\right|_{\Gamma_k^m} = 0. \quad (4.126)$$

- *rigid and impermeable wall* $\Gamma_k^m \subset \partial\Omega_{hW}$: Velocity vector components v_{im} on the face Γ_k^m are set equal to zero

$$v_{im} = 0\,, \quad (4.127)$$

leading to a zero value of the face-normal velocity $V_m^W = v_{im} \cdot {}^i n_k^m = 0$ on the face Γ_k^m. Similarly to the inlet boundary, a zero normal derivative of the pressure correction function Ψ is prescribed at the wall

$$\left.\frac{\partial \Psi}{\partial \boldsymbol{n}_k^m}\right|_{\Gamma_k^m} = 0. \tag{4.128}$$

- *outlet* $\Gamma_k^m \subset \partial\Omega_{hO}$: The following type of boundary condition is stated

$$p_m \boldsymbol{n}_k^m - \frac{1}{\mathrm{Re}^{(0)}} \frac{\partial \boldsymbol{v}_m}{\partial \boldsymbol{n}_k^m} = p_O \boldsymbol{n}_k^m, \tag{4.129}$$

where p_O is the given dimensionless value of the outlet pressure. Considering Eq. (4.93), the pressure correction function on the face Γ_k^m corresponds to the Dirichlet boundary condition

$$\Psi_m = 0. \tag{4.130}$$

The substitution of the derivative $\frac{\partial \Psi}{\partial \boldsymbol{n}_k^m}$ in Eq. (4.121) with Eq. (4.124) yields

$$\sum_{m=1}^{4} \frac{\partial \Psi}{\partial \boldsymbol{n}_k^m} |\Gamma_k^m| = \sum_{m=1}^{4} \left(\hat{V}_m - V_m^{n+1} \right) |\Gamma_k^m| = \sum_{m=1}^{4} \hat{V}_m |\Gamma_k^m| \quad \Longrightarrow \quad \sum_{m=1}^{4} V_m^{n+1} |\Gamma_k^m| = 0,$$

i.e., the face-normal velocity V_m^{n+1} a the time level $(n+1)$ satisfies the divergence-free condition exactly. It should be noted that at the outlet boundary $\partial\Omega_{hO}$, i.e., $\Gamma_k^m \subset \partial\Omega_{hO}$, the $\frac{\partial \Psi}{\partial \boldsymbol{n}_k^m}$ values are unknown. Thus, to ensure that the aforementioned condition for the face-normal velocity V_m^{n+1} is satisfied at the outlet boundary $\partial\Omega_{hO}$, the face-normal velocity V_m^{n+1} on the face $\Gamma_k^m \subset \partial\Omega_{hO}$ must be computed as

$$V_{m_O}^{n+1} = -\frac{1}{|\Gamma_k^{m_O}|} \sum_{\substack{m=1 \\ m \neq m_O}}^{4} V_m^{n+1} |\Gamma_k^m|, \tag{4.131}$$

where m_O is the index of the outlet face $\Gamma_k^{m_O}$ of the control volume $\Omega_k \in \mathcal{M}$.

Boundary conditions given by Eqs. (4.125), (4.127) and (4.129) are used for the solution of Eq. (4.119), while Eqs. (4.126), (4.128) and (4.130) are utilised for the solution of the Poisson equation for the pressure correction function (4.121).

With the application of the interpolation method and corresponding boundary conditions, the solution of Eq. (4.119) leads to a system of linear algebraic equations $\mathbf{A}_{\mathrm{NS}} \cdot \mathbf{x}_{\mathrm{NS}} = \mathbf{b}_{\mathrm{NS}}$ for $3N_{CV}$ unknown values $(\delta\hat{v}_i)_k$, $i = 1, 2, 3$, $k = 1, 2, \ldots N_{CV}$, where $\mathbf{A}_{\mathrm{NS}}$ is a square matrix of order $3N_{CV}$, $\mathbf{x}_{\mathrm{NS}}$ is the column vector of unknowns defined as $\mathbf{x}_{\mathrm{NS}} = \big[[(\delta\hat{v}_1)_1, (\delta\hat{v}_2)_1, (\delta\hat{v}_3)_1], \ldots, [(\delta\hat{v}_1)_k, (\delta\hat{v}_2)_k, \quad (\delta\hat{v}_3)_k], \ldots, [(\delta\hat{v}_1)_{N_{CV}}, (\delta\hat{v}_2)_{N_{CV}}, (\delta\hat{v}_3)_{N_{CV}}] \big]^T$, and the right hand-side vector $\mathbf{b}_{\mathrm{NS}}$ consists of known values from the time level n. Similarly, the solution of the Poisson equation (4.121) leads to a system of linear algebraic equations $\mathbf{A}_{\mathrm{Poi}} \cdot \mathbf{x}_{\mathrm{Poi}} = \mathbf{b}_{\mathrm{Poi}}$ for N_{CV} unknown values $(\Psi)_k$, $k = 1, 2, \ldots N_{CV}$, where $\mathbf{A}_{\mathrm{Poi}}$ is a square matrix of order N_{CV}, $\mathbf{x}_{\mathrm{Poi}}$ is the column vector of unknowns defined as $\mathbf{x}_{\mathrm{Poi}} = [(\Psi)_1, \ldots, (\Psi)_k, \ldots, (\Psi)_{N_{CV}}]^T$, and $\mathbf{b}_{\mathrm{Poi}}$ is the right hand-side vector of the system of linear equations.

The above-described numerical method is implemented using the software MATLAB (MathWorks, Natick, USA). As the two systems of linear algebraic equations contain sparse matrices ($\mathbf{A}_{\mathrm{NS}}$ or $\mathbf{A}_{\mathrm{Poi}}$), it is favourable to use an iterative solution. In this work, we employ the biconjugate gradient stabilised (BI-CGSTAB) method with the incomplete LU preconditioner that is a standard part of the aforementioned MATLAB software. The matrix $\mathbf{A}_{\mathrm{NS}}$ is newly created at each time level by using the program language C++ via the MEX interface. For the incomplete LU decomposition, the UMFPACK library is used with drop tolerances of 10^{-4} and 10^{-5} for the matrices $\mathbf{A}_{\mathrm{NS}}$ and $\mathbf{A}_{\mathrm{Poi}}$, respectively. The convergence process is monitored with a relative residuum res defined as

$$res = \frac{\|\mathbf{b} - \mathbf{A} \cdot \mathbf{x}\|_{l_2}}{\|\mathbf{b}\|_{l_2}}. \tag{4.132}$$

The convergence criterion is chosen as $res < \varepsilon$, where the tolerance is set equal to $\varepsilon = 10^{-8}$ for both systems of linear algebraic equations. In all our simulations, the computational domain $\Omega \subset \mathbb{R}^3$ is initialised ($t^0 = 0$) with the following values:

$$(v_i^0)_k = \frac{1}{|\Omega_k|} \int_{\Omega_k} v_i(\boldsymbol{x}, 0)\, \mathrm{d}\Omega = 0, \quad (\Psi)_k = 0, \quad (p^0)_k = \frac{1}{|\Omega_k|} \int_{\Omega_k} p(\boldsymbol{x}, 0)\, \mathrm{d}\Omega = p_O,$$

where $k = 1, 2, \ldots, N_{CV}$ and p_O is a dimensionless value of static pressure given as the outlet boundary condition.

Although the applied second-order implicit Crank-Nicolson scheme is unconditionally stable, it is appropriate to restrict the size of time step Δt with the CFL condition

$$\Delta t = \min_k \left[\mathrm{CFL} \left(\frac{1}{|\Omega_k|} \sum_{m=1}^{4} \left| V_m^n \cdot |\Gamma_k^m| \right| \right)^{-1} \right] \tag{4.133}$$

due to the following reasons:

- a large time step Δt may cause a large local error in time discretisation because of the convective term linearisation (4.96),
- with increasing time step Δt, the matrix $\mathbf{A}_{\mathrm{NS}}$ becomes more ill-conditioned, leading to a decrease in computational efficiency when solving the system of linear algebraic equations $\mathbf{A}_{\mathrm{NS}} \cdot \mathbf{x}_{\mathrm{NS}} = \mathbf{b}_{\mathrm{NS}}$.

Based on our numerical experiments, the following empirical formula for the calculation of a suitable CFL value is proposed:

$$\mathrm{CFL} = \sqrt[3]{\frac{\max\{|\Omega_k|\}_{k=1}^{N_{CV}}}{\min\{|\Omega_k|\}_{k=1}^{N_{CV}}}}.$$

Software verification

In order to determine the computational ability of the developed CFD code, a process of software verification is carried out. For this purpose, an idealised model of end-to-side anastomosis (Fig. 4.8) is reconstructed according to the parameters given by Bertolotti

et al. in [11,12]. As apparent from Fig. 4.8, the adopted bypass model consists of a 75% stenosed native artery and a graft of equal diameter ($D = 3\,\mathrm{mm}$), which intersects the artery at the angle of 45°. The simulation of pulsatile blood flow is performed according to the inlet flow rate waveforms taken from [12] and shown in Fig. 4.9 with the following characteristic flow parameters: the Womersley number of 2.16 and the average inlet Reynolds numbers of 89.4 and 152.2 for the native artery and bypass graft, respectively. Fig. 4.10 (left) shows the bypass geometry reconstructed for the purpose of the software verification with a detailed view at the structure of the computational mesh. Further for the sake of completeness, Fig. 4.10 (right) lists the number of nodes and elements used in the original and reconstructed bypass models.

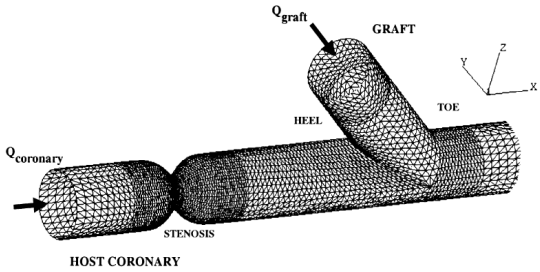

Fig. 4.8. Model of end-to-side coronary bypass with stenosed native artery [11,12].

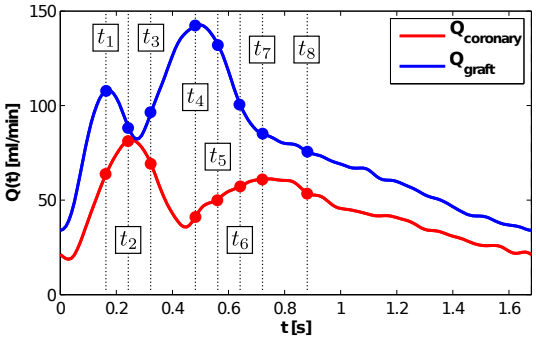

Fig. 4.9. Inlet flow rate waveforms for the native artery and bypass graft [12].

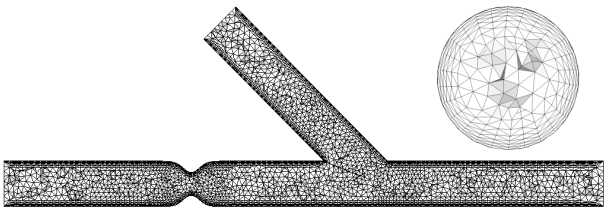

bypass model	No. of nodes	No. of elements
Bertolotti *et al.* [12]	129,356	88,831
present study	34,328	189,814

Fig. 4.10. Tetrahedral computational mesh with a detailed view at the cross-section in the native artery (*left*). Overview of mesh parameters (*right*).

The numerical results obtained with the developed in-house CFD software are shown in Fig. 4.11 together with the experimental and numerical data taken from [12]. Note that the velocity profiles in this figure are displayed at eight time instants of the cardiac cycle indicated in Fig. 4.9. Comparing the velocity profiles with each other, it can be observed that our numerical results are in very good qualitative and quantitative agreement with the numerical ones published by Bertolotti *et al.* and computed with a finite element solver. As for the noticeable differences between the numerical and experimental (Doppler velocimeter) data, the authors of [12] admit that the observed deviations may be caused by several unintentional errors (e.g., ultrasonic beam reflection) resulting in smoothed velocity profiles and velocity overestimation near the model walls.

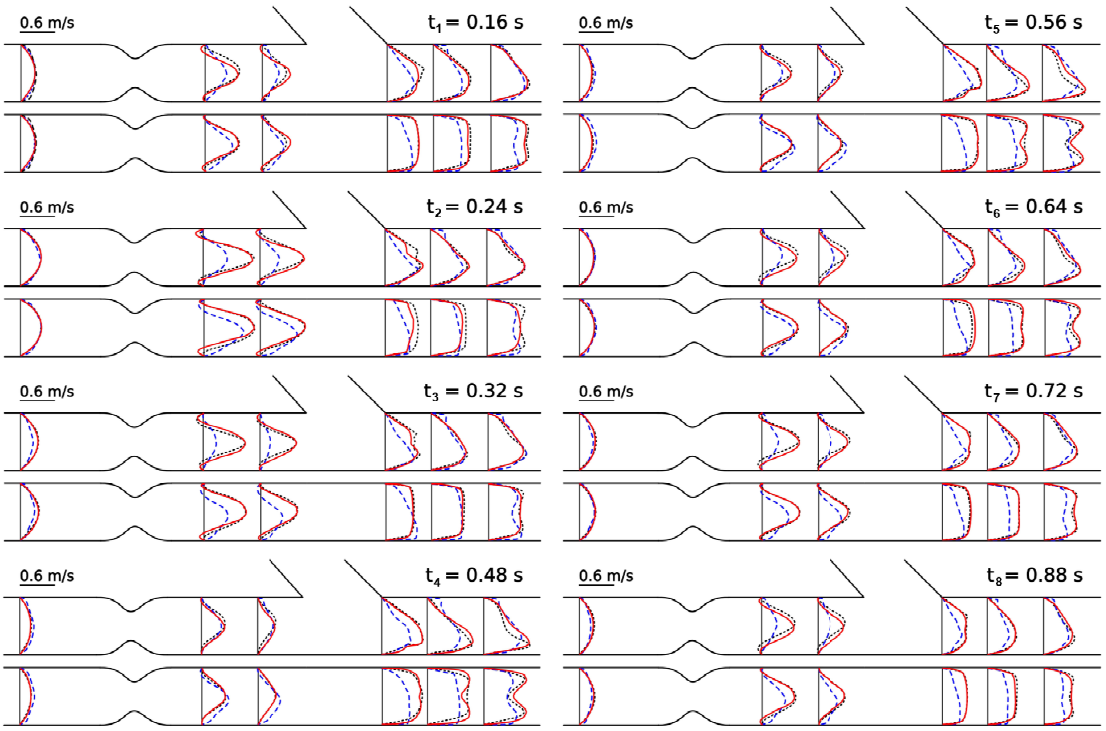

Fig. 4.11. Comparison of our numerical results (—) with the numerical (- - -) and experimental (- - -) results published in [12]. The velocity profiles are shown in vertical (*top*) and horizontal (*bottom*) sections at eight time instants denoted in Fig. 4.9.

4.4.2 Stabilised projection method

Compared to the modified projection method described in Section 4.4.1, the present numerical method is intended for the numerical simulation of pulsatile incompressible generalised Newtonian flow. In other words, the numerical solution of the dimensionless time-dependent system of incompressible Navier-Stokes equations (4.87)–(4.88) is carried out for Newtonian ($\theta = 0$, Eq. (4.13)) as well as non-Newtonian ($\theta = 1$, Carreau-Yasuda model, Eq. (4.16)) fluids.

The stabilised projection method is based on the same principles as the previously described modified variant in Section 4.4.1. Namely, by integrating the momentum equations Eq. (4.88) in time by means of an implicit multistep method and substituting the time derivative by a difference formula of second order accuracy, we obtain

$$\frac{3v_i^{n+1} - 4v_i^n + v_i^{n-1}}{2\Delta t} + \frac{\partial}{\partial x_j}\left(v_i^{n+1} v_j^{n+1}\right) + \frac{\partial p^{n+1}}{\partial x_i} = \\ = \frac{1}{\mathrm{Re}^{(\theta)}} \frac{\partial}{\partial x_j}\left[\eta(\dot{\gamma})^{(\theta)}\left(\frac{\partial v_i^{n+1}}{\partial x_j} + \frac{\partial v_j^{n+1}}{\partial x_i}\right)\right], \qquad (4.134)$$

where $i, j = 1, 2, 3$ and Δt is a chosen fixed time step. To satisfy the divergence-free condition (4.87) for velocity v_i^{n+1}, i.e., $\frac{\partial v_i^{n+1}}{\partial x_i} = 0$, and to determine the pressure values p^{n+1} at the time level $(n+1)$, the computation is divided into the following steps: In

the first step, intermediate velocity components $\hat{v}_i$ are computed from

$$\frac{3\hat{v}_i - 4v_i^n + v_i^{n-1}}{2\Delta t} + \frac{\partial}{\partial x_j}\left(\hat{v}_i\hat{v}_j\right) + \frac{\partial p^n}{\partial x_i} = \frac{1}{\mathrm{Re}^{(\theta)}}\frac{\partial}{\partial x_j}\left[\eta(\dot{\gamma})^{(\theta)}\left(\frac{\partial \hat{v}_i}{\partial x_j} + \frac{\partial \hat{v}_j}{\partial x_i}\right)\right], \quad (4.135)$$

where the values of velocity and pressure from the previous time levels n and $(n-1)$ are known. In the second step, the pressure is used to project the intermediate velocity vector $\hat{\boldsymbol{v}}$ onto the divergence-free velocity field to obtain the values of velocity and pressure at the next time level $(n+1)$. Hence, the velocity components v_i^{n+1} are computed from

$$\frac{3}{2}\frac{v_i^{n+1} - \hat{v}_i}{\Delta t} + \frac{\partial}{\partial x_i}(p^{n+1} - p^n) = 0 \quad \Longrightarrow \quad v_i^{n+1} = \hat{v}_i - \frac{\partial \Psi}{\partial x_i}, \quad (4.136)$$

while a pressure correction function is introduced

$$\Psi = \frac{2}{3}\Delta t(p^{n+1} - p^n) \quad (4.137)$$

and used for the computation of pressure p^{n+1}. By taking the divergence of Eq. (4.136) to satisfy the continuity Eq. (4.87) for the computed velocity field v_i^{n+1} at the time level $(n+1)$, we derive the Poisson equation for the pressure correction function Ψ

$$\frac{\partial v_i^{n+1}}{\partial x_i} = \frac{\partial \hat{v}_i}{\partial x_i} - \frac{\partial^2 \Psi}{\partial x_i \partial x_i} = 0 \quad \Longrightarrow \quad \frac{\partial^2 \Psi}{\partial x_i \partial x_i} = \frac{\partial \hat{v}_i}{\partial x_i}. \quad (4.138)$$

The newly computed values of v_i^{n+1} and p^{n+1} usually do not satisfy Eq. (4.134) exactly. It is, therefore, necessary to repeat the above described process until a convergence criterion is satisfied. For this purpose, let us introduce the iteration index s such that $v_i^{s=0} = v_i^n$ and $p^{s=0} = p^n$. Then, the whole iteration process can be written as follows:

$$\frac{3\hat{v}_i - 4v_i^n + v_i^{n-1}}{2\Delta t} + \frac{\partial}{\partial x_j}(\hat{v}_i\hat{v}_j) + \frac{\partial p^s}{\partial x_i} = \frac{1}{\mathrm{Re}^{(\theta)}}\frac{\partial}{\partial x_j}\left[\eta(\dot{\gamma})^{(\theta)}\left(\frac{\partial \hat{v}_i}{\partial x_j} + \frac{\partial \hat{v}_j}{\partial x_i}\right)\right], \quad (4.139)$$

$$\frac{\partial^2 \Psi}{\partial x_i \partial x_i} = \frac{\partial \hat{v}_i}{\partial x_i}, \quad (4.140)$$

$$v_i^{s+1} = \hat{v}_i - \frac{\partial \Psi}{\partial x_i}, \quad (4.141)$$

$$p^{s+1} = p^s + \frac{3}{2\Delta t}\Psi. \quad (4.142)$$

The computation is repeated for $s = 0, 1, 2, 3, ...$ until Ψ ceases to meet the convergence criterion given by Eq. (4.167). At the end of the iteration process, we set $v_i^{n+1} = v_i^{s+1}$ and $p^{n+1} = p^{s+1}$. If a large time step Δt is taken, the pressure values may be overestimated during the inner iteration process. For this reason, it is appropriate to introduce an under-relaxation parameter $\alpha \in (0, 1]$ and rewrite Eq. (4.142)

$$p^{s+1} = p^s + \alpha\frac{3}{2\Delta t}\Psi. \quad (4.143)$$

Similarly to Section 4.4.1, the space discretisation of the system of Eqs. (4.139)–(4.142) is carried out with the cell-centred finite volume method formulated for hybrid

unstructured tetrahedral grids, Fig. 4.7. In accordance with the principles of this method, Eqs. (4.139)–(4.142) are integrated over each control volume Ω_k, $k = 1, 2, \ldots, N_{CV}$ and modified with the integral average (4.101) and the Gauss-Ostrogradsky theorem

$$\frac{3}{2\Delta t}(\hat{v}_i)_k - \frac{2}{\Delta t}(v_i^n)_k + \frac{1}{2\Delta t}(v_i^{n-1})_k + \frac{1}{|\Omega_k|}\oint\limits_{\partial\Omega_k} \hat{v}_i\hat{v}_j \cdot {}^j n_k \,\mathrm{d}\Gamma + \frac{1}{|\Omega_k|}\oint\limits_{\partial\Omega_k} p^s \cdot {}^i n_k \,\mathrm{d}\Gamma =$$
$$= \frac{1}{\mathrm{Re}^{(\theta)}|\Omega_k|}\oint\limits_{\partial\Omega_k} \eta(\dot{\gamma})^{(\theta)} \left(\frac{\partial \hat{v}_i}{\partial x_j} + \frac{\partial \hat{v}_j}{\partial x_i}\right) \cdot {}^j n_k \,\mathrm{d}\Gamma, \tag{4.144}$$

$$\oint\limits_{\partial\Omega_k} \frac{\partial \Psi}{\partial x_i} \cdot {}^i n_k \,\mathrm{d}\Gamma \equiv \oint\limits_{\partial\Omega_k} \frac{\partial \Psi}{\partial \boldsymbol{n}_k} \,\mathrm{d}\Gamma = \oint\limits_{\partial\Omega_k} \hat{v}_i \cdot {}^i n_k \,\mathrm{d}\Gamma, \tag{4.145}$$

$$(v_i^{s+1})_k = (\hat{v}_i)_k - \frac{1}{|\Omega_k|}\oint\limits_{\partial\Omega_k} \Psi \cdot {}^i n_k \,\mathrm{d}\Gamma, \tag{4.146}$$

$$(p^{s+1})_k = (p^s)_k + \alpha\frac{3}{2\Delta t}(\Psi)_k, \tag{4.147}$$

where ${}^i n_k$ is the i-th component of the outward unit vector $\boldsymbol{n}_k = [{}^1 n_k, {}^2 n_k, {}^3 n_k]^T$ normal to the boundary $\partial\Omega_k$ of the tetrahedral control volume $\Omega_k \in \mathcal{M}$. Linearisation of the convective term in Eq. (4.144)

$$\oint\limits_{\partial\Omega_k} \hat{v}_i\hat{v}_j \cdot {}^j n_k \,\mathrm{d}\Gamma \approx \oint\limits_{\partial\Omega_k} \hat{v}_i v_j^s \cdot {}^j n_k \,\mathrm{d}\Gamma = \oint\limits_{\partial\Omega_k} \hat{v}_i V^s \,\mathrm{d}\Gamma, \tag{4.148}$$

where $V^s = v_j^s \cdot {}^j n_k$, and linearisation of the viscous term in Eq. (4.144)

$$\frac{1}{\mathrm{Re}^{(\theta)}|\Omega_k|}\oint\limits_{\partial\Omega_k} \eta(\dot{\gamma})^{(\theta)} \left(\frac{\partial \hat{v}_i}{\partial x_j} + \frac{\partial \hat{v}_j}{\partial x_i}\right) \cdot {}^j n_k \,\mathrm{d}\Gamma \approx$$
$$\approx \frac{1}{\mathrm{Re}^{(\theta)}|\Omega_k|}\oint\limits_{\partial\Omega_k} \eta(\dot{\gamma}(v^n))^{(\theta)} \left(\frac{\partial \hat{v}_i}{\partial x_j} + \frac{\partial v_j^s}{\partial x_i}\right) \cdot {}^j n_k \,\mathrm{d}\Gamma, \tag{4.149}$$

where v_j^s is applied to split the interconnected system of Eqs. (4.144) into three independent equations, yield

$$\frac{3}{2\Delta t}(\hat{v}_i)_k - \frac{2}{\Delta t}(v_i^n)_k + \frac{1}{2\Delta t}(v_i^{n-1})_k + \frac{1}{|\Omega_k|}\oint\limits_{\partial\Omega_k} \hat{v}_i V^s \,\mathrm{d}\Gamma + \frac{1}{|\Omega_k|}\oint\limits_{\partial\Omega_k} p^s \cdot {}^i n_k \,\mathrm{d}\Gamma =$$
$$= \frac{1}{\mathrm{Re}^{(\theta)}|\Omega_k|}\oint\limits_{\partial\Omega_k} \eta(\dot{\gamma}(v^n))^{(\theta)} \left(\frac{\partial \hat{v}_i}{\partial x_j} + \frac{\partial v_j^s}{\partial x_i}\right) \cdot {}^j n_k \,\mathrm{d}\Gamma. \tag{4.150}$$

For the elimination of potential non-physical oscillations, the system of equations (4.145)–(4.147) and (4.150) is completed with the equation for the face-normal velocity

$$V^{s+1} = \hat{V} - \frac{\partial \Psi}{\partial \boldsymbol{n}_k}, \tag{4.151}$$

where $\hat{V} = \hat{v}_i \cdot {}^i n_k$ is the intermediate face-normal velocity. In the next step, the surface integrals in the system of Eqs. (4.145)–(4.147), (4.150) and (4.151) are approximated according to the formula (4.118)

$$\frac{3}{2\Delta t}(\hat{v}_i)_k - \frac{2}{\Delta t}(v_i^n)_k + \frac{1}{2\Delta t}(v_i^{n-1})_k + \frac{1}{|\Omega_k|}\sum_{m=1}^{4} \hat{v}_{im}|_{\text{upwind}}\, V_m^s\, |\Gamma_k^m| +$$

$$+\frac{1}{|\Omega_k|}\sum_{m=1}^{4} p_m^s\, {}^i n_k^m |\Gamma_k^m| = \frac{1}{\text{Re}^{(\theta)}|\Omega_k|}\sum_{m=1}^{4} \eta(\dot{\gamma}(v^n))_m^{(\theta)} \left(\frac{\partial \hat{v}_i}{\partial x_j}\bigg|_{\Gamma_k^m} + \frac{\partial v_j^s}{\partial x_i}\bigg|_{\Gamma_k^m} \right) {}^j n_k^m |\Gamma_k^m|, \quad (4.152)$$

$$\sum_{m=1}^{4} \frac{\partial \Psi}{\partial \boldsymbol{n}_k^m}|\Gamma_k^m| = \sum_{m=1}^{4} \hat{v}_{im} \cdot {}^i n_k^m |\Gamma_k^m| \equiv \sum_{m=1}^{4} \hat{V}_m |\Gamma_k^m|, \quad (4.153)$$

$$(v_i^{s+1})_k = (\hat{v}_i)_k - \frac{1}{|\Omega_k|}\sum_{m=1}^{4} \Psi_m \cdot {}^i n_k^m |\Gamma_k^m|, \quad (4.154)$$

$$(p^{s+1})_k = (p^s)_k + \alpha \frac{3}{2\Delta t}(\Psi)_k, \quad (4.155)$$

$$V_m^{s+1} = \hat{V}_m - \frac{\partial \Psi}{\partial \boldsymbol{n}_k^m}, \quad (4.156)$$

where $\hat{V}_m$ is the intermediate face-normal velocity on the m-th face Γ_k^m of the tetrahedral control volume $\Omega_k \in \mathcal{M}$. Note that the values of the face-normal velocity V_m^{s+1} computed with the help of Eq. (4.156) are used as the values of face-normal velocity V_m^s in Eq. (4.152) at the next inner iteration level.

To be able to carry out numerical computations according to Eqs. (4.152)–(4.156), it is necessary to determine the values of $\hat{v}_{im}|_{\text{upwind}}$, p_m^s, $\hat{v}_{im}$, Ψ_m, and the derivatives $\frac{\partial \Psi}{\partial \boldsymbol{n}_k^m}$, $\frac{\partial \hat{v}_i}{\partial x_j}\Big|_{\Gamma_k^m}$, $\frac{\partial v_j^s}{\partial x_i}\Big|_{\Gamma_k^m}$ on the m-th face Γ_k^m of the control volume Ω_k. In this work, the computation of $\hat{v}_{im}|_{\text{upwind}}$ is based on the scheme

$$\hat{v}_{im}|_{\text{upwind}} = \frac{1}{2}\Big((\hat{v}_i)_L + (\hat{v}_i)_R\Big) - \frac{1}{2}\,\beta \cdot \text{sgn}(V_m^s)\Big((\hat{v}_i)_R - (\hat{v}_i)_L\Big), \quad (4.157)$$

where $\beta \in [0,1]$, 'sgn' denotes the sign function, $(\hat{v}_i)_L$ and $(\hat{v}_i)_R$ are the intermediate velocity vector components defined in the centres of the adjacent control volumes Ω_L and Ω_R, respectively, see Fig. 4.12. The remaining values and derivatives on the face Γ_k^m are determined with the help of the interpolation method, as shown in Appendix B.

For the above described stabilised projection method, the non-dimensional boundary conditions at the domain boundary $\partial\Omega_h$ are implemented as follows:

- *inlet* $\Gamma_k^m \subset \partial\Omega_{hI}$: We prescribe Dirichlet boundary conditions for the velocity vector components $\hat{v}_{im}$ and zero derivatives of velocity vector components

$$\hat{v}_{im} = v_{iI}, \quad \frac{\partial \hat{v}_i}{\partial x_j}\bigg|_{\Gamma_k^m} = 0, \quad i,j = 1,2,3, \quad (4.158)$$

  where v_{iI} are the given dimensionless components of the velocity vector $\boldsymbol{v}_I$ and the face-normal velocity $\hat{V}_m^I$ on the face Γ_k^m is computed as $\hat{V}_m^I = v_{iI} \cdot {}^i n_k^m$. The normal

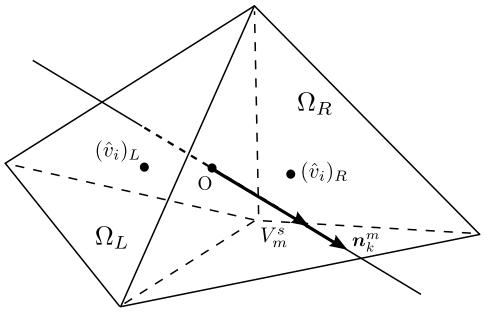

Fig. 4.12. Values of $(\hat{v}_i)_L$ and $(\hat{v}_i)_R$ defined in centres of two adjacent tetrahedral control volumes Ω_L, Ω_R.

derivative of the pressure correction function Ψ on the border face Γ_k^m is

$$\left.\frac{\partial \Psi}{\partial \boldsymbol{n}_k^m}\right|_{\Gamma_k^m} = 0. \tag{4.159}$$

- *rigid and impermeable wall* $\Gamma_k^m \subset \partial\Omega_{hW}$: Because of the non-slip boundary condition, all velocity components $\hat{v}_{im}$ on the border face Γ_k^m are set equal to zero

$$\hat{v}_{im} = 0\,, \tag{4.160}$$

leading to a zero value of the face-normal velocity $\hat{V}_m^W = \hat{v}_{im} \cdot {}^i n_k^m = 0$. Similarly to the inlet boundary, a zero normal derivative of the pressure correction function Ψ is prescribed at the wall

$$\left.\frac{\partial \Psi}{\partial \boldsymbol{n}_k^m}\right|_{\Gamma_k^m} = 0. \tag{4.161}$$

- *outlet* $\Gamma_k^m \subset \partial\Omega_{hO}$: For the following type of boundary, we apply

$$p_m = p_O, \quad \left.\frac{\partial \hat{v}_i}{\partial x_j}\right|_{\Gamma_k^m} = 0, \quad i,j = 1,2,3, \tag{4.162}$$

where p_O is the given dimensionless value of the outlet pressure. For the pressure correction function on the border face Γ_k^m, we prescribe the Dirichlet boundary condition

$$\Psi_m = 0. \tag{4.163}$$

Because of reasons already mentioned in Section 4.4.1, the face-normal velocity V_m^{s+1} on the face $\Gamma_k^m \subset \partial\Omega_{hO}$ must be computed according to Eq. (4.131) with $n \equiv s$.

Boundary conditions (4.158), (4.160) and (4.162) are used for the solution of Eq. (4.152), while Eqs. (4.159), (4.161) and (4.163) are applied to the solution of the Poisson equation for the pressure correction function (4.153).

In blood flow simulations, where the outlet pressure varies with time or is, for example, computed via a lumped parameter model (see Appendix C), the time variations of the Dirichlet outlet boundary condition for pressure $(4.162)_1$ may be the cause of computational instabilities during the solution of Eq. (4.152), especially if a large time step Δt is chosen. For example, when a time-dependent outlet pressure is prescribed, discontinuities in the computed pressure field may occur due to the fact that the inner process is initiated by the pressure at the time level n, but the prescribed outlet boundary condition uses the pressure corresponding to the next time level $(n+1)$. To avoid this difficulties, it is, therefore, advisable to correct the pressure values $(p^n)_k$, $k = 1,2,\ldots,N_{CV}$ in the whole computational domain before the begin of inner iterations at each time level

$$(p^n)_k \longrightarrow (p^n)_k + (p^n_{\mathrm{cor}})_k\,, \tag{4.164}$$

where $(p^n_{\mathrm{cor}})_k$ are the values of the correction pressure in the centre of each tetrahedral control volume $\Omega_k \in \mathcal{M}$. By using Eqs. (4.101) and (B.2), the correction pressure $(p^n_{\mathrm{cor}})_k$ is computed from the solution of the discrete form

$$\sum_{m=1}^{4} \frac{\partial p^n_{\mathrm{cor}}}{\partial \boldsymbol{n}^m_k} |\Gamma^m_k| = 0 \tag{4.165}$$

of the Laplace equation

$$\frac{\partial^2 p^n_{\mathrm{cor}}}{\partial x_i \partial x_i} = 0 \tag{4.166}$$

with the following boundary conditions:

- *outlet* $\Gamma^m_k \subset \partial\Omega_{hO}$:
  - time-dependent outlet pressure, i.e., $p_O = p_O(t)$: $p^n_{\mathrm{cor}} = p_O(t^{n+1}) - p_O(t^n)$;
  - constant outlet pressure, i.e., $p_O = \mathrm{const.}$: $p^n_{\mathrm{cor}} = 0$;
- *inlet* $\Gamma^m_k \subset \partial\Omega_{hI}$ and *impermeable and inelastic wall* $\Gamma^m_k \subset \partial\Omega_{hW}$: $\dfrac{\partial p^n_{\mathrm{cor}}}{\partial \boldsymbol{n}^m_k} = 0$.

The computation of the pressure correction p_{cor} according to Eq. (4.166) is motivated by Eqs. (4.137) and (4.138).

With the application of the interpolation method and corresponding boundary conditions, the numerical implementation of Eq. (4.152) leads to a system of three independent linear algebraic equations $\mathbf{A}_{\mathrm{NS}} \cdot \mathbf{x}_i = \mathbf{b}_i$, $i = 1, 2, 3$ for unknown intermediate velocity values $\mathbf{x}_i = [(\hat{v}_i)_1, \ldots, (\hat{v}_i)_k, \ldots, (\hat{v}_i)_{N_{CV}}]^T$, while Eq. (4.153) results in a system of linear algebraic equations $\mathbf{A}_{\mathrm{Poi}} \cdot \mathbf{x}_{\mathrm{Poi}} = \mathbf{b}_{\mathrm{Poi}}$ for unknown values $\mathbf{x}_{\mathrm{Poi}} = [(\Psi)_1, \ldots, (\Psi)_k, \ldots, (\Psi)_{N_{CV}}]^T$. The above-described numerical method is implemented in the software MATLAB (MathWorks, Natick, USA) in the same way as already mentioned in Section 4.4.1. The convergence process is monitored by means of a relative residuum res (4.132). The convergence criterion for the systems of Eqs. (4.152) and (4.153) is $res < 10^{-8}$, whereas for the inner iteration process it is given as

$$\frac{1}{N_{CV}} \|\boldsymbol{\Psi}\|_{l_2} < 10^{-2}. \tag{4.167}$$

Software verification

Similarly to Section 4.4.1, the computational algorithm described above is verified for blood flow simulations in a previously introduced model of distal anastomosis, see Fig. 4.8. However, compared to the previous numerical simulations, the present verification is focused on the computational ability of the developed software in the field of steady non-Newtonian blood flow. For this purpose, we refer to the works by Bertolotti *et al.* [11] and Chen *et al.* [20], which, among others, performed a comparison of axial velocity profiles for both Newtonian and non-Newtonian flows by considering three different flow rate ratios between the graft and native artery ($Q^{(G)} : Q^{(A)} = \frac{1}{2} : \frac{1}{2}, \frac{3}{4} : \frac{1}{4}, \frac{7}{8} : \frac{1}{8}$).

In this Ph.D. thesis, the comparison of numerical data is utilised for the anastomosis model described earlier and which in [20] is known as the '$D3$ case' (a model with grafting distance set to three times of the host artery diameter D). To enable a straightforward

comparison between our computed results and those published in [11, 20], the complete constitutive model for blood's non-Newtonian rheology, in this case the Carreau-Yasuda model, is adopted as well. The obtained results in the form of velocity profiles in two planes are shown in Fig. 4.13 together with those computed by the finite element solvers introduced in the two aforementioned papers. As apparent from Fig. 4.13, a relatively good agreement was achieved between our numerical results and those taken from [11,20]. Regarding the small, but visible differences, we assume that the main reason for their occurrence may be the use of qualitatively and quantitatively different computational meshes and the application of different numerical methods.

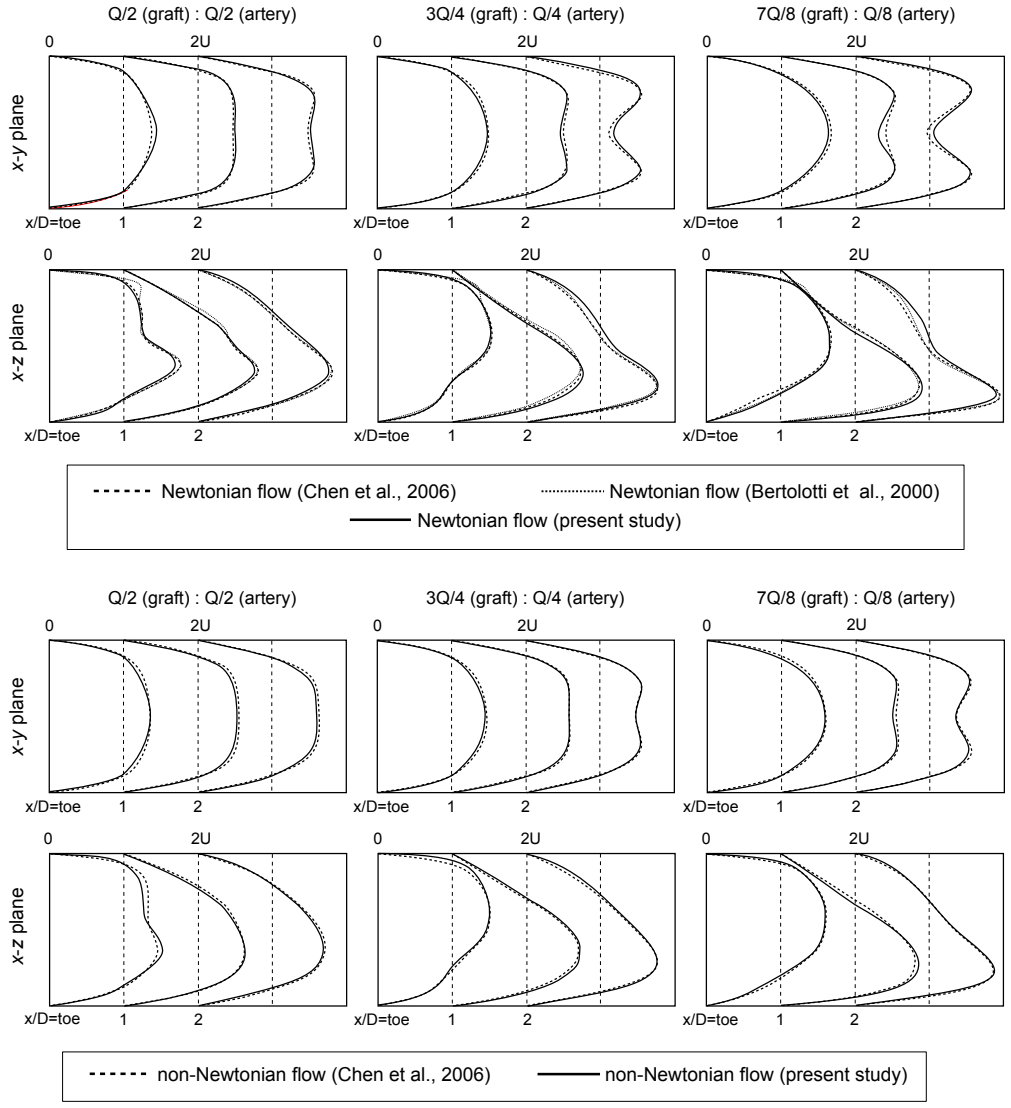

Fig. 4.13. Comparison of axial velocity profiles for the Newtonian (*top*) and non-Newtonian (*bottom*) flows in the x–z and x–y planes. The comparison is performed for three different ratios of inlet flow rate between the bypass graft and native artery $\left(Q^{(G)} : Q^{(A)} = \frac{1}{2} : \frac{1}{2}, \frac{3}{4} : \frac{1}{4}, \frac{7}{8} : \frac{1}{8}\right)$. Note that the Newtonian axial velocity profiles computed by Bertolotti *et al.* [11] are available only in the x–z plane.

Chapter 5

Numerical results

The chapter is designed to present the reader with a detailed analysis and discussion of numerical results obtained using in-house software, algorithms of which are based on the numerical methods described in the previous chapter. To achieve a better overview, the content of this chapter is divided into three sections according to the used

- blood viscosity model (Newtonian × non-Newtonian),
- bypass geometry (idealised × realistic/patient-specific),
- flow conditions (steady × pulsatile).

The simplifications and general assumptions made for the modelling purposes in this chapter were mentioned and justified at the beginning of Chapter 4.

5.1 Steady non-Newtonian blood flow in idealised bypass models

The main objective of this section is to perform an analysis of bypass hemodynamics under average flow conditions and to determine the importance of non-Newtonian blood rheology in selected idealised bypass models. Some of the numerical results obtained for Newtonian and non-Newtonian blood flows in coronary and femoral bypasses were presented at conferences [B.4–B.8] and published in peer-reviewed journals [A.1–A.3].

For the study of average flow conditions and blood viscosity models, an idealised in-plane bypass geometry with damaged native artery is chosen, Fig. 5.1. However, compared to other studies such as [11], where only a distal part of the bypass was considered, a complete bypass model based on the one introduced in [95] is applied. The main advantage of this geometry lies in the presence of both the proximal and distal anastomoses, avoiding so any potential errors arising from the prescription of unsuitable inlet conditions. Tab. 5.1 provides an overview of the main geometrical and flow parameters used for the coronary and femoral bypasses presented in this section. The remaining parameters such as the junction angle α and diameter ratio $D : d$ are

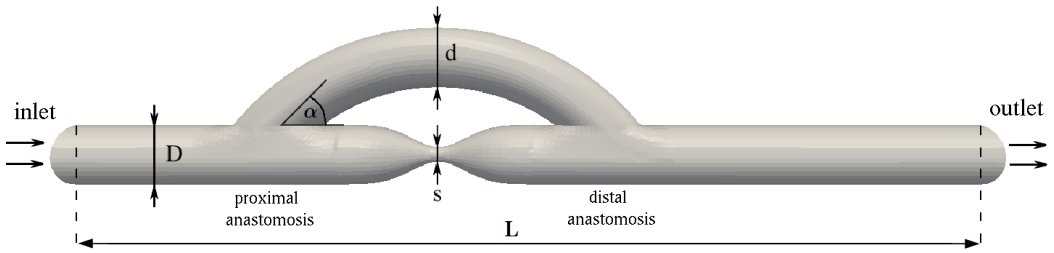

Fig. 5.1. Idealised bypass model. Parameters D and d denote the artery and graft diameters, respectively, L is the length of the native artery, and s is the diameter of the stenosed portion of the native artery.

bypass model	diameter D [m]	length L [m]	$\mathrm{Re}_{\mathrm{inlet}}$	type of arterial damage	number of cells
coronary	0.0033	0.05	230	occlusion ($s = 0D$)	195 840
				stenosis ($s = 0.25D$)	195 840
femoral	0.0068	0.10	125	occlusion ($s = 0D$)	187 248
				stenosis ($s = 0.25D$)	211 824

Tab. 5.1. Geometrical and flow parameters of idealised coronary and femoral bypasses denoted in Fig. 5.1. Here, $\mathrm{Re}_{\mathrm{inlet}}$ is the inlet Reynolds number taken from [38].

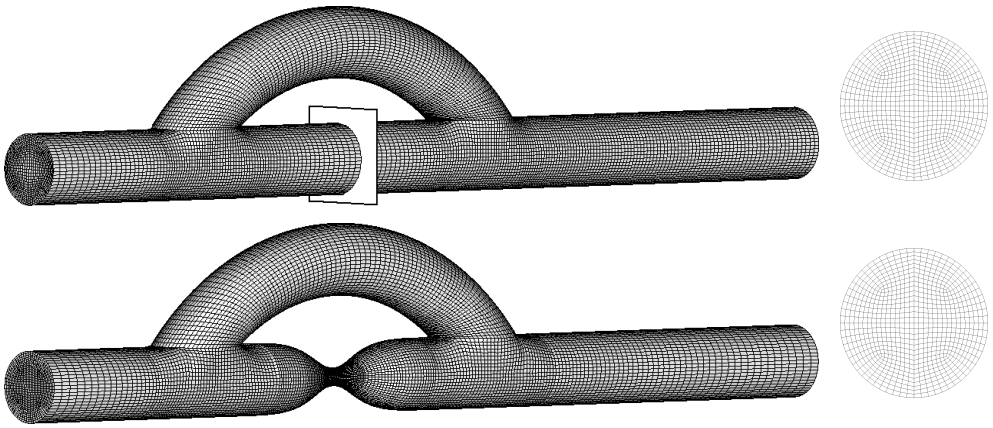

Fig. 5.2. Unstructured hexahedral computational mesh – coronary bypass model with occlusion (*top*) and 75% stenosis (*bottom*). Detailed views at the cross section area of the native artery (*right*).

set to correspond to average values regardless of the actual bypass type, i.e., $\alpha = 45°$ and $D : d = 1 : 1$ ($D = d$), Fig. 5.1. As apparent from Tab. 5.1, the damage of the native artery is considered to be either an occlusion (complete vessel blockage) or an 75% axisymmetric stenosis (shape described by the Gaussian function), see Fig. 5.2. The same figure shows examples of computational meshes for the occluded and stenosed coronary bypasses generated with the help of the commercial software package HyperMesh (Altair Engineering, Troy, USA). The number of hexahedral cells required to model each bypass type is listed in Tab. 5.1.

The objective of this section, which is the quantification of non-Newtonian effects, requires the blood to be treated as an incompressible generalised Newtonian fluid. For this purpose, the governing equations of blood flow (4.4)–(4.5) have to be coupled with an appropriate constitutive relation describing the shear-thinning behaviour of blood. Among the many viscosity models reviewed in Section 2.3, two well-known non-Newtonian models with appropriate parameters are chosen: the Carreau-Yasuda model (4.2) and the modified Cross model (4.3). The selection of two models is made in order to perform a quantitative as well as qualitative comparison of their properties. In addition, the blood is also modelled as a Newtonian fluid (4.1) with density $\varrho = 1050\,\mathrm{kg\,m^{-3}}$ so that the extent of the non-Newtonian behaviour under different flow conditions can be easily determined.

After taking into consideration all the necessary modelling assumptions listed and justified at the beginning of Chapter 4, the mathematical model for steady non-Newtonian blood flow is non-dimensionalised and modified in the sense of the artificial compressibility method (ACM), as described in Sections 4.1 and 4.3. The obtained conservative system of Navier-Stokes equations (4.36), (4.24), (4.37) and (4.27) or (4.29) is numerically solved using the cell-centred finite volume method formulated for unstructured hexahedral grids, see Section 4.3.1, and the classical explicit four-stage Runge-Kutta time-stepping scheme of fourth order accuracy in the fictitious time $\tilde{t}$ (4.83). To suppress any unwanted numerical oscillations and to stabilise the numerical solution, the Jameson's artificial viscosity (4.72)–(4.79) is used, as well. In accordance with Section 4.1, the following reference values required in the subsequent non-dimensionalisation of the governing equations are chosen

- for the coronary bypass models:

$$\left.\begin{array}{ll} \mathrm{Re}_{\,\mathrm{inlet}} = 230, & L_{ref} = 0.0033\,\mathrm{m}, \\ \varrho_{ref} = 1\,050\,\mathrm{kg\,m^{-3}}, & \eta^{(\theta)}_{ref} = 3.45 \times 10^{-3}\,\mathrm{Pa\,s},\ \theta = 0,1,2, \end{array}\right\} v_{ref} = 0.23\,\mathrm{m\,s^{-1}},$$

- for the femoral bypass models:

$$\left.\begin{array}{ll} \mathrm{Re}_{\,\mathrm{inlet}} = 125, & L_{ref} = 0.0068\,\mathrm{m}, \\ \varrho_{ref} = 1\,050\,\mathrm{kg\,m^{-3}}, & \eta^{(\theta)}_{ref} = 3.45 \times 10^{-3}\,\mathrm{Pa\,s},\ \theta = 0,1,2, \end{array}\right\} v_{ref} = 0.06\,\mathrm{m\,s^{-1}}.$$

As apparent from the reference values listed above, the reference dynamic viscosity $\eta^{(\theta)}_{ref}$, $\theta = 0,1,2$ is set equal for all three viscosity models considered in this section, i.e., for the Newtonian ($\theta = 0$) and both non-Newtonian ($\theta = 1,2$) ones. To enable better comparison between the viscosity models and bypass types considered in the present flow problem, the following boundary conditions in the dimensional form are prescribed:

- **inlet** $\partial\Omega_{hI}$ – fully developed 3D velocity profile specified according to the inlet Reynolds number $\mathrm{Re}_{\,\mathrm{inlet}}$ from Tab. 5.1

$$v_{1I}(r) = 2\,\bar{U}\left[1 - \left(\frac{2r}{D}\right)^2\right], \quad v_{2I} = v_{3I} = 0\,\mathrm{m\,s^{-1}},$$

  where $r = \sqrt{x_2^2 + x_3^2}$ denotes the distance from the artery centreline and $\bar{U} = \frac{\mathrm{Re}_{\,\mathrm{inlet}}\,\eta}{D\,\varrho}$ is the average inlet velocity computed in dependence on the type of the native artery (coronary artery: $0.23\,\mathrm{m\,s^{-1}}$, femoral artery: $0.06\,\mathrm{m\,s^{-1}}$);

- **outlet** $\partial\Omega_{hO}$ – constant pressure of 12 000 Pa corresponding to the average arterial pressure;

- **wall** $\partial\Omega_{hW}$ – non-slip boundary condition, i.e., $\boldsymbol{v} = \boldsymbol{0}$.

At corresponding boundaries of the computational domain $\Omega_h \subset \mathbb{R}^3$, the remaining primitive variables are extrapolated from the flow field. The convergence history of the iterative process is monitored with the dimensionless relative residuum *res* defined by Eq. (4.86) and shown in Fig. 5.3 for selected simulations. On the basis of several preliminary computations, the constant β_2 of the Jameson's artificial viscosity, see Eqs. (4.74)–(4.79), is set equal to 0.005 and 0.0005 for the Newtonian and non-Newtonian flows, respectively. Lastly, note that all numerical results presented in this section are shown in the dimensional form using the reference values mentioned above.

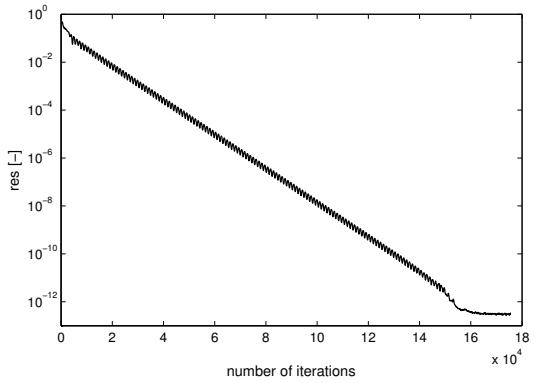

a) occluded coronary artery, non-Newtonian fluid (CY, $\beta_2 = 0.0005$)

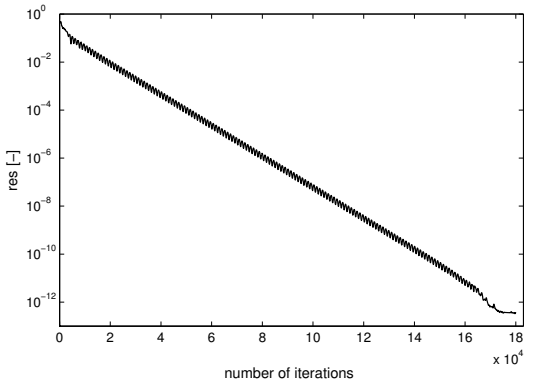

b) occluded coronary artery, non-Newtonian fluid (C, $\beta_2 = 0.0005$)

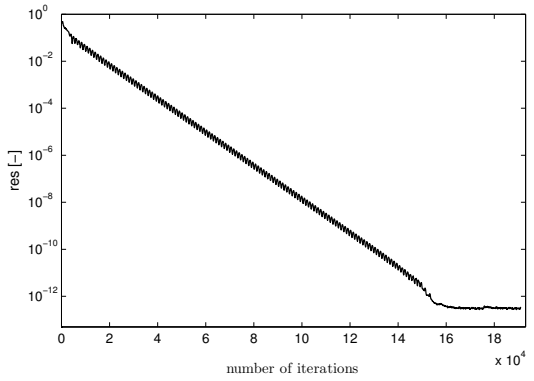

c) occluded femoral artery, Newtonian fluid ($\beta_2 = 0.005$)

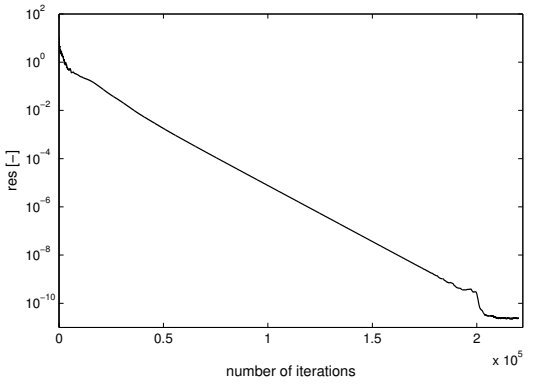

d) stenosed femoral artery, non-Newtonian fluid (CY, $\beta_2 = 0.0005$)

Fig. 5.3. Convergence history for selected blood flow simulations (CY = Carreau-Yasuda model, C = modified Cross model).

5.1.1 Analysis of blood flow

In order to enable some form of comparison between the results obtained for the coronary and femoral bypasses, the analysis of the Newtonian and non-Newtonian flow fields will be based on longitudinal slices of selected velocity profiles and velocity iso-lines and secondary flow streamlines displayed at nine selected cross-sections (A–H). The location of each cross-section is indicated in Fig. 5.4 for both types of arterial damage.

A) Coronary bypass

From the Newtonian velocity profiles in Fig. 5.5, it is quite apparent that the blood flow in the occluded coronary bypass model is in some aspects similar to that in the stenosed model (e.g., at the proximal anastomosis). On the other hand, there are several noticeable differences, especially in the second half of the graft and around the distal anastomosis. These differences can be clearly attributed to the various types of arterial damage, which determine the amount of blood going through the graft and consequently influence the velocity distribution in relevant parts of both bypass models. This is particularly the case of the distal anastomosis, which is either characterised by skewed

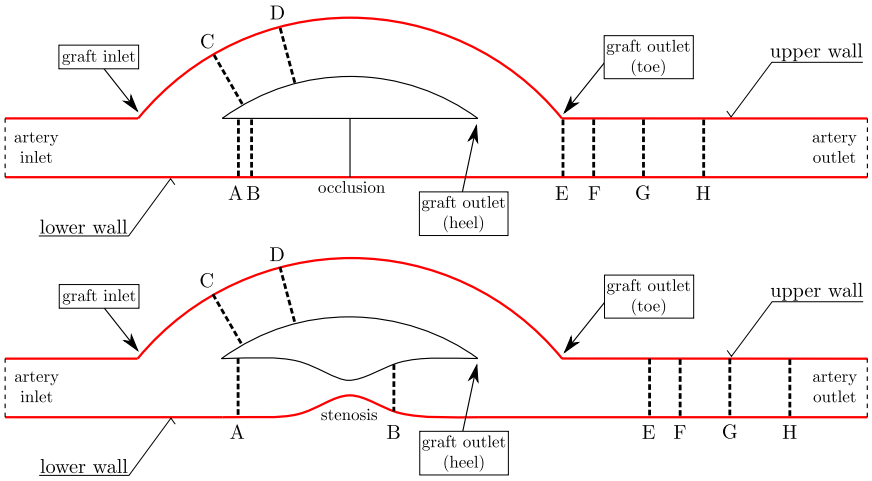

Fig. 5.4. Position of cross-sections A–H along the occluded (*top*) and stenosed (*bottom*) bypass models. The upper and lower walls used for the visualisation of shear stress stimulation are marked in red.

velocity profiles with weak back flow near the lower arterial wall, Fig. 5.5a, or is filled with double velocity profiles, Fig. 5.5b. In both cases, the resulting flow field is affected by the absence/presence of the residual flow through the arterial narrowing.

Based on a preliminary analysis of the non-Newtonian velocity profiles shown in Fig. 5.5, several observations can be made. Among them, it is possible to mention the relatively small decrease in peak velocity in the occluded bypass when non-Newtonian rheology is considered, Fig. 5.5a. This behaviour is in clear contrast to the considerably more viscous non-Newtonian flow in the stenosed model, Fig. 5.5b, which can be attributed to lower shear rates associated with the flow distribution between the arterial stenosis and graft. Another observation worth mentioning is that the non-Newtonian effects in the stenosed bypass model also exhibit an apparent dependence on the viscosity model. In other words, the range of shear rate present in this bypass model enables the quantitative differences between the Carreau-Yasuda model and the modified Cross model (Fig. 4.1) to become apparent: In certain areas, the Carreau-Yasuda model yields a higher viscosity than the modified Cross model (for example, compare the velocity profiles downstream from the distal anastomosis in Fig. 5.5b).

Another insight into the importance of non-Newtonian rheology in the two considered coronary bypass models can be gained from the velocity iso-lines and secondary flow streamlines listed in Tab. 5.2 and Tab. 5.3. According to them, a comparison of the Newtonian and non-Newtonian velocity patterns computed for the occluded bypass, Tab. 5.2 (left), yields no significant diferences. Although this result supports our previous observation of rather negligible non-Newtonian effects in this bypass model, it should be noted that the secondary flow streamlines show some deviation in the first half of the graft, see cross-sections C a D in Tab. 5.2 (right). As for the non-Newtonian blood flow in the stenosed bypass, several relevant changes in hemodynamics become apparent by referring to the Newtonian flow characteristics shown in Tab. 5.3. Besides the blunt velocity profiles and reduced stream skewness (see velocity iso-lines in cross-sections C–

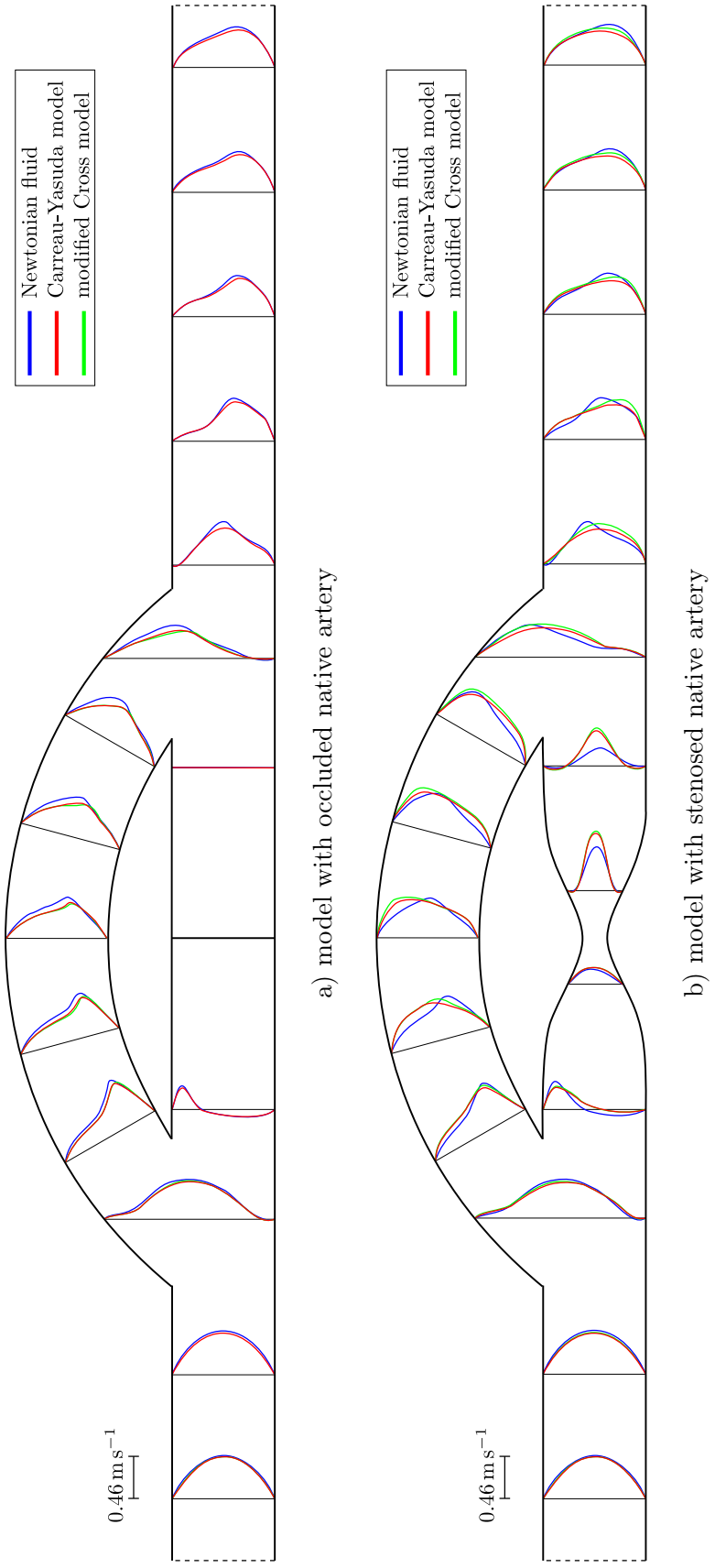

Fig. 5.5. 2D slices of Newtonian and non-Newtonian velocity profiles at selected cross-sections of the coronary bypass model.

H), which are two of the most obvious demonstrations of non-Newtonian rheology, a suppression of recirculation zones takes place, as well (see, for example, the lower part of the cross-section A). In this case, the introduction of the shear-dependent viscosity into the flow model also seems to significantly affect the secondary motion of the blood,

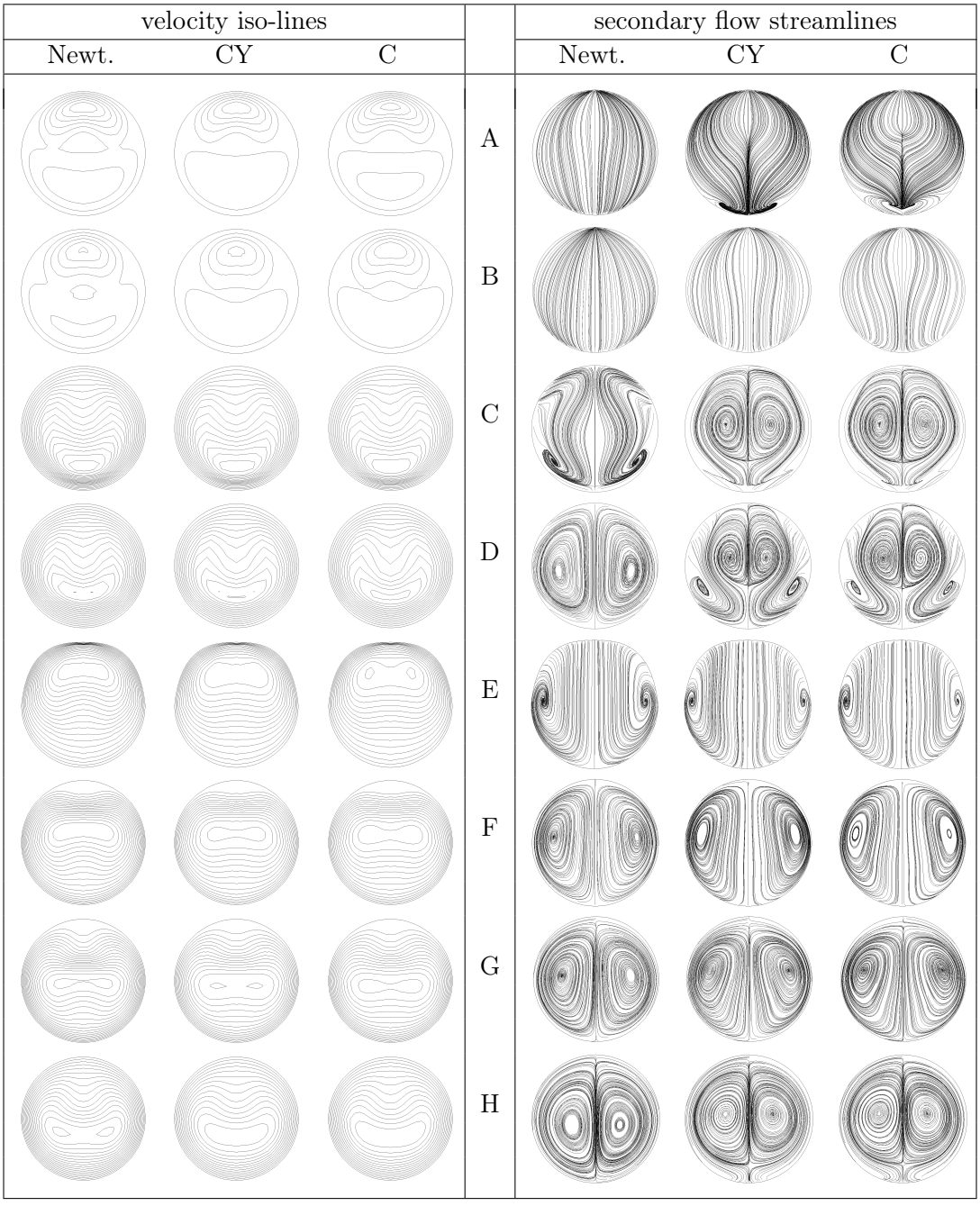

Tab. 5.2. Coronary bypass with occluded native artery – velocity iso-lines and secondary flow streamlines at selected cross-sections A–H, Fig. 5.4 (*top*). (Newt. = Newtonian fluid, CY = Carreau-Yasuda model, C = modified Cross model)

as apparent from cross-sections A, C and D in Tab. 5.3 (right).

B) Femoral bypass

Comparing the non-Newtonian effects observed in the occluded femoral bypass, Fig. 5.6a, with those in the coronary model, Fig. 5.5a, an increase in non-Newtonian flow charac-

velocity iso-lines				secondary flow streamlines		
Newt.	CY	C		Newt.	CY	C
			A		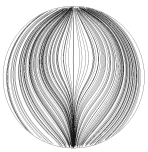	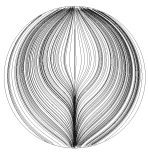
			B	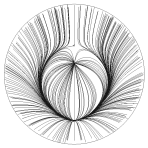	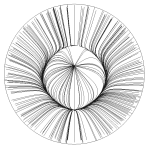	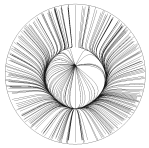
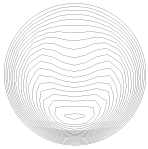	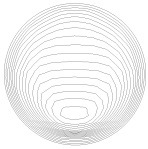	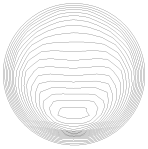	C			
		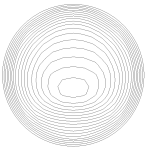	D		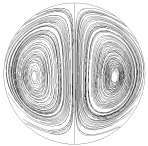	
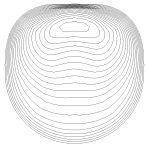	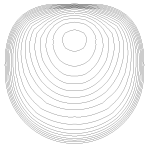		E			
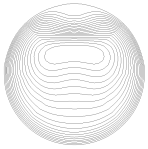	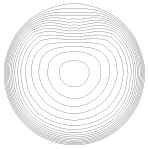	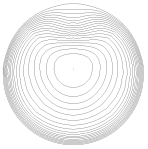	F			
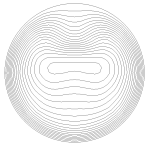		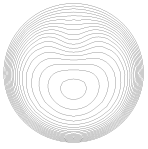	G			
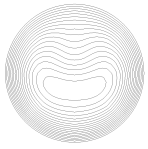			H		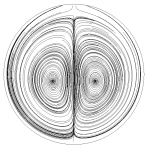	

Tab. 5.3. Coronary bypass with stenosed native artery – velocity iso-lines and secondary flow streamlines at selected cross-sections A–H, Fig. 5.4 (*bottom*). (Newt. = Newtonian fluid, CY = Carreau-Yasuda model, C = modified Cross model)

teristics can be noted. The differences, which can be clearly attributed to the lower inlet Reynolds number applied in the case of the femoral bypass (see Tab. 5.1), are particularly obvious in the region before the occlusion and in the first half of the graft. For example, according to the velocity iso-lines in cross-sections A and B, Tab. 5.4 (left), the large recirculation, presiding before the arterial blockage and characteristic for the Newtonian flow, disappears completely when non-Newtonian rheology is introduced. Another feature associated with higher blood viscosity includes blunter and less skewed velocity profiles, which are well apparent from cross-sections C–H. By contrast, the secondary flow does not appear to be overly affected by the non-Newtonian behaviour, Tab. 5.4 (right), especially in the graft and downstream from the distal anastomosis (cross-sections C–H). The only significant exception to this rule is the area before the occlusion (cross-sections A and B), where the suppression of recirculation causes weakening or even ceasing of secondary motion.

Analogously to the occluded femoral bypass, the non-Newtonian blood flow in the model with stenosed native artery, Fig. 5.6b, exhibits some features dissimilar to those found in its coronary counterpart, Fig. 5.5b. However, compared to the occluded models, the differences between the Newtonian and non-Newtonian velocity profiles are now rather small. Some indication of increased viscosity can be noted at the proximal anastomosis and around the arterial narrowing, where it takes the characteristic form of a partly suppressed recirculation zone and several reduced peak velocities, see Fig. 5.6b. In accordance with the occluded femoral bypass, the introduction of non-Newtonian rheology brings changes not only to the velocity distribution, but also influences the strength of the secondary flow, as apparent from cross-sections A and B in Tab. 5.5. Besides the small changes in velocity patterns visible, for example, in cross-sections E–H, Tab. 5.5 (left), the overall primary and secondary flows do not appear to be significantly affected by the shear-dependent viscosity in any way.

5.1.2 Wall shear stress distribution

In Section 3.3.2, we addressed the problem of graft failure resulting from intimal thickening, triggering of which is closely related to disturbed hemodynamics and inadequate shear stress stimulation of vascular endothelial cells. With this in mind, it is, therefore, appropriate to perform an analysis of wall shear stress (WSS) distribution in the four considered coronary and femoral bypasses, in addition to the analysis of flow fields carried out in the previous section. For this purpose, we introduce the normalised WSS magnitude in the following form:

$$\overline{\mathrm{WSS}} = |\boldsymbol{\tau}_W|/\tau_m, \tag{5.1}$$

where $|\boldsymbol{\tau}_W|$ is the WSS magnitude (5.3) and $\tau_m = \frac{8\eta_{ref}^2 \,\mathrm{Re}_{\mathrm{inlet}}}{\varrho_{ref}\, L_{ref}^2}$ is the WSS of Poiseuille flow determined on the basis of the inlet Reynolds number listed in Tab. 5.1. For the coronary and femoral arteries, we get $\tau_m = 1.9153\,\mathrm{Pa}$ and $\tau_m = 0.2451\,\mathrm{Pa}$, respectively.

In order to provide a qualitative as well as quantitative comparison of the WSS values computed for the steady flow conditions, the distribution of this hemodynamical wall parameter is visualised in two forms: as colour maps with different views of the bypass

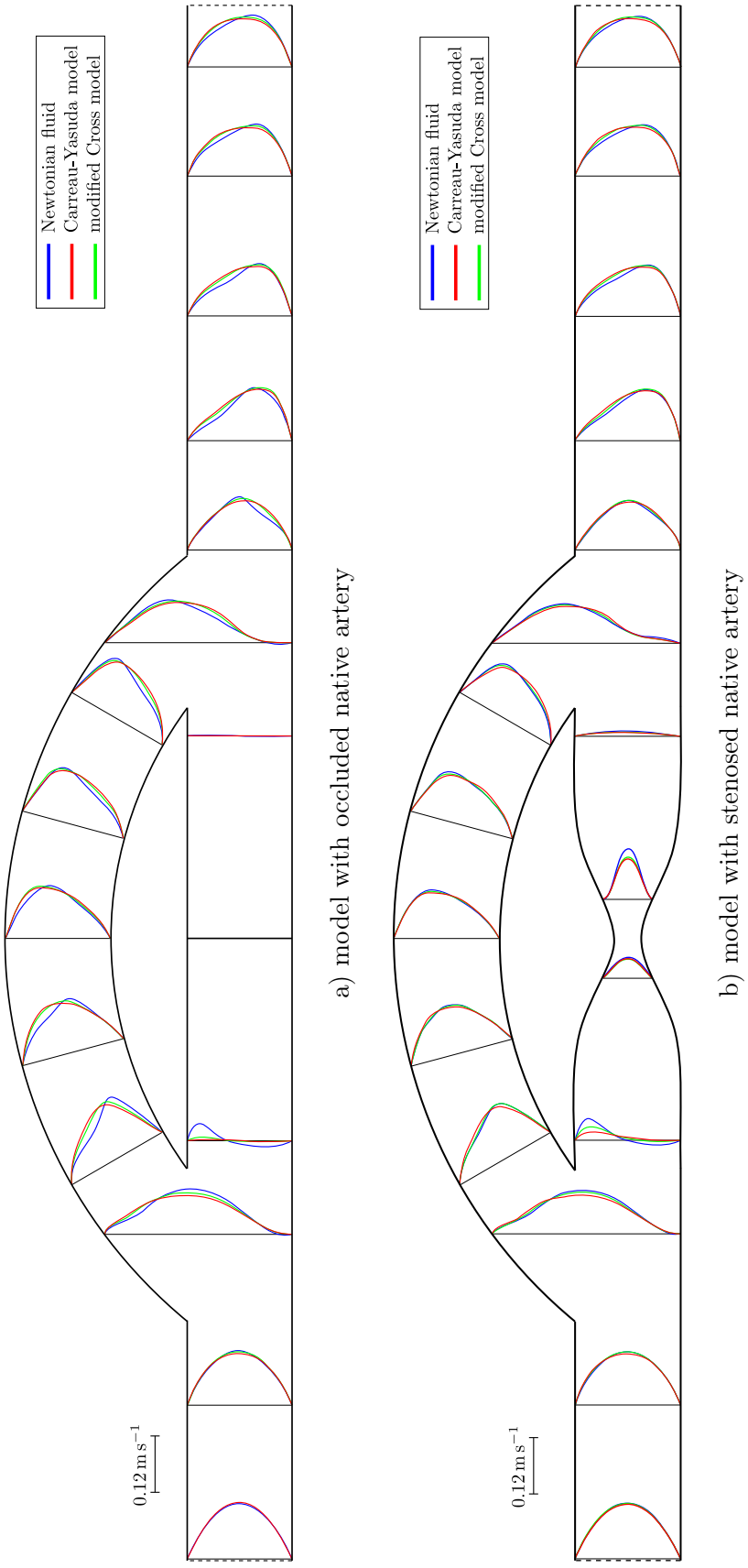

Fig. 5.6. 2D slices of Newtonian and non-Newtonian velocity profiles at selected cross-sections of the femoral bypass model.

models and as graphs, giving a detailed insight into the influence of non-Newtonian rheology on the shear stress stimulation in relevant parts of the four bypass models.

A) Coronary bypass

From Fig. 5.7a and Fig. 5.8a, it is possible to deduce that the complex bypass geom-

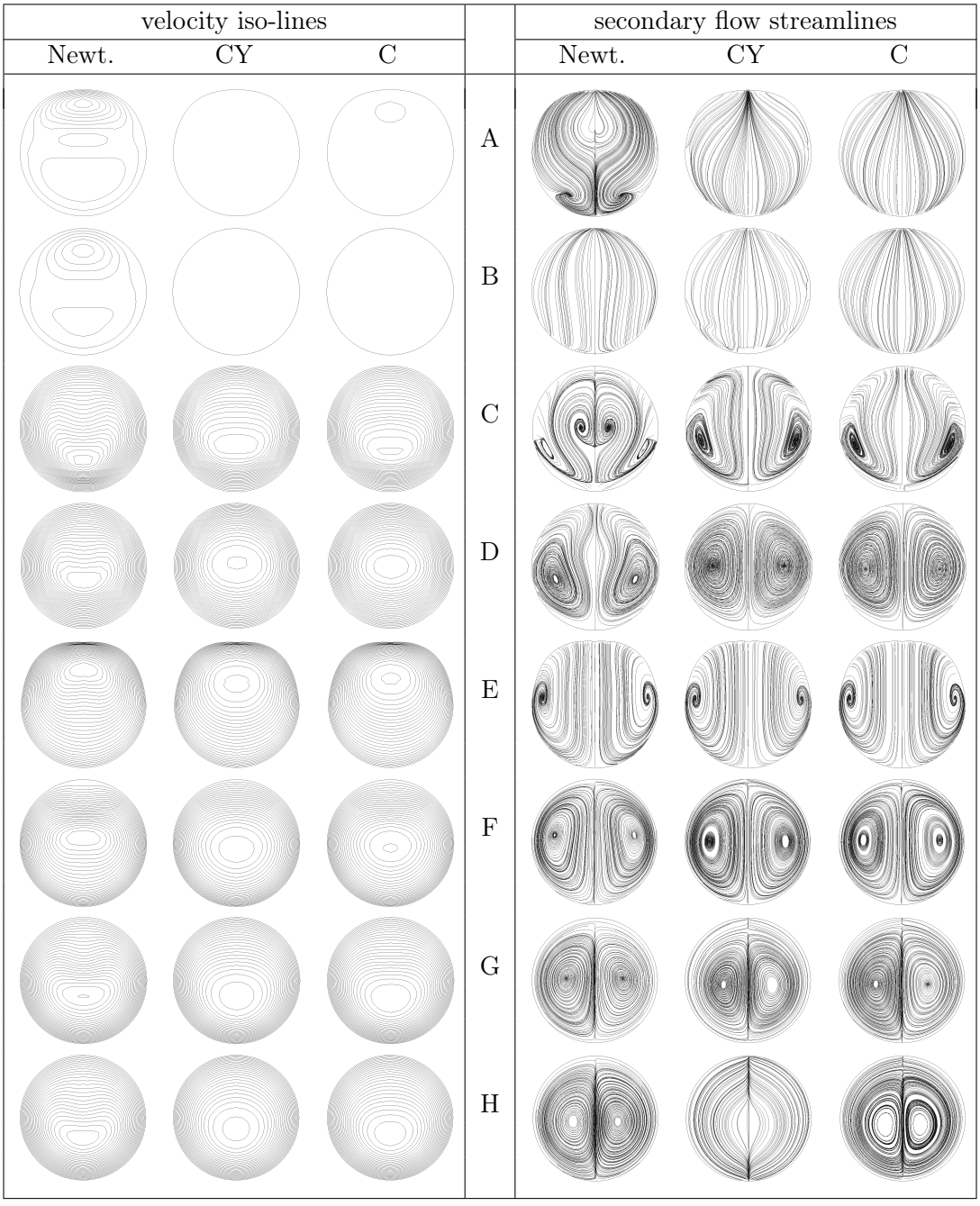

Tab. 5.4. Femoral bypass with occluded native artery – velocity iso-lines and secondary flow streamlines at selected cross-sections A–H, Fig. 5.4 (top). (Newt. = Newtonian fluid, CY = Carreau-Yasuda model, C = modified Cross model)

etry with either occluded or stenosed native artery is associated with a characteristic distribution pattern of WSS values. Both colour maps indicate three areas that are especially worth noting: the large zone surrounding the arterial blockage/narrowing with $\overline{\mathrm{WSS}} < 0.5$ and the proximal and distal anastomoses distinctive with their localised shear

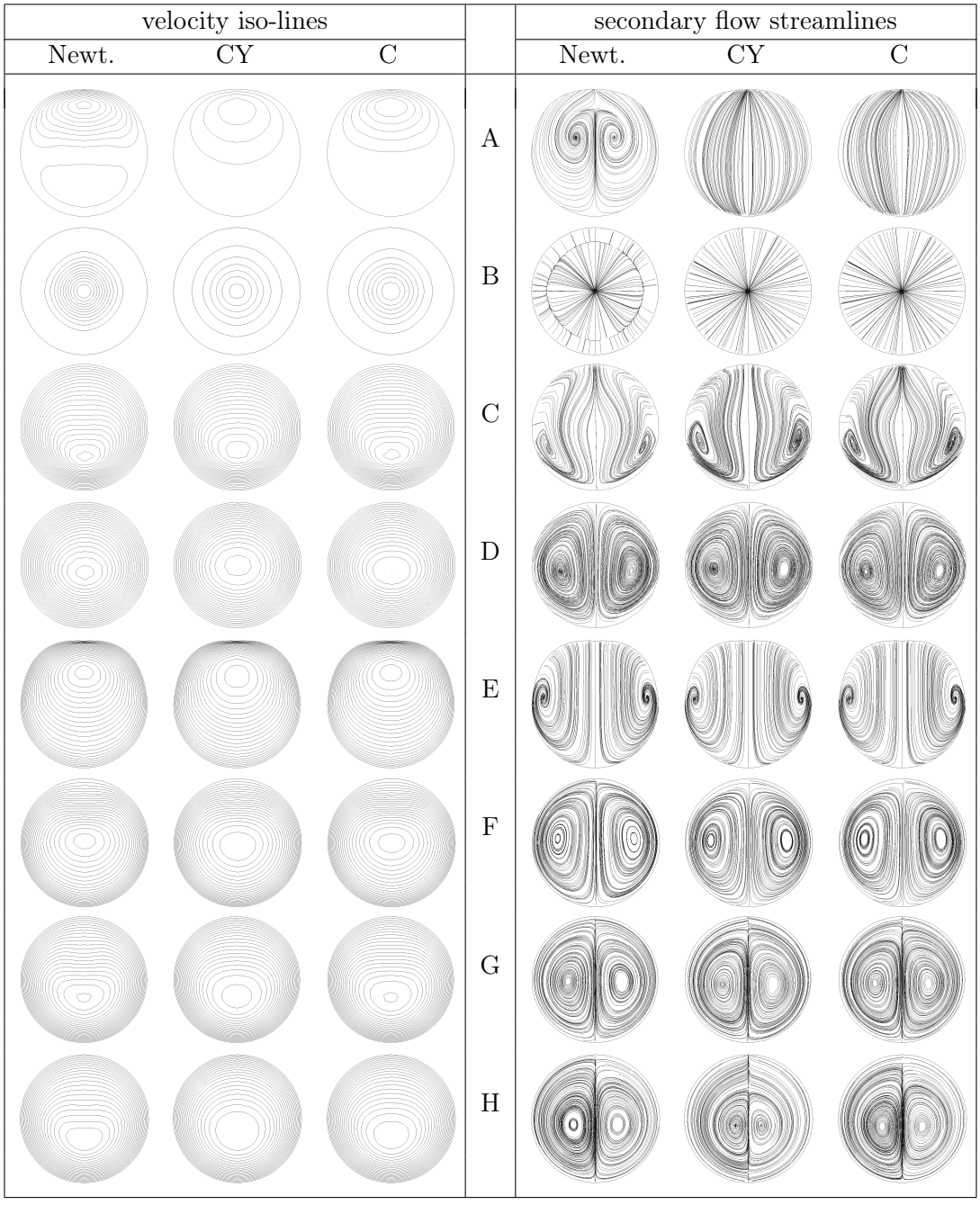

Tab. 5.5. Femoral bypass with stenosed native artery – velocity iso-lines and secondary flow streamlines at selected cross-sections A–H, Fig. 5.4 (bottom). (Newt. = Newtonian fluid, CY = Carreau-Yasuda model, C = modified Cross model)

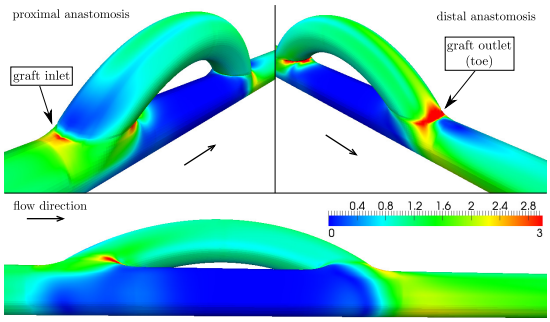

a) Newtonian flow

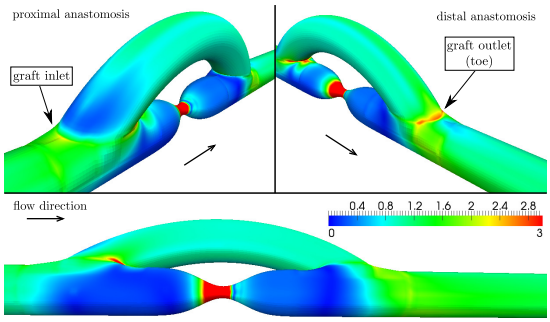

a) Newtonian flow

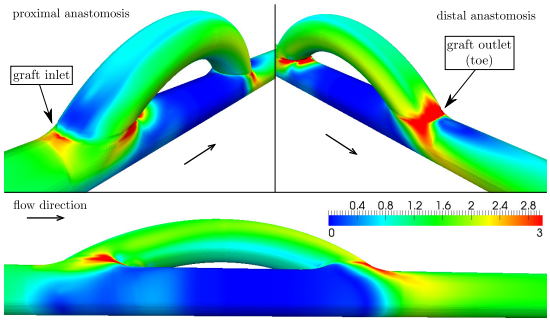

b) non-Newtonian flow (CY model)

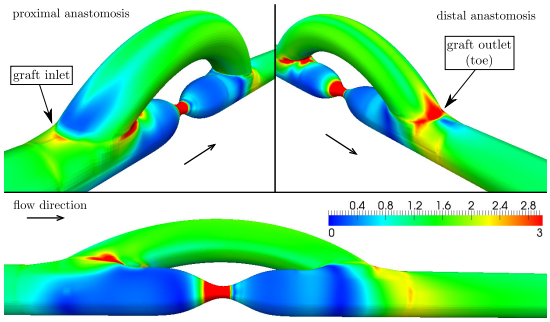

b) non-Newtonian flow (CY model)

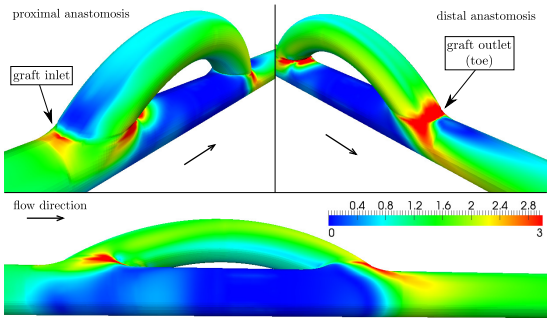

c) non-Newtonian flow (C model)

Fig. 5.7. Occluded coronary bypass – distribution of the normalised WSS magnitude

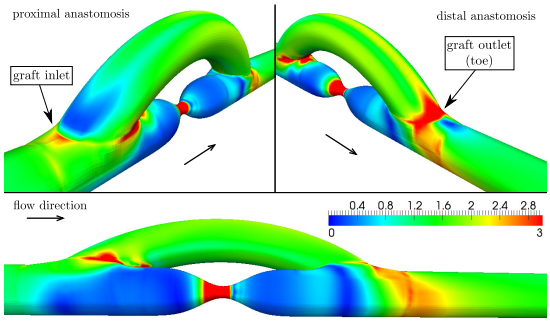

c) non-Newtonian flow (C model)

Fig. 5.8. Stenosed coronary bypass – distribution of the normalised WSS magnitude

stress increase/decrease. Since shear-dependent viscosity can considerably affect the flow field, it can also change the shear stress stimulation in certain parts of the bypass models, as apparent from Fig. 5.7b,c and Fig. 5.8b,c. One of the most obvious changes takes place at the distal anastomosis (toe), where the region with $\overline{\mathrm{WSS}} > 2.5$ doubles its size and extends farther along the suture line and down to the arterial floor. This behaviour is particularly noticeable in Fig. 5.8c, where $\overline{\mathrm{WSS}}$ increases from values around 1.4 up to 2.7. Although not so extensive, something similar occurs at the proximal anastomosis, where it affects the shear stress stimulation along the suture line.

A quantitative comparison of the normalised WSS magnitude for the Newtonian and two non-Newtonian flows can be gained from the graphs in Fig. 5.9. For example, ac-

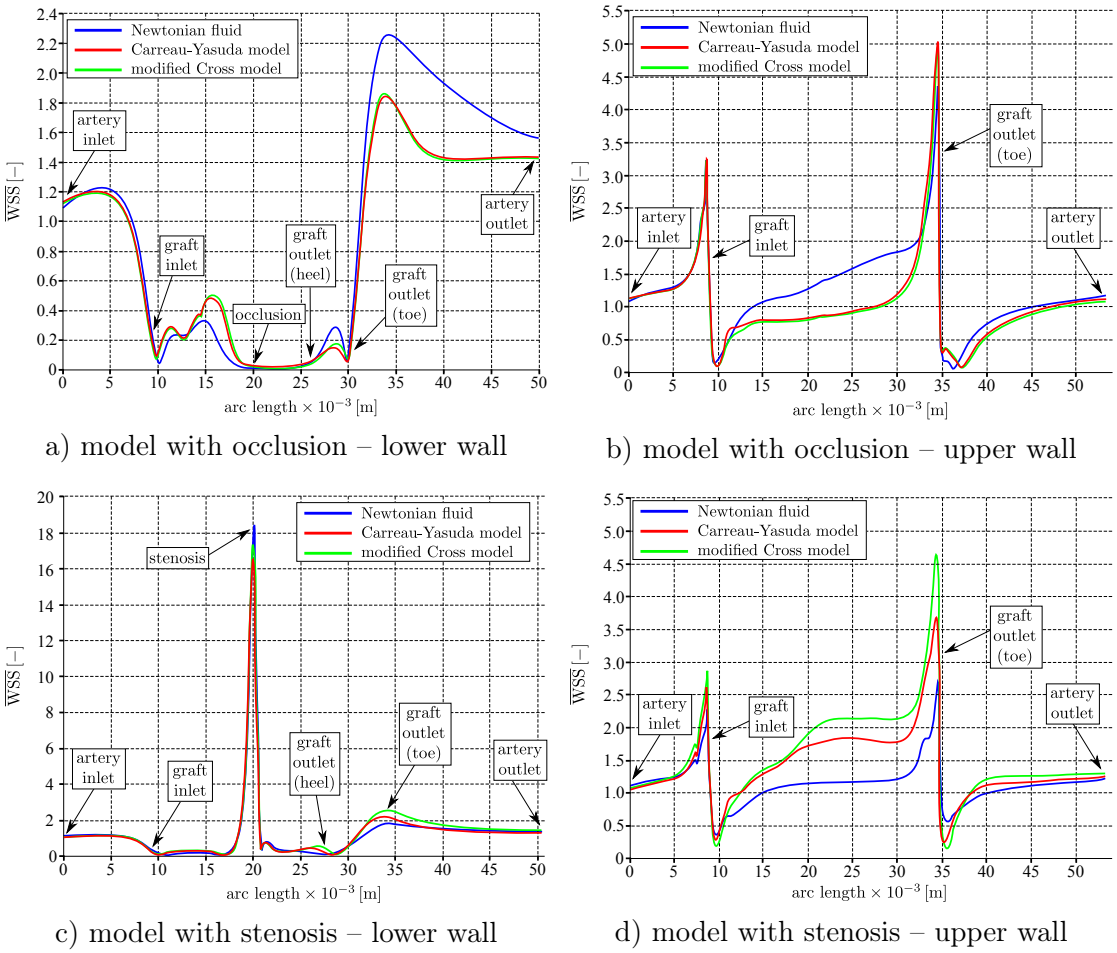

a) model with occlusion – lower wall

b) model with occlusion – upper wall

c) model with stenosis – lower wall

d) model with stenosis – upper wall

Fig. 5.9. Normalised WSS magnitude $\overline{\mathrm{WSS}}$ in the occluded (*top*) and stenosed (*bottom*) coronary bypass models. For the position of the upper and lower walls, see Fig. 5.4.

cording to Fig. 5.9a,b, the lower and upper walls of the occluded bypass appear to be stimulated the same way in all three flows, with only two distinct exceptions: the arterial floor and ceiling (areas opposite or downstream of the distal anastomosis, see Fig. 3.16). In both cases, the Newtonian flow demonstrates higher shear stress stimulation than the two non-Newtonian flows. At this point, it should be noted that this observation is in agreement with our conclusion drawn on the basis of the velocity profiles shown in Fig. 5.5a. Namely, that the non-Newtonian effects in the occluded coronary bypass model are relatively small, except at the distal anastomosis. By contrast, the development of WSS at the lower and upper walls of the stenosed bypass shows not only differences between the Newtonian and non-Newtonian flows, but also between the two applied viscosity models, Fig. 5.9c,d. This behaviour, which was noted previously in Section 5.1.1, is pronounced in the area opposite the distal anastomosis, Fig. 5.9c, and along the upper wall of the graft continuing downstream to the outlet of the native artery, Fig. 5.9d.

B) Femoral bypass

Similarly to the coronary models discussed previously, the occluded and stenosed femoral

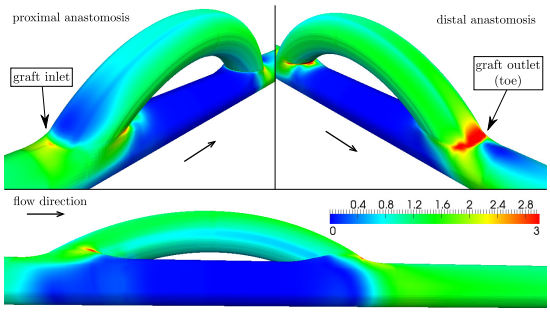

a) Newtonian flow

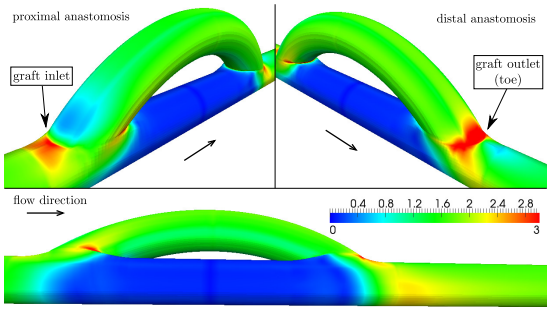

b) non-Newtonian flow (CY model)

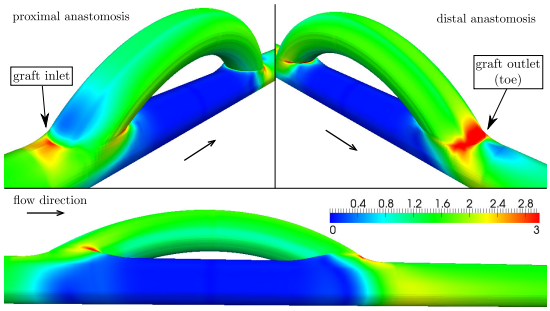

c) non-Newtonian flow (C model)

Fig. 5.10. Occluded femoral bypass – distribution of the normalised WSS magnitude

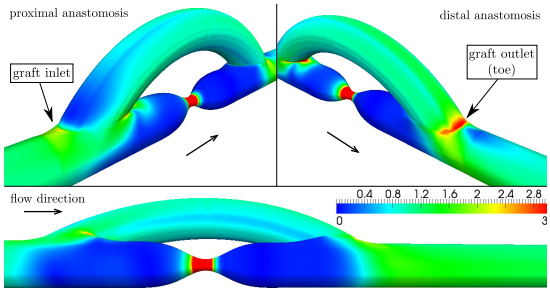

a) Newtonian flow

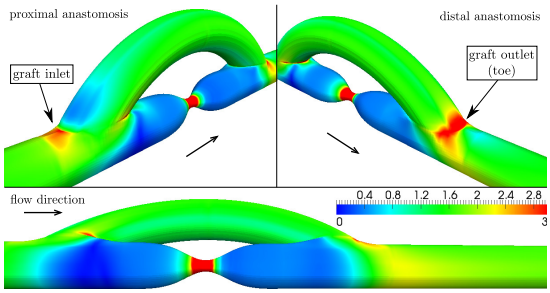

b) non-Newtonian flow (CY model)

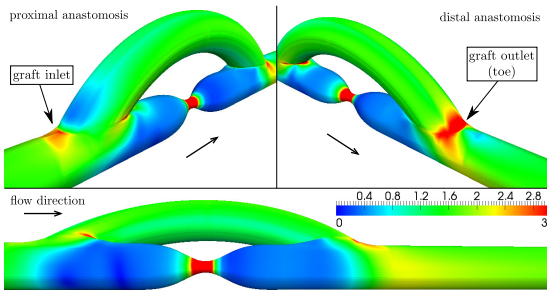

c) non-Newtonian flow (C model)

Fig. 5.11. Stenosed femoral bypass – distribution of the normalised WSS magnitude

bypasses show a distinct geometry-dependent distribution of the normalised WSS magnitude, Fig. 5.10a and Fig. 5.11a. In other words, the presence of very low ($\overline{\text{WSS}} < 0.5$) and/or very high ($\overline{\text{WSS}} > 2.5$) shear stress values is once again associated with the disturbed blood flow around the occlusion/stenosis and at both proximal and distal anastomoses. According to Fig. 5.10b,c and Fig. 5.11b,c, a change to this form of shear stress stimulation can be brought by the non-Newtonian rheology, which shows a tendency to affect at least two of the above mentioned areas (low shear stress appears to prevail around the damaged part of the native artery regardless of the viscosity model under consideration).

The extent, to which the blood's non-Newtonian behaviour changes the shear stress distribution, can be shown on the example of the occluded femoral bypass, Fig. 5.10.

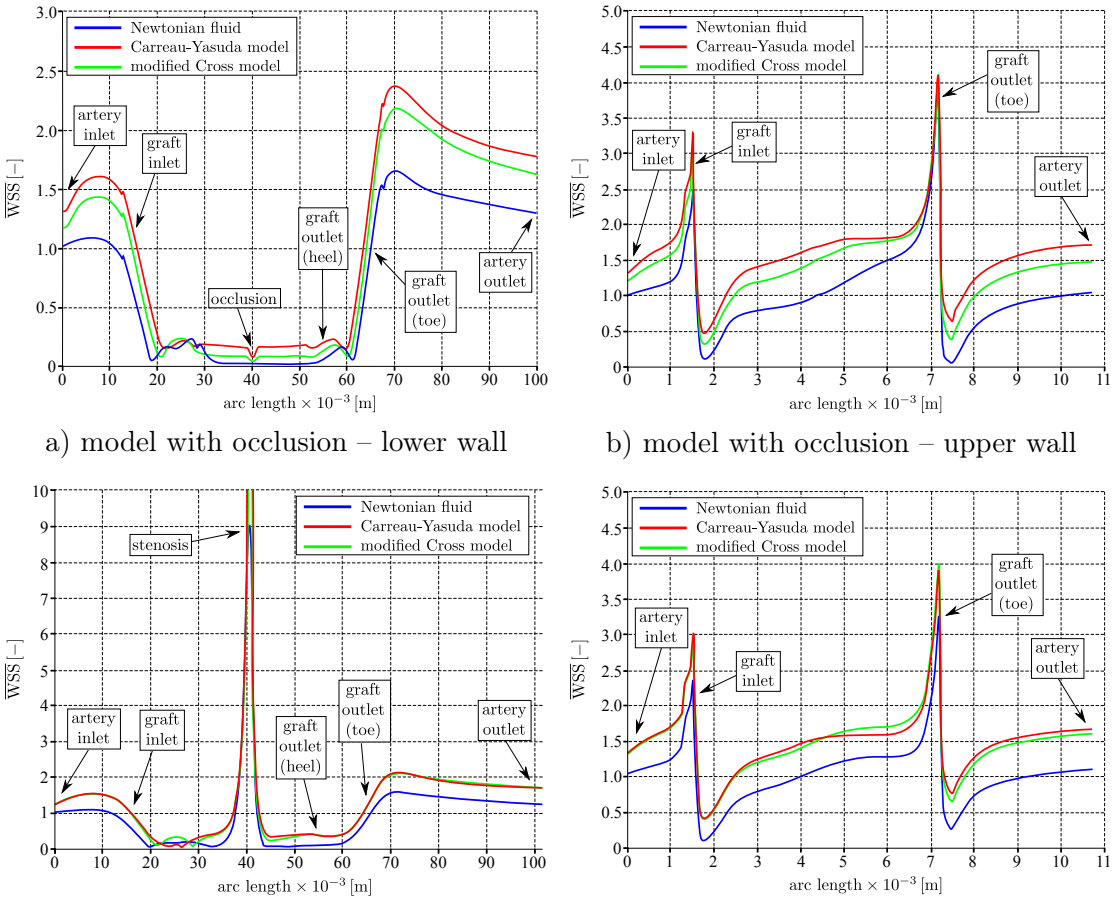

a) model with occlusion – lower wall

b) model with occlusion – upper wall

c) model with stenosis – lower wall

d) model with stenosis – upper wall

Fig. 5.12. Normalised WSS magnitude $\overline{\mathrm{WSS}}$ in the occluded (*top*) and stenosed (*bottom*) femoral bypass models. For the position of the upper and lower walls, see Fig. 5.4.

Here, the proximal anastomosis experiences a significant increase in WSS magnitude resulting, on one hand, in a reduction of the low shear area at the graft inlet and, on the other hand, exposing the adjacent part of the native artery to greater shear load. A similar observation can be made for the distal anastomosis, where the low shear area located downstream from the toe almost disappears when non-Newtonian rheology is considered. Finally, the change in shear stress stimulation of the arterial floor should be noted as well, since its form and extent is similar in both occluded and stenosed bypass models.

Although the colour maps in Fig. 5.10b,c and Fig. 5.11b,c show qualitatively very similar WSS distributions for both non-Newtonian flows, a little bit more detailed insight can be gained from the graphs in Fig. 5.12. For example, on the basis of Fig. 5.12a,b, it can be concluded that quantitatively differences between both non-Newtonian models do exist and that the Carreau-Yasuda model appears to give higher WSS values than the modified Cross model. However, it should be noted that these differences are very small, usually about 0.05 Pa. Moreover, in the model with stenosed native artery, both

non-Newtonian models seem to be in almost perfect agreement regarding the shear stress stimulation at the lower and upper walls, see Fig. 5.12c,d.

5.1.3 Discussion and conclusions

Compared to other studies, which considered only the distal part of the bypass such as [20], the application of a complete bypass model brought several benefits. Besides the possibility to avoid the prescription of an inlet boundary condition at the graft, which is not always available, a complete bypass model enabled an identification of non-Newtonian effects in other relevant areas, for example, at the proximal anastomosis and around the arterial blockage/narrowing, which can consequently influence the downstream blood flow under consideration. Taking into account all the observations made so far, the following facts can be concluded: First, the blood flow in the complete bypass models demonstrates strong dependence on geometry and type of arterial damage (occlusion/stenosis). Second, flow conditions are one of the main factors determining whether the blood's non-Newtonian behaviour becomes apparent or not, confirming so the importance of the inlet Reynolds number in this type of flow problems. Third, the Carreau-Yasuda model and the modified Cross model give qualitatively comparable results, making us inclined to believe that both non-Newtonian models can be interchangeable if coronary or femoral flow conditions are used.

When discussing the impact of non-Newtonian rheology on a potential post-operative bypass graft failure, it is important to take all the necessary factors into consideration. Thus, in accordance with Section 3.3, several relevant observations can be made, especially at both anastomoses, where the risk of intimal hyperplasia is known to be the highest. In the idealised coronary and femoral bypasses, when blood is modelled as a shear-thinning fluid, the resulting flow field appears to be affected in both positive and negative ways. An example of a positive effect can be found in the form of reduced or even suppressed flow disturbances around the damaged part of the native artery, which would otherwise mean enhanced risk of thrombosis due to accumulation of blood cells. As for the negative effects, it is possible to mention the tendency of the non-Newtonian flow to emphasise the differences in WSS distribution at the toe and along the suture line, where low and high values are in close proximity to each other. Here, any sudden transition from low to very high WSS values and vice versa is unwanted not only because a short-time exposure to extremely high shear stress is known to enhance the risk of blood cell damage and partial thrombus activation (see Section 2.1), but because it may also trigger biochemical and morphological changes within the vascular wall contributing so to intimal hyperplasia formation and consequently to the loss of graft patency (see Section 3.3).

Finally, it should be noted that the validity of all the conclusions draw in this section is limited. One of the major limitations is the assumption of steady flow conditions despite the fact that the blood flow through the vascular system is pulsatile by nature. Another issue is the blood's non-Newtonian behaviour, which, as demonstrated in this section, strongly depends on the actual flow problem and geometry and, thus, requires individual approach.

5.2 Pulsatile Newtonian blood flow in idealised coronary bypass models in dependence on three main geometric parameters

Compared to the previous section, where the steady non-Newtonian blood flow was of main interest, the content of this section is more focused on the analysis of geometry influence on the pulsatile bypass hemodynamics and the distribution of selected hemodynamical wall parameters (cycle-averaged WSS and OSI). The numerical results analysed and discussed here were presented at selected conferences [B.9–B.11] and published in peer-reviewed journals [A.4] and [A.5].

Considering all the surgical techniques typically used for bypass grafting of end-to-side anastomoses, several important geometrical parameters crucial for the resulting flow field can be identified. In addition to the so-called distance of grafting[1], there are three other geometrical parameters, whose influence on the flow field is closely studied in this Ph.D. thesis:

- **Stenosis degree** characterises the narrowing of the native artery and is defined as

$$\text{stenosis degree} = \frac{D - s}{D} \cdot 100\%\,,$$

  where D is the native artery diameter and s is the diameter of the narrowed artery, Fig. 5.1. In clinical vascular surgery, the stenosis degree is an important indicator of artery damage and its severity. In bypass graft surgery, the need for surgical intervention is determined by the degree of arterial narrowing, which is usually greater than 70%, depending on the artery damage and the surgeon's experience.
- **Junction angle** (α), also known as the anastomotic or bifurcation angle, is the angle between the native artery and the implanted bypass graft, Fig. 5.1. The choice of the angle may be decided by the surgeon during a bypass surgery depending on the actual condition of the native artery (small angles require larger artery incision and a longer suture line, which may further damage the native artery).
- **Diameter ratio** ($D : d$) represents the ratio between the native artery diameter D and the graft diameter d, Fig. 5.1. The diameter ratio is important for the application of bypass grafts with adequate inner diameters so that the amount of blood supply restored to the distal part of the native artery is sufficient for downstream tissue perfusion. For example, a small-diameter graft with a gradually thickening tunica intima at the distal anastomosis will restrict blood flow more than a graft with diameter similar to that of the native artery [61]. Although the graft diameter may seem to be one of the most optional parameters used in bypass surgery, in reality, the surgeon's choice of an appropriate vascular graft is limited by the performed surgery type (cuffed/non-cuffed bypass grafts [99]) and used graft material (autologous/synthetic), see Chapter 3.

Because the idealised bypass geometry introduced in the previous section makes it easy to change any of the three parameters mentioned above, it is employed in this section, as well. For the purpose of comparing results, the bypass model proportions are chosen to be equal regardless of the actual geometrical parameter value, Fig. 5.1: the native

[1] The distance of grafting is a distance between the distal anastomosis and the narrowed or occluded part of the native artery studied, for example, in [12].

artery length is set at $L = 50$ mm and the native artery diameter is set to $D = 0.003$ m, corresponding to an average right coronary artery (RCA) [12]. To provide a smooth and realistic transition between the damaged and non-damaged artery parts, the narrowing of the native artery is once again modelled with the help of the Gaussian function.

An overview of the various bypass model configurations analysed in this section is shown in Fig. 5.13. Values below each geometrical parameter title refer to the displayed model configuration (from top to bottom), i.e., the left column represents models with various stenosis degrees (50%, 65%, 75%, 85%, 100% – fully occluded native artery), the middle column represents models with various junction angles ($\alpha = 30°$, 35°, 45°, 55°, 70°) and, finally, the right column includes models with various graft diameters ($D:d =$ 1:0.5; 1:1; 1:1.5; 1:1∼0.5; 1:0.5∼1). The models marked with diameter ratios 1:1∼0.5 and 1:0.5∼1 represent bypass grafts with decreasing (from $1D$ to $0.5D$) and increasing (from $0.5D$ to $1D$) diameters, respectively. For future reference, we also introduce a reference bypass model, the parameters of which have the following reference values: 75% stenosis, junction angle $\alpha = 45°$ and diameter ratio $D : d =$ 1:1. Therefore, configurations with those values depicted in Fig. 5.13 are represented by only one model – the reference bypass model. For the generation of unstructured tetrahedral computational meshes, the tools of the commercial software package HyperMesh (Altair Engineering, Troy, USA) are used with the resulting number of cells listed in Tab. 5.6. As an example, Fig. 5.14 shows the final mesh obtained for the reference bypass model and Fig. 5.15 displays the longitudinal section of four selected models with apparent mesh refinement near the model walls.

The present hemodynamical study is carried out in coronary bypasses, where, as seen in Section 5.1, the non-Newtonian behaviour of blood is negligible. Thus, the assumption of Newtonian blood flow is adopted in the current flow problem, i.e., the blood is modelled as an incompressible Newtonian fluid with density $\varrho = 1060\,\mathrm{kg\,m^{-3}}$ and dynamic viscosity $\eta = 3.45 \times 10^{-3}\,\mathrm{Pa\,s}$. Further simplifications and assumptions in the modelling are mentioned and discussed in detail at the beginning of Chapter 4.

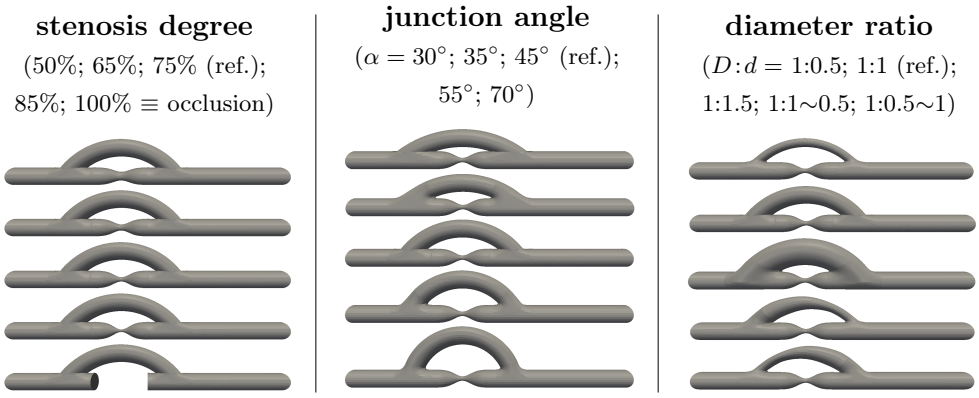

Fig. 5.13. Overview of all 3D bypass model configurations considered within this study. Each column represents a model in which a specific parameter is varied while the other two parameters remain constant and are equal to the reference values: stenosis degree 75%, junction angle $\alpha = 45°$ or diameter ratio $D : d =$ 1:1.

stenosis degree		junction angle α		diameter ratio $D:d$	
50%	503 759	30°	309 518	1:0.5	309 921
65%	501 314	35°	301 243	1:1 (ref.)	256 461
75% (ref.)	256 461	45° (ref.)	256 461	1:1.5	314 444
85%	314 294	55°	230 513	1:1∼0.5	294 806
100%	274 498	70°	228 519	1:0.5∼1	298 238

Tab. 5.6. Number of tetrahedral cells required to model all bypass configurations mentioned in Fig. 5.13.

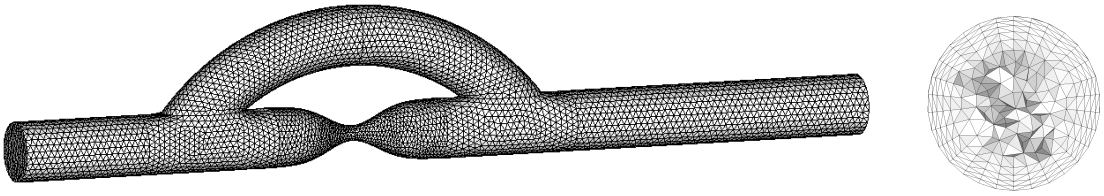

Fig. 5.14. Unstructured tetrahedral computational mesh for the reference bypass model with a detailed view at the cross section in the native artery.

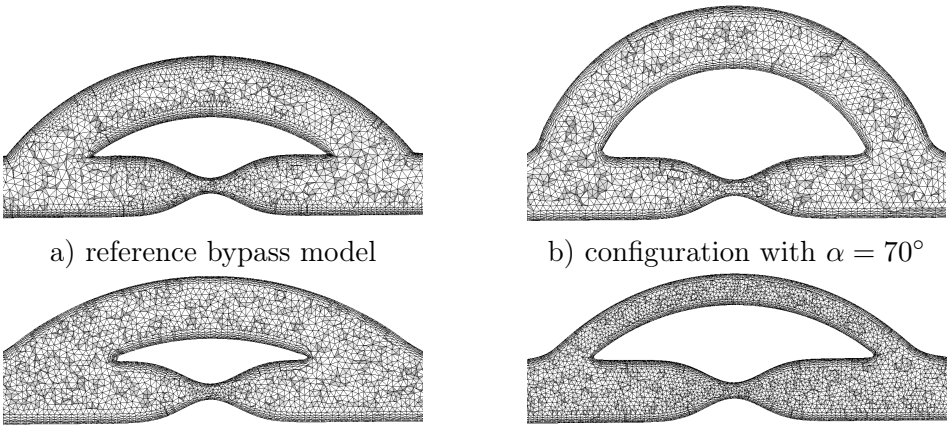

a) reference bypass model b) configuration with $\alpha = 70°$

c) configuration with $\alpha = 35°$ d) configuration with $D : d$ =1:0.5

Fig. 5.15. Detailed view at the mesh structure of four selected bypass configurations.

Because the blood flow in human arteries is known to be pulsatile, the prescription of realistic blood flow conditions is another issue that needs to be addressed at this point. In this Ph.D. thesis, this problem is approached by considering a time-dependent inlet flow rate $Q(t)$, Fig. 5.16, which is taken from [12] and should correspond to flow rate values measured in the right coronary artery during rest. For the purpose of numerical simulations, the flow rate is prescribed in the form of the following Fourier series

$$Q(t) = Q_0 + \sum_{q=1}^{5} Q_q \cos\left(q\omega t - \varphi_q\right), \tag{5.2}$$

where $\omega = 2\pi/T$ is the angular frequency determined from the cardiac cycle period $T = 1.68\,\mathrm{s}$, $Q_0 = 65.07\,\mathrm{ml\,min^{-1}}$ represents the average inlet flow rate and Q_q and φ_q, $q = 1, ..., 5$ are the amplitude and the phase angle, respectively, see Fig. 5.16.

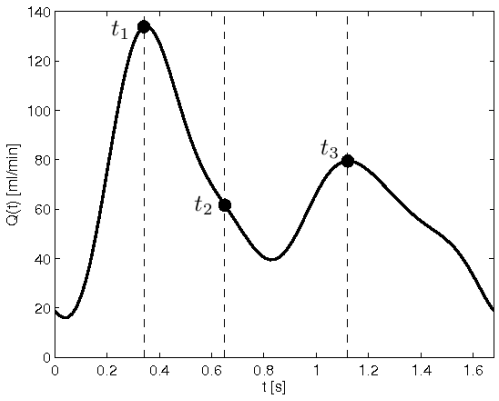

q	$Q_q\,[\mathrm{ml\,min^{-1}}]$	$\varphi_q\,[\mathrm{rad}]$
1	18.149	1.944
2	34.828	2.836
3	12.329	-2.124
4	9.107	-1.875
5	2.944	-0.447

Fig. 5.16. Time-dependent inlet flow rate $Q(t)$ corresponding to the right coronary artery during rest [12]. The denoted time instants $t_1 = 0.34\,\mathrm{s}$ (systole), $t_2 = 0.65\,\mathrm{s}$ (late systole) and $t_3 = 1.12\,\mathrm{s}$ (diastole) are later used for the visualisation of numerical results. The table on the right shows an overview of the amplitude and phase angle values necessary for the Fourier series (5.2).

The equations governing the pulsatile blood flow, which have the form of the dimensionless non-linear system of Navier-Stokes equations (4.87)–(4.88) for the incompressible Newtonian fluid ($\theta = 0$), are numerically solved by means of the modified projection method and the finite volume method formulated for hybrid unstructured tetrahedral grids, see Section 4.4.1. For the non-dimensionalisation of the system of Navier-Stokes equations according to Section 4.1, the following reference values are chosen regardless of the bypass configuration used:

$$\left.\begin{array}{ll} L_{ref} \equiv D = 0.003\,\mathrm{m}, & \varrho_{ref} = 1060\,\mathrm{kg\,m^{-3}}, \\ U_{ref} = \frac{4\,Q_0}{\pi\,D^2} = 0.153\,\mathrm{m\,s^{-1}}, & \eta_{ref} = 3.45 \times 10^{-3}\,\mathrm{Pa\,s}, \end{array}\right\} \mathrm{Re} = \frac{U_{ref}\,L_{ref}\,\varrho_{ref}}{\eta_{ref}} = 141.4.$$

For the purpose of result analysis and comparison, the numerical simulations are carried out for the same values of boundary conditions prescribed at the corresponding computational domain boundaries. Written in the dimensional form, the values are as follows:

- **inlet** $\partial\Omega_{hI}$ – 3D Womersley velocity profile

$$\begin{aligned} v_{1I}(r,t) &= \Re\left\{ \mathrm{Wo}\sqrt{\mathrm{i}^3} \left[\frac{J_0(\mathrm{Wo}\sqrt{\mathrm{i}^3}\frac{2r}{D}) - J_0(\mathrm{Wo}\sqrt{\mathrm{i}^3})}{2J_1(\mathrm{Wo}\sqrt{\mathrm{i}^3}) - \mathrm{Wo}\sqrt{\mathrm{i}^3}\,J_0(\mathrm{Wo}\sqrt{\mathrm{i}^3})} \right] \frac{4Q(t)}{\pi D^2} \right\}, \\ v_{2I} &= v_{3I} = 0, \end{aligned}$$

  where $\Re\{.\}$ denotes the real part of the function defined in the complex plane, $\mathrm{i} = \sqrt{-1}$ is the imaginary unit, $r = \sqrt{x_2^2 + x_3^2}$ denotes the distance from the artery centreline, $D = 0.003$ m is the diameter of the native artery, $J_0(.)$ and $J_1(.)$ are the Bessel functions of the first kind of order zero and one, respectively, $Q(t)$ is the time-dependent flow rate prescribed in the form of Fourier series (5.2) and $\mathrm{Wo} = 0.5D\sqrt{\omega\varrho/\eta} = 1.61$ is the Womersley number;

- **outlet** $\partial\Omega_{hO}$ – constant pressure of 12 000 Pa (average arterial pressure);

• **impermeable and rigid walls** $\partial\Omega_{hW}$ – non-slip boundary condition, i.e., $\boldsymbol{v} = \mathbf{0}$.

At corresponding boundaries of the computational domain $\Omega \subset \mathbb{R}^3$, the remaining primitive variables are extrapolated from the flow field. The Womersley velocity profile is discussed in detail in the monograph [C.2] co-authored by the author of this Ph.D. thesis. For further information about the Womersley number and its various modifications, see, for example, [109]. Lastly, note that all numerical results presented in this section and achieved after three full cardiac cycle periods are shown in the dimensional form using the reference values mentioned above.

5.2.1 Analysis of blood flow

For the analysis of velocity evolution in all the studied bypass models, the obtained results are presented in two forms. First, the results are presented as 3D velocity profiles so that the complex three-dimensional behaviour of the flow can be captured. Second, the results are presented as 2D slices that represent the longitudinal sections of their spatial counterparts and should enable a detailed quantitative comparison between the investigated models. For each set of results corresponding to one of the three geometrical parameters (stenosis degree, junction angle and diameter ratio), the velocity development is shown at three different time instants: $t_1 = 0.35\,\mathrm{s}$, $t_2 = 0.65\,\mathrm{s}$ and $t_3 = 1.12\,\mathrm{s}$, Fig. 5.16.

Stenosis degree: Comparing the 3D velocity profiles shown in Figs. 5.17–5.19, changes in the stenosis degree seem to have the strongest impact on the flow field in the distal anastomosis. With lower stenosis degrees ($\leq$50%), the existence of a strong residual flow through the arterial narrowing significantly contributes to the formation of double-velocity profiles. In the other bypass models ($\geq$65%), the insufficient or even absent residual flow results in velocity profiles that, particularly during the acceleration phase, Fig. 5.17, become skewed in the direction of the arterial floor. A better insight into the flow differences between the five studied bypass models can be gained from the 2D slices of the velocity profiles, Figs. 5.17–5.19 (left). Taking the different value ranges of each figure into account ($0.6\,\mathrm{m\,s^{-1}}$, $0.3\,\mathrm{m\,s^{-1}}$, $0.4\,\mathrm{m\,s^{-1}}$, respectively), profiles A–D indicate flow patterns that closely resemble each other regardless of the actual time. The only exception is represented by the model with a stenosis degree of 50%, which shows a behaviour completely different from that of the other four bypasses.

Junction angle: By changing the junction angle, the shape of the velocity profiles is more affected than the magnitude of the velocity, Figs. 5.20–5.22. According to the 3D velocity profiles, an increase in the angle causes the flow to become more skewed to the lower wall at the entrance of the graft and downstream from the distal anastomosis. In particular, the latter is characterised by velocity profiles that take the form of a U shape for higher angles and inlet velocities. According to the 2D slices of the velocity profiles in Figs. 5.20–5.22, the investigated bypass models can be divided into two categories. The first category includes the small angle models (30° and 35°), the flow of which is characterised by strong forward flow in the upper part of the vessel before the stenosis (profile A) and by less skewed velocity profiles (C and D) downstream from the distal anastomosis. Different behaviour is observed in the velocity profiles (C and D) of the second category of models with $\alpha \geq 45°$. A distinct transient state between the two groups is not observed in the 2D slices.

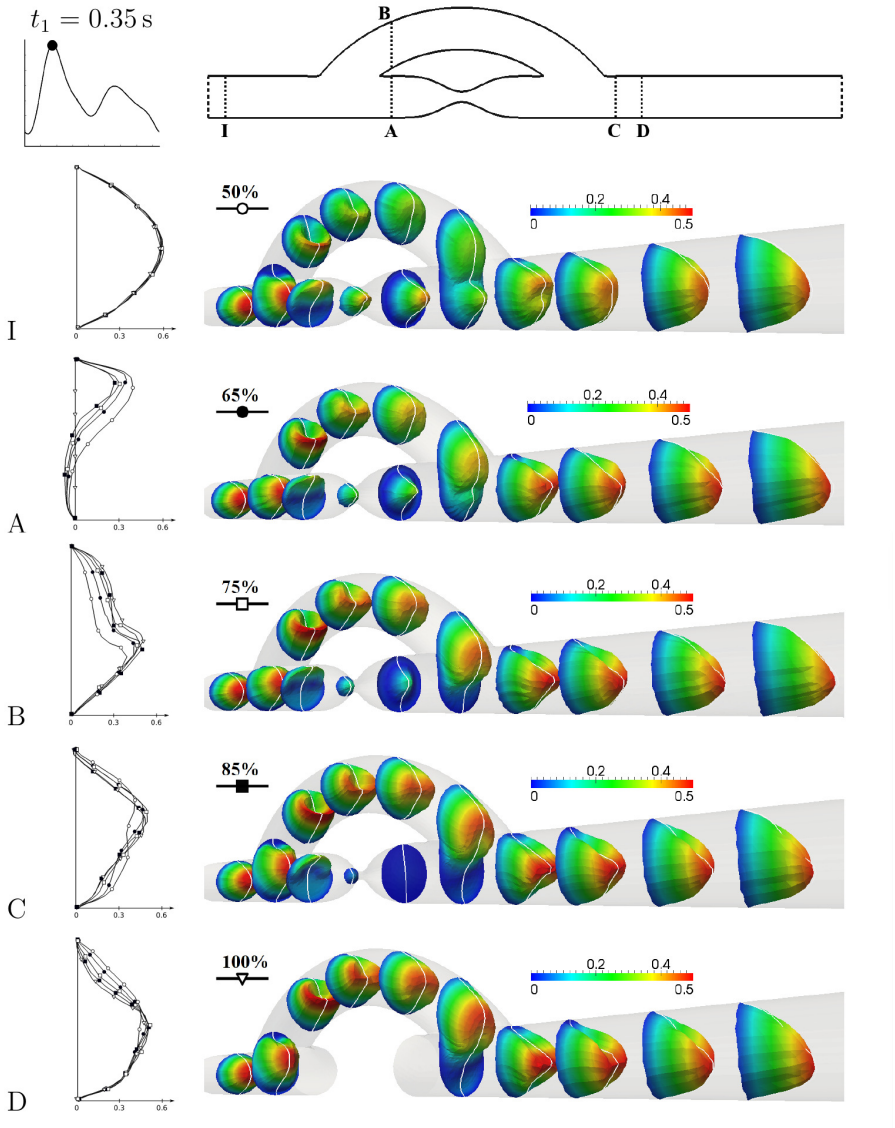

Fig. 5.17. 2D and 3D velocity profiles for various stenosis degrees at time $t_1 = 0.35\,\mathrm{s}$ (*from top to bottom*: 50%, 65%, 75%, 85%, 100%). The 2D slices of the velocity profiles at the left are displayed with the maximum value range set to $0.6\,\mathrm{m\,s^{-1}}$ and markers corresponding to each stenosis degree.

Diameter ratio: In comparison to the previous two parameters, changes in the diameter ratio have a much greater impact on the resulting flow field. The diameter ratio affects not only the shape of the velocity profiles but also the overall velocity magnitude, Figs. 5.23–5.25. While an increase in the graft diameter leads to a decrease in velocity magnitude and blunter 3D velocity profiles, a reduction in diameter tends to considerably increase the velocity and intensify the skew of the flow observed downstream from the distal anastomosis. The permanent shifting of the peak velocity to the arterial floor is also apparent from the 2D slices of the velocity profiles, Figs. 5.23–5.25 (left). A very

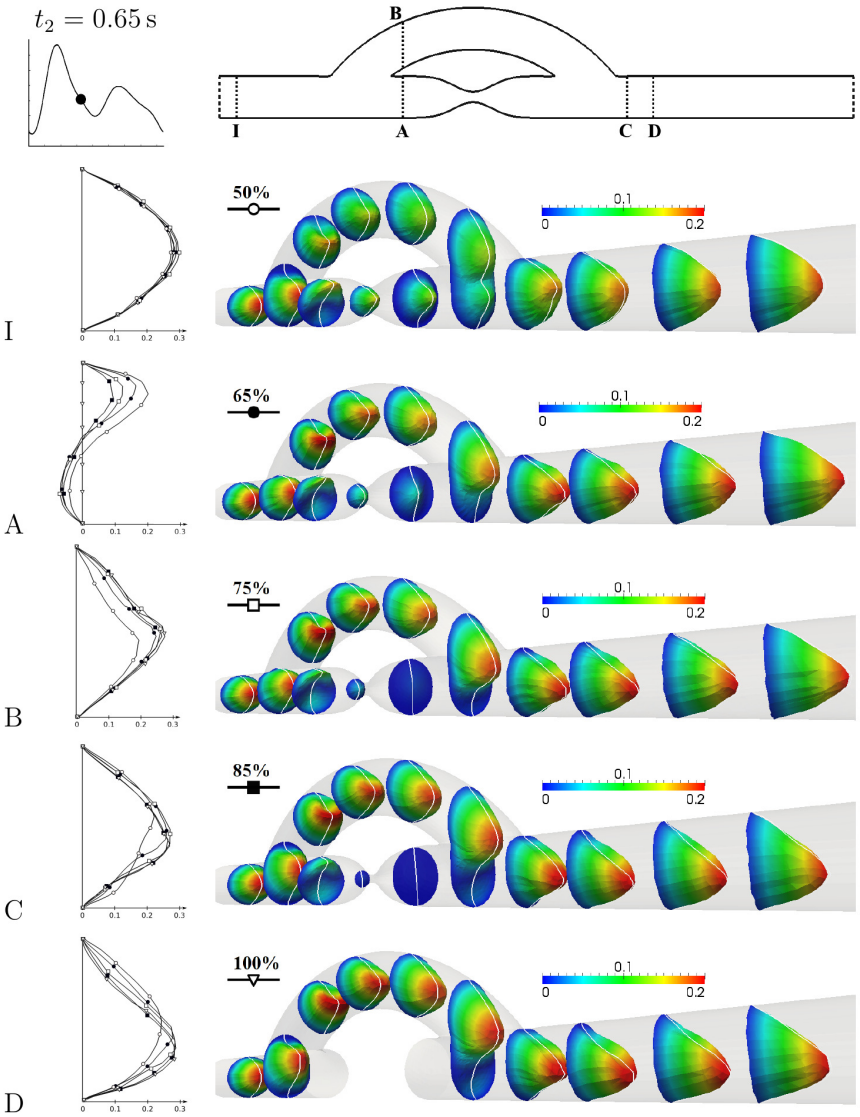

Fig. 5.18. 2D and 3D velocity profiles for various stenosis degrees at time $t_2 = 0.65\,\mathrm{s}$ (*from top to bottom*: 50%, 65%, 75%, 85%, 100%). The 2D slices of the velocity profiles at the left are displayed with the maximum value range set to $0.3\,\mathrm{m\,s^{-1}}$ and markers corresponding to each stenosis degree.

similar behaviour is observed for the model with the tapered graft ($D : d$ =1:1∼0.5), though with a flow that is more strongly skewed than when the diameter ratio is 1:0.5. By contrast, the geometry of the bypass model with gradually increasing graft diameter values (1:0.5∼1) demonstrates a tendency to suppress or even remove flow irregularities in the distal part of the native artery (profiles B–D). An increasing diameter ratio is also associated with the appearance of large recirculation zones within the graft – either in its first half ($D : d$ =1:1.5) or in its lower half near the distal anastomosis (1:0.5∼1), Figs. 5.23–5.25 (right).

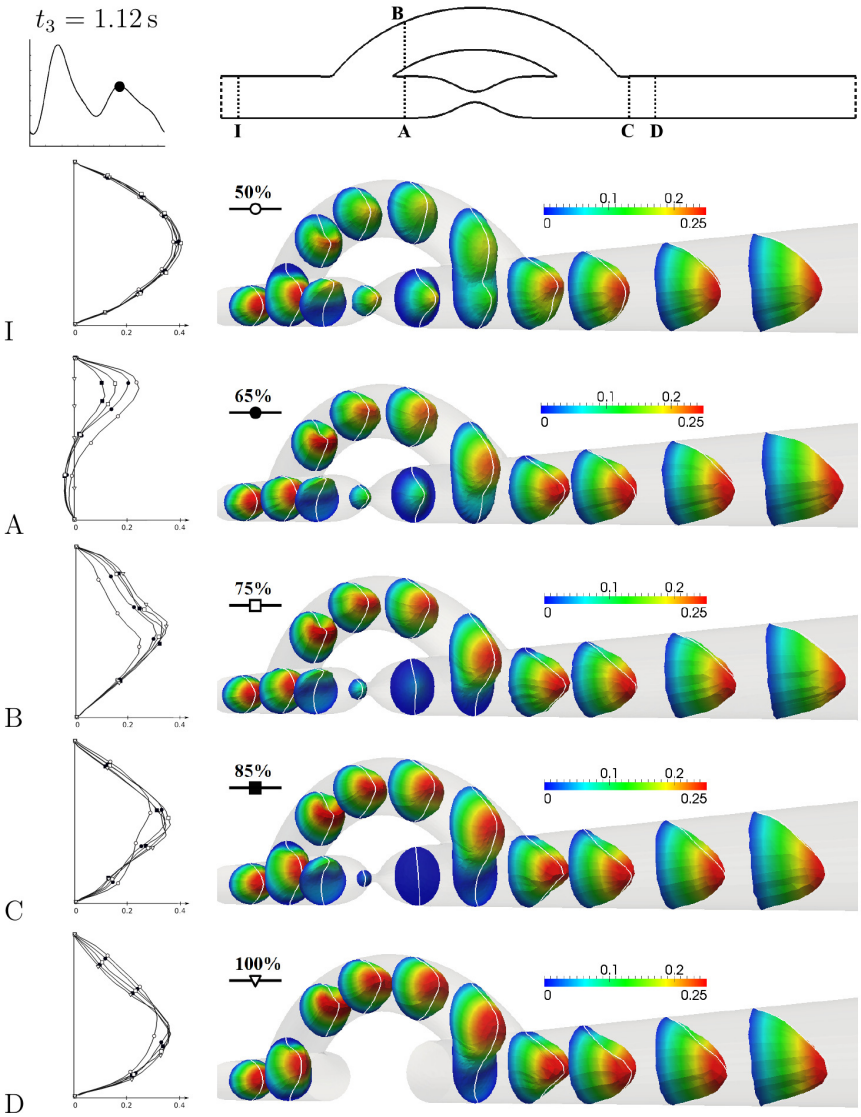

Fig. 5.19. 2D and 3D velocity profiles for various stenosis degrees at time $t_3 = 1.12\,\mathrm{s}$ (*from top to bottom*: 50%, 65%, 75%, 85%, 100%). The 2D slices of the velocity profiles at the left are displayed with the maximum value range set to $0.4\,\mathrm{m\,s^{-1}}$ and markers corresponding to each stenosis degree.

5.2.2 Wall shear stress distribution

To visualise the shear results for each bypass model configuration, let us define the normalised cycle-averaged wall shear stress (WSS) magnitude according to the paper [199]

$$\overline{|\boldsymbol{\tau}_W|} = \frac{1}{T}\int_0^T \frac{|\boldsymbol{\tau}_W|}{\tau_m}\mathrm{d}t, \tag{5.3}$$

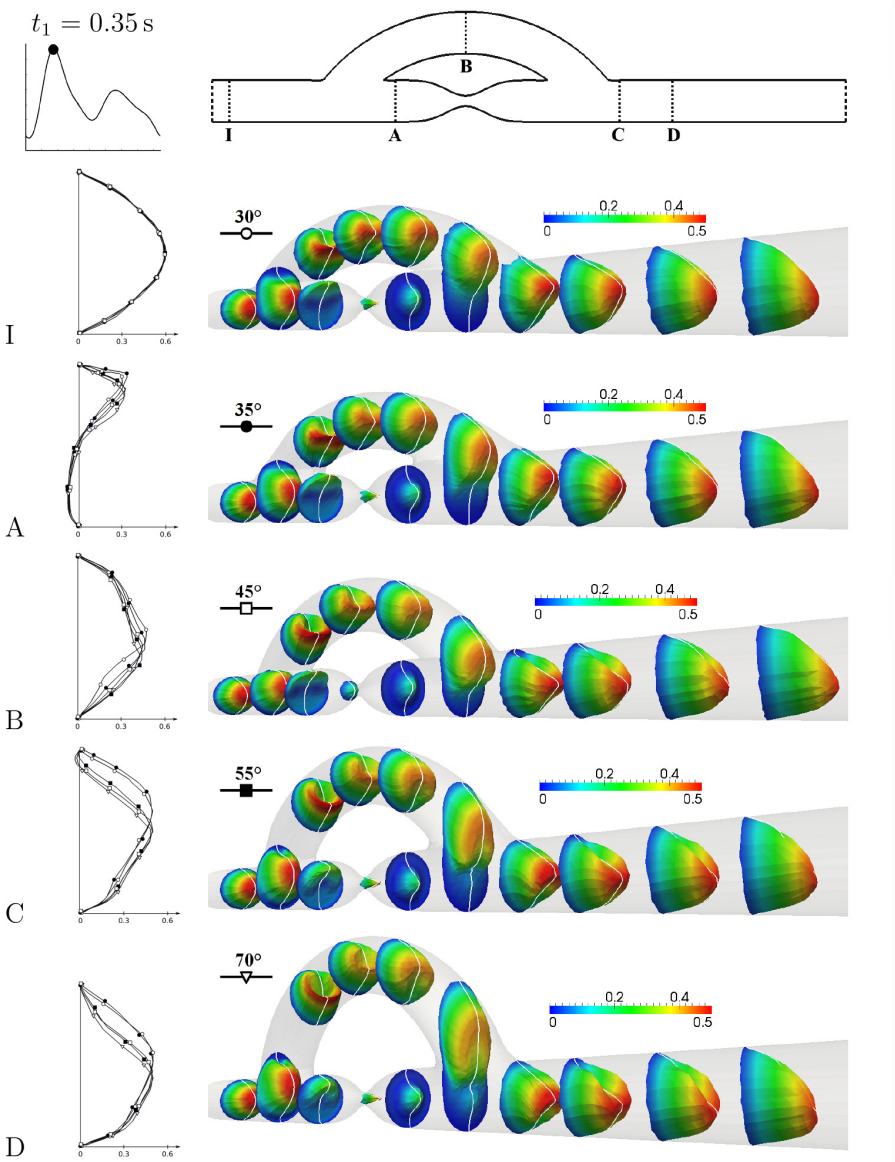

Fig. 5.20. 2D and 3D velocity profiles for various junction angles at time $t_1 = 0.35\,\mathrm{s}$ (*from top to bottom*: 30°, 35°, 45°, 55°, 70°). The 2D slices of the velocity profiles at the left are displayed with the maximum value range set to $0.6\,\mathrm{m\,s^{-1}}$ and markers corresponding to each junction angle.

where T is the period of the cardiac cycle, $|\boldsymbol{\tau}_W|$ is the WSS magnitude and $\tau_m = \frac{8\eta^2\,\mathrm{Re}}{\varrho\,D^2} = 1.41\,\mathrm{Pa}$ is the WSS of Poiseuille flow determined from the average inlet flow rate Q_0. As intimal hyperplasia is associated with low and oscillating shear stress ($|\boldsymbol{\tau}_W| < 0.5\,\mathrm{Pa}$ [52]) all shear results presented in this section are presented with lowered value ranges (in the normalised form between 0 and 2). In this sense, the reference bypass model is characterised by several areas with extensively low WSS (normalised values below 0.4) localised at the entrance of the graft, around the stenosis and downstream from the distal anastomosis, Fig. 5.26 (left). Each of the three studied geometrical parameters shows a

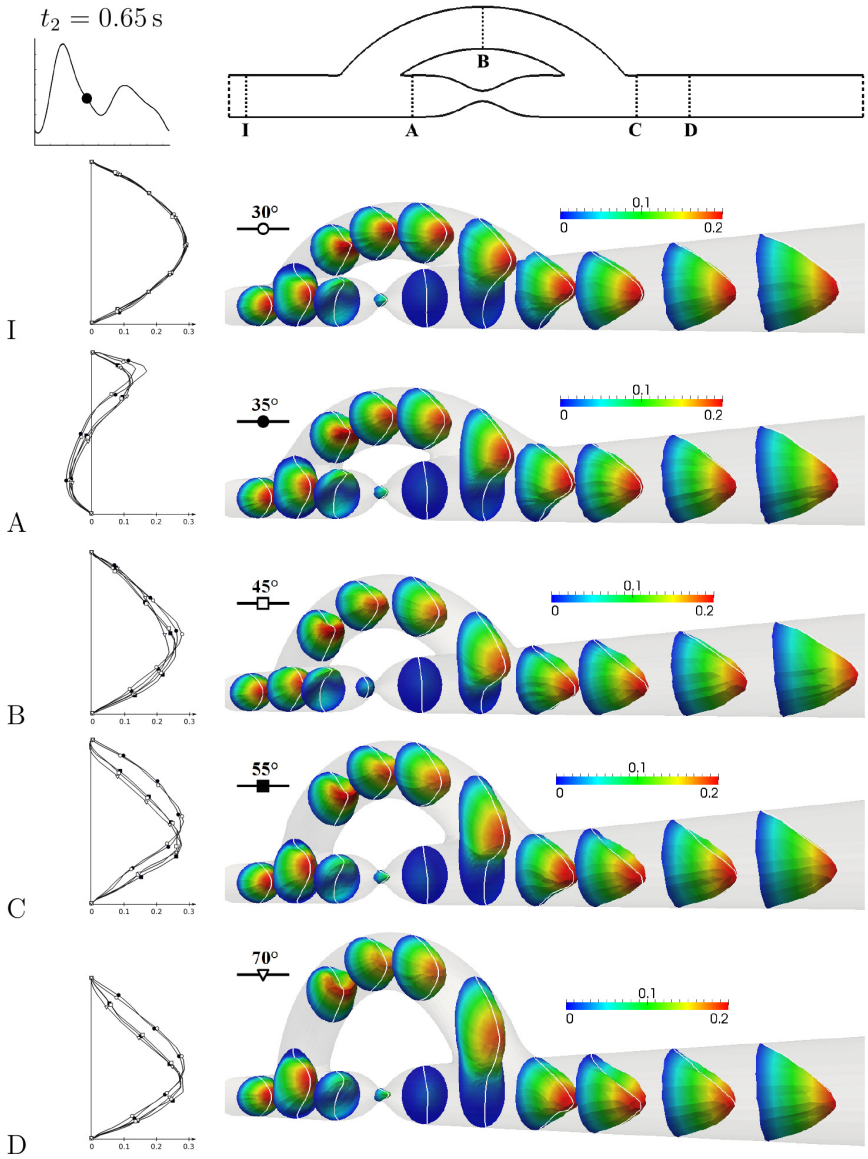

Fig. 5.21. 2D and 3D velocity profiles for various junction angles at time $t_2 = 0.65\,\mathrm{s}$ (*from top to bottom*: 30°, 35°, 45°, 55°, 70°). The 2D slices of the velocity profiles at the left are displayed with the maximum value range set to $0.3\,\mathrm{m\,s^{-1}}$ and markers corresponding to each junction angle.

tendency to affect at least one of these areas in both ways – negatively or positively.

Stenosis degree: Surprisingly, increasing the stenosis degree from 50% to 100% has a barely significant effect on the WSS magnitude distribution around the arterial narrowing, Fig. 5.27 (left), despite the gradual decrease in the amount of blood flowing through the stenosis. Distinct differences between all models are, however, observed at the graft entrance, where a relatively large region of low WSS extends far into the graft for the lower stenosis degrees (50% and 65%), whereas the size of this region appears not to change in all the models with stenoses greater than 75%. The patterns of the WSS

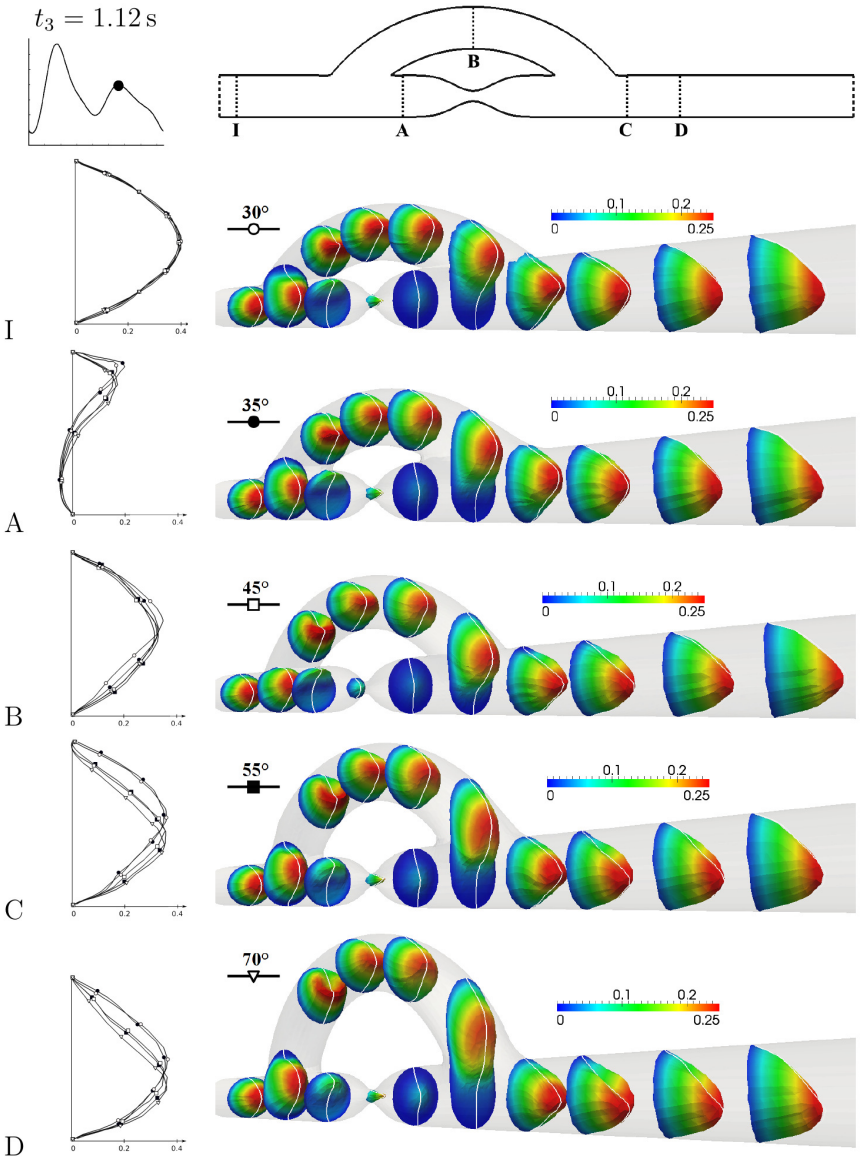

Fig. 5.22. 2D and 3D velocity profiles for various junction angles at time $t_3 = 1.12\,\mathrm{s}$ (*from top to bottom*: 30°, 35°, 45°, 55°, 70°). The 2D slices of the velocity profiles at the left are displayed with the maximum value range set to $0.4\,\mathrm{m\,s^{-1}}$ and markers corresponding to each junction angle.

distribution at the distal anastomosis are very similar, regardless of the actual stenosis degree. Moreover, the WSS magnitude observed at the arterial ceiling is higher than that at the graft entrance near the proximal suture line.

Junction angle: Compared to the previous parameter, the size of the low WSS region at the graft entrance remains uninfluenced by the change of the junction angle α, Fig. 5.28 (left), although a small decrease in the WSS magnitude occurs along the bypass graft for increases in the angle ($\alpha \geq 45°$). In the pre- and post-stenotic regions, the WSS distribution patterns in each investigated model closely resemble each other without an

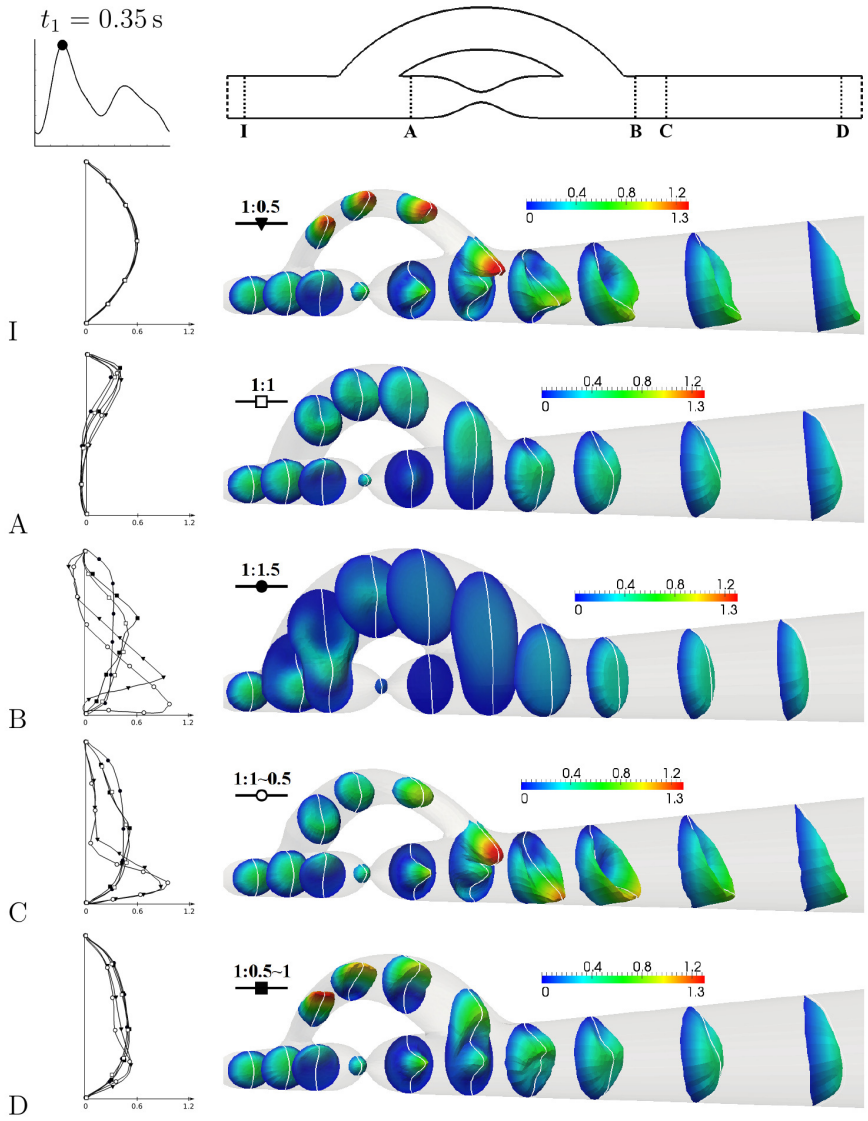

Fig. 5.23. 2D and 3D velocity profiles for various diameter ratios at time $t_1 = 0.35\,\mathrm{s}$ (*from top to bottom*: $D : d =$ 1:0.5, 1:1, 1:1.5, 1:1∼0.5, 1:0.5∼1). The 2D slices of the velocity profiles at the left are displayed with the maximum value range set to $1.2\,\mathrm{m\,s^{-1}}$ and markers corresponding to each diameter ratio.

appreciable influence of α. A completely opposite situation is observed downstream from the toe, particularly at the arterial ceiling. Here, a larger angle causes the wall to be exposed to lower shear stress, with a growing area of extremely low values in the vicinity of the toe.

Diameter ratio: When the graft diameter is varied, Fig. 5.29 (left), a distinct correlation between the diameter ratio and the occurrence of low WSS can be found at the proximal anastomosis, particularly at the entrance of the graft. Here, a reduction of the graft lumen either reduces or eliminates an extensively low shear stress, which

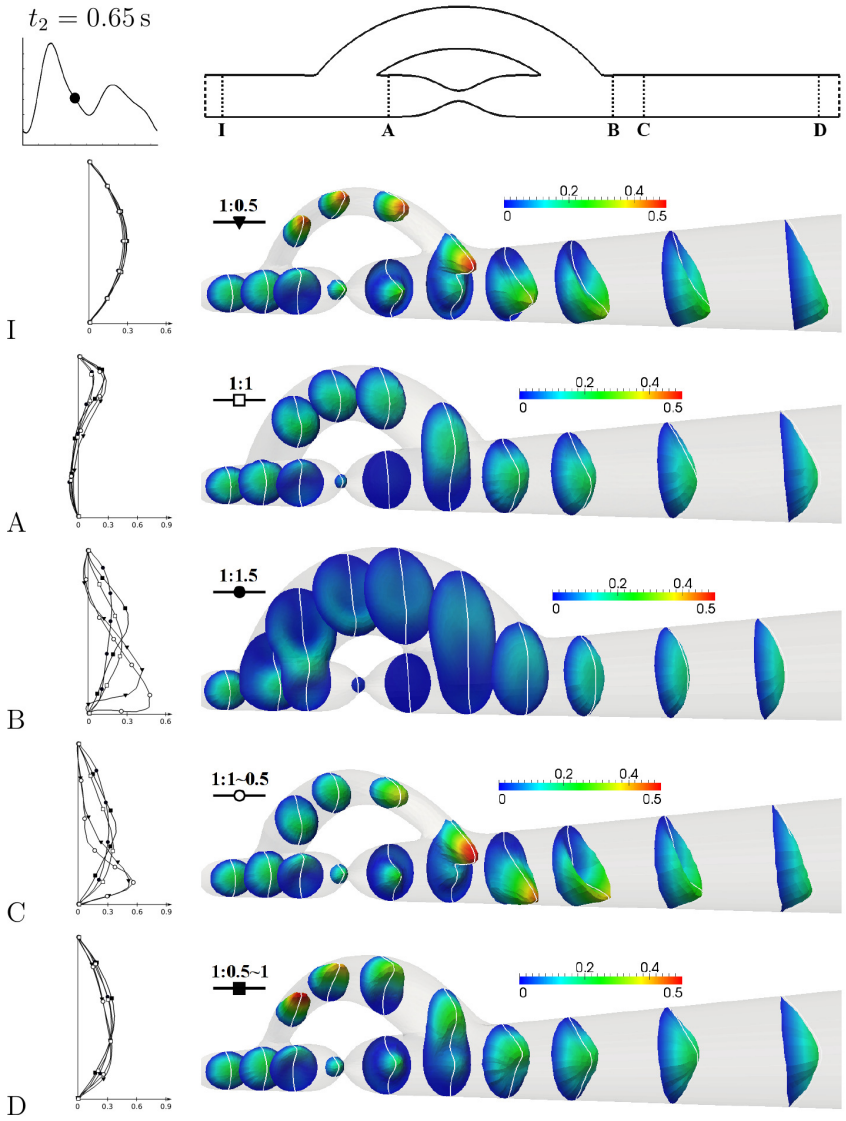

Fig. 5.24. 2D and 3D velocity profiles for various diameter ratios at time $t_2 = 0.65\,\mathrm{s}$ (*from top to bottom*: $D : d =$ 1:0.5, 1:1, 1:1.5, 1:1∼0.5, 1:0.5∼1). The 2D slices of the velocity profiles at the left are displayed with the maximum value range set to $0.9\,\mathrm{m\,s^{-1}}$ and markers corresponding to each diameter ratio.

can be observed in the model with $D : d$ =1:1.5, Fig. 5.29b (left). The wall of the pre-stenotic region experiences almost the same shear stimulation in all the investigated bypass models, in contrast to the area behind the stenosis, where the magnitude of the WSS values appears to be strongly dependent on the diameter ratio, i.e, an increase in the graft diameter results in significant decrease in WSS values. Distinct differences between the WSS distribution patterns are also observed at the distal anastomosis and at the arterial ceiling. The smaller the graft exit, the more inadequate the shear stimulation becomes, resulting in regions with low WSS that may even extend far downstream from

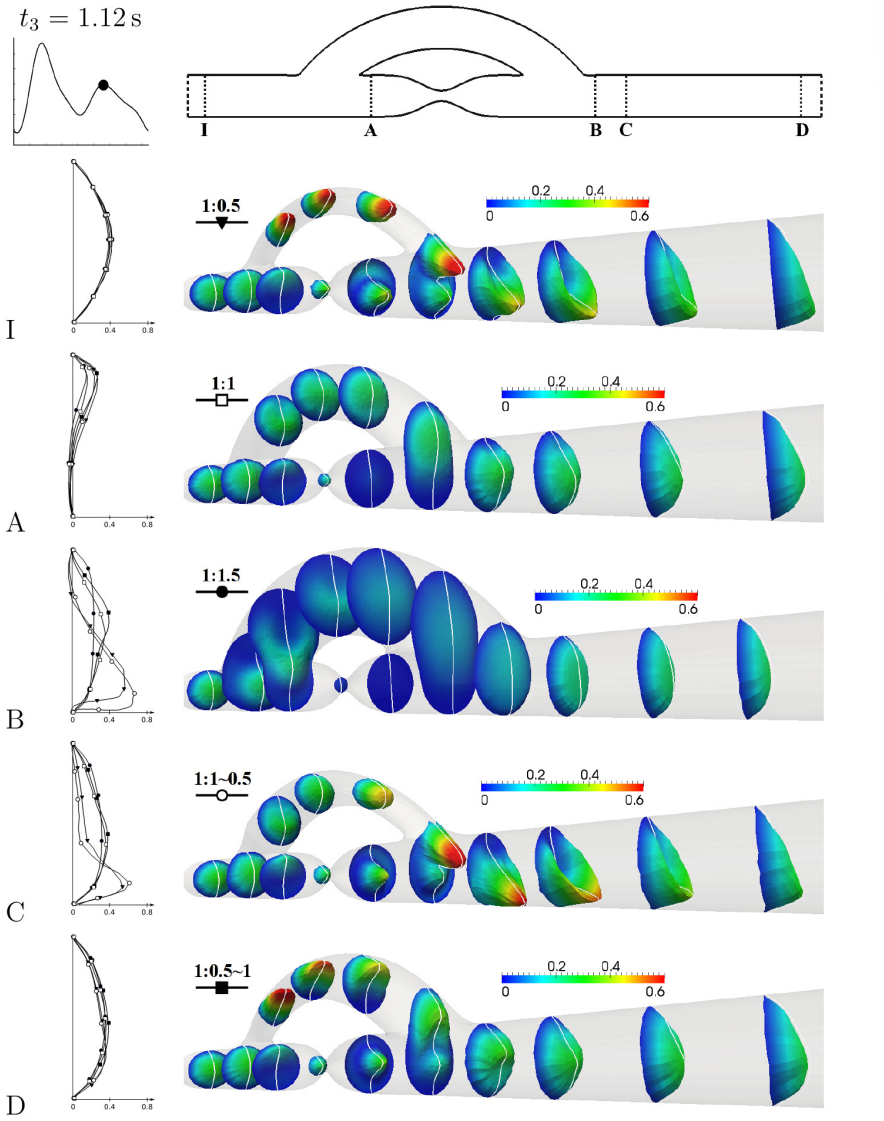

Fig. 5.25. 2D and 3D velocity profiles for various diameter ratios at time $t_3 = 1.12\,\mathrm{s}$ (*from top to bottom*: $D : d$ = 1:0.5, 1:1, 1:1.5, 1:1∼0.5, 1:0.5∼1). The 2D slices of the velocity profiles at the left are displayed with the maximum value range set to $0.8\,\mathrm{m\,s^{-1}}$ and markers corresponding to each diameter ratio.

the toe.

The comparison between the models with constant and varying diameter ratios, Fig. 5.29a-b (left) and Fig. 5.29c-d (left), respectively, reveals another interesting tendency originating from the change in the graft diameter. A gradual enlargement or reduction of the graft diameter yields shear results that, on the one hand, resemble those of the previous models (1:0.5, 1:1, 1:1.5) and, on the other hand, exhibit larger or even previously unobserved areas with extremely low WSS values. One of these areas includes the lower part of the widening graft before the distal anastomosis, Fig. 5.29d (left).

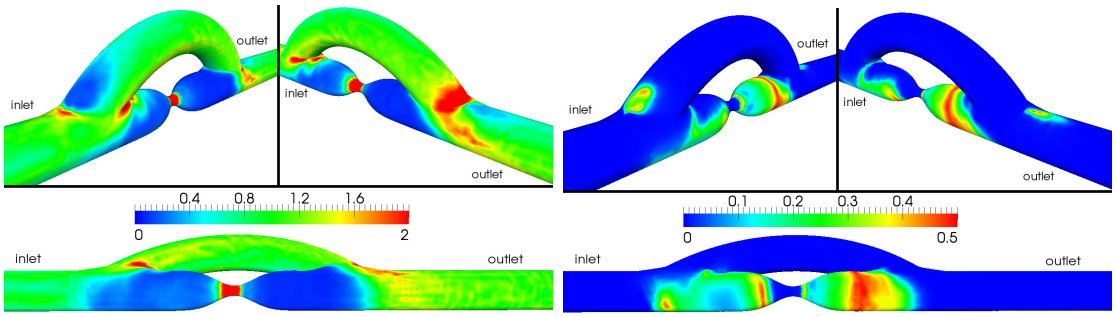

Fig. 5.26. Distribution of normalised cycle-averaged WSS magnitude (*left*) and OSI (*right*) for the reference bypass model (75% stenosis of the native artery, junction angle $\alpha = 45°$ and diameter ratio $D : d = 1{:}1$).

5.2.3 Oscillatory shear index distribution

To determine the intensity of shear oscillations, the well-known oscillatory shear index (OSI) is introduced according to the study [54]

$$\mathrm{OSI} = \frac{1}{2}\left(1 - \frac{\left|\int_0^T \boldsymbol{\tau}_W \,\mathrm{d}t\right|}{\int_0^T |\boldsymbol{\tau}_W| \,\mathrm{d}t}\right), \tag{5.4}$$

where $\boldsymbol{\tau}_W$ is the WSS vector and T is the period of the cardiac cycle. The OSI values range from 0 to 0.5. In the reference bypass model, Fig. 5.26 (right), areas with high shear oscillations (OSI above 0.3) have a distribution similar to those with low WSS magnitude, namely, at the graft entrance, around the stenosis and at the distal anastomosis near the toe and the arterial ceiling.

Stenosis degree: The change in stenosis degree in the coronary bypass affects not only the extent of WSS oscillations but also the expanse of oscillations in all three areas, Fig. 5.27 (right). Increasing the arterial narrowing from 50% to 85% considerably reduces the OSI level at the graft entrance and in the native artery before the stenosis, whereas the vicinity of the toe experiences an opposite trend.

Junction angle: The OSI distribution remains almost unchanged with variations in the junction angle α, Fig. 5.28 (right). The regions of the native artery before and after the stenosis exhibit a very similar OSI pattern, despite the increasing angle between the native artery and the bypass graft. By contrast, the arterial ceiling near the toe is exposed to gradually increasing shear oscillations in a relatively small area.

Diameter ratio: The influence of the diameter ratio $D : d$ on the occurrence of high OSI values is more significant than those of the other two geometrical parameters, Fig. 5.29 (right). An increase in the graft diameter at the proximal anastomosis leads to an extensive area with high WSS oscillations that extend far into the graft. The opposite behaviour is observed at the distal anastomosis, where the decrease in the graft diameter initiates the occurrence of high OSI values at the arterial ceiling near the toe. By comparing Fig. 5.29a-b (right) and Fig. 5.26 (right), it can be noted that the OSI in

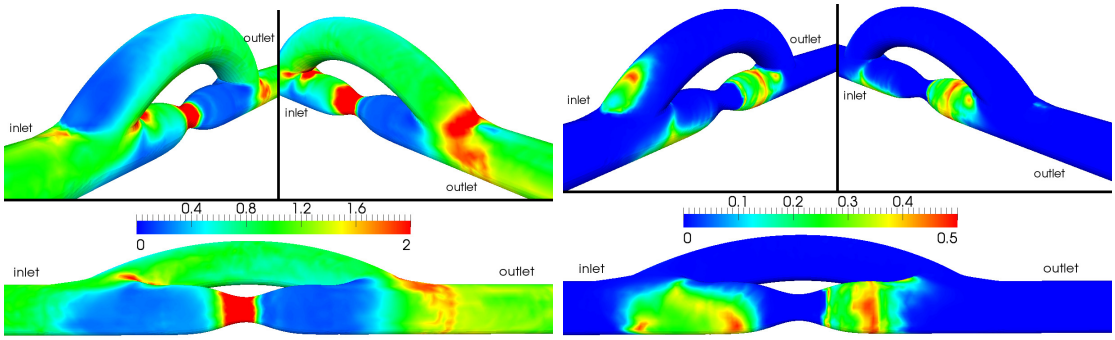

(a) stenosis degree: 50%

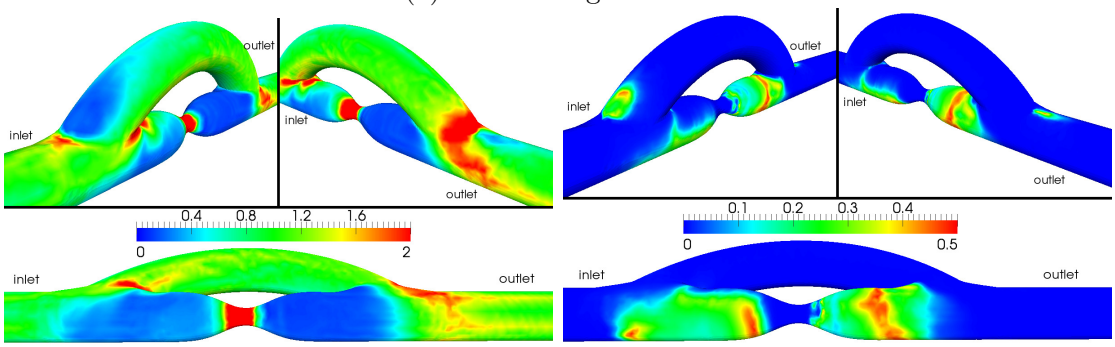

(b) stenosis degree: 65%

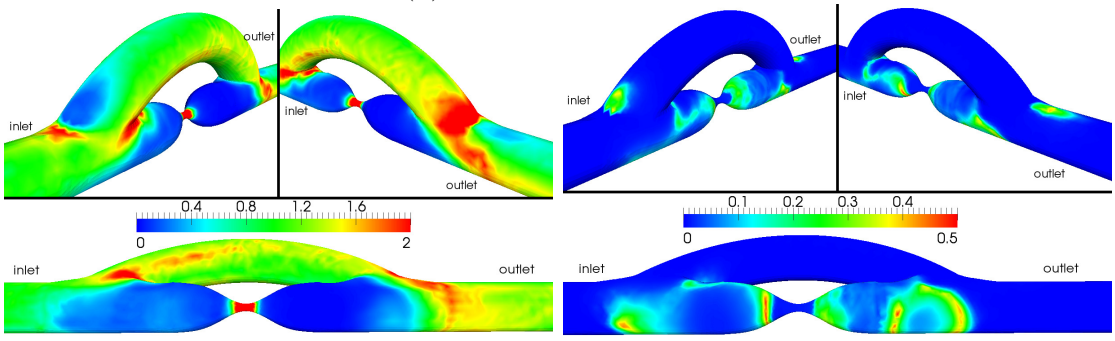

(c) stenosis degree: 85%

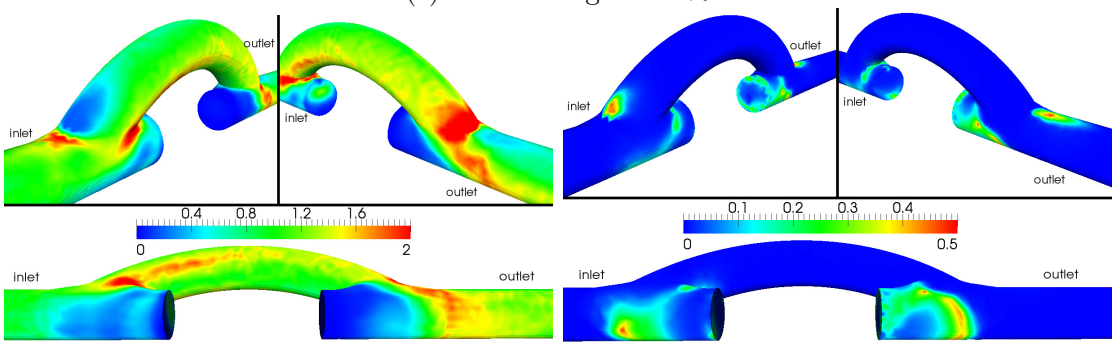

(d) stenosis degree: 100% (occlusion)

Fig. 5.27. Distribution of normalised cycle-averaged WSS magnitude (*left*) and OSI (*right*) for four bypass models with different stenosis degrees. Values corresponding to the reference bypass model are shown in Fig. 5.26 (left).

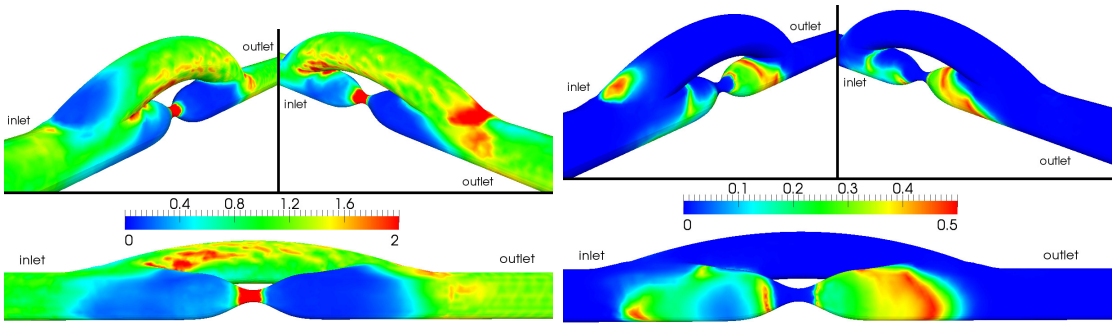

(a) junction angle: 30°

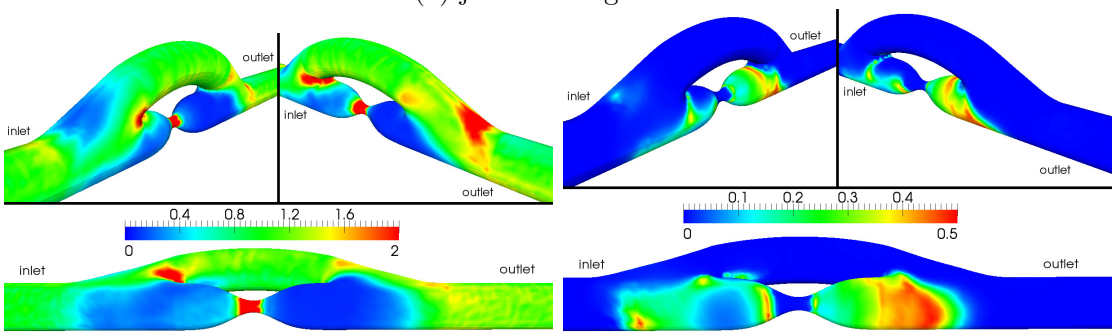

(b) junction angle: 35°

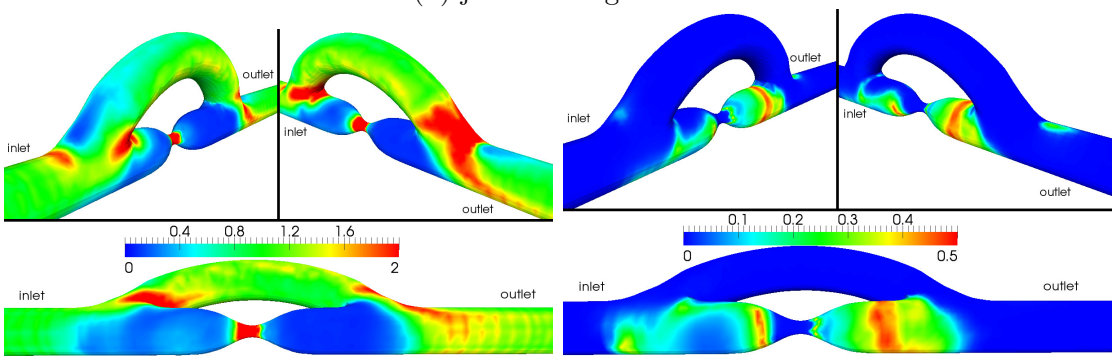

(c) junction angle: 55°

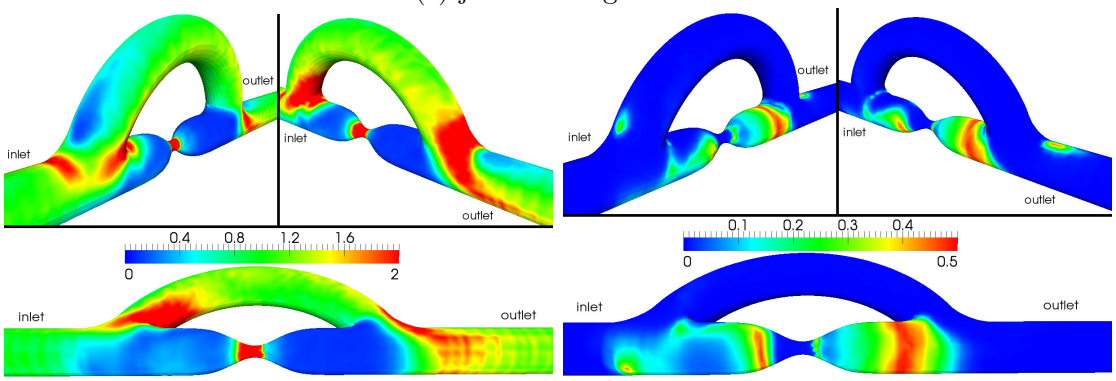

(d) junction angle: 70°

Fig. 5.28. Distribution of normalised cycle-averaged WSS magnitude (*left*) and OSI (*right*) for four bypass models with different junction angles α. Values corresponding to the reference bypass model are shown in Fig. 5.26 (left).

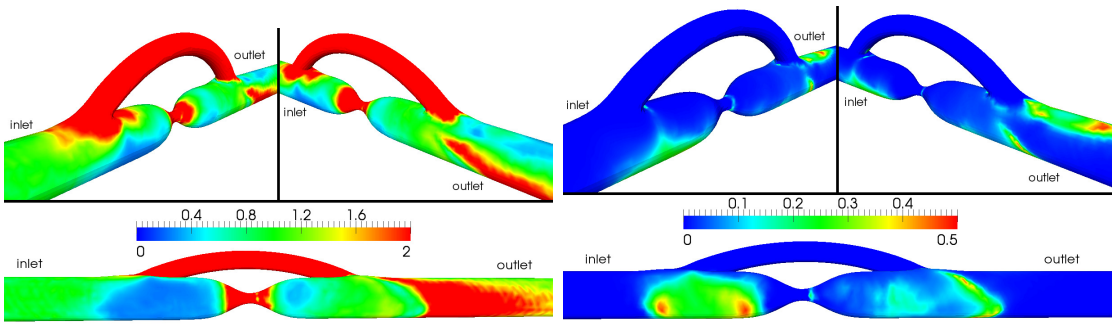

(a) diameter ratio: 1:0.5

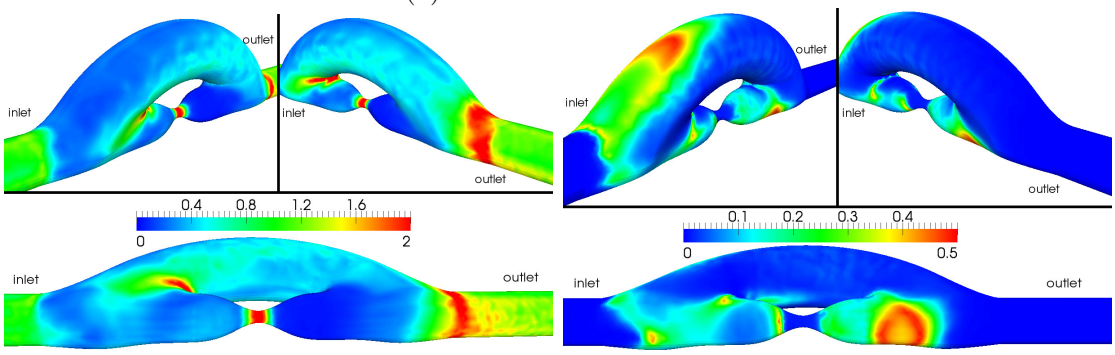

(b) diameter ratio: 1:1.5

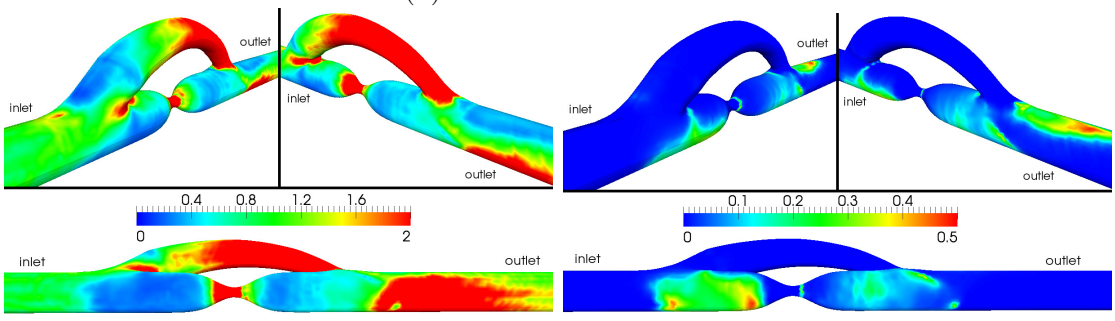

(c) diameter ratio: 1:1∼0.5

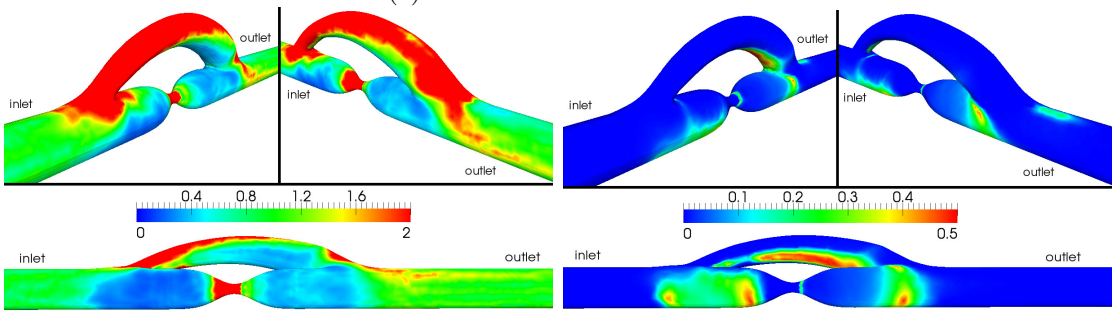

(d) diameter ratio: 1:0.5∼1

Fig. 5.29. Distribution of normalised cycle-averaged WSS magnitude (*left*) and OSI (*right*) for the bypass models with constant and varying diameter ratios $D : d$. Values corresponding to the reference bypass model are shown in Fig. 5.26 (left).

the region before the stenosis tends to decrease with decreasing graft diameter, whereas the shear oscillations increase in the post-stenosis area.

The graft diameter at both anastomoses, as well as its variation along the bypass, plays an important role in all three mentioned areas. For example, the tapered graft tends to suppress shear oscillations behind the stenosis and at the arterial floor but at the cost of very high OSI values at the arterial ceiling, as can be seen from comparing Fig. 5.29c (right) with Fig. 5.29a (right) and Fig. 5.26 (right). A different behaviour is noted for the widening graft. Here, the gradual diameter increase eliminates almost all oscillations near the toe region and even suppresses high shear oscillations at the graft entrance and in the post-stenotic region, as can be seen from comparing Fig. 5.29d (right) with Fig. 5.26 (right). However, the geometry of the widening graft promotes shear oscillations in regions that were previously unaffected, such as the lower part of the bypass graft, which is characterised by very high OSI values, Fig. 5.29d (right).

5.2.4 Discussion of results

When determining the suitability of a bypass geometry for potential use in clinical practice, it is necessary to take into consideration various factors and their impact on performance and patency of implanted bypass grafts, see Section 3.3. In the following discussion, the obtained results are evaluated on the basis of these factors such as potential tissue damage, risk of thrombosis and the presence of low and oscillating WSS.

Stenosis degree: Although the stenosis degree in bypasses is a geometrical parameter that the surgeon cannot change and the value of which increases continuously due to the growth of the atherosclerotic plaque, its significance in arterial grafting is not negligible, particularly when evaluating the possibility of bypass failure. In this sense, the differences in the numerical results for the smallest stenosis degree (50%) and the remaining models ($\geq$65%) reflect the fact that arterial stenoses smaller than 50% are commonly described as hemodynamically insignificant. In other words, arterial stenoses below the critical value of 50% do not seem to have any significant impact on blood supply to downstream tissues. Hence, the grafting of such arteries may have no clear benefit for the patient. In addition, a low flow rate in the graft would considerably enhance the risk of graft closure due to thrombosis, see the thrombotic threshold velocity (TTV) mentioned in Section 3.3.

Junction angle: In contrast to the stenosis degree, the junction angle is a parameter that may be chosen by the surgeon. According to the numerical results presented above, low angles show a tendency to favourably influence the presence of low and oscillating WSS at the distal anastomosis near the toe. In this regard, excessively large anastomotic angles should be avoided during surgeries if possible, as they often lead to considerable skew of the flow at the graft entrance; see, for example, the 3D velocity profiles in Figs. 5.20–5.22. However, a smaller angle increases the injury to the healthy tissue of the native artery, and a longer suture line is necessary for the anastomosis. A longer incision also represents a certain risk to the bypassed artery due to its irreversible damage or even destruction. In this sense, the best choice appears to be a middle path that ensures a relatively uniform flow field but does not require a complicated implementation technique.

Diameter ratio: According to our observations, the diameter ratio, defined as the diameter of the native artery relative to the graft diameter, is the most crucial parameter for coronary artery bypass grafting (CABG). The computed flow fields and shear results are strongly sensitive to the diameter mismatch between both vessels. Moreover, the diameter ratio not only influences the vicinity of both anastomoses but affects the global hemodynamics. Considering all the factors (velocity, WSS, OSI) involved in the evaluation of a bypass geometry, each of the considered graft configurations exhibits advantages and disadvantages. The major disadvantage of the small-diameter graft ($d \leq 0.5D$) is that the healing process at both anastomoses, which is known to be closely connected with the formation of a neointimal layer in synthetic grafts [61], would further decrease the diameter of the graft and considerably enhance the risk of bypass failure due to the loss of patency. Conversely, the permanent presence of several large-sized recirculation zones in the large-diameter grafts ($d \geq 1.5D$) would naturally affect the risk of thrombosis due to the possibility of blood cell accumulation [16]. The geometry of the tapered graft, which is, in some way, used as a reversed venous graft due to the presence of valves, yields flow and shear results similar to the model with $D : d$ =1:0.5. Although the observations are consistent with our expectations, the tapered graft has extreme effects on the skew of the flow and shear oscillations, particularly downstream from the distal anastomosis; see the 2D slices in Figs. 5.23–5.25 and the OSI in Fig. 5.29c (right). Significantly more favourable shear stimulation at the arterial ceiling can be achieved for the widening graft. Unfortunately, the presence of the recirculation zone and low and oscillating WSS near the lower wall of this graft reduces all the benefits of this bypass geometry due to the enhanced risk of thrombus formation, Fig. 5.29d.

5.2.5 Conclusion

In light of the observations made in this section, it is possible to conclude that the most important geometrical parameter for bypass grafting seems to be the diameter ratio $D : d$. The pulsatile blood flow and the values of WSS and OSI show to be very sensitive to changes in the graft diameter. Overall, the most favourable flow field can be most likely observed for the reference bypass model with a diameter ratio $D : d$ =1:1. With this in mind, it can be concluded that grafts with diameters close to the diameter of the native artery would yield more advantageous hemodynamics while reducing the probability of bypass failure due to thrombosis or intimal hyperplasia.

5.3 Pulsatile non-Newtonian blood flow in realistic aorto-coronary bypass models

Taking advantage of the latest medical imaging techniques (CT, MRI, ...), the research in the field of bypass hemodynamics is currently being directed towards patient-specific modelling. As seen in one of the recent studies [162], bypass geometries reconstructed from CT/MRI scans are gradually preferred to the idealised ones because of their potential to bring the research closer to the clinical practice and consequently to the medical community. With this in mind, the present section is primarily focused on the use of patient-specific models that include grafting techniques commonly used for aorto-

coronary bypasses. Note that some of the numerical results were presented at selected conferences [B.12–B.17] and published in a peer-reviewed journal [A.7].

The numerical simulation of pulsatile blood flow is carried out in three different geometries reconstructed from CT scans, Figs. 5.30–5.31, provided by the courtesy of the University Hospital in Pilsen. The primary reconstruction process is carried out in software Amira (Visualization Sciences Group, Burlington, USA) and finished in the commercial software package HyperMesh (Altair Engineering, Troy, USA). Depending on the number of coronary arteries bypassed in the grafting procedure, the three reconstructed models are further denoted as single, double and triple bypasses with individual and/or sequential grafts, Fig. 5.32. The term individual or sequential graft refers to an implanted venous graft with one or at least two distal anastomoses, respectively. Further relevant terminology for each of the three aorto-coronary bypasses is mentioned in Fig. 5.32, which also shows the unstructured tetrahedral computational meshes generated with the help of the commercial software package HyperMesh (Altair Engineering, Troy, USA) and refined in the vicinity of all walls in order to resolve the boundary layer with sufficient accuracy. The number of tetrahedral cells required to model the single, double and triple bypasses shown in Fig. 5.32 is 362 437, 476 241 and 879 480, respectively.

All the necessary general assumptions for the current flow problem were established

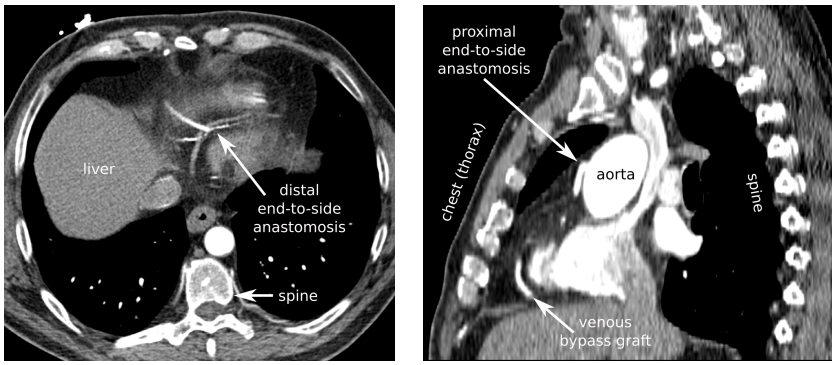

Fig. 5.30. Single aorto-coronary bypass – selected axial (*left*) and sagittal (*right*) CT scans of the chest region.

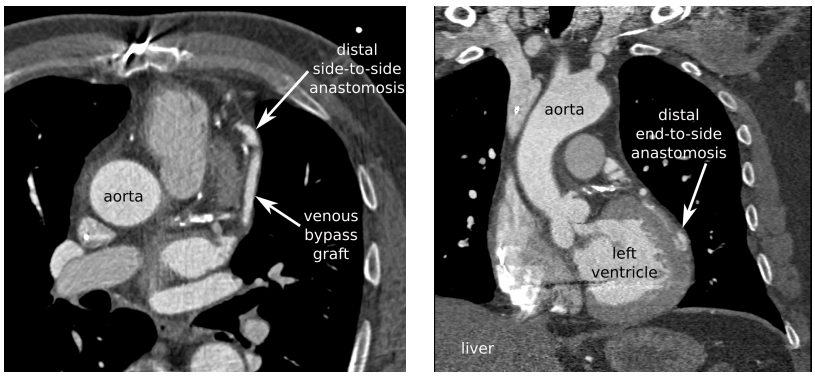

Fig. 5.31. Double aorto-coronary bypass – selected axial (*left*) and coronal (*right*) CT scans of the chest region.

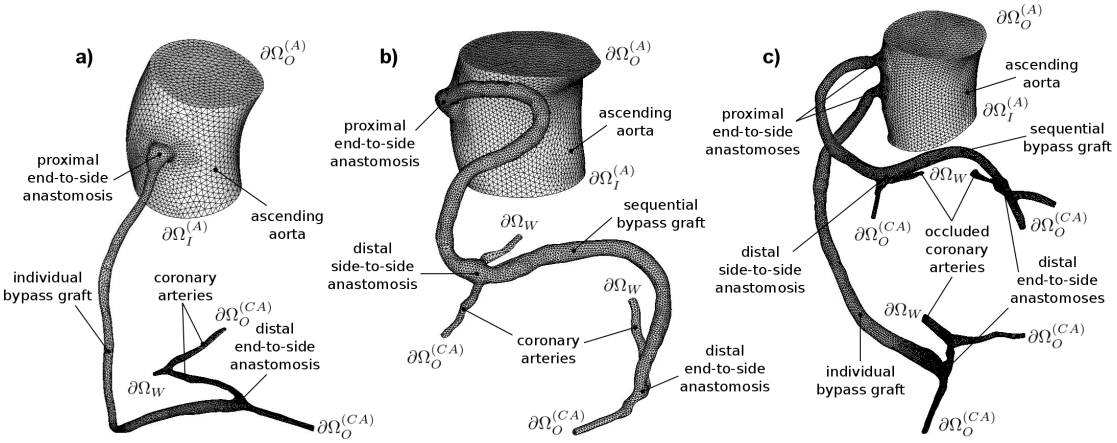

Fig. 5.32. Unstructured tetrahedral computational meshes for the single (a), double (b), and triple (c) aorto-coronary bypass with corresponding computational domain boundaries and relevant terminology.

at the beginning of Chapter 4, making the blood rheology the only issue that needs to be addressed in more detail. While Section 5.1 included an analysis of blood's non-Newtonian behaviour by means of two constitutive models, the present section assumes the blood to be an incompressible generalised Newtonian fluid with constant density $\varrho = 1050\,\mathrm{kg\,m^{-3}}$, whose shear-dependent dynamic viscosity is described only by one non-Newtonian model – the Carreau-Yasuda model (4.2). Also for the sake of comparison, the dynamic viscosity of blood modelled as a Newtonian fluid is chosen to be equal to the infinite viscosity η_∞ of the Carreau-Yasuda model.

The mathematical model describing the pulsatile blood in the three considered bypass models has the form of the non-linear system of Navier-Stokes equations (4.87)–(4.88) for the Newtonian ($\theta = 0$) and non-Newtonian ($\theta = 1$) fluids. For the non-dimensionalisation of the governing equations according to Section 4.1, the reference values are chosen as:

$$\left.\begin{array}{ll} L_{ref} \equiv D_{(A)} = 0.036\,\mathrm{m}, & \varrho_{ref} = 1050\,\mathrm{kg\,m^{-3}}, \\ U_{ref} = \frac{4\,Q_0}{\pi\,D_{(A)}^2} = 0.1592\,\mathrm{m\,s^{-1}}, & \eta_{ref} = 0.00345\,\mathrm{Pa\,s}, \end{array}\right\} \mathrm{Re} = \frac{U_{ref}\,L_{ref}\,\varrho_{ref}}{\eta_{ref}} = 1\,744.3,$$

where $D_{(A)}$ is the diameter of the ascending aorta and $Q_0 = 112.56\,\mathrm{ml\,s^{-1}}$ is the average aortic inlet flow rate determined from the waveform shown in Fig. 5.33 (left). The numerical solution of the dimensionless equations (4.87)–(4.88) is carried out in the sense of the stabilised projection method and the cell-centred finite volume method formulated for hybrid unstructured tetrahedral grids. In accordance with the principles described in Section 4.4.2, the dimensionless time step Δt is set equal to the value of 0.0884, which corresponds to 50 time levels per one cardiac cycle period. The under-relaxation parameter α in Eq. (4.156) is chosen as 0.7.

In this section, the assumption of flow conditions at rest is adopted in all three aorto-coronary bypass models. Partly due to unavailability of patient-specific data, and partly because of our attempt to compare the three bypass models with each other, the same flow conditions are applied in all models, Fig. 5.32:

- **aortic inlet** $\partial\Omega_{hI}^{(A)}$ – constant time-dependent velocity profile $|\boldsymbol{v}_I|$ computed from the flow rate waveform shown in Fig. 5.33 (left). Note that according to the authors of [124], the non-parabolic velocity profile used as an inlet boundary condition for the ascending aorta is preferable to the parabolic one, especially if measured 3D data are unavailable;
- **aortic outlet** $\partial\Omega_{hO}^{(A)}$ – time-dependent outlet pressure $p_O^{(A)}$ corresponding to the pressure waveform shown in Fig. 5.33 (right);
- **coronary artery outlets** $\partial\Omega_{hO}^{(CA)}$ – two different approaches:
  - *Section 5.3.1:* constant outlet pressure $p_O^{(CA)}$ corresponding to the average arterial blood pressure of 12 000 Pa is prescribed at all outlets;
  - *Section 5.3.2:* each outlet is coupled to one three-element Windkessel model. For more details on lumped (0D) models, see Appendix C;
- **impermeable and rigid walls, occluded proximal coronary arteries** $\partial\Omega_{hW}$ – non-slip boundary condition, i.e., $\boldsymbol{v} = \boldsymbol{0}$.

At corresponding boundaries of the computational domain $\Omega_h \subset \mathbb{R}^3$, the remaining primitive variables are extrapolated from the flow field.

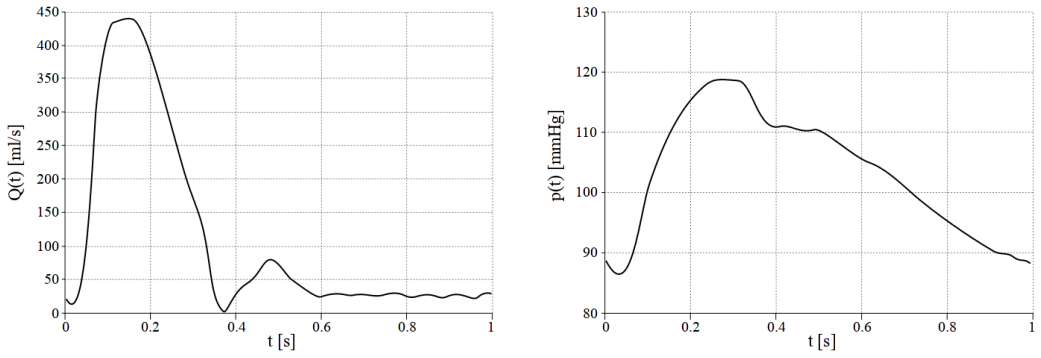

Fig. 5.33. Waveforms of flow rate $Q(t)$ [ml s^{-1}] (*left*) and pressure $p(t)$ [mmHg, 1 mmHg = 133.333 Pa] (*right*) prescribed at the inlet $\partial\Omega_{hI}^{(A)}$ and outlet $\partial\Omega_{hO}^{(A)}$ of the ascending aorta, respectively. The waveforms are taken from [135].

At this point, it is appropriate to mention that all numerical results presented in this section and achieved after three full cardiac cycle periods are shown in the dimensional form using the reference values mentioned above. For the flow field analysis, we also employ three selected time instants of the cardiac cycle ($t_1 = 0.16\,\mathrm{s}$, $t_2 = 0.48\,\mathrm{s}$ and $t_3 = 0.80\,\mathrm{s}$) with regard to their importance in the phases of the heartbeat (systole, early diastole and late diastole, respectively). The distribution of hemodynamical wall parameters is evaluated by means the cycle-averaged wall shear stress (WSS) and oscillatory shear index (OSI)

$$\mathrm{WSS} = \frac{1}{T}\int_0^T |\boldsymbol{\tau}_W|\,\mathrm{d}t, \qquad \mathrm{OSI} = \frac{1}{2}\left(1 - \frac{\left|\int_0^T \boldsymbol{\tau}_W\,\mathrm{d}t\right|}{\int_0^T |\boldsymbol{\tau}_W|\,\mathrm{d}t}\right), \tag{5.5}$$

where $\boldsymbol{\tau}_W$ is the WSS vector and T is the period of the cardiac cycle. To evaluate the presence of non-Newtonian effects and to assess their importance within the bypass

models, the following quantities are further introduced:

$$\Delta\mathrm{WSS} = \mathrm{WSS}|_{\text{non-New}} - \mathrm{WSS}|_{\text{New}}\,, \qquad \Delta\mathrm{OSI} = \mathrm{OSI}|_{\text{non-New}} - \mathrm{OSI}|_{\text{New}}\,, \tag{5.6}$$

where the subscripts 'non-New' and 'New' denote values corresponding to non-Newtonian and Newtonian flow, respectively.

5.3.1 Analysis of non-Newtonian effects

As apparent from the title, the main interest of this section is in the analysis of pulsatile non-Newtonian blood flow in the three aorto-coronary bypass models reconstructed from CT scans. The rheological behaviour of blood is studied in relevant areas of the bypass grafts provided the pressure at all coronary artery outlets corresponds to the constant average arterial pressure. Lastly, note that the numerical results obtained for the non-Newtonian blood flow are also used in the following subsection as a mean of comparison.

A) Blood flow in the bypass grafts

To assess the Newtonian and non-Newtonian flow fields in the individual and sequential grafts, Tab. 5.7 summarises the values of the mean and maximum Reynolds numbers ($\mathrm{Re}_{\mathrm{mean}}$ and $\mathrm{Re}_{\mathrm{max}}$) at the upstream end of the grafts and, in the case of the sequential grafts, also between both distal anastomoses. From the overview, two things become immediately apparent. The first one is related to the values of the maximum Reynolds number, which, regardless of the bypass type, remain below 820 and support our assumption of laminar blood flow made at the beginning of Chapter 4[2].The second observation is based on the minimal differences between the Newtonian and non-Newtonian values ($\Delta \leq 3.6$), which are indicative of almost identical flow fields, and consequently negligible non-Newtonian effects.

The flow pulsatility in the bypass grafts, which is given by the prescribed boundary conditions and characterised by the Womersley number ranging from 2–3.5, is very well apparent from the non-Newtonian flow rate waveforms shown in Fig. 5.34. The

[2] According to [107], the critical Reynolds number for blood flow is around 2 100.

aorto-coronary bypass		D_{av} [mm]	$\mathrm{Re}_{\mathrm{mean}}$ [−]			$\mathrm{Re}_{\mathrm{max}}$ [−]		
			New	non-New	Δ	New	non-New	Δ
single	indiv.	3.0	214.5	210.9	3.6	370.4	366.8	3.6
double	seq. (1^{st})	4.7	338.6	336.0	2.6	560.5	558.0	2.5
	seq. (2^{nd})	5.1	187.0	185.4	1.6	295.6	294.3	1.3
triple	indiv.	4.4	264.6	261.9	2.7	450.0	447.6	2.4
	seq. (1^{st})	4.0	488.1	484.6	3.5	817.7	814.7	3.0
	seq. (2^{nd})	4.2	379.6	376.8	2.8	629.5	627.1	2.4

Tab. 5.7. Mean and maximum Reynolds numbers computed for the Newtonian and non-Newtonian flows in the upstream parts of the individual and sequential grafts with average diameter D_{av}. Here, '1^{st}' and '2^{nd}' denote the first and second half of the sequential graft before and after the side-to-side anastomosis, respectively, and Δ is the absolute difference between the Newtonian and non-Newtonian values.

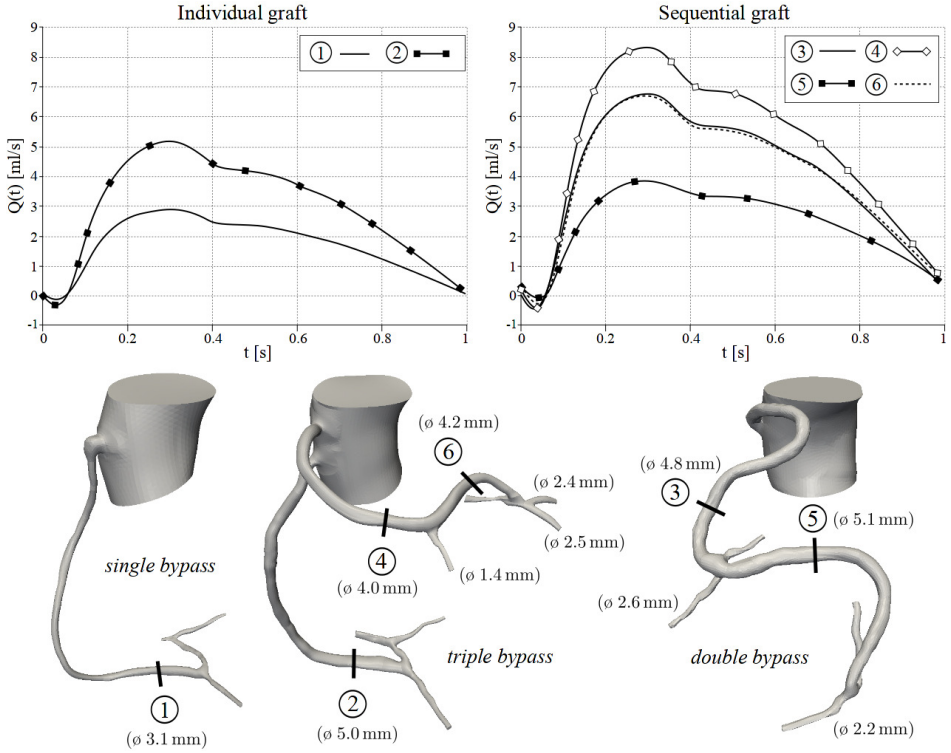

Fig. 5.34. Non-Newtonian flow rate waveforms in the individual and sequential grafts of the three aorto-coronary bypasses. The location of each displayed waveform 1–6 is denoted in the models with corresponding average diameter. The diameter of each coronary artery at the distal anastomoses of the sequential grafts are given, as well.

waveforms for the downstream end of the individual and sequential grafts demonstrate qualitatively similar features with a short back flow phase at the beginning of the cardiac cycle and maximum flow rate at time around 0.3 s. It is also important to note that the short phase of the negative flow rate is a result of our prescribed boundary conditions and not a normal phenomenon. In other words, the occurrence of back flow in the considered bypass models is caused by the reversed pressure drop within the computational domain, i.e., the aortic outlet pressure $p_O^{(A)}$ becomes smaller than the coronary one $p_O^{(CA)}$.

As shown in Fig. 5.34, the blood flow in the four grafts is strongly affected by the diameter of the vessels involved in the bypassing. A very good example is given by the sequential grafts. Here, the use of the reversed saphenous vein as a bypassing conduit is partly responsible for the lower flow rates observed in the second part of the grafts, i.e., the continuously increasing graft diameter contributes to lower flow velocities as can be seen from comparing the average graft diameters in Tab. 5.7 and Fig. 5.34. Another significant parameter determining the flow rate in the relevant parts of the sequential graft is the coronary diameter at the side-to-side and end-to-side anastomoses. In the case of the double bypass, the graft experiences a considerable flow decrease after the side-to-side anastomosis due to wider artery at the first outflow (2.6 mm compared to the average diameter of 2.2 mm at the second outflow, see Fig. 5.34). By contrast, the amount of blood removed at the side-to-side anastomosis of the triple bypass is much lower because

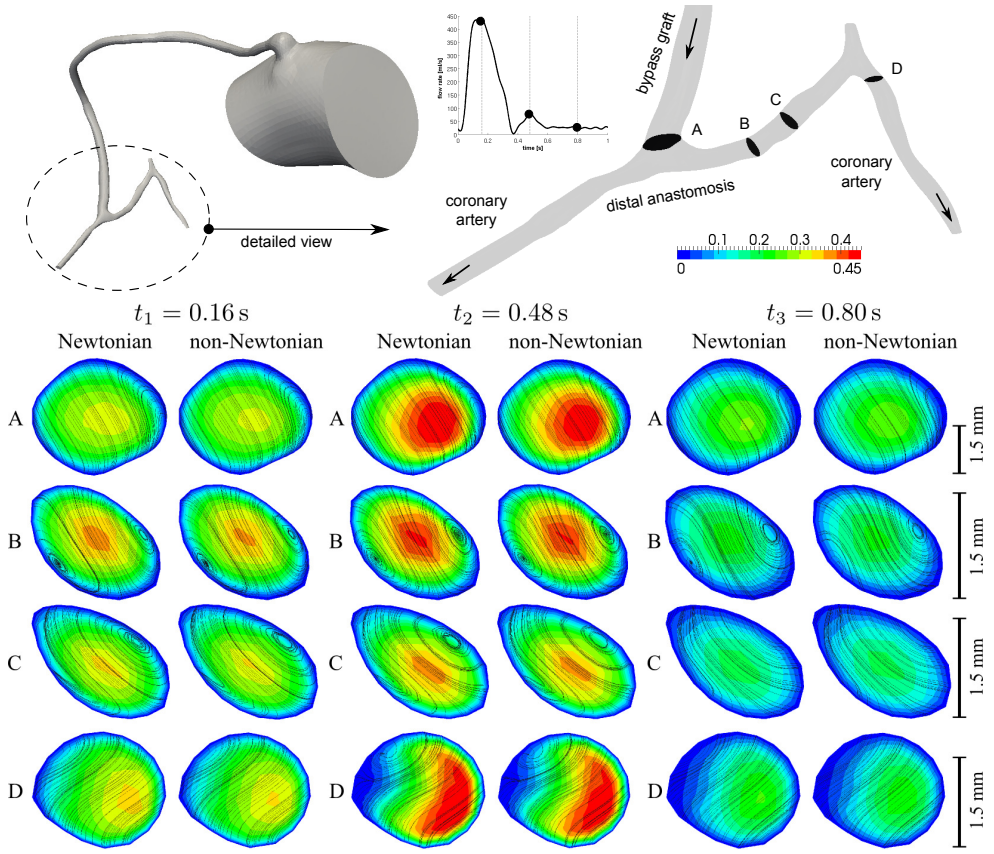

Fig. 5.35. Iso-surfaces of velocity magnitude with secondary flow streamlines at four selected cross-sections in the distal end-to-side anastomosis of the single bypass model. The Newtonian and non-Newtonian results are shown with a maximum value range of $0.45\,\mathrm{m\,s^{-1}}$ at three different time instants of the cardiac cycle ($t_1 = 0.16\,\mathrm{s}$, $t_2 = 0.48\,\mathrm{s}$, $t_3 = 0.80\,\mathrm{s}$). To represent the true size of each cross-section, the reference scale of 1.5 mm is given at the right side of each row.

the diameter of the native artery at the first outflow (1.4 mm) is significantly smaller than that of the downstream arteries (2.4 mm and 2.5 mm). Overall, a small decrease of flow rate in the second part of the graft is desirable, because it usually means lower risk of thrombosis and higher patency rate of the implanted bypass graft [51, 191].

B) Velocity distribution and secondary flow patterns

As pointed out above, the parameters of the graft and coronary arteries can significantly affect the resulting blood flow, which in turn may consequently determine the long-term patency of the implanted bypass grafts. By comparing Figs. 5.35–5.37 for the three aorto-coronary bypasses, it becomes also apparent that the velocity distribution in the vicinity of each distal anastomosis is strongly influenced by the geometry of the anastomosis and the connected native artery. See, for example, the cross-sections B in Fig. 5.36 or A in Fig. 5.37. As for the much higher velocity magnitude observed in several cross-sections such as A in Fig. 5.36, its cause is to be sought in the higher flow rate and

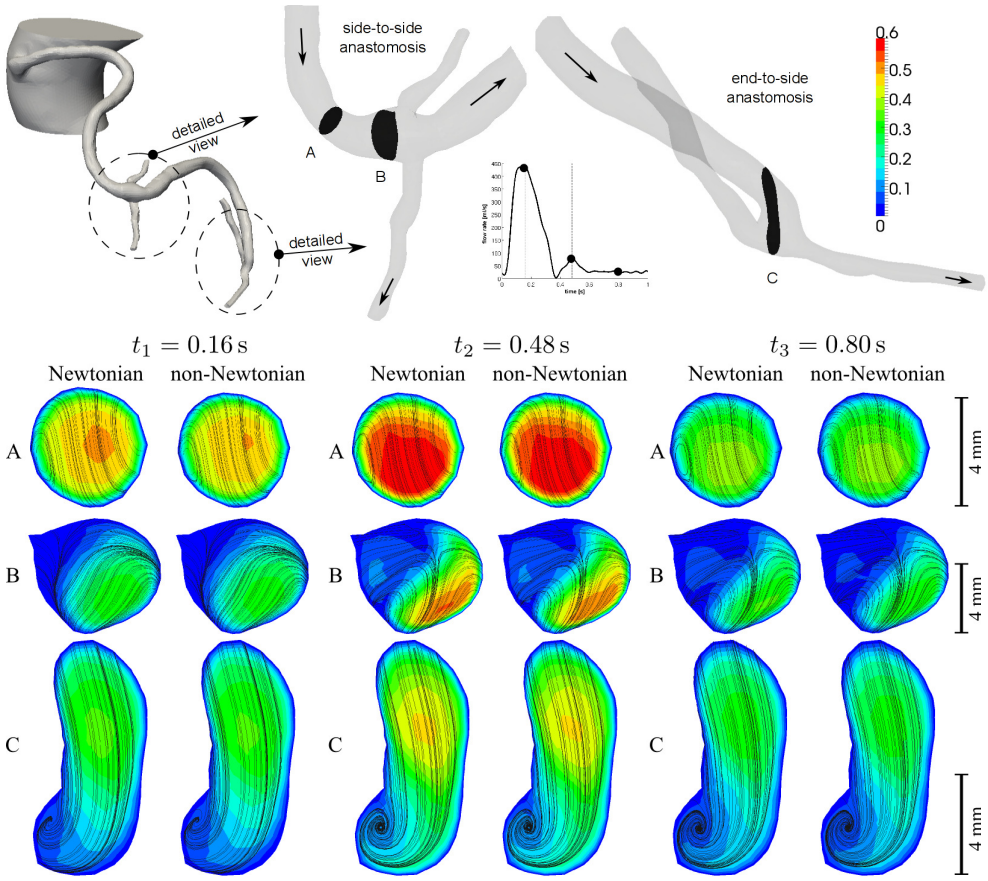

Fig. 5.36. Iso-surfaces of velocity magnitude with secondary flow streamlines at three selected cross-sections in the distal side-to-side and end-to-side anastomoses of the double bypass model. The Newtonian and non-Newtonian results are shown with a maximum value range of $0.6\,\mathrm{m\,s^{-1}}$ at three different time instants of the cardiac cycle ($t_1 = 0.16\,\mathrm{s}$, $t_2 = 0.48\,\mathrm{s}$, $t_3 = 0.80\,\mathrm{s}$). To represent the true size of each cross-section, the reference scale of 4 mm is given at the right side of each row.

narrower diameter of the sequential graft. Further, it can be noted that from the three time instants displayed in Figs. 5.35–5.37, only the early diastole ($t_2 = 0.48\,\mathrm{s}$) gives any indication of enhanced flow and blood filling of the graft and coronary arteries, which is in accordance with the flow waveforms shown in Fig. 5.34.

Different behaviour between the three considered bypasses can be observed in relation to secondary flow. In the case of the single bypass, the secondary motion of the fluid is mostly restricted to the proximal branch of the occluded coronary artery (cross-sections B and C in Fig. 5.35), where it remains almost unchanged most of the cardiac cycle. In contrast to this, the secondary flow in the double and triple bypasses demonstrates a strong dependence on the incoming flow, especially during diastole when the motion becomes particularly pronounced (cross-sections B and C in Fig. 5.36 and C and D in Fig. 5.37). The effect of non-Newtonian rheology of blood on pulsatile flow in the three aorto-coronary bypasses can be noted in slightly reduced peak velocities, as can be seen from the cross-section A in Fig. 5.36. Otherwise, the effect of shear-dependent viscosity

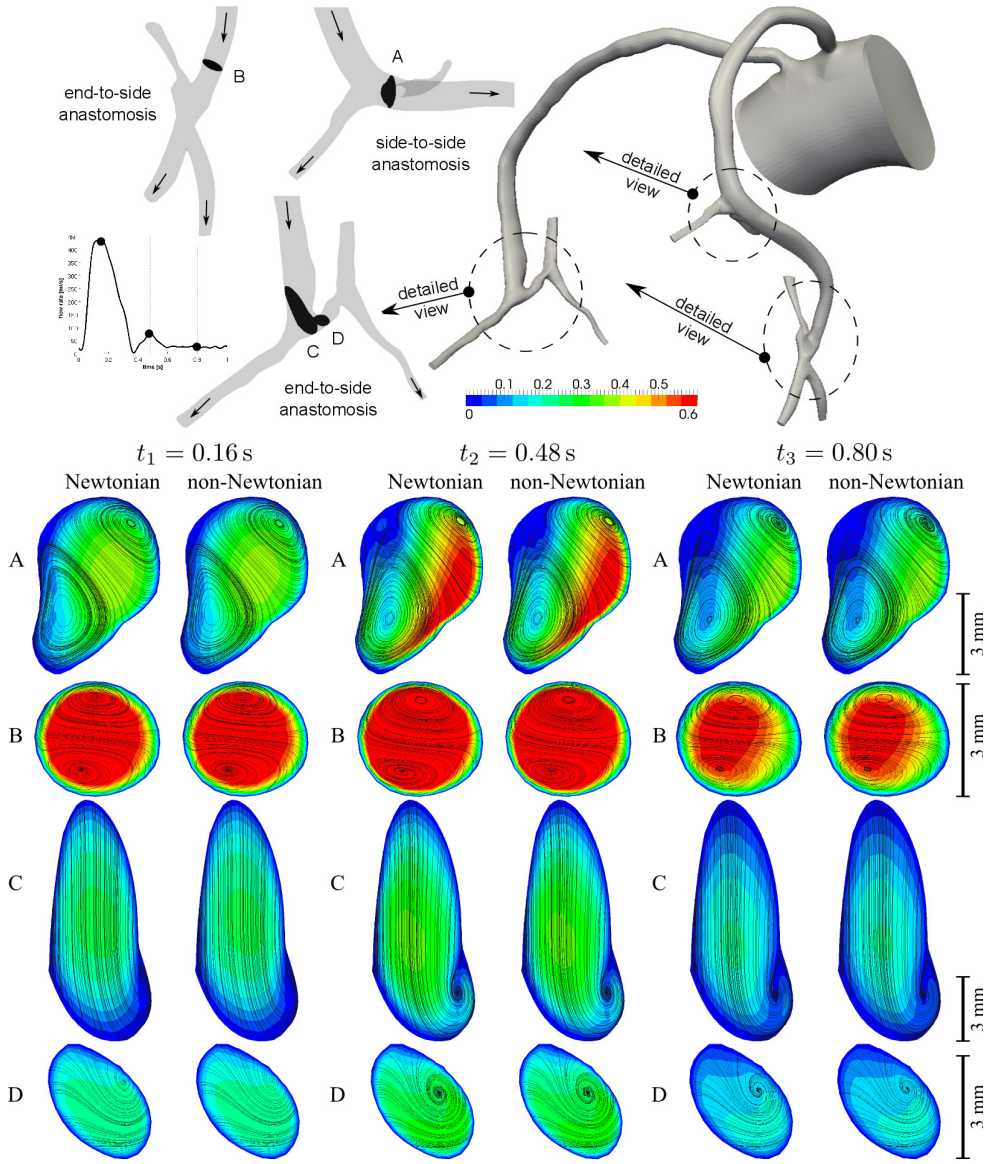

Fig. 5.37. Iso-surfaces of velocity magnitude with secondary flow streamlines at four selected cross-sections in the individual and sequential grafts of the triple bypass model. The Newtonian and non-Newtonian results are shown with a maximum value range of $0.6\,\mathrm{m\,s^{-1}}$ at three different time instants of the cardiac cycle ($t_1 = 0.16\,\mathrm{s}$, $t_2 = 0.48\,\mathrm{s}$, $t_3 = 0.80\,\mathrm{s}$). To represent the true size of each cross-section, the reference scale of 3 mm is given at the right side of each row.

on the distribution of velocity is rather insignificant, supporting our earlier observation of negligible non-Newtonian effects mentioned in connection with Tab. 5.7.

C) Wall shear stress and oscillatory shear index

As intimal hyperplasia is associated with low and oscillating shear stress ($|\boldsymbol{\tau}_W| < 0.5\,\mathrm{Pa}$ [52]), all cycle-averaged WSS results presented in this section are shown with lowered value ranges between 0 and 3 Pa. In this sense, the distal end-to-side anastomosis of the

single bypass is characterised by a distinct area with lower WSS localised opposite the entrance of the graft and along the suture line, Fig. 5.38b. Besides lower shear values, the area in the vicinity of the suture line also exhibits a tendency to high shear oscillations as is very well apparent from the OSI distributions in Fig. 5.39b. It is interesting to note that by introducing blood's non-Newtonian viscosity, the values of both hemodynamical wall parameters WSS and OSI tend to be affected rather negatively. In other words, low WSS is further decreased ($\Delta\text{WSS} < 0$ in Fig. 5.38(right)) and the intensity of shear stress oscillations increases in the relevant areas of the distal anastomosis ($\Delta\text{OSI} > 0$ in Fig. 5.39(right)). This phenomenon, especially in connection with intimal thickening, which is known to be stimulated by low and oscillating shear stress, is undesirable. On the other hand, it is important to note that the differences between both flows are very small in most areas of the single bypass ($|\Delta\text{WSS}| \leq 0.3\,\text{Pa}$ and $|\Delta\text{OSI}| \leq 0.05$).

The distribution of WSS in the double bypass reveals higher shear stimulation in the first half of the sequential graft up to the side-to-side anastomosis, Fig. 5.40a. This result is in agreement with intraoperative observations that for the sequential graft indicate higher blood flow and WSS in the proximal segment of the implanted bypass graft [51, 191]. On the other hand, the decrease of WSS values in the second part of the sequential graft is closely connected with the flow field, which is known to be strongly affected by the diameter of the vessels involved in the bypassing, as mentioned above. This assumption is further supported by the high WSS values that can be found along the sequential graft of the triple bypass, Fig. 5.43a, and that are the result of small decrease of flow rate downstream from the side-to-side anastomosis, see Fig. 5.34.

Regarding the presence of almost zero WSS values in the proximal part of both coronary arteries of the double bypass, it is important to mention that both arteries are modelled as occluded, which in turn results in two large 'dead water' zones and no shear stimulation. As is apparent from the detailed views in Fig. 5.40b,c, the flow stagnation also influences the immediate vicinity of both distal anastomoses, which particularly in the case of the side-to-side anastomosis exhibits a tendency to shear oscillations ($\text{OSI} > 0$ in Fig. 5.42a). Similarly to the previous bypass model, non-Newtonian blood flow in the double bypass is characterised by localised changes of shear stress. For example, one of the areas, where the non-Newtonian behaviour of blood has a positive impact on WSS and OSI, is the curvature of the venous graft at the side-to-side anastomosis. Here, the non-Newtonian flow exhibits a tendency to increase shear stress ($\Delta\text{WSS} > 0$ in Fig. 5.41b), while decreasing its oscillation ($\Delta\text{OSI} < 0$ in Fig. 5.42b). Otherwise, the WSS and OSI differences between the non-Newtonian and Newtonian flows are mostly below 0.1 Pa, Fig. 5.41, and 0.05, Fig. 5.42, respectively.

For the distal anastomoses of the triple bypass, Fig. 5.43 and 5.45, it is possible to observe WSS and OSI distributions similar to those at the anastomoses of the single and double bypass models. In this case, the end-to-side anastomosis of the individual graft may serve as an example, since its arterial floor is also characterised by a lower shear stress area opposite the graft entrance, as can be seen from comparing Fig. 5.38b and Fig. 5.43d. Regarding the influence of blood's non-Newtonian viscosity on shear stress in the triple bypass, most WSS and OSI changes are observed to be around 0.1 Pa, Fig. 5.44, and 0.05, Fig. 5.45, respectively.

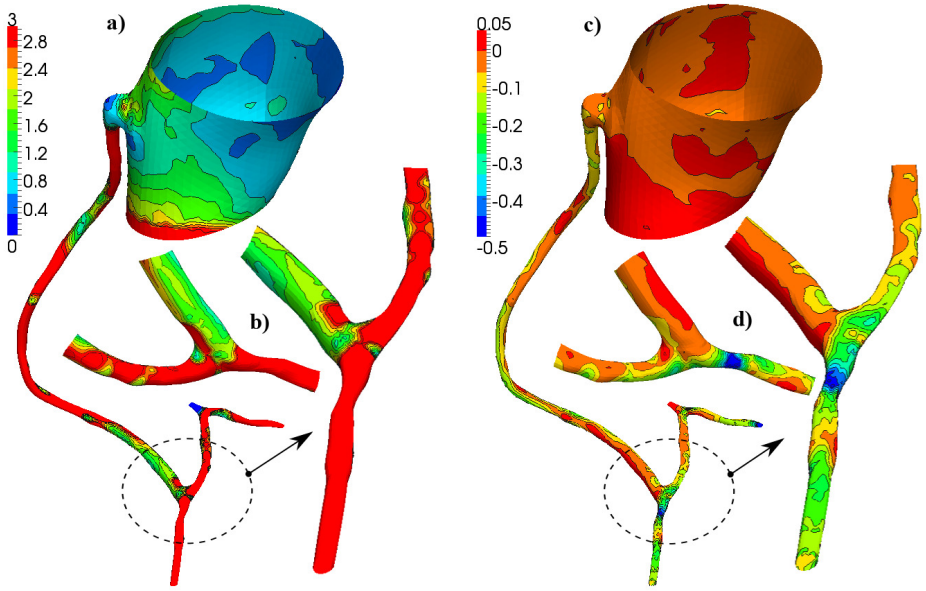

Fig. 5.38. Non-Newtonian cycle-averaged WSS magnitude (*left*) and ΔWSS (*right*) for the single bypass model with two detailed views at the distal end-to-side anastomosis. Note that the WSS results on the left are shown with lowered value ranges between 0 and 3 Pa.

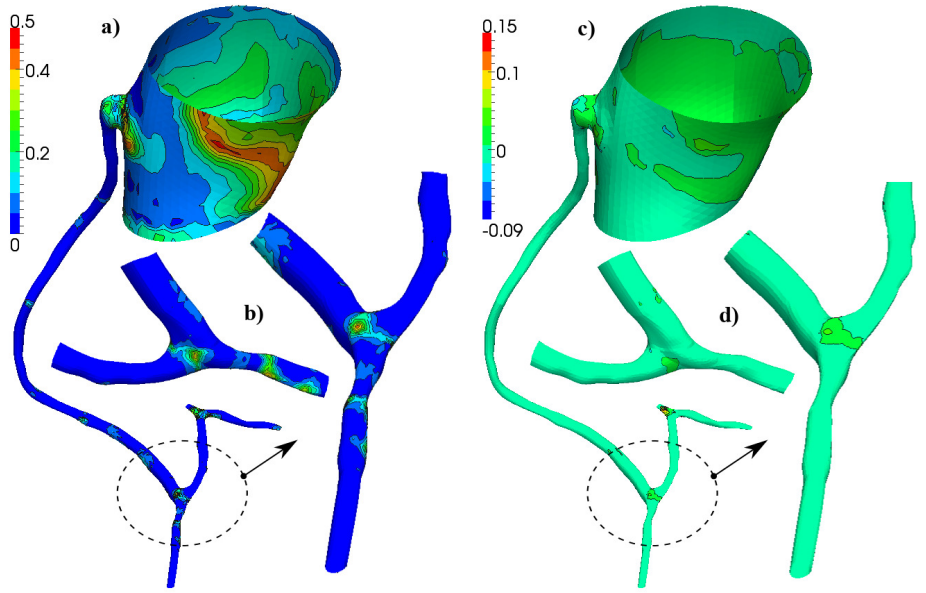

Fig. 5.39. Non-Newtonian OSI (*left*) and ΔOSI (*right*) for the single bypass model with two detailed views at the distal end-to-side anastomosis with the branch of the right coronary artery.

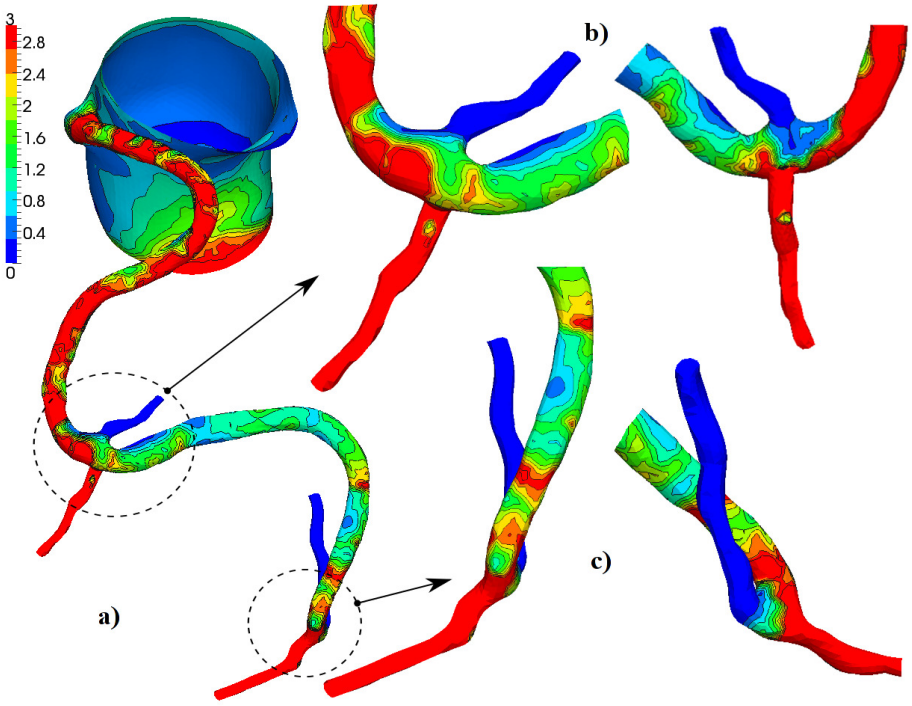

Fig. 5.40. Non-Newtonian cycle-averaged WSS magnitude for the double bypass model (a) with detailed views at the distal side-to-side (b) and end-to-side (c) anastomoses. Note that the results are shown with lowered value ranges between 0 and 3 Pa.

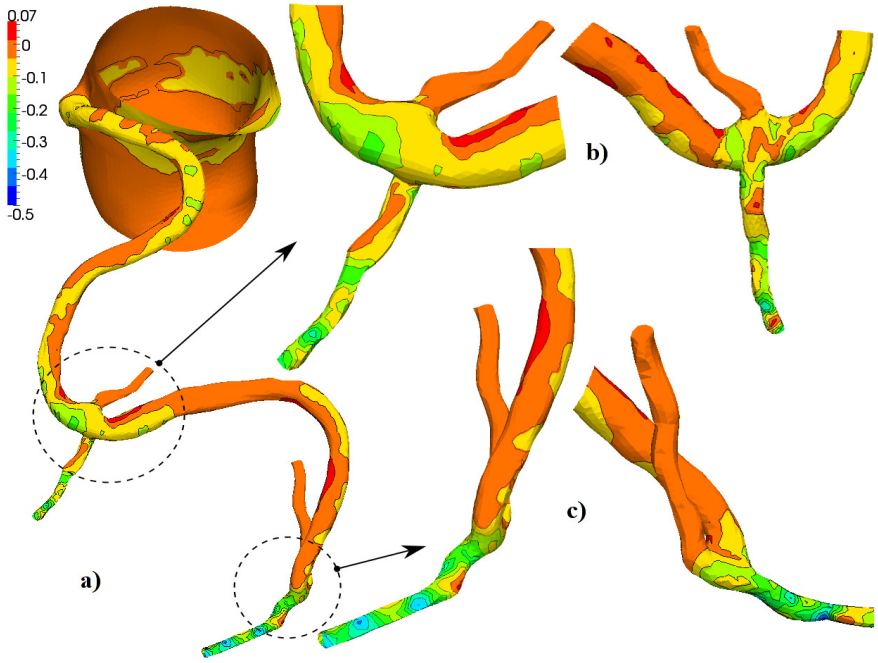

Fig. 5.41. ΔWSS for the double bypass model (a) with detailed views at the distal side-to-side (b) and end-to-side (c) anastomoses.

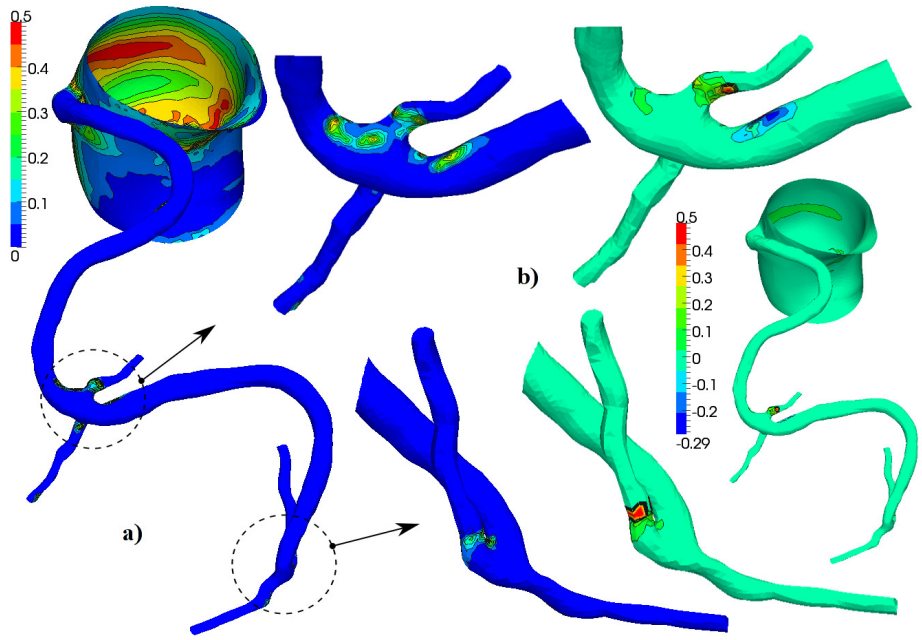

Fig. 5.42. Non-Newtonian OSI (a) and ΔOSI (b) for the double bypass model with detailed views at both distal anastomoses.

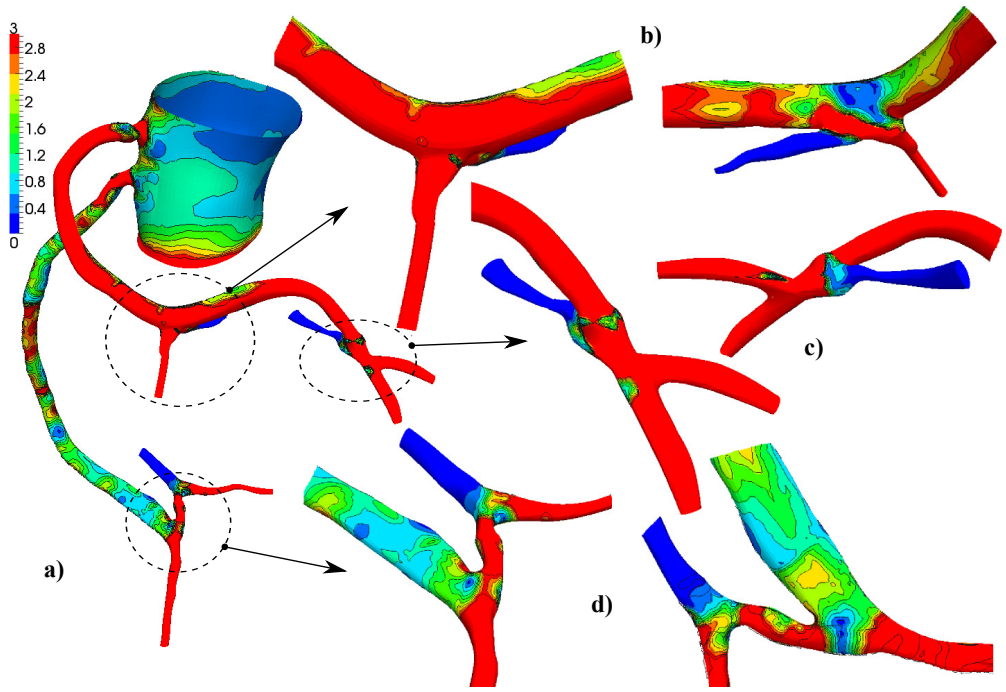

Fig. 5.43. Non-Newtonian cycle-averaged WSS magnitude for the triple bypass model (a) with detailed views at the distal side-to-side (b) and end-to-side (c) anastomoses of the sequential graft and at the distal end-to-side anastomosis (d) of individual graft. Note that the results are shown with lowered value ranges between 0 – 3 Pa.

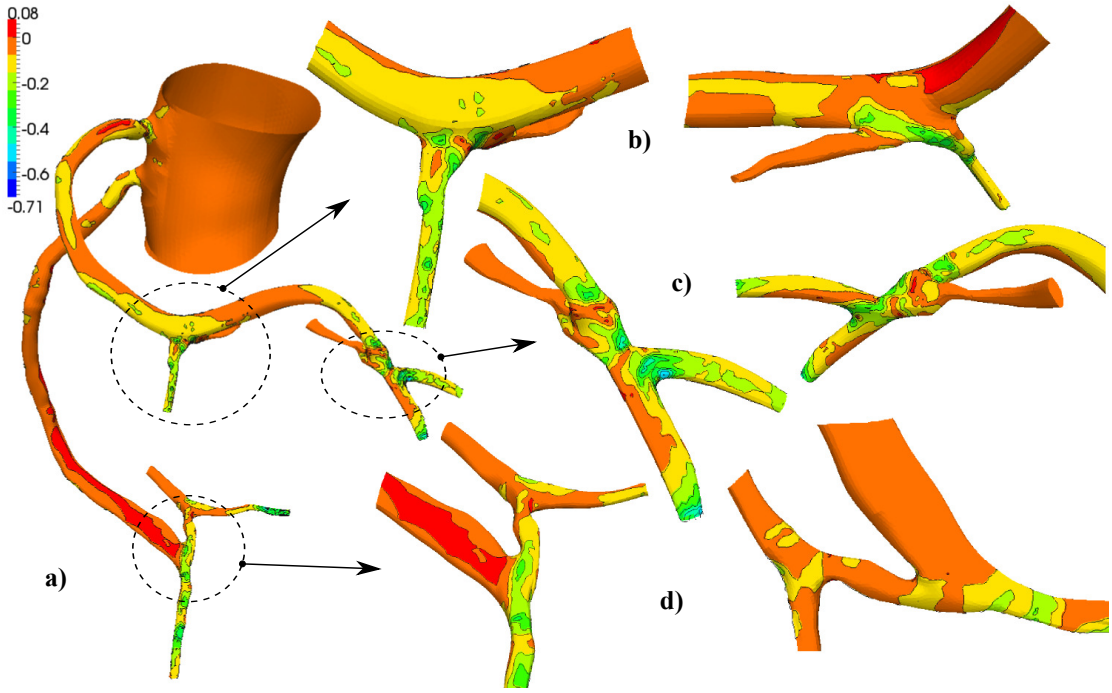

Fig. 5.44. ΔWSS for the triple bypass model (a) with detailed views at the distal side-to-side (b) and end-to-side (c) anastomoses of the sequential graft and at the distal end-to-side anastomosis (d) of individual graft.

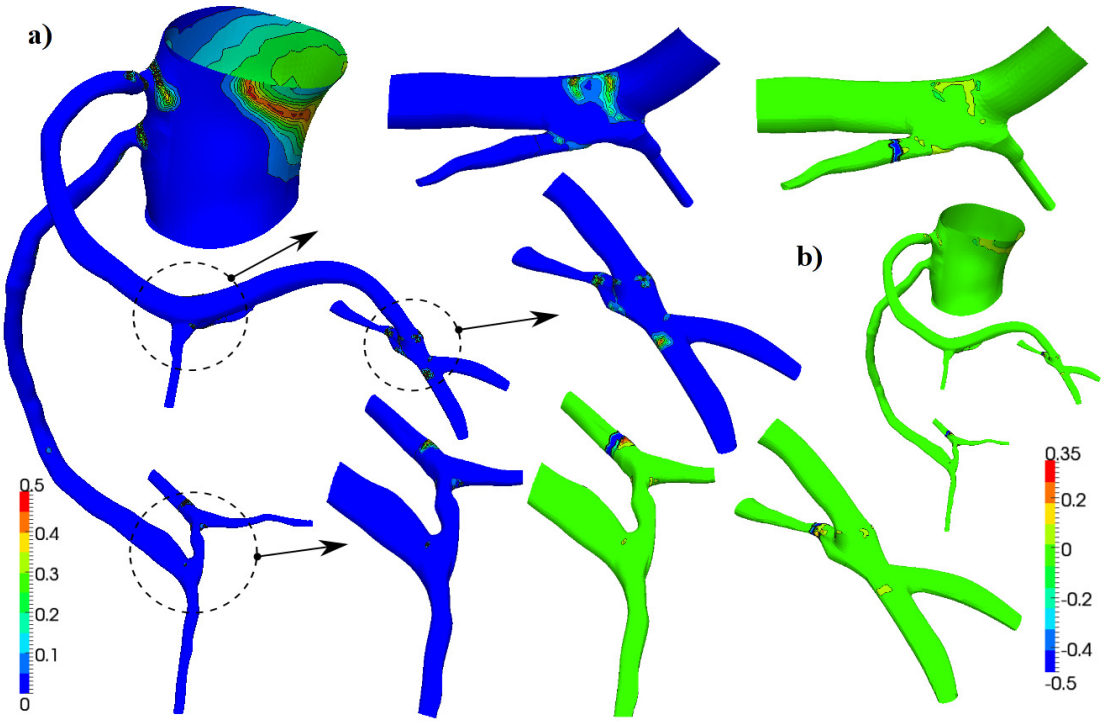

Fig. 5.45. Non-Newtonian OSI (a) and ΔOSI (b) for the triple bypass model with detailed views at the three distal anastomoses.

5.3.2 Application of the three-element Windkessel model

As noted earlier, the prescription of constant pressure at all coronary artery outlets has an unwanted side effect in the form of non-realistic flow waveforms and phases of reversed pressure drop. The application of lumped (0D) models is one of the ways on how to avoid the necessity to know the outlet pressure prior to the computation and to approximate the response of the vascular bed to the bypass hemodynamics in a more realistic way [162]. For the purpose of this Ph.D. thesis, we apply the lumped model in the form of the three-element Windkessel model, Fig. 5.46.

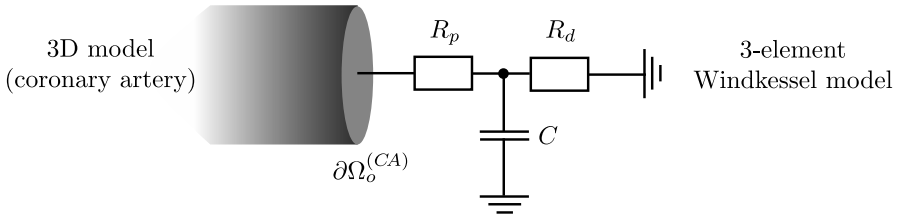

Fig. 5.46. Schematic drawing of the three-element Windkessel model coupled to an outlet of the 3D model.

In all three aorto-coronary bypass models introduced earlier, the Windkessel model is used as an outflow boundary condition and coupled to each coronary artery outlet $\partial\Omega_{hO}^{(CA)_s}$, $s = 1, ..., N_{out}$, where N_{out} is the number of all outlets (single bypass: $N_{out} = 2$, double bypass: $N_{out} = 2$, triple bypass: $N_{out} = 5$, see Fig. 5.47). Analytically, the Windkessel model applied at the outlet $\partial\Omega_{hO}^{(CA)_s}$ is represented through the following equations for the unknown pressures p_d^s and $p_O^{(CA)_s}$:

$$\frac{\mathrm{d}\, p_d^s}{\mathrm{d}\, t} + \frac{p_d^s}{C^s R_d^s} = \frac{1}{C^s} Q_O^{(CA)_s}\,, \qquad p_O^{(CA)_s} = p_d^s + R_p^s\, Q_O^{(CA)_s}\,, \tag{5.7}$$

where p_d^s is the distal pressure (pressure in arterioles and capillaries), $Q_O^{(CA)_s}$ is the flow rate provided by the 3D model, C^s is the capacitance and R_p^s and R_d^s are the proximal and distal resistances, respectively. The unknown pressure $p_O^{(CA)_s}$, necessary for the 3D model, is obtained by solving Eq. (5.7) by means of an explicit Euler method. The parameters R_p^s, R_d^s and C^s for each coronary artery outlet $\partial\Omega_{hO}^{(CA)_s}$, $s = 1, ..., N_{out}$ are listed in Tab. 5.8. For more details on the 3-element Windkessel model and its lumped parameters, see Appendix C.

A) Blood flow in the bypass grafts

Tab. 5.9 summarises the mean and maximum Reynolds numbers calculated at the upstream ends of the individual and sequential grafts for both types of outlet boundary conditions (constant outlet pressure × Windkessel model). From the listed values, it is very well apparent that the differences between both computed flow fields are substantial ($126.9 \leq \Delta \leq 460.2$). It is also worth noting that the blood flow, which is the result of the constant outlet pressure, is at least two times higher than the one with the Windkessel pressures ($\mathrm{Re}_{\mathrm{mean}} \approx 180 \div 485$ compared to $50 \div 150$).

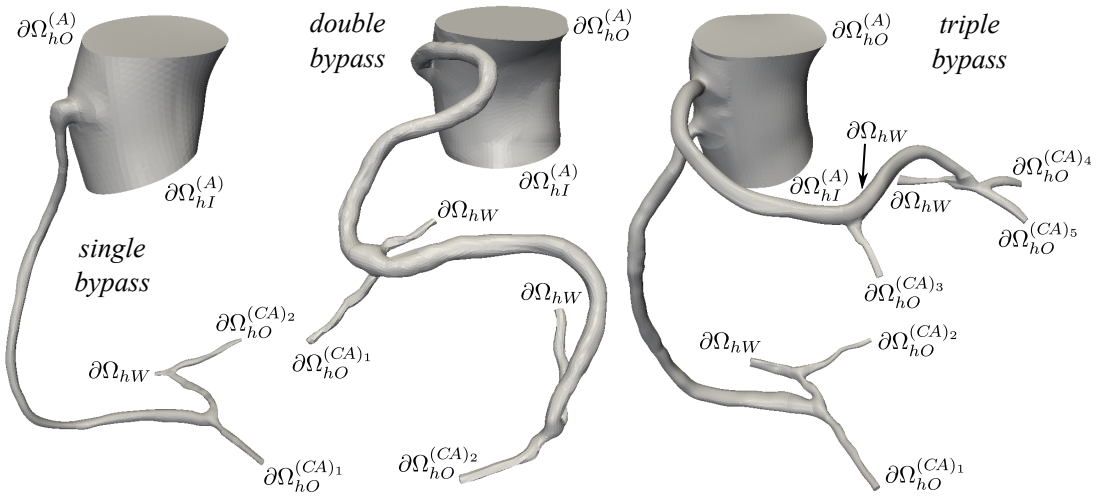

Fig. 5.47. Computational domain boundaries in the three bypass models.

coronary artery outlets	A [mm^2]	$R_p \times 10^6$ [Pa s m^{-3}]	$R_d \times 10^6$ [Pa s m^{-3}]	$C \times 10^{-10}$ [m^3 Pa^{-1}]
single bypass				
$\partial\Omega_{hO}^{(CA)_1}$	4.69	1 173.56	11 808.96	1.52
$\partial\Omega_{hO}^{(CA)_2}$	1.56	3 528.21	35 502.56	0.51
double bypass				
$\partial\Omega_{hO}^{(CA)_1}$	1.75	3 145.14	31 648.00	0.57
$\partial\Omega_{hO}^{(CA)_2}$	3.23	1 704.02	17 146.75	1.05
triple bypass				
$\partial\Omega_{hO}^{(CA)_1}$	3.05	1 804.59	18 158.69	0.99
$\partial\Omega_{hO}^{(CA)_2}$	1.25	4 403.20	44 307.20	0.41
$\partial\Omega_{hO}^{(CA)_3}$	1.50	3 669.33	36 922.67	0.49
$\partial\Omega_{hO}^{(CA)_4}$	2.52	2 184.27	21 977.78	0.82
$\partial\Omega_{hO}^{(CA)_5}$	2.77	1 987.00	19 994.22	0.90

Tab. 5.8. Values of proximal R_p and distal R_d resistances and capacitance C occurring in the 3-element Windkessel model, Fig. 5.46, coupled to each coronary artery outlet shown in Fig. 5.47. Here, A is the cross-sectional area of each outlet.

Another way on how to study the dissimilarities in the blood flows is the visualisation of flow rate and pressure waveforms. For this purpose, several relevant cross-sections of the three bypass models are chosen with respect to the distal end-to-side (ETS) and side-to-side (STS) anastomoses, see Fig. 5.48. On the basis of the waveforms shown in Figs. 5.49–5.51, it can be noted that the results associated with the lumped model significantly differ from those computed with the help of the fixed outlet pressure. For example, the amount of blood that goes through the individual graft of the single bypass varies by up to 51%, while the difference in average pressure is around 640 Pa.

aorto-coronary bypass		D_{av} [mm]	Re_{mean} [−]			Re_{max} [−]		
			const.	WM	Δ	const.	WM	Δ
single	indiv.	3.0	210.9	84.0	126.9	366.8	192.8	174.0
double	seq. (1^{st})	4.7	336.0	93.9	242.1	558.0	224.8	333.2
	seq. (2^{nd})	5.1	185.4	56.2	129.2	294.3	133.1	161.2
triple	indiv.	4.4	261.9	83.5	178.4	447.6	196.3	251.3
	seq. (1^{st})	4.0	484.6	146.7	337.9	814.7	354.5	460.2
	seq. (2^{nd})	4.2	376.8	112.2	264.6	627.1	271.0	356.1

Tab. 5.9. Mean and maximum Reynolds numbers computed for the non-Newtonian flow in the upstream parts of the individual and sequential grafts with average diameter D_{av}. Here, '1^{st}' and '2^{nd}' denote the first and second half of the sequential graft before and after the side-to-side anastomosis, respectively, and Δ is the absolute difference between the computed values (constant outlet pressure × Windkessel model, WM).

Probably one of the most interesting time intervals is the beginning of the cardiac cycle (time between 0 s and 0.1 s). As mentioned in Section 5.3.1, all the bypass models with prescribed outlet pressure of 12 000 Pa experience a short phase of reversed flow, which can be clearly attributed to the reversed pressure drop, see Figs. 5.49–5.51 (right). By contrast, all the bypass models coupled to the lumped model are characterised by the absence of this reversed flow phase, Figs. 5.49–5.51 (left), which is a direct consequence of the fact that the outlet pressure sought via the Windkessel model is always lower or equal to that of the aortic outlet as apparent from Figs. 5.49–5.51 (right).

B) Wall shear stress and oscillatory shear index

Seeing as the hemodynamical wall parameters – wall shear stress (WSS) and oscillatory shear index (OSI) – are closely connected to the local hemodynamics, it is not surprising that the shear results computed for the two types of outlet boundary conditions are quite different, Figs. 5.52–5.57. In other words, the decrease of WSS values in relation with

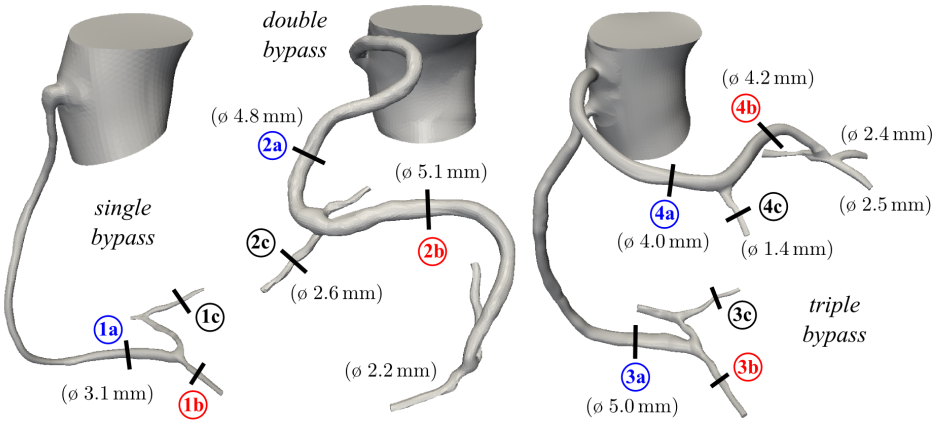

Fig. 5.48. The location of flow rate and pressure waveforms shown in Figs. 5.49–5.51 for the single (*left*), double (*middle*) and triple (*right*) aorto-coronary bypasses.

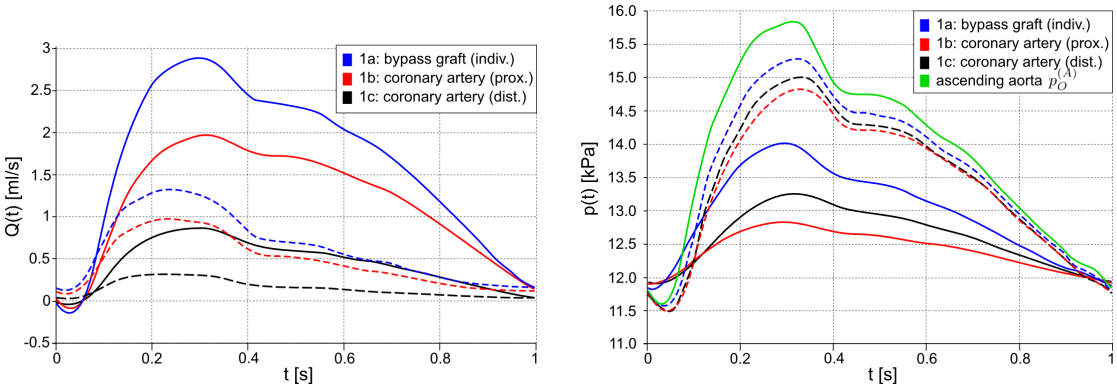

Fig. 5.49. Single aorto-coronary bypass – waveforms of flow rate (*left*) and pressure (*right*) at locations denoted in Fig. 5.48. Solid (—) and dashed (– –) lines represent the results obtained by the prescription of constant outlet pressure and the application of the three-element Windkessel model, respectively.

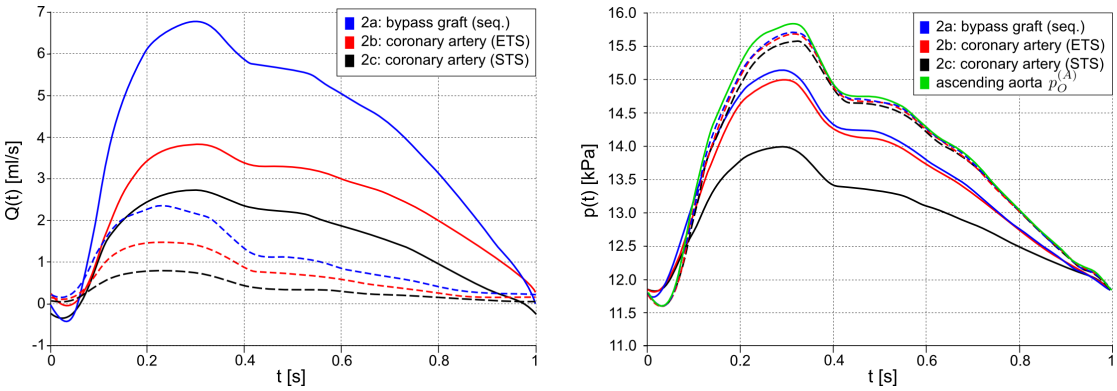

Fig. 5.50. Double aorto-coronary bypass – waveforms of flow rate (*left*) and pressure (*right*) at locations denoted in Fig. 5.48. Solid (—) and dashed (– –) lines represent the results obtained by the prescription of constant outlet pressure and the application of the three-element Windkessel model, respectively.

the application of the Windkessel model is clearly affected by the lower flow rates that are very well apparent from the waveforms shown in Figs. 5.49–5.51.

In the case of the single bypass model, several relevant WSS differences can be noted on the basis of Fig. 5.52. For example, the detailed views at the proximal and distal anastomoses of the individual graft show a significant WSS decrease of around 1.5 Pa in certain regions. Among them, the regions commonly denoted as suture line, heel and toe (see Fig. 3.16), i.e., those known to be prone to intimal thickening, are particularly affected with shear stimulation usually below 0.5 Pa. At this point, it is also worth noting that the introduction of the Windkessel model shows a tendency to increase the extent of low WSS regions, as apparent from the vicinity of the proximal anastomosis in Fig. 5.52. A considerable decrease in WSS values as a result of the coupled lumped models can be also observed in the double and triple two aorto-coronary bypass models, Fig. 5.53 and

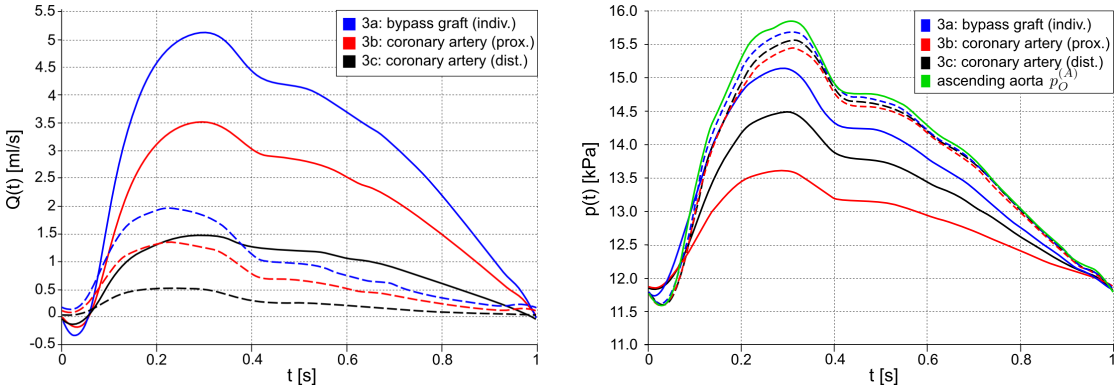

a) individual graft

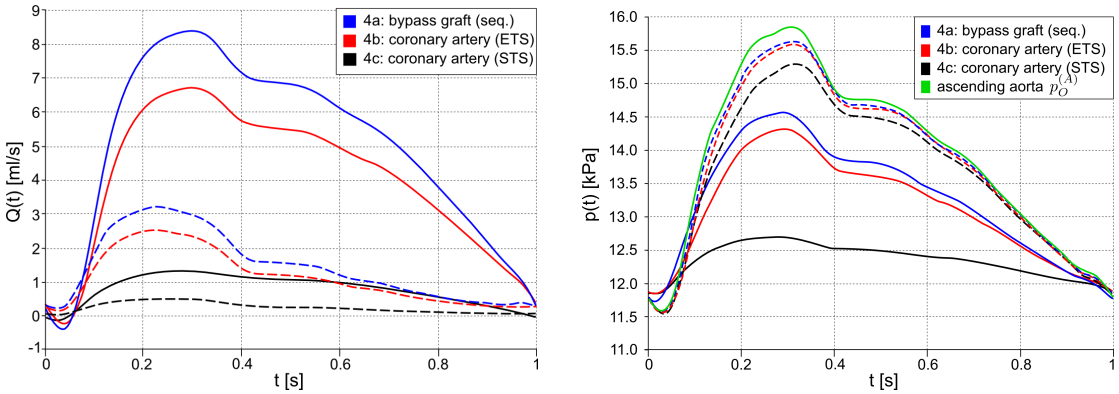

b) sequential graft

Fig. 5.51. Triple aorto-coronary bypass – waveforms of flow rate (*left*) and pressure (*right*) at locations denoted in Fig. 5.48. Solid (—) and dashed (– –) lines represent the results obtained by the prescription of constant outlet pressure and the application of the three-element Windkessel model, respectively.

Fig. 5.54, respectively. Here, the decrease is most pronounced in the bypass grafts, in which the difference in cycle-averaged shear stimulation can reach up to 2 Pa.

Compared to the WSS magnitude, the oscillatory character of the shear stress in the single bypass seems to be positively affected by the application of the Windkessel model, Fig. 5.55. Particularly worth noting is the suppression of unwanted shear oscillations at the distal anastomosis, where OSI values greater than 0.35 are almost completely absent from the areas prone to intimal thickening. Surprisingly, a different behaviour occurs in the case of the double bypass model, Fig. 5.56. Here, the distal side-to-side anastomosis of the sequential graft experiences an increase in shear oscillations (OSI increases up to 0.5), while the OSI maps at distal end-to-side anastomosis remain almost unchanged in the vicinity of the suture line and heel. At the proximal and distal anastomoses of the triple bypass model, a certain form of all the previously observed behaviours can be noted, Fig. 5.57. In other words, shear oscillations are both suppressed and promoted when the Windkessel model is considered, as seen from the distal anastomoses of the sequential graft.

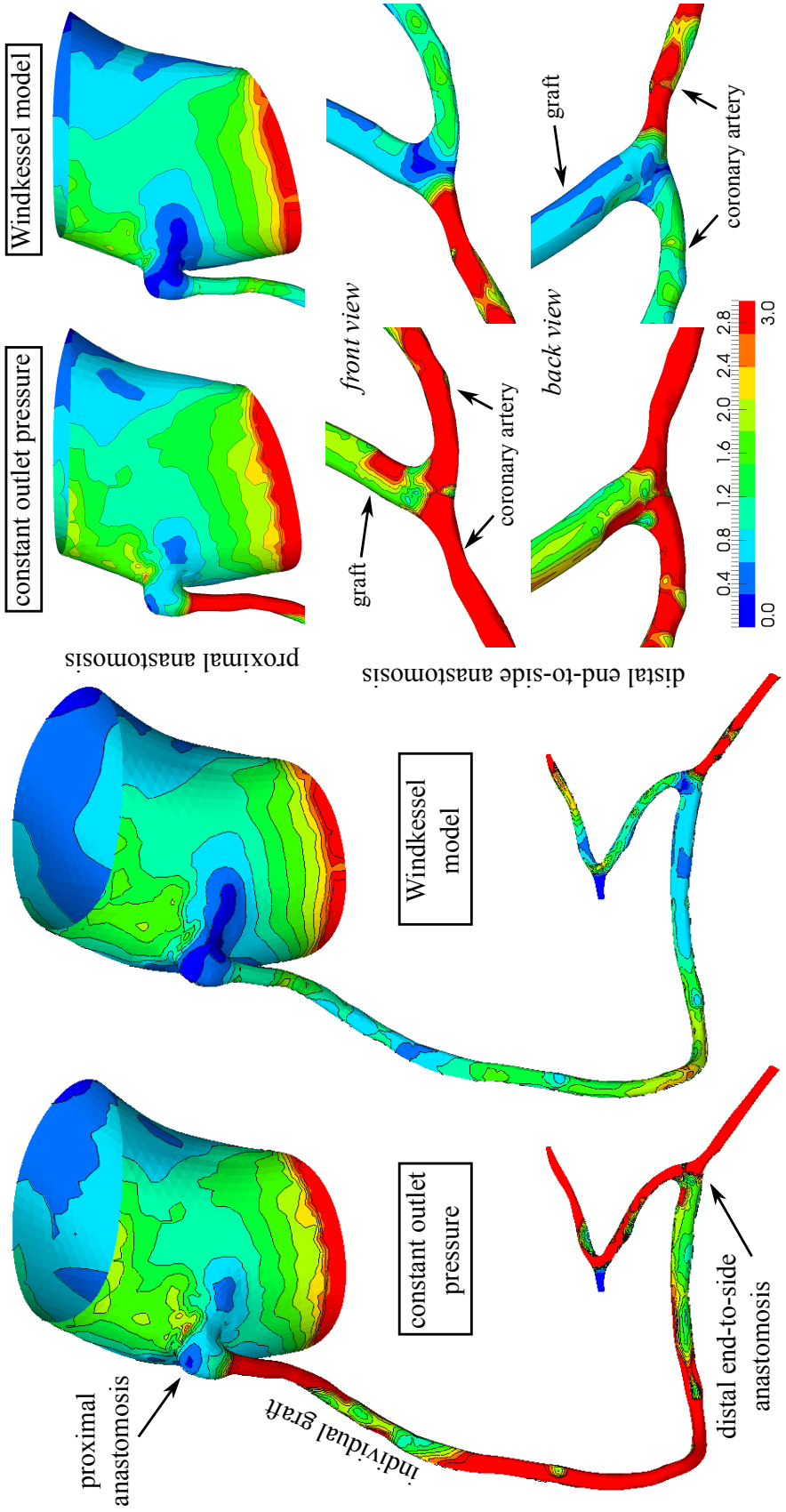

Fig. 5.52. Effect of outlet boundary conditions on the distribution of cycle-averaged WSS [Pa] in the single aorto-coronary bypass model with detailed views at the proximal and distal anastomoses.

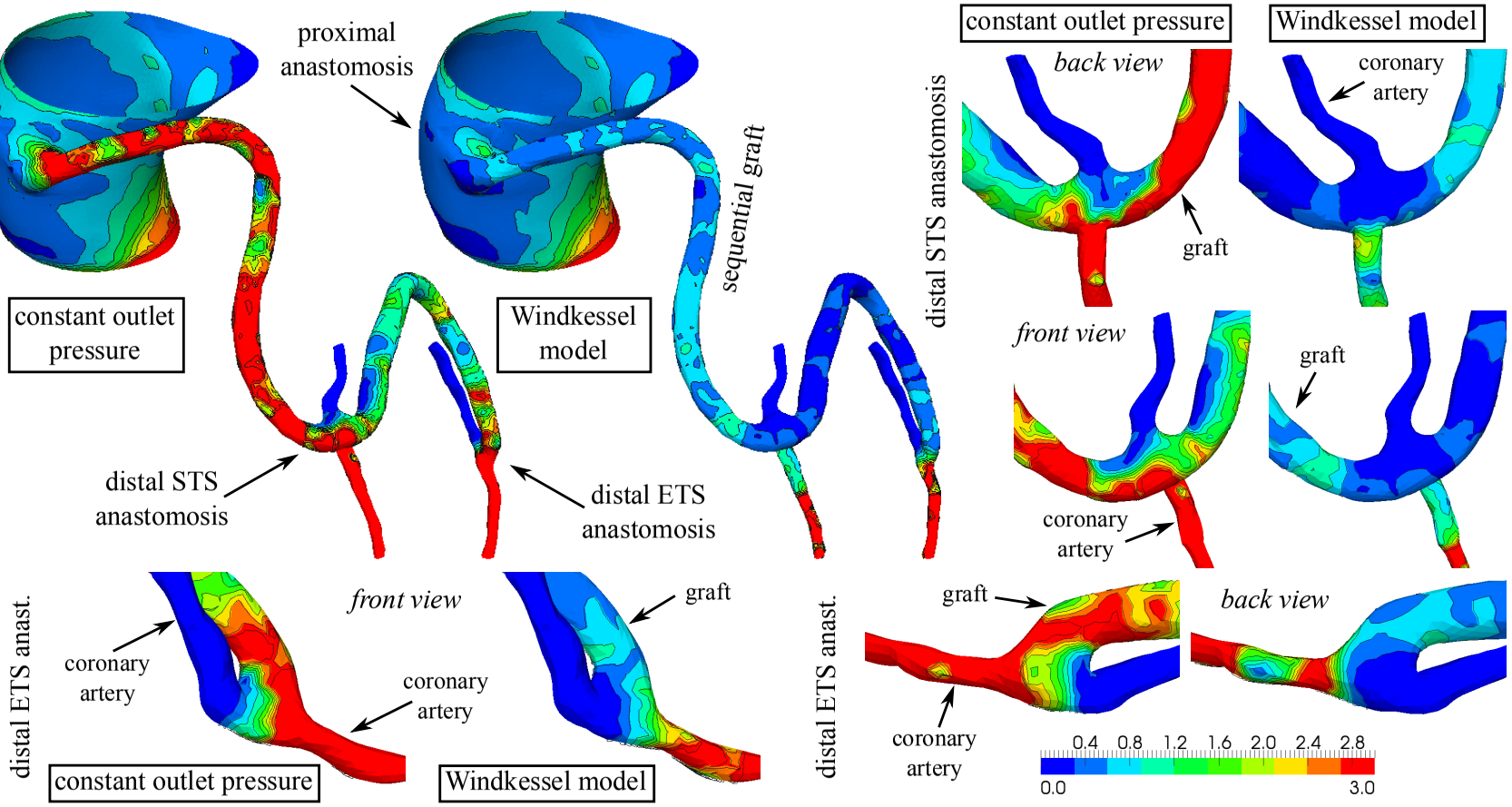

Fig. 5.53. Effect of outlet boundary conditions on the distribution of cycle-averaged WSS [Pa] in the double aorto-coronary bypass model with detailed views at the distal side-to-side (STS) and end-to-side (ETS) anastomoses.

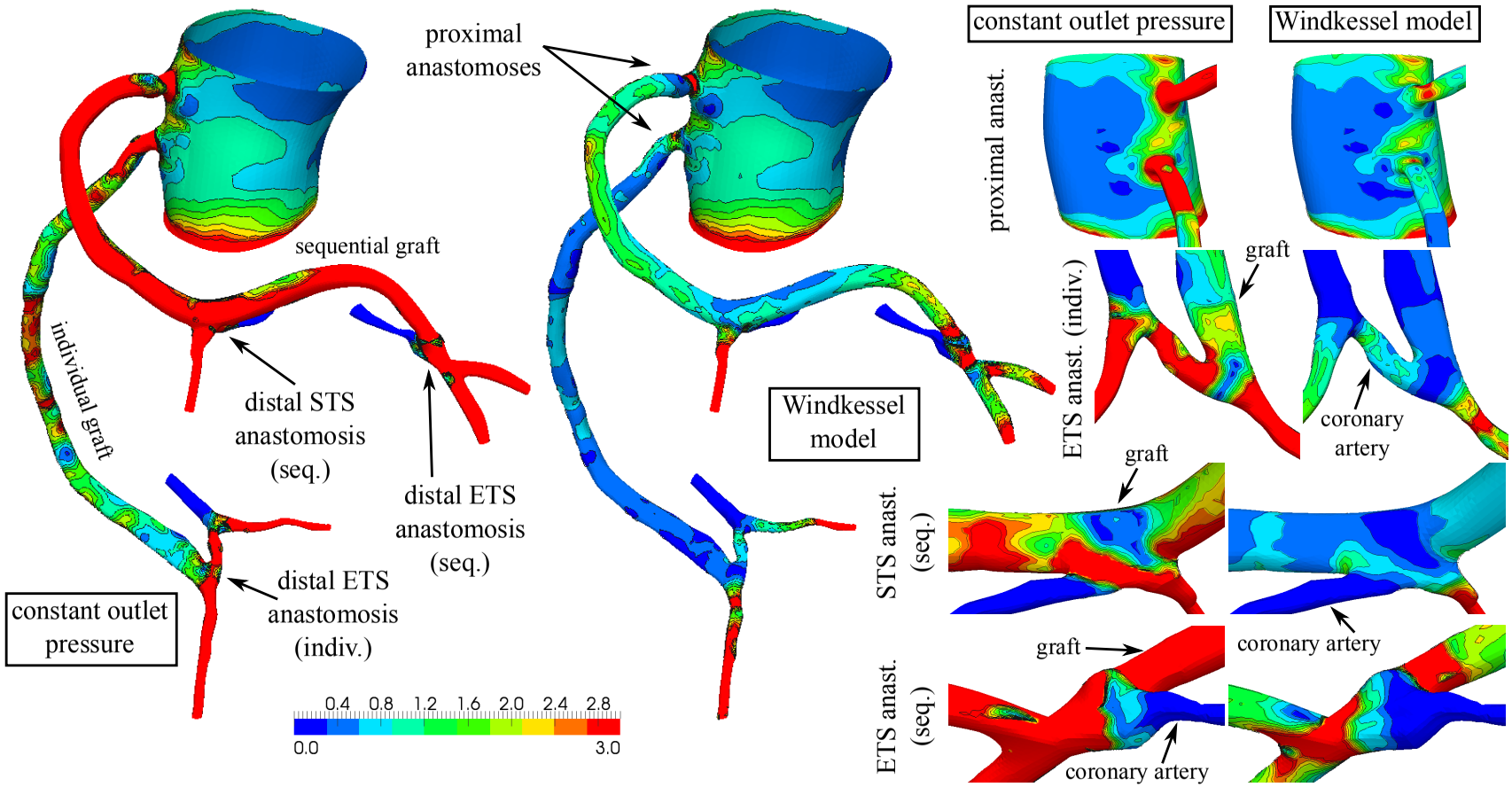

Fig. 5.54. Effect of outlet boundary conditions on the distribution of cycle-averaged WSS [Pa] in the triple aorto-coronary bypass model with detailed views at the proximal and distal side-to-side (STS) and end-to-side (ETS) anastomoses.

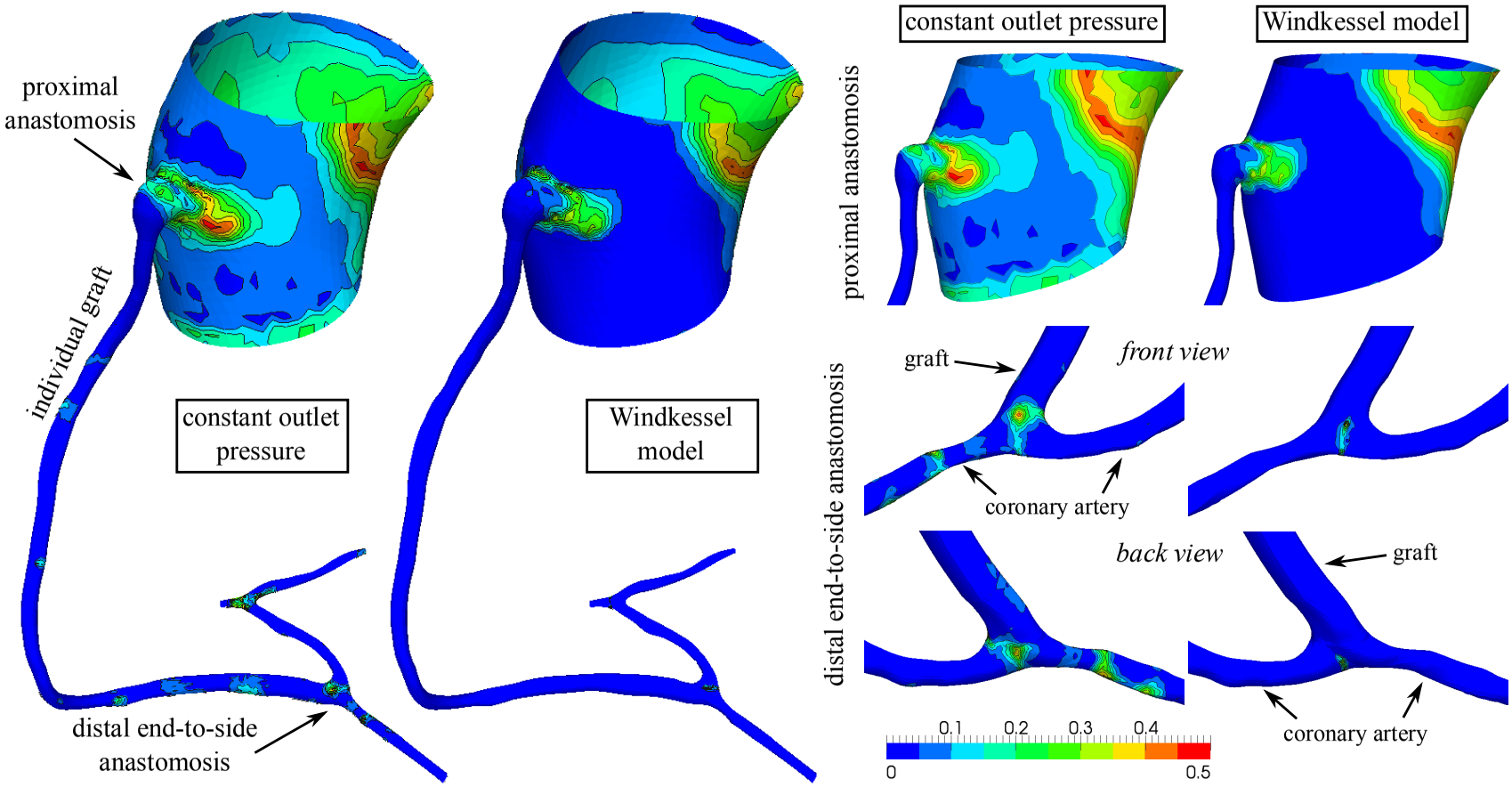

Fig. 5.55. Effect of outlet boundary conditions on the distribution of OSI [–] in the single aorto-coronary bypass model with detailed views at the proximal and distal anastomoses.

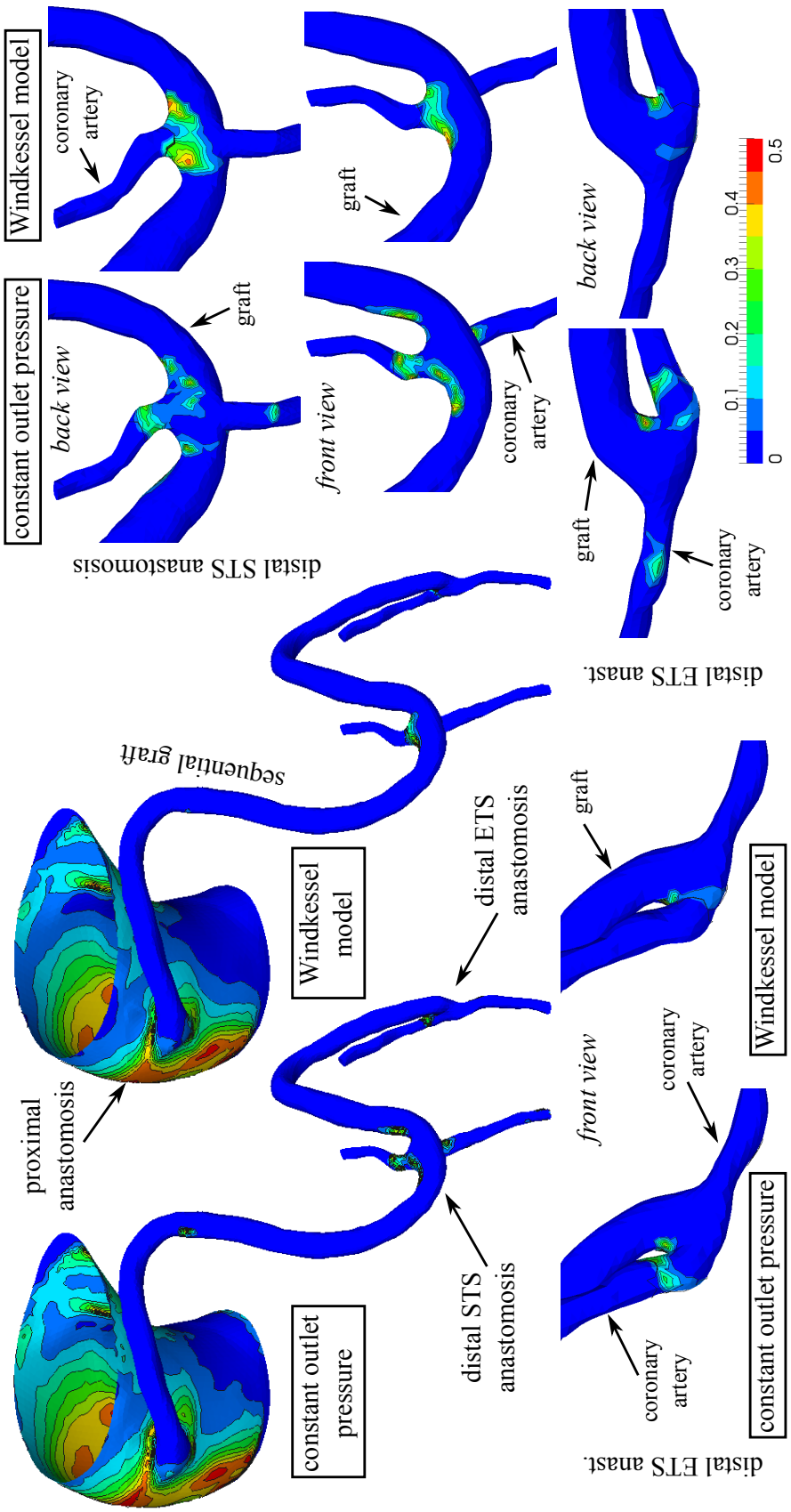

Fig. 5.56. Effect of outlet boundary conditions on the distribution of OSI [–] in the double aorto-coronary bypass model with detailed views at the distal side-to-side (STS) and end-to-side (ETS) anastomoses.

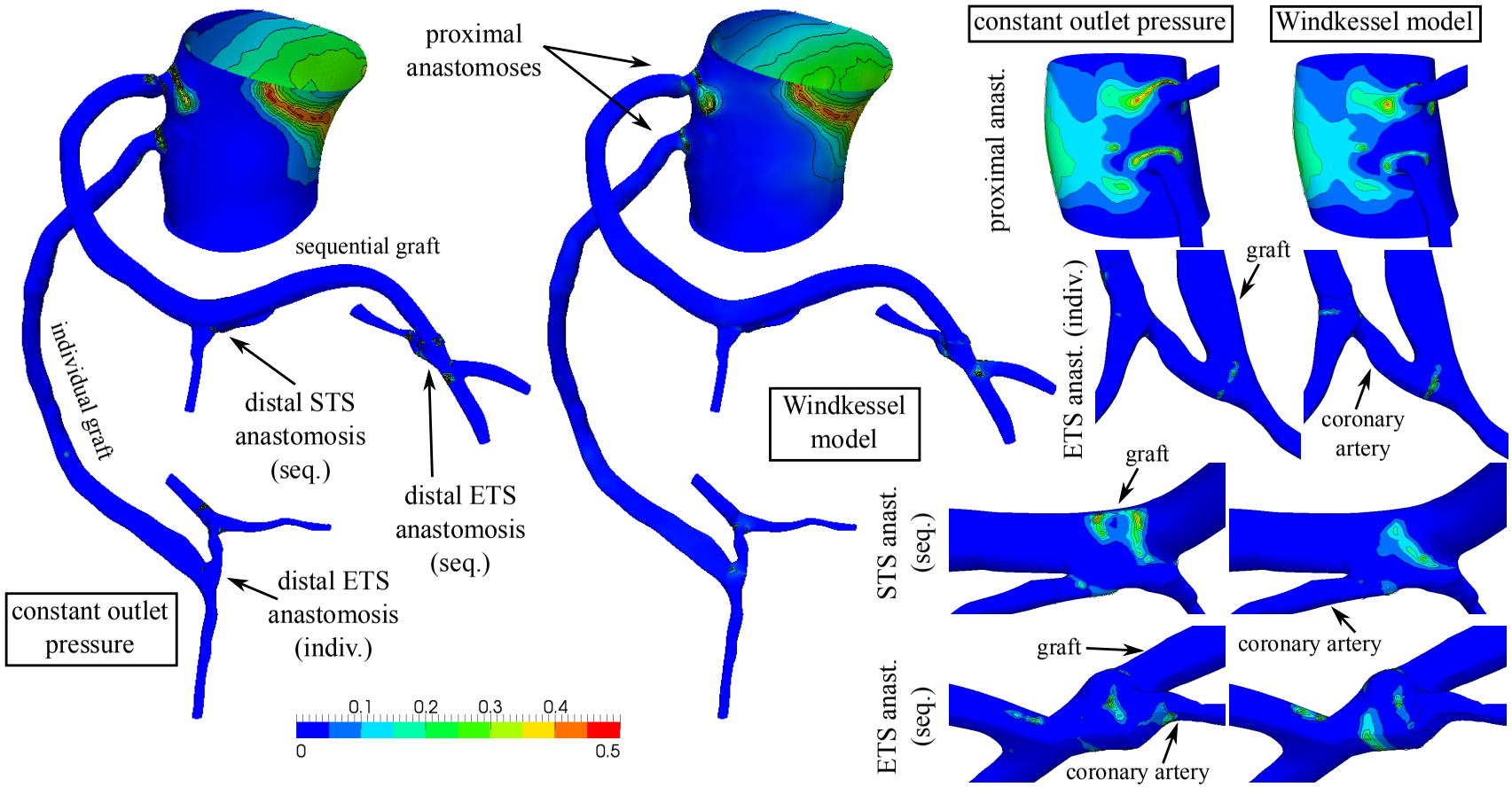

Fig. 5.57. Effect of outlet boundary conditions on the distribution of OSI [–] in the triple aorto-coronary bypass model with detailed views at the proximal and distal side-to-side (STS) and end-to-side (ETS) anastomoses.

5.3.3 Discussion and conclusions

The numerical simulations of pulsatile blood flow in the single, double and triple bypasses indicate that the velocity patterns and the qualitative distribution of hemodynamical wall parameters (WSS and OSI) are not significantly influenced by the non-Newtonian viscosity of the blood. On the other hand, it is important to mention that, although very small, the differences between the non-Newtonian and Newtonian flow exist, as can be seen from the distributions of ΔWSS and ΔOSI presented in Section 5.3.1. The most significant changes in WSS (up to 0.7 Pa) have local character and are observed mainly downstream from the distal anastomoses, i.e., in areas of little importance to the formation of intimal hyperplasia. Overall, the changes in WSS and OSI caused by the non-Newtonian viscosity of blood are strongly affected by the patient-specific bypass geometry and flow conditions.

From the numerical results shown in Section 5.3.1, it is possible to draw another very important conclusion. Namely, our observations suggest that the diameter of the vessels involved in the bypassing is more important for the flow and WSS distribution than the blood's non-Newtonian viscosity. In other words, the use of reversed saphenous vein grafts and the placing of small-sized arteries appear to be one of the main determinants of the patency and overall performance of the implanted bypass grafts, as the diameter of the vessels may predetermine the resulting flow field and shear stimulation. The flow dependence on the diameter is particularly noticeable in the sequential grafts, whose downstream flow rate is strongly influenced by the diameter of the coronary artery at the side-to-side anastomosis.

As to the results presented in Section 5.3.2, it can be concluded that the introduction of the three-element Windkessel model fulfilled its purpose, which was to prevent the occurrence of non-realistic flow waveforms and phases of reversed pressure drop. On the other hand, the existence of the time-dependent Windkessel pressure at the coronary artery outlets resulted in flow fields and shear distributions almost completely different from those observed in Section 5.3.1. This leads us to the question whether the Windkessel model will give a better approximation of the real coronary blood flow than the constant outlet pressure commonly prescribed in this type of numerical simulations [136]. The answer to this question can be found by comparing the shape of the computed wave-

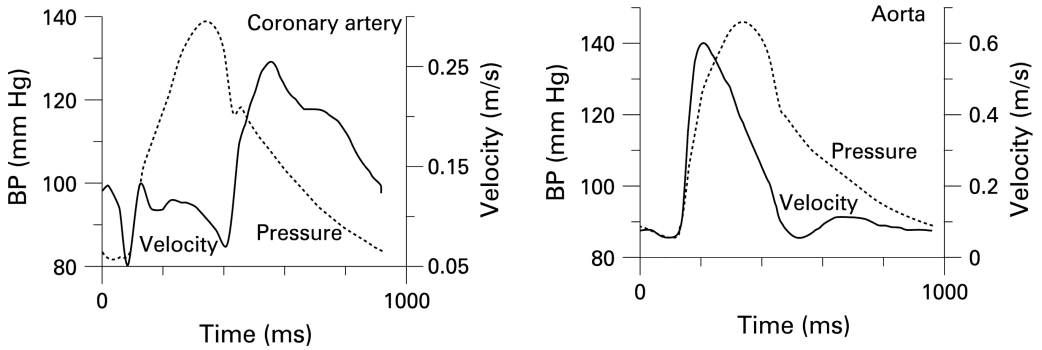

Fig. 5.58. Velocity and blood pressure (BP) waveforms for coronary artery (*left*) and aorta (*right*) taken from [31].

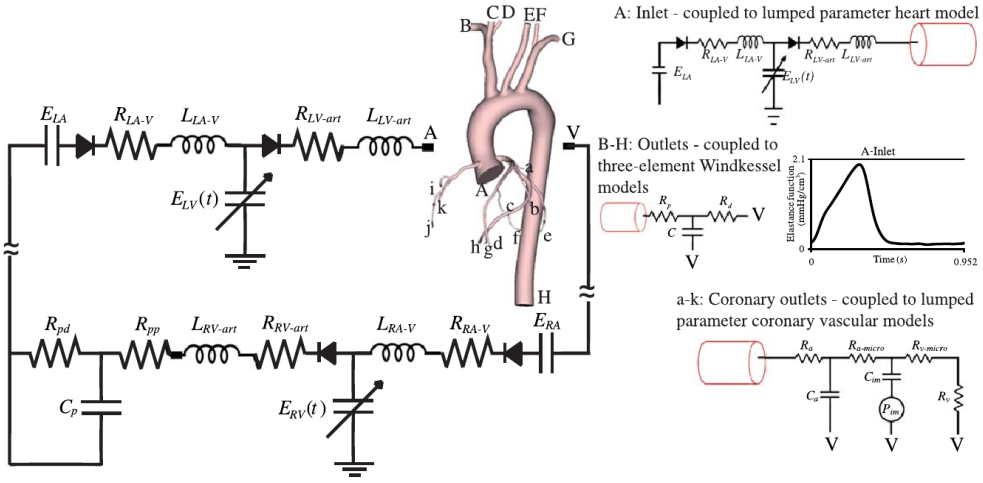

Fig. 5.59. Schematic drawing of closed loop system with a lumped parameter model of downstream coronary vascular beds according to [77].

forms, Figs. 5.49–5.51, with those measured in real coronary arteries, Fig. 5.58 (left)[3].

From Fig. 5.58 (left), two things become quite apparent: 1) The coronary flow reaches its maximum during the diastolic phase of the cardiac cycle. 2) Despite the delayed blood filling of the coronary arteries, the pressure waveforms remain almost identical to those found in the aorta, Fig. 5.58 (right). Comparing these two observations with our results, it becomes clear that the Windkessel model can bring some improvements to the existing 3D flow model such as the similarity of aortic and coronary pressure waveforms, but is unable to reproduce the realistic coronary flow waveforms[4]. According to the papers [77] and [162], a more complex lumped model (see, for example, Fig. 5.59) is one of the ways to overcome this weakness and to achieve the unique character of the coronary flow, which is a result of the ability of the coronary circulation to store blood in dependence on the ventricular pressure.

[3]The velocity and pressure waveforms in Fig. 5.58 are taken as an illustration of coronary blood flow. For flow rate waveforms, it is possible to refer to the paper [163] (although without the corresponding pressure waveforms).

[4]Although the Windkessel model fails to capture the delayed peak flow, it can satisfactorily simulate the physiological range of coronary flow (e.g., in a 2.5 mm coronary artery [31]: $0.25 \div 1.23$ ml/s). As an example, let us take the flow rate waveform of the coronary artery (ETS) shown in Fig. 5.50 (left): constant outlet pressure: $-0.4 \div 3.9$ ml/s, Windkessel model: $0 \div 1.5$ ml/s.

Chapter 6
Conclusions

6.1 Summary of present work

The purpose of the Ph.D. thesis was the finite volume modelling of steady and pulsatile blood flow in complete idealised and patient-specific bypass models. In accordance with the trends of recent years, the simulations were carried out by considering blood's non-Newtonian rheology and the effect of various geometrical and physiological parameters.

In *Chapter 1*, the motivation and objectives for the work were outlined and put into context with some of the most significant numerical and experimental studies published on bypass hemodynamics. Considering the focus of the Ph.D. thesis, the content of *Chapter 2* provided an insight into the biology of human blood and associated selected biological and abiological factors such as the hematocrit and shear rate with certain types of flow behaviour (e.g., the Fåhræus-Lindqvist effect). Then, on the basis of the mentioned main factors, the rest of the chapter was designed as a comprehensive list of non-Newtonian viscosity models commonly used for the description of blood rheology.

The first half of *Chapter 3* was dedicated to bypass grafting. Besides a brief historical overview, the reasons leading to the implantation of bypass grafts and some of the most common basic grafting techniques were mentioned and described in detail. To connect the performance of the artificially created detours with their mechanical properties, the advantages and disadvantages of autologous and synthetic grafts were provided and summarised with regard to their failure rates. The second half of the chapter was aimed at hemodynamics-vessel interaction, which is nowadays widely recognised as one of the CVD triggers [91, 113]. When discussing pathological changes in blood vessels, special attention was paid to thickening of tunica intima known as 'intimal hyperplasia', which in most cases is the main reason for graft failure. In this regard, relevant terminology for the distal anastomosis region was introduced and linked to sites prone to pathological changes. To facilitate the identification of these sites, a list of hemodynamical indicators was given as well.

All the necessary assumptions and modelling simplifications adopted in this work were summarised and justified at the beginning of *Chapter 4*. Consequently, the mathematical model governing the motion of blood as an incompressible generalised Newtonian fluid was described and, for the purpose of this work, converted to its non-dimensional form. Because of the missing time-dependent term in the continuity equation, two different solution strategies were taken into consideration. The first one was represented by the artificial compressibility method [27], while the second one utilised the principle of the projection methods [26, 179]. In both approaches, the spatial discretisation was carried out by means of the cell-centred finite volume method formulated for unstructured hexahedral or tetrahedral computational meshes. The developed computational algorithms based on the segregated approach were verified by Newtonian as well as non-Newtonian blood flow simulations.

All numerical results, obtained with the help of the computational algorithms mentioned above, were presented and analysed in *Chapter 5*. The content of this chapter was organised in such a manner that each section covered a certain area of interest:

• *non-Newtonian behaviour of blood (idealised geometry)*

The first section was aimed at the analysis of non-Newtonian effects in occluded and stenosed bypass models with either coronary or femoral native artery. Applying average boundary conditions corresponding to each of the considered bypass types, non-Newtonian effects computed with two different non-Newtonian viscosity models (the Carreau-Yasuda model and the modified Cross model) were analysed and discussed on the basis of velocity patterns, secondary flow streamlines and WSS distributions.

The presented results proved that regardless of the used viscosity model, the bypass hemodynamics is profoundly affected by the complex geometry and the type of arterial damage (occlusion × stenosis). In accordance with other hemodynamical studies such as [83,84,95], disturbed flow fields and non-uniform WSS distributions were noted in relevant areas of proximal and distal anastomoses. As for the occurrence of non-Newtonian effects, it was noted that the prescribed flow conditions (coronary × femoral) are one of the main factors determining the nature of blood rheology. In this case, it was also concluded that the two applied non-Newtonian models are interchangeable as they gave qualitatively comparable results.

• *geometry influence on pulsatile blood flow*

On the basis of the conclusions drawn above, the focus of the second section was aimed at the study of bypass geometry, when pulsatile Newtonian blood flow was taken into consideration. Here, changes in local hemodynamics were observed in dependence on three geometrical parameters known as stenosis degree [83, 84], junction angle [95] and diameter ratio [199]. Compared to other studies addressing the issue of bypass geometry, our configurations also included two bypass models made up of tapered or widening grafts, each representing a reversed or partially stenosed graft.

The analysis of selected velocity profiles and cycle-averaged WSS and oscillatory shear index (OSI) distributions yielded some interesting insights. Namely, that any changes to stenosis degree or junction angle resulted in rather small changes in flow and shear stimulation, when compared to the changes caused by an increase/decrease in the graft diameter. As the bypass hemodynamics seemed to be particularly sensitive to any changes in the diameter ratio, it was concluded that this particular geometrical parameter is one of the factors that may predetermine the graft failure in the future and as such should be paid attention to during bypass surgery. Regarding the tapered and widening grafts, improved anastomosis flow and shear stress distributions were achieved, however, at the cost of abnormal shear stimulation in previously unaffected regions.

• *patient-specific bypass models, application of the three-element Windkessel model*

The main objective of the third section was the application of bypass models reconstructed from CT scans that were provided by the courtesy of the University Hospital in Pilsen. The models represented three most common types of aorto-coronary bypasses and were denoted as single, double and triple according to their number of distal anastomoses. By adopting the assumption of pulsatile non-Newtonian blood flow, the flow waveforms, velocity patterns and WSS and OSI distributions served as a means to a detailed analysis of complex flow fields in real aorto-coronary bypasses.

After the comparison of Newtonian and non-Newtonian results, it was once again confirmed that the shear-dependent nature of blood rheology is strongly dependent on the prescribed flow conditions and geometry. Aside from negligible non-Newtonian effects, another observation was made that, in this case, could be attributed to the diameters of the vessels involved in the bypassing. As an example, it is possible to mention the flow division between the distal anastomoses in sequential grafts that was noted to be governed by the native arteries located at the side-to-side anastomoses. In other words, higher blood flow and better shear stress stimulation were achieved in grafts, where the diameter of the side-to-side artery was smaller compared to that located at the end-to-side anastomosis. Note that this correlation between downstream flow rate and side-to-side artery diameter is closely related to the risk of graft failure, which is in accordance with the results presented in the clinical study [191].

The second part of the third section mapped our first attempt at multiscale blood flow modelling, which was primarily motivated by our effort to prevent the occurrence of non-physiological flow irregularities originating from the prescribed boundary conditions (back flow caused by reversed pressure drop). In accordance with the recent trends in patient-specific blood flow modelling, a lumped parameter (0D) model in the form of the three-element Windkessel model was introduced and applied as an outflow boundary condition. The ability of the Windkessel model to approximate the response of the downstream vascular bed, especially when patient-specific data are unavailable, was tested by comparing the computed flow and shear results with those obtained by the constant outlet pressure. As demonstrated by the flow and pressure waveforms, our expectations regarding the elimination of non-realistic back flow were met even despite the fact that the 0D model was unable to reproduce the unique coronary flow waveforms.

6.2 Contributions and perspectives

The main purpose of this Ph.D. thesis was to contribute to the growing area of research focused on bypass hemodynamics and to provide a guide for medical doctors in search of an optimal graft design. It is author's belief that better understanding of hemodynamics and its influence on graft patency may be crucial, as any extra knowledge of potential complications prior to surgery can bring benefits not only to vascular surgeons in their pre-operative planning, but also to patients in the form of shorter recovery phases.

In accordance with the objectives of this work outlined in Section 1.3, all blood flow simulations were carried out in complete idealised as well as patient-specific bypass models to avoid potential flow inaccuracies resulting from the prescription of unreliable inlet boundary values, as discussed in [95]. Considering the lack of studies addressing the influence of bypass geometry on hemodynamics in a systematic and comprehensive manner, a part of the Ph.D. thesis addressed the role of three important geometrical parameters (stenosis degree, junction angle and diameter ratio) in terms of blood flow and shear stress stimulation. For the sake of completeness, a hemodynamical study of previously unpublished models of tapered and widening grafts was provided, as well. By using verified computational algorithms, the relevance of blood's non-Newtonian behaviour was assessed and on the basis of obtained numerical results refuted in (aorto-)coronary bypasses. Another major contribution of this work is related to the application of the

three-element Windkessel model, which although unable to reproduce the unique coronary flow waveforms, was able to eliminate non-physiological back flow and to provide coronary flow within the physiological range.

With reference to several recent studies on blood flow modelling, e.g., [77,162], it can be noted that the current trends encourage the application of models that are based on patient-specific data and often combine 3D simulations with lumped parameter models in order to achieve personalised boundary conditions. Although the use of the 0D models is not so constraining as a prescribed outlet pressure and in many cases may lead to physiologically realistic results, it necessitates an estimation of patient-specific Windkessel or other lumped model parameters. Among the various estimation strategies outlined, e.g., in [195], the methodology [138] based on a multiscale approach in combination with the unscented Kalman filter seems to be the most promising for future work, especially if patient-specific MRI or Doppler blood flow measurements are available.

Appendix A

Calculation of shear rate

The non-Newtonian viscosity models mentioned in Section 2.3.2 and listed in Tab. 2.7, including the Carreau-Yasuda model (4.2) and the modified Cross model (4.3) applied in this Ph.D. thesis, require the shear rate $\dot{\gamma}$ to be a known quantity. The calculation of shear rate is based on the well-known formula mentioned, for example, in [100] or [141],

$$\dot{\gamma} = 2\sqrt{D_{II}}\,, \tag{A.1}$$

where D_{II} is the second invariant of the rate of deformation tensor $\mathbf{D} = \frac{1}{2}\left(\nabla \boldsymbol{v} + (\nabla \boldsymbol{v})^T\right)$ defined as

$$D_{II} = \frac{1}{2}\left(tr\mathbf{D}^2 - (tr\mathbf{D})^2\right)\,, \tag{A.2}$$

where $tr\mathbf{D}$ is the trace of $\mathbf{D}$. Because the blood flow is generally assumed to be a flow of an incompressible fluid, the continuity equation yields $tr\mathbf{D} = 0$, and thus, Eq. (A.2) simplifies to

$$D_{II} = \frac{1}{2}\,tr\mathbf{D}^2 = \frac{1}{2}\,d_i^j d_j^i\,, \tag{A.3}$$

where d_{ij} are the components of the rate of deformation tensor $\mathbf{D}$

$$d_{ij} = \frac{1}{2}\left(\frac{\partial v_i}{\partial x_j} + \frac{\partial v_j}{\partial x_i}\right)\,, \quad i,j = 1,2,3\,. \tag{A.4}$$

Substituting Eq. (A.3) into Eq. (A.1), the formula for the calculation of the shear rate gets the following final form

$$\dot{\gamma} = \sqrt{2\,tr\mathbf{D}^2}\,. \tag{A.5}$$

Considering the Cartesian coordinates in 3D, the trace of the rate of deformation tensor

$$\mathbf{D} = \begin{bmatrix} \frac{\partial u}{\partial x} & \frac{1}{2}\left(\frac{\partial u}{\partial y} + \frac{\partial v}{\partial x}\right) & \frac{1}{2}\left(\frac{\partial u}{\partial z} + \frac{\partial w}{\partial x}\right) \\ \frac{1}{2}\left(\frac{\partial u}{\partial y} + \frac{\partial v}{\partial x}\right) & \frac{\partial v}{\partial y} & \frac{1}{2}\left(\frac{\partial v}{\partial z} + \frac{\partial w}{\partial y}\right) \\ \frac{1}{2}\left(\frac{\partial u}{\partial z} + \frac{\partial w}{\partial x}\right) & \frac{1}{2}\left(\frac{\partial v}{\partial z} + \frac{\partial w}{\partial y}\right) & \frac{\partial w}{\partial z} \end{bmatrix} \tag{A.6}$$

has the form

$$\begin{aligned} tr\mathbf{D}^2 \;=\; & \left(\frac{\partial u}{\partial x}\right)^2 + \left(\frac{\partial v}{\partial y}\right)^2 + \left(\frac{\partial w}{\partial z}\right)^2 + \\ & + \;\frac{1}{2}\left[\left(\frac{\partial u}{\partial y} + \frac{\partial v}{\partial x}\right)^2 + \left(\frac{\partial u}{\partial z} + \frac{\partial w}{\partial x}\right)^2 + \left(\frac{\partial v}{\partial z} + \frac{\partial w}{\partial y}\right)^2\right], \end{aligned} \tag{A.7}$$

which yields the following shear rate formula

$$\begin{aligned} \dot{\gamma} \;=\; & \left\{2\left[\left(\frac{\partial u}{\partial x}\right)^2 + \left(\frac{\partial v}{\partial y}\right)^2 + \left(\frac{\partial w}{\partial z}\right)^2\right] + \right. \\ & \left. + \;\left(\frac{\partial u}{\partial y} + \frac{\partial v}{\partial x}\right)^2 + \left(\frac{\partial u}{\partial z} + \frac{\partial w}{\partial x}\right)^2 + \left(\frac{\partial v}{\partial z} + \frac{\partial w}{\partial y}\right)^2\right\}^{1/2}. \end{aligned} \tag{A.8}$$

Appendix B

Interpolation method

To perform numerical computations according to Eqs. (4.119)–(4.124) or (4.152)–(4.156), it is necessary to determine values and derivatives on the control volume's faces. For this purpose, let us introduce an arbitrary flow quantity Φ, whose value $(\Phi)_k$ is defined in the centre of the tetrahedral control volume $\Omega_k \in \mathcal{M}$, Fig. B.1. To compute Φ_m as a value of Φ at the mid-point O of the m-th face Γ_k^m of the control volume Ω_k, we employ the interpolation formula taken from [30]

$$\Phi_m = (\Phi)_k + \frac{(\Phi)_{l_m} - (\Phi)_k}{\gamma_k + \gamma_{l_m}} \cdot \gamma_k = \frac{\gamma_{l_m}(\Phi)_k + \gamma_k(\Phi)_{l_m}}{\gamma_k + \gamma_{l_m}}\,, \tag{B.1}$$

where γ_k and γ_{l_m} are the minimal distances between the face Γ_k^m and the centres S_k and S_{l_m} of the adjacent control volumes Ω_k and Ω_{l_m}, respectively, see Fig. B.1. In accordance with [76], $\frac{\partial \Phi}{\partial \boldsymbol{n}_k^m}$ as a derivative of Φ in the direction of the outward unit vector $\boldsymbol{n}_k^m$ normal to the m-th face Γ_k^m of the control volume Ω_k is approximated at the mid-point O as

$$\left.\frac{\partial \Phi}{\partial \boldsymbol{n}_k^m}\right|_{\Gamma_k^m} \approx \frac{(\Phi)_{l_m} - (\Phi)_k}{\gamma_k + \gamma_{l_m}}. \tag{B.2}$$

In addition to the interpolation formulas (B.1) and (B.2), the algorithm of the stabilised projection method from Section 4.4.2 also requires the evaluation of derivatives of Φ in the direction of the Cartesian coordinates x_i, $i = 1, 2, 3$ on the face Γ_k^m of the control volume Ω_k, i.e., $\left.\frac{\partial \Phi}{\partial x_i}\right|_{\Gamma_k^m}$. For this purpose, let us introduce Φ_{A_i}, $i = 1, 2, 3$ as the values of the arbitrary flow quantity Φ in the vertices of the m-th face Γ_k^m that is shared

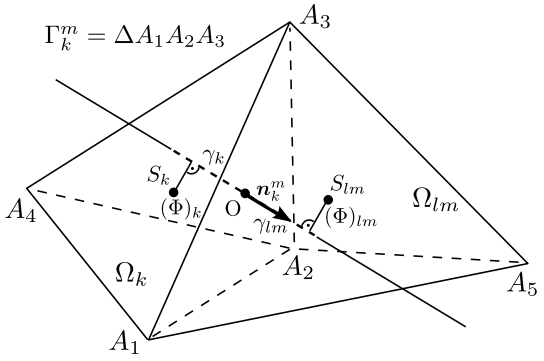

Fig. B.1. Two adjacent tetrahedral control volumes $\Omega_k = A_1A_2A_3A_4$ and $\Omega_{l_m} = A_1A_2A_3A_5$ with their common face $\Gamma_k^m = \Delta A_1A_2A_3$. Here, S_k and S_{lm} are the centres of the aforementioned control volumes.

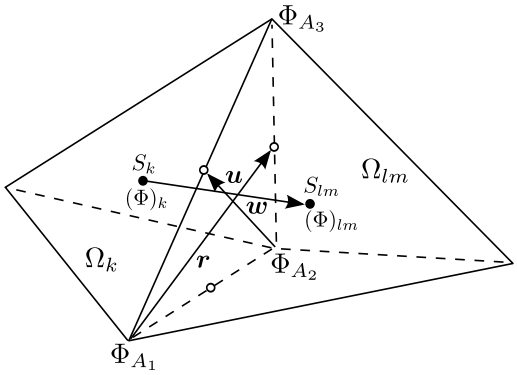

Fig. B.2. Orientation of the vectors $\boldsymbol{u}$, $\boldsymbol{r}$ and $\boldsymbol{w}$ on the face Γ_k^m of the tetrahedral control volume Ω_k.

by two adjacent control volumes Ω_k and Ω_{lm}, Fig. B.2,

$$\Phi_{A_i} = \frac{1}{M}\sum_{\mu=1}^{M}(\Phi)_\mu, \tag{B.3}$$

where $(\Phi)_\mu,\ \mu = 1, 2, \ldots, M$ are the values of Φ defined in the centres of all control volumes containing the vertex A_i. In accordance with Fig. B.2, we define the direction vector $\boldsymbol{u}$ connecting the centres S_k and S_{lm} of the adjacent control volumes Ω_k and Ω_{lm}, respectively, the direction vector $\boldsymbol{r}$ connecting the vertex A_1 with the middle of the opposite edge A_2A_3 of the face Γ_k^m, and the direction vector $\boldsymbol{w}$ connecting the vertex A_2 with the middle of the opposite edge A_1A_3 of the face Γ_k^m. Then, the derivatives of the flow quantity Φ in the direction of the vectors $\boldsymbol{u}$, $\boldsymbol{r}$ and $\boldsymbol{w}$ are computed as

$$\begin{aligned}
\frac{\partial\Phi}{\partial\boldsymbol{u}} &= \frac{(\Phi)_{l_m} - (\Phi)_k}{\|\boldsymbol{u}\|_{l_2}},\\
\frac{\partial\Phi}{\partial\boldsymbol{r}} &= \frac{\frac{1}{2}(\Phi_{A_2} + \Phi_{A_3}) - \Phi_{A_1}}{\|\boldsymbol{r}\|_{l_2}},\\
\frac{\partial\Phi}{\partial\boldsymbol{w}} &= \frac{\frac{1}{2}(\Phi_{A_1} + \Phi_{A_3}) - \Phi_{A_2}}{\|\boldsymbol{w}\|_{l_2}}.
\end{aligned} \tag{B.4}$$

Taking Eq. (B.4) into consideration, the derivative of the flow quantity Φ in the direction of the Cartesian coordinate x_i computed on the face Γ_k^m is obtained with the following linear combination:

$$\left.\frac{\partial\Phi}{\partial x_i}\right|_{\Gamma_k^m} = \frac{\partial\Phi}{\partial\boldsymbol{u}}c_{1i} + \frac{\partial\Phi}{\partial\boldsymbol{r}}c_{2i} + \frac{\partial\Phi}{\partial\boldsymbol{w}}c_{3i}, \tag{B.5}$$

where the values of c_{ij} are determined from the matrix equation

$$\begin{bmatrix} u_1 & r_1 & w_1\\ u_2 & r_2 & w_2\\ u_3 & r_3 & w_3 \end{bmatrix} \cdot \begin{bmatrix} c_{11} & c_{12} & c_{13}\\ c_{21} & c_{22} & c_{23}\\ c_{31} & c_{32} & c_{33} \end{bmatrix} = \begin{bmatrix} 1 & 0 & 0\\ 0 & 1 & 0\\ 0 & 0 & 1 \end{bmatrix}. \tag{B.6}$$

Appendix C

The three-element Windkessel model

The three-element Windkessel model also known as the RCR lumped parameter model falls into the category of lumped (0D) models [169]. The main idea of the lumped models is to replace the complex spatial structure of the cardiovascular system with a single tube, whose properties are equivalent to those of the whole vascular network. In other words, the lumped models are a variant of the 'black box' concept [202], where only the relation between the input and output from the box is studied without any knowledge of the internal workings of the system. In the case of the cardiovascular system, the lumped models are mainly used to reproduce a physiological relationship between blood pressure and flow rate without the need to model the whole vascular network [162].

The simplified models of arterial system in the form of lumped models are based on the analogy between the governing equations used in fluid mechanics, classical mechanics and electrical engineering, Tab. C.1. According to [195, 202], most lumped models used in cardiovascular biomechanics often include the following three basic elements:

- *resistance* R corresponds to the viscous friction at the interface between blood and the vessel wall arising from the non-slip boundary condition at the wall and blood's rheological properties;
- *inductance* L represents the inertia of the blood during the acceleration or deceleration phases of the cardiac cycle;
- *capacitance* C as a measure of vessel compliance represents the amount of change in the pressure difference required to produce a certain change in the vessel volume.

Note that besides the three basic elements, some literature, e.g., [202] mentions other lumped elements such as *reactance* or *impedance*[1], which mostly represent the combined effects of the three basic elements. Because of the hydraulic-electrical analogue, Tab. C.1, the hemodynamics in the arterial system can be modelled in terms of an electric circuit combining selected lumped elements in a suitable manner. One of the main advantages of this approach is the possibility to use the well-established methods for the analysis of electric circuits such as the branch and loop current methods [116]. Another considerable advantage arising from the application of electric circuits is the fact that these circuits can be easily manipulated, built and tested, both analytically and experimentally, making them one of the most convenient tools in blood flow modelling.

The description of the simplest lumped models, which usually include a resistance-compliance-inductance combination, is known as the *mono-compartment description* [169]. Part of this description is also the already mentioned Windkessel[2] model, whose

[1] Reactance as a combination of blood inertia and wall elasticity is often associated with the resistance to wave propagation and reflection in human vessels. Impedance, on the other hand, refers to the combined effects of viscous resistance and reactance.

[2] The term 'Windkessel' (in German 'air chamber') is based on the so-called Windkessel effect, which refers to the effect of aorta distension following blood ejection from the left ventricle during systole [46].

	fluid mechanics	classical mechanics	electrical engineering
resistance	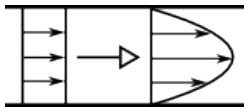 $\Delta p(t) = R\,Q(t)$ $Q(t) = \dfrac{\Delta p(t)}{R}$	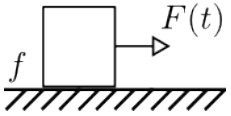 $F(t) = f\,u(t)$	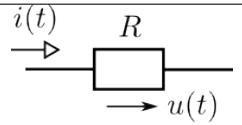 $u(t) = R\,i(t)$ (Ohm's law)
	Δp [Pa] ... pressure difference/drop R [Pa s m^{-3}] ... viscous resistance Q [m^3 s^{-1}] ... flow rate	F [N] ... driving force f [kg s^{-1}] ... friction coefficient u [m s^{-1}] ... friction (relative) velocity	u [V] ... voltage/electric potential R [Ω] ... electrical resistance i [A] ... electric current
inductance	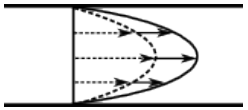 $\Delta p(t) = L\dfrac{\mathrm{d}}{\mathrm{d}\,t}Q(t)$ $Q(t) = \dfrac{1}{L}\displaystyle\int_0^T \Delta p(t)\,\mathrm{d}\,t$	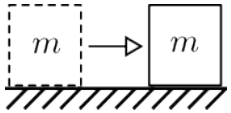 $F(t) = m\dfrac{\mathrm{d}}{\mathrm{d}\,t}u(t)$	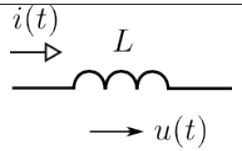 $u(t) = L\dfrac{\mathrm{d}}{\mathrm{d}\,t}i(t)$
	Δp [Pa] ... pressure difference/drop L [Pa s^2 m^{-3}] ... inertance Q [m^3 s^{-1}] ... flow rate	F [N] ... acting force m [kg] ... mass of the solid object u [m s^{-1}] ... velocity	u [V] ... voltage/electric potential L [H] ... electrical inductance i [A] ... electric current
capacitance	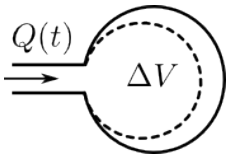 $\Delta p(t) = \dfrac{1}{C}\displaystyle\int_0^T Q(t)\,\mathrm{d}\,t$ $Q(t) = C\dfrac{\mathrm{d}}{\mathrm{d}\,t}\Delta p(t)$	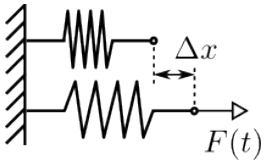 $F(t) = k\,\Delta x$ $F(t) = k\displaystyle\int_0^T u(t)\,\mathrm{d}\,t$	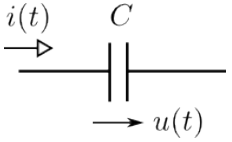 $u(t) = \dfrac{1}{C}\displaystyle\int_0^T i(t)\,\mathrm{d}\,t$
	Δp [Pa] ... pressure difference/drop C [m^3 Pa^{-1}] ... capacitance Q [m^3 s^{-1}] ... flow rate	F [N] ... applied force k [N m^{-1}] ... spring constant/stiffness Δx [m] ... length change, u [m s^{-1}] ... velocity	u [V] ... voltage/electric potential C [F] ... electrical capacitance i [A] ... electric current

Tab. C.1. Analogy between the analytical descriptions of resistance, inductance and capacitance in fluid mechanics, classical mechanics and electrical engineering [116, 195, 202].

first variation (the two-element Windkessel model, Fig. C.1a) was firstly proposed by Stephen Hales in 1733 [169] and mathematically formulated by Otto Frank in 1899 [42]. Since then the original two-element Windkessel model has been extended to include other lumped elements resulting in the three- and four-element Windkessel models shown in Fig. C.1b,c, respectively. Tab. C.2 provides a summary of the main advantages and disadvantages of these three models, which besides the use as an outflow boundary condition, have also found application as loads in artificial heart and valve studies or as a means to derive cardiac output. Other use and clincial relevance of the Windkessel model is listed, for example, in [195].

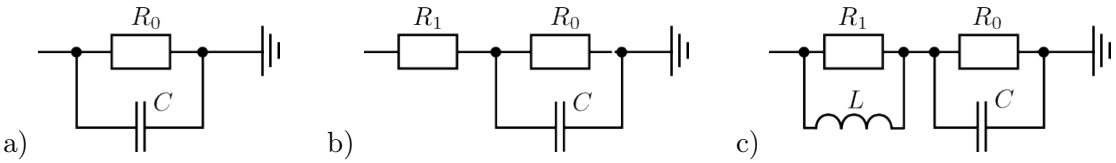

Fig. C.1. Electrical diagrams of the two- (a), three- (b) and four-element (c) Windkessel models [195].

WM type	advantages	disadvantages
2-element (RC model)	• a very simple Windkessel model mathematically described since 1899 [42] • is able to describe the compliance of large arteries and the dissipative nature of peripheral arteries	• cannot simulate the high frequency components in the arterial impedance • the shape of pressure and flow rate waveforms is of very poor quality • cannot simulate the pulse wave transmission effect
3-element (RCR model)	• is able to better describe the high frequency components in the arterial impedance than the 2-element Windkessel model	• cannot correctly describe the features of arterial impedance in the medium frequency range (small errors) • tends to overestimate the arterial compliance
4-element (RLCR model)	• is able to correctly describe the arterial impedance at all frequencies • its estimation of the arterial compliance is accurate	• very difficult identification of model parameters (inertance) ⇒ most studies give preference to the 3-element Windkessel model

Tab. C.2. Advantages and disadvantages of the three basic Windkessel models (WMs) according to [169, 195].

Given the widespread application of the Windkessel model in recent years, see, for example, [162], this simple lumped model is also used in this Ph.D. thesis for the calculation of the outlet pressure p_O in Section 5.3.2. Considering the difficult estimation of parameters in the case of the four-element Windkessel model and the low-quality wave-

forms generated by the two-element Windkessel model, Tab. C.2, it is obvious that the choice of the lumped model for this Ph.D. thesis fell on the three-element Windkessel model, Fig. C.1b. Thus, in the remainder of this appendix, this model will be addressed in more detail.

The standard three-element Windkessel model consists of two resistors with resistances R_p and R_d and one capacitor with capacitance C connected according to Fig. C.2. In this lumped model, the proximal and distal resistances R_p and R_d represent the characteristic resistance of the proximal arteries and the peripheral resistance occurring in arterioles and capillaries of the downstream vascular bed, respectively. The capacitance C stands for the total compliance of the arterial system. Based on the analogy between flow and electrical quantities listed in Tab. C.3, the governing equations of the three-element Windkessel model, describing the physiological relationship between blood pressure p_O and flow rate Q_O at a specific location in the arterial system, can be derived using the well-known Kirchhoff's circuit laws [116] and relationships given in Tab. C.1:

1) Flow through the resistor R_p, Fig. C.2: Because of the law of conservation of mass, the flow rate remains unchanged ($Q_O = Q_d$), but the presence of the resistor results in pressure decrease

$$\Delta p = p_O(t) - p_d(t) = R_p\, Q_O(t), \tag{C.1}$$

where p_d is the distal pressure representing the pressure in arterioles and capillaries of the downstream vascular bed.

2) Flow division at the node A in Fig. C.2 according to the law of conservation of mass[3]:

$$Q_O(t) = Q_{R_d}(t) + Q_C(t) = \frac{1}{R_d}\left(p_d(t) - p_h(t)\right) + C\frac{\mathrm{d}}{\mathrm{d}\,t}\left(p_d(t) - p_h(t)\right), \tag{C.2}$$

where p_h is the blood pressure in the thoracic vena cava, near the right atrium of the heart, which is also known as the central venous pressure (CVP). The normal range of CVP is between 3 to 8 mmHg ($400 - 1\,700$ Pa), although negative values of this pressure are known to occur as well [175].

[3] In the electrical analogy, this law corresponds to the the Kirchhoff's first law also known as the Kirchhoff's nodal rule [116]: "At any node in an electrical circuit, the sum of currents flowing into that node is equal to the sum of currents flowing out of that node."

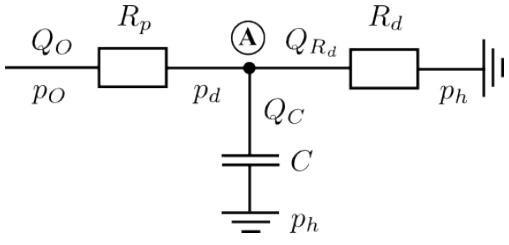

Fig. C.2. Schematic drawing of the three-element Windkessel model.

pressure $p\,[\mathrm{Pa}]$	$\Longleftrightarrow$	voltage $u\,[\mathrm{V}]$
flow rate $Q\,[\mathrm{m^3\,s^{-1}}]$	$\Longleftrightarrow$	current $i\,[\mathrm{A}]$
resistance $R\,[\mathrm{Pa\,s\,m^{-3}}]$	$\Longleftrightarrow$	resistance $R\,[\Omega]$
capacitance $C\,[\mathrm{m^3\,Pa^{-1}}]$	$\Longleftrightarrow$	capacitance $C\,[F]$

Tab. C.3. Analogy between basic flow and electrical quantities.

In Section 5.3.2 of this Ph.D. thesis, the three-element Windkessel model is used as an outflow boundary condition and coupled to each coronary artery outlet of the three different 3D aorto-coronary bypass models. Depending on the flow rate Q_O calculated by the 3D model at a specific outlet, the lumped model is able to provide a corresponding physiological value of blood pressure p_O by solving the system of equations for the unknown pressures p_d and p_O[4]

$$\frac{\mathrm{d}}{\mathrm{d}\,t}p_d(t) + \frac{p_d(t)}{CR_d} = \frac{1}{C}Q_O(t), \qquad p_O(t) = p_d(t) + R_p\,Q_O(t), \tag{C.3}$$

where the parameters R_p, R_d and C have to be attuned to this specific outlet. In this Ph.D. thesis, the resistance and capacitance parameters are determined in accordance with data published in [162], Figs. C.3–C.4,

$$R_p = \frac{k_{R_p}}{A}, \qquad R_d = \frac{k_{R_d}}{A}, \qquad C = k_C \cdot A, \tag{C.4}$$

where A is the cross-sectional area of the outlet, $k_{R_p} = 0.55 \times 10^4\,\mathrm{Pa\,s\,m^{-1}}$, $k_{R_d} = 5.54 \times 10^4\,\mathrm{Pa\,s\,m^{-1}}$ and $k_C = 324.6 \times 10^{-7}\,\mathrm{m\,Pa^{-1}}$. Other methods of how the parameters may be determined, for example, by tuning to patient-specific data, are described in [195].

[4]Note that for reasons of simplicity, the right atrial pressure p_h occurring in Eq. (C.2) is assumed to be equal to zero and is, therefore, dropped from Eq. (C.3).

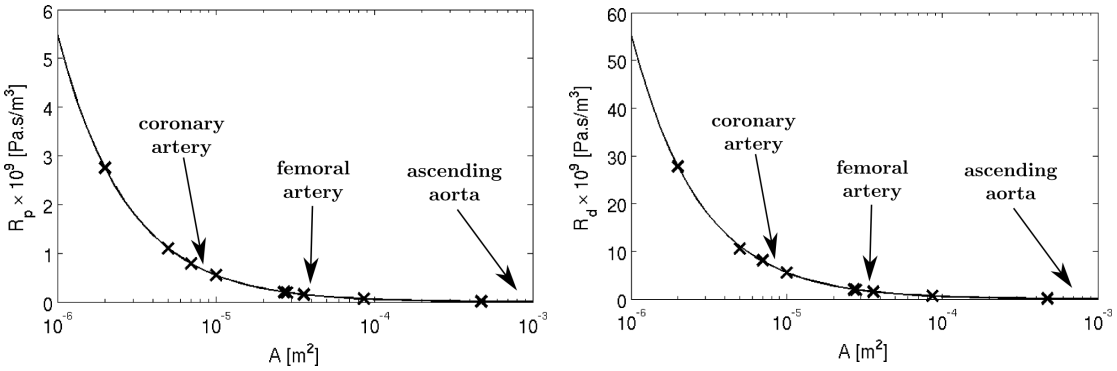

Fig. C.3. Proximal R_p (*left*) and distal R_d (*right*) resistances as functions of cross-sectional area A based on data from [162].

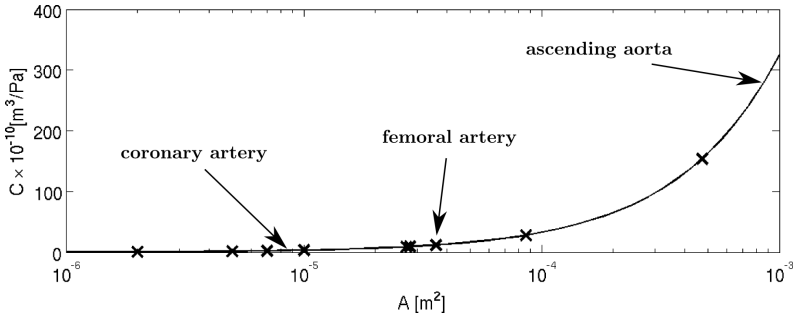

Fig. C.4. Capacitance C as a function of cross-sectional area A based on data from [162].

Bibliography

[1] Agoshkov, V., Quarteroni, A., Rozza, G.: Shape design in aorto-coronaric bypass anastomoses using perturbation theory. *SIAM Journal on Numerical Analysis*, **44**(1), (2006), 367–384.

[2] Allaire, E., Melliere, D., Poussier, B., Kobeiter, H., Desgranges, P., Becquemin, J.P.: Iliac artery rupture during balloon dilatation: What treatment? *Annals of Vascular Surgery*, **17**(3), (2003), 306–314.

[3] Anand, M., Rajagopal, K., Rajagopal, K.R.: A model incorporating some of the mechanical and biochemical factors underlying clot formation and dissolution in flowing blood. *Journal of Theoretical Medicine*, **5**(3-4), (2003), 183–218.

[4] Anderson, G.H., Hellums, J.D., Moake, J.L., Alfrey, C.P.: Platelet lysis and aggregation in shear fields. *Blood Cells*, **4(3)**(3), (1978), 499–511.

[5] Baskurt, O.K., Hardeman, M.R., Rampling, M.W., Meiselman, H.J. (edit.): *Handbook of hemorheology and hemodynamics*. 1st edition, IOS Press, Amsterdam, 2007.

[6] Baskurt, O.K., Meiselman, H.J.: Blood rheology and hemodynamics. *Seminars in Thrombosis and Hemostasis*, **29**(5), (2003), 435–450.

[7] Bassiouny, H.S., White, S., Glagov, S., Choi, E., Giddens, D.P., Zarins, C.K.: Anastomotic intimal hyperplasia: Mechanical injury or flow induced. *Journal of Vascular Surgery*, **15**(4), (1992), 708–717.

[8] Beneš, L., Louda, P., Kozel, K., Keslerová, R., Štigler, J.: Numerical simulations of flow through channels with T-junction. *Applied Mathematics and Computation*, **219**(13), (2013), 7225–7235.

[9] Benson Viscometers, Ltd.: What is plasma viscosity (PV), 2012, URL `http://www.bensonviscometers.com/clinical-information/what-is-pv.aspx`.

[10] Berger, S.A., Jou, L.D.: Flows in stenotic vessels. *Annual Review of Fluid Mechanics*, **32**(1), (2000), 347–382.

[11] Bertolotti, C., Deplano, V.: Three-dimensional numerical simulations of flow through a stenosed coronary bypass. *Journal of Biomechanics*, **33**(8), (2000), 1011–1022.

[12] Bertolotti, C., Deplano, V., Fuseri, J., Dupouy, P.: Numerical and experimental models of post-operative realistic flows in stenosed coronary bypasses. *Journal of Biomechanics*, **34**(8), (2001), 1049–1064.

[13] Bonert, M., Myers, J.G., Fremes, S., Williams, J., Ethier, C.R.: A numerical study of blood flow in coronary artery bypass graft side-to-side anastomoses. *Annals of Biomedical Engineering*, **30**(5), (2002), 599–611.

[14] Brass, L.F., Stalker, T.J.: Mechanisms of platelet activation. In: *Platelets in hematologic and cardiovascular disorders: A clinical handbook* (edit.: P. Gresele, V. Fuster, J.A. López, C.P. Page, J. Vermylen), pp. 485–540, Cambridge University Press, New York, 2008.

[15] Briley, W.R., Buggeln, R.C., McDonald, H.: Solution of the incompressible Navier-Stokes equations using artificial compressibility methods. In: *Lecture Notes in*

Physics – 11th International Conference on Numerical Methods in Fluid Dynamics, vol. 323, Springer Verlag, 1989, pp. 156–160.

[16] Buchanan, J.R., Kleinstreuer, C., Comer, J.K.: Rheological effects on pulsatile hemodynamics in a stenosed tube. *Computers & Fluids*, **29**(6), (2000), 695–724.

[17] Budu-Grajdeanu, P., Schugart, R.C., Friedman, A., Valentine, C., Agarwal, A.K., Rovin, B.H.: A mathematical model of venous neointimal hyperplasia formation. *Theoretical Biology & Medical Modelling*, **5**(2), doi:10.1186/1742-4682-5-2.

[18] Chandran, K.B., Rittgers, S.E., Yoganathan, A.P.: *Biofluid mechanics: The human circulation*. 1st edition, Taylor & Francis, Boca Raton, 2007.

[19] Chaturani, P., Palanisamy, V.: Pulsatile flow of power-law fluid model for blood flow under periodic body acceleration. *Biorheology*, **27**(5), (1990), 747–758.

[20] Chen, J., Lu, X.Y., Wang, W.: Non-Newtonian effects of blood flow on hemodynamics in distal vascular graft anastomoses. *Journal of Biomechanics*, **39**(11), (2006), 1983–1995.

[21] Chien, S., Sung, K.L.P., Schmid-Schönbein, G.W., Skalak, R., Schmalzer, E.A., Usami, S.: Rheology of leukocytes. *Annals of the New York Academy of Sciences*, **516**, (1987), 333–347.

[22] Cho, Y.I., Cho, D.J.: Hemorheology and microvascular disorders. *Korean Circulation Journal*, **41**(6), (2011), 287–295.

[23] Cho, Y.I., Kensey, K.R.: Effects of the non-Newtonian viscosity of blood on flows in a diseased arterial vessel. Part 1: Steady flows. *Biorheology*, **28**(3-4), (1991), 241–262.

[24] Choi, D., Merkle, C.L.: Application of time-iterative schemes to incompressible flow. *AIAA Journal*, **23**(10), (1985), 1518–1524.

[25] Choi, H., Moin, P.: Effects of the computational time step on numerical solutions of turbulent flow. *Journal of Computational Physics*, **113**(1), (1994), 1–4.

[26] Chorin, A.J.: Numerical solution of the Navier-Stokes equations. *Mathematics of Computation*, **22**, (1968), 745–762.

[27] Chorin, A.J.: A numerical method for solving incompressible viscous flow problems. *Journal of Computational Physics*, **135**, (1997), 118–125, (reprint of the original paper published by Chorin in 1967).

[28] Chua, L.P., Zhang, J., Zhou, T.: Numerical study of a complete anastomosis model for the coronary artery bypass. *International Communications in Heat and Mass Transfer*, **32**(3-4), (2005), 473–482.

[29] Das, B., Johnson, P.C., Popel, A.S.: Computational fluid dynamic studies of leukocyte adhesion effects on non-Newtonian blood flow through microvessels. *Biorheology*, **37**(3), (2000), 239–258.

[30] Davidson, L.: A pressure correction method for unstructured meshes with arbitrary control volumes. *International Journal for Numerical Methods in Fluids*, **22**(4), (1996), 265–281.

[31] Davies, J.E., Parker, K.H., Francis, D.P., Hughes, A.D., Mayet, J.: What is the role of the aorta in directing coronary blood flow? *Heart*, **94**(12), (2008), 1545–1547.

[32] Davies, P.F.: Hemodynamic shear stress and the endothelium in cardiovascular pathophysiology. *Nature Reviews Cardiology*, **6**(1), (2009), 16–26.

[33] Dobrin, P.B., Littooy, F.N., Golan, J., Blakeman, B., Fareed, J.: Mechanical and histologic changes in canine vein grafts. *Journal of Surgical Research*, **44**(3), (1988), 259–265.

[34] Dominik, J.: *Kardiochirurgie*. Grada Publishing, Praha, 1998, (in Czech).

[35] Eguchi, Y., Karino, T.: Measurement of rheologic property of blood by a falling-ball blood viscometer. *Annals of Biomedical Engineering*, **36**(4), (2008), 545–553.

[36] Elert, G.: The physics factbook – An encyclopedia of scientific essays, 2012, URL `http://hypertextbook.com/facts/`.

[37] Enderle, J.D., Blanchard, S.M., Bronzino, J.D.: *Introduction to biomedical engineering*. 1st edition, Academic Press, San Diego, 2000.

[38] Ethier, C.R., Steinman, D.A., Zhang, X., Karpik, S.R., Ojha, M.: Flow waveform effects on end-to-side anastomotic flow patterns. *Journal of Biomechanics*, **31**(7), (1998), 609–617.

[39] Ferziger, J.H., Perić, M.: *Computational methods for fluid dynamics*. 2nd edition, Springer Verlag, Heidelberg, 1999.

[40] Formichi, M., Raybaud, G., Benichou, H., Ciosi, G.: Rupture of the external iliac artery during balloon angioplasty: Endovascular treatment using a covered stent. *Journal of Endovascular Surgery*, **5**(1), (1998), 37–41.

[41] Foshager, M.C., Sane, S.S.: Evaluation of lower extremity bypass grafts with use of color duplex sonography. *RadioGraphics*, **16**(1), (1996), 9–25.

[42] Frank, O.: Die Grundform des arteriellen Pulses, erste Abhandlung: Mathematische Analyse. *Zeitschrift für Biologie*, **37**, (1899), 483–526.

[43] Frauenfelder, T., Boutsianis, E., Schertler, T., Husmann, L., Leschka, S., Poulikakos, D., Marincek, B., Alkadhi, H.: Flow and wall shear stress in end-to-side and side-to-side anastomosis of venous coronary artery bypass grafts. *Biomedical Engineering Online*, **6**, doi:10.1186/1475-925X-6-35.

[44] Freitas, R.A.: *Nanomedicine, Volume I: Basic capabilities*. 1st edition, Landes Bioscience, Austin, 1999.

[45] Fry, D.L.: Acute vascular endothelial changes associated with increased blood velocity gradients. *Circulation Research*, **22**(2), (1968), 165–197.

[46] Fung, Y.C.: *Biomechanics: Mechanical properties of living tissues*. 2nd edition, Springer Verlag, New York, 1993.

[47] Galdi, G.P., Rannacher, R., Robertson, A.M., Turek, S.: *Hemodynamical flows – Modeling, analysis and simulation*. 1st edition, Birkhäuser Verlag, Basel, 2008.

[48] Glagov, S.: Intimal hyperplasia, vascular modeling, and the restenosis problem. *Circulation*, **89**(6), (1994), 2888–2891.

[49] Gray, J.D., Owen, I., Escudier, M.P.: Dynamic scaling of unsteady shear-thinning non-Newtonian fluid flows in a large-scale model of a distal anastomosis. *Experiments in Fluids*, **43**(4), (2007), 535–546.

[50] Greenwald, S.E., Berry, C.L.: Improving vascular grafts: The importance of mechanical and haemodynamic properties. *Journal of Pathology*, **190**(3), (2000), 292–299.

[51] Grondin, C.M., Limet, R.: Sequential anastomoses in coronary artery grafting: Technical aspects and early and late angiographic results. *The Annals of Thoracic Surgery*, **23**(1), (1977), 1–8.

[52] Haruguchi, H., Teraoka, S.: Intimal hyperplasia and hemodynamic factors in arterial bypass and arteriovenous grafts: A review. *Journal of Artificial Organs*, **6**(4), (2003), 227–235.

[53] Hasson, J.E., Megerman, J., Abbott, W.M.: Increased compliance near vascular anastomoses. *Journal of Vascular Surgery*, **2**(3), (1985), 419–423.

[54] He, X., Ku, D.N.: Pulsatile flow in the human left coronary artery bifurcation: Average conditions. *Journal of Biomechanical Engineering*, **118**(1), (1996), 74–82.

[55] Henry, F.S., Küpper, C., Lewington, N.P.: Simulation of flow through a Miller cuff bypass graft. *Computer Methods in Biomechanics and Biomedical Engineering*, **5**(3), (2002), 207–217.

[56] Herman, I.P.: *Physics of the human body.* 1st edition, Springer Verlag, New York, 2007.

[57] Hirsch, C.: *Numerical computation of internal and external flows, Volume 1 & 2.* John Wiley & Sons, Chichester, 1990.

[58] Hirsch, C.: *Numerical computation of internal and external flows: The fundamentals of computational fluid dynamics, Volume 1.* 2nd edition, Butterworth-Heinemann, Oxford, 2007.

[59] Hofer, M., Rappitsch, G., Perktold, K., Trubel, W., Schima, H.: Numerical study of wall mechanics and fluid dynamics in end-to-side anastomoses and correlation to intimal hyperplasia. *Journal of Biomechanics*, **29**(10), (1996), 1297–1308.

[60] Hoffmann, K.A., Chiang, S.T.: *Computational fluid dynamics, Volume 1 & 2.* Engineering Education System, Wichita, 2000.

[61] How, T.V., Black, R.A., Hughes, P.E.: Hemodynamics of vascular prostheses. In: *Advances in hemodynamics and hemorheology, Volume 1* (edit.: T.V. How), pp. 373–423, JAI Press, 1996.

[62] Huang, P.Y., Hellums, J.D.: Aggregation and disaggregation kinetics of human blood platelets: Part II. Shear-induced platelet aggregation. *Biophysical Journal*, **65**(1), (1993), 344–353.

[63] Hughes, P.E., How, T.V.: Effects of geometry and flow division on flow structures in models of the distal end-to-side anastomosis. *Journal of Biomechanics*, **29**(7), (1996), 855–872.

[64] Hwang, M., Berceli, S.A., Garbey, M., Kim, N.H., Tran-Son-Tay, R.: The dynamics of vein graft remodeling induced by hemodynamic forces: A mathematical model. *Biomechanics and Modeling in Mechanobiology*, **11**(3-4), (2012), 411–423.

[65] Ikeda, Y., Handa, M., Kawano, K., Kamata, T., Murata, M., Araki, Y., Anbo, H., Kawai, Y., Watanabe, K., Itagaki, I., Sakai, K., Ruggeri, Z.M.: The role of

von Willebrand factor and fibrinogen in platelet aggregation under varying shear stress. *The Journal of Clinical Investigation*, **87**(4), (1991), 1234–1240.

[66] Jameson, A., Schmidt, W., Turkel, E.: Numerical solution of the Euler equations by finite volume methods using Runge-Kutta time-stepping schemes. *AIAA paper 81-1259*.

[67] Janalík, J.: *Viskozita tekutin a její měření*. VŠB-TU, Ostrava, 2012, URL `http://www.338.vsb.cz/PDF/TEXTviskozitaPDF.pdf`.

[68] Johnston, B.M., Johnston, P.R., Corney, S., Kilpatrick, D.: Non-Newtonian blood flow in human right coronary arteries: Steady state simulations. *Journal of Biomechanics*, **37**(5), (2004), 709–720.

[69] Junker, R., Heinrich, J., Ulbrich, H., Schulte, H., Schönfeld, R., Köhler, E., Assmann, G.: Relationship between plasma viscosity and the severity of coronary heart disease. *Arteriosclerosis, Thrombosis, and Vascular Biology*, **18**(6), (1998), 870–875.

[70] Kabinejadian, F., Chua, L.P., Ghista, D.N., Sankaranarayanan, M., Tan, Y.S.: A novel coronary artery bypass graft design of sequential anastomoses. *Annals of Biomedical Engineering*, **38**(10), (2010), 3135–3150.

[71] Kabinejadian, F., Ghista, D.N.: Compliant model of a coupled sequential coronary arterial bypass graft: Effects of vessel wall elasticity and non-Newtonian rheology on blood flow regime and hemodynamic parameters distribution. *Medical Engineering & Physics*, **34**(7), (2011), 860–872.

[72] Kannan, R.Y., Salacinski, H.J., Butler, P.E., Hamilton, G., Seifalian, A.M.: Current status of prosthetic bypass grafts: A review. *Journal of Biomedical Materials Research Part B: Applied Biomaterials*, **74**(1), (2005), 570–581.

[73] Kapadia, M.R., Popowich, D.A., Kibbe, M.R.: Modified prosthetic vascular conduits. *Circulation*, **117**(14), (2008), 1873–1882.

[74] Keslerová, R., Kozel, K.: Numerical study of steady and unsteady flow for power-law type generalized Newtonian fluids. *Computing*, **95**(1), (2013), S409–S424.

[75] Kidson, I.G.: The effect of wall mechanical properties on patency of arterial grafts. *Annals of the Royal College of Surgeons of England*, **65**(1), (1983), 24–29.

[76] Kim, D., Choi, H.: A second-order time-accurate finite volume method for unsteady incompressible flow on hybrid unstructured grids. *Journal of Computational Physics*, **162**(2), (2000), 411–428.

[77] Kim, H.J., Vignon-Clementel, I.E., Figueroa, C.A., Jansen, K.E., Taylor, C.A.: Developing computational methods for three-dimensional finite element simulations of coronary blood flow. *Finite Elements in Analysis and Design*, **46**(6), (2010), 514–525.

[78] Kim, J., Moin, P.: Application of a fractional-step method to incompressible Navier-Stokes equations. *Journal of Computational Physics*, **59**(2), (1985), 308–323.

[79] Kim, S., Kong, R.L., Popel, A.S., Intaglietta, M., Johnson, P.C.: Temporal and spatial variations of cell-free layer width in arterioles. *American Journal of Physiology. Heart and Circulatory Physiology*, **293**(3), (2007), H1526–H1535.

[80] Kleinstreuer, C., Buchanan, J.R., Lei, M., Truskey, G.A.: Computational analysis of particle-hemodynamics and prediction of the onset of arterial diseases. In: *Biomechanical systems: Techniques and applications, Volume II: Cardiovascular techniques* (edit.: C.T. Leondes), pp. 1–69, CRC Press, New York, 2001.

[81] Kleinstreuer, C., Lei, M., Archie, J.P.: Hemodynamics simulations and optimal computer-aided designs of branching blood vessels. In: *Biomechanical systems: Techniques and applications, Volume IV: Biofluid methods in vascular and pulmonary systems* (edit.: C.T. Leondes), pp. 1–59, CRC Press, New York, 2001.

[82] Kleinstreuer, C., Nazemi, M., Archie, J.P.: Hemodynamics analysis of a stenosed carotid bifurcation and its plaque-mitigating design. *Journal of Biomechanical Engineering*, **113**(3), (1991), 330–335.

[83] Ko, T.H., Ting, K., Yeh, H.C.: Numerical investigation on flow fields in partially stenosed artery with complete bypass graft: An in vitro study. *International Communications in Heat and Mass Transfer*, **34**(6), (2007), 713–727.

[84] Ko, T.H., Ting, K., Yeh, H.C.: A numerical study on the effects of anastomotic angle on the flow fields in a stenosed artery with a complete bypass graft. *International Communications in Heat and Mass Transfer*, **35**(10), (2008), 1360–1367.

[85] Konstantinov, I.E.: The first coronary artery bypass operation and forgotten pioneers. *The Annals of Thoracic Surgery*, **64**(5), (1997), 1522–1523.

[86] Konstantinov, I.E.: Robert H. Goetz: The surgeon who performed the first successful clinical coronary artery bypass operation. *The Annals of Thoracic Surgery*, **69**(6), (2000), 1966–1972.

[87] Krajíček, M.: Filosofie a praxe cévních náhrad. *Medical Tribune*, **9**, (in Czech), URL `http://www.tribune.cz/clanek/11776`.

[88] Kroll, M.H., Hellums, J.D., McIntire, L.V., Schafer, A.I., Moake, J.L.: Platelets and shear stress. *Blood*, **88**(5), (1996), 1525–1541.

[89] Ku, D.N.: Blood flow in arteries. *Annual Review of Fluid Mechanics*, **29**, (1997), 399–434.

[90] Ku, D.N., Allen, R.C.: Vascular grafts. In: *The biomedical engineering handbook, vol. 1 & 2* (edit.: J.D. Bronzino), 2nd edition, pp. 1–8, CRC Press, Boca Raton, 2000.

[91] Ku, D.N., Giddens, D.P., Zarins, C.K., Glagov, S.: Pulsatile flow and atherosclerosis in the human carotid bifurcation – Positive correlation between plaque location and low oscillating shear stress. *Arteriosclerosis, Thrombosis, and Vascular Biology*, **5**(3), (1985), 293–302.

[92] Kupari, M., Hekali, P., Keto, P., V. P. Poutanen, M.J.T., Standerstkjöld-Nordenstam, C.G.: Relation of aortic stiffness to factors modifying the risk of atherosclerosis in healthy people. *Arteriosclerosis, Thrombosis, and Vascular Biology*, **14**(3), (1994), 386–394.

[93] Kwak, D., Chang, J.L.C., Shanks, S.P., Chakravarthy, S.K.: A three-dimensional incompressible Navier-Stokes solver using primitive variables. *AIAA Journal*, **24**(3), (1986), 390–396.

[94] Le, H., Moin, P.: An improvement of fractional step methods for the incompressible Navier-Stokes equations. *Journal of Computational Physics*, **92**(2), (1991), 369–379.

[95] Lee, D., Su, J.M., Liang, H.Y.: A numerical simulation of steady flow fields in a bypass tube. *Journal of Biomechanics*, **34**(11), (2001), 1407–1416.

[96] Lee, K.E., Lee, J.S., Yoo, J.Y.: A numerical study on steady flow in helically sinuous vascular prostheses. *Medical Engineering & Physics*, **33**(1), (2011), 38–46.

[97] Lee, S.S., Ahn, K.H., Lee, S.J., Sun, K., Goedhart, P.T., Hardeman, M.R.: Shear induced damage of red blood cells monitored by the decrease of their deformability. *Korea-Australia Rheology Journal*, **16**(3), (2004), 141–146.

[98] Lei, M., Archie, J.P., Kleinstreuer, C.: Computational design of a bypass graft that minimizes wall shear stress gradients in the region of the distal anastomosis. *Journal of Vascular Surgery*, **25**(4), (1997), 637–646.

[99] Lei, M., Kleinstreuer, C., Archie, J.P.: Geometric design improvements for femoral graft-artery junctions mitigating restenosis. *Journal of Biomechanics*, **29**(12), (1996), 1605–1614.

[100] Leuprecht, A., Perktold, K.: Computer simulation of non-Newtonian effects on blood flow in large arteries. *Computer Methods in Biomechanics and Biomedical Engineering*, **4**(2), (2001), 149–163.

[101] Leuprecht, A., Perktold, K., Prosi, M., Berk, T., Trubel, W., Schima, H.: Numerical study of hemodynamics and wall mechanics in distal end-to-side anastomoses of bypass grafts. *Journal of Biomechanics*, **35**(2), (2002), 225–236.

[102] LeVeque, R.J.: *Finite volume methods for hyperbolic problems*. Cambridge University Press, Cambridge, 2002.

[103] Leverett, L.B., Hellums, J.D., Alfrey, C.P., Lynch, E.C.: Red blood cell damage by shear stress. *Biophysical Journal*, **12**(3), (1972), 257–273.

[104] Lichtman, M.A.: Rheology of leukocytes, leukocyte suspensions, and blood in leukemia. Possible relationship to clinical manifestations. *The Journal of Clinical Investigation*, **52**(2), (1973), 350–358.

[105] Longest, P.W., Kleinstreuer, C.: Computational haemodynamics analysis and comparison study of arterio-venous grafts. *Journal of Medical Engineering & Technology*, **24**(3), (2000), 102–110.

[106] Lopera, J.E., Trimmer, C.K., Josephs, S.G., Anderson, M.E., Schuber, S., Li, R., Dolmatch, B., Toursarkissian, B.: Multidetector CT angiography of infrainguinal arterial bypass. *RadioGraphics*, **28**(2), (2008), 529–549.

[107] Loth, F., Fischer, P.F., Bassiouny, H.S.: Blood flow in end-to-side anastomoses. *Annual Review of Fluid Mechanics*, **40**(1), (2008), 367–393.

[108] Louda, P., Kozel, K., Příhoda, J.: Numerical solution of 2D and 3D viscous incompressible steady and unsteady flows using artificial compressibility method. *International Journal for Numerical Methods in Fluids*, **56**(8), (2008), 1399–1407.

[109] Loudon, C., Tordesillas, A.: The use of the dimensionless Womersley number to characterize the unsteady nature of internal flow. *Journal of Theoretical Biology*, **191**(1), (1998), 63–78.

[110] Lévy, B.I.: Artery changes with aging: Degeneration or adaptation? *Dialogues in Cardiovascular Medicine*, **6**(2), (2001), 104–111.

[111] Mackey, J., Mensah, G.: *The atlas of heart disease and stroke*. 1st edition, WHO Press, Geneve, 2004, URL `http://www.who.int/cardiovascular_diseases/resources/atlas/en/`.

[112] Macosko, C.W.: *Rheology – Principles, measurements, and applications*. 1st edition, John Wiley & Sons, New York, 1994.

[113] Malek, A.M., Alper, S.L., Izumo, S.: Hemodynamic shear stress and its role in atherosclerosis. *JAMA – The Journal of the American Medical Association*, **282**(21), (1999), 2035–2042.

[114] Malek, A.M., Izumo, S.: Mechanism of endothelial cell shape change and cytoskeletal remodeling in response to fluid shear stress. *Journal of Cell Science*, **109**(4), (1996), 713–726.

[115] Marcinkowska-Gapińska, A., Gapinski, J., Elikowski, W., Jaroszyk, F., Kubisz, L.: Comparison of three rheological models of shear flow behavior studied on blood samples from post-infarction patients. *Medical & Biological Engineering & Computing*, **45**(9), (2007), 837–844.

[116] Mayer, D.: *Úvod do teorie elektrických obvodů*. SNTL – Nakladatelství technické literatury, Praha, 1981.

[117] Mendis, S., Puska, P., Norrving, B.: *Global atlas of cardiovascular disease prevention and control*. 1st edition, WHO Press, Geneve, 2011, URL `http://whqlibdoc.who.int/publications/2011/9789241564373_eng.pdf`.

[118] Merrill, E.W.: Rheology of blood. *Physiological Reviews*, **49**(4), (1969), 863–888.

[119] Merrill, E.W., Cokelet, G.C., Britten, A., Wells, R.E.: Non-Newtonian rheology of human blood: Effect of fibrinogen deduced by 'subtraction'. *Circulation Research*, **13**(1), (1963), 48–55.

[120] Merrill, E.W., Gilliland, E.R., Cokelet, G., Shin, H., Britten, A., Wells, R.E.: Rheology of human blood, near and at zero flow – Effects of temperature and hematocrit level. *Biophysical Journal*, **3**(3), (1963), 199–213.

[121] Merrill, E.W., Gilliland, E.R., Lee, T.S., Salzman, E.W.: Blood rheology: Effect of fibrinogen deduced by addition. *Circulation Research*, **18**(4), (1966), 437–446.

[122] Migliavacca, F., Dubini, G.: Computational modeling of vascular anastomoses. *Biomechanics and Modeling in Mechanobiology*, **3**(4), (2005), 235–250.

[123] Mishra, B.K., Verma, N.: Effects of stenosis on non-Newtonian flow of blood in blood vessels. *Australian Journal of Basic & Applied Sciences*, **4**(4), (2010), 588–601.

[124] Morbiducci, U., Ponzini, R., Gallo, D., Bignardi, C., Rizzo, G.: 3D measured velocity profiles as inlet boundary conditions in computational hemodynamic models of the human aorta. *Journal of Biomechanics*, **45(S1)**, (2012), S141.

[125] Morris, C.L., Rucknagel, D.L., Shukla, R., Gruppo, R.A., Smith, C.M., Blackshear, P.: Evaluation of the yield stress of normal blood as a function of fibrinogen concentration and hematocrit. *Microvascular Research*, **37**(3), (1989), 323–338.

[126] Morris, C.L., Smith, C.M., Blackshear, P.L.: A new method for measuring the yield stress in thin layers of sedimenting blood. *Biophysical Journal*, **52**(2), (1987), 229–240.

[127] Morrow, J.S., Rimm, D.L., Kennedy, S.P., Cianci, C.D., J. H, .S., Weed, S.A.: Of membrane stability and mosaics: The spectrin cytoskeleton. In: *Handbook of physiology* (edit.: J. Hoffman, J. Jamieson), pp. 485–540, Oxford University Press, London, 1997.

[128] Mueller, R.L., Rosengart, T.K., Isom, O.W.: The history of surgery for ischemic heart disease. *The Annals of Thoracic Surgery*, **63**(3), (1997), 869–878.

[129] Muto, A., Model, L., Ziegler, K., Eghbalieh, S.D.D., Dardik, A.: Mechanisms of vein graft adaptation to the arterial circulation: Insights into the neointimal algorithm and management strategies. *Circulation Journal*, **74**(8), (2010), 1501–1512.

[130] Nash, G.B.: Blood rheology and ischaemia. *Eye*, **5**(2), (1991), 151–158.

[131] Nichols, M., Townsend, N., Scarborough, P., Rayner, M.: *European cardiovascular disease statistics 2012 edition*. European Heart Network, Oxford, 2012.

[132] Nichols, W.W., O'Rourke, M.F.: *McDonald's blood flow in arteries: Theoretic, experimental, and clinical principles*. 5$^{\text{th}}$ edition, CRC Press, London, 2005.

[133] O'Brien, T.P., P.Grace, Walsh, M., Burke, P., McGloughlin, T.: Computational investigations of a new prosthetic femoral-popliteal bypass graft design. *Journal of Vascular Surgery*, **42**(6), (2006), 1169–1175.

[134] Ojha, M., Leask, R.L., Johnston, K.W., David, T.E., Butany, J.: Histology and morphology of 59 internal thoracic artery grafts and their distal anastomoses. *The Annals of Thoracic Surgery*, **70**(4), (2000), 1338–1344.

[135] Olufsen, M.S., Peskin, C.S., Kim, W.Y., Pedersen, E.M., Nadim, A., Larsen, J.: Numerical simulation and experimental validation of blood flow in arteries with structured-tree outflow conditions. *Annals of Biomedical Engineering*, **28**(11), (2000), 1281–1299.

[136] Owida, A.A., Do, H., Morsi, Y.S.: Numerical analysis of coronary artery bypass grafts: An overview. *Computer Methods and Programs in Biomedicine*, **108**(2), (2012), 689–705.

[137] Pan, W., Caswell, B., Karniadakis, G.E.: A low-dimensional model for the red blood cell. *Soft Matter*, **6**(18), (2010), 4366–4376.

[138] Pant, S., Fabrèges, B., Gerbeau, J.F., Vignon-Clementel, I.: A methodological paradigm for patient-specific multi-scale CFD simulations: From clinical measure-

ments to parameter estimates for individual analysis. *International Journal for Numerical Methods in Biomedical Engineering*, (2014), (in press).

[139] Papaharilaou, Y., Doorly, D.J., Sherwin, S.J.: The influence of out-of-plane geometry on pulsatile flow within a distal end-to-side anastomosis. *Journal of Biomechanics*, **35**(9), (2002), 1225–1239.

[140] Patrick, C.W., Sampath, R., McIntire, L.V.: Fluid shear stress effects on cellular function. In: *The biomedical engineering handbook, vol. 1 & 2* (edit.: J.D. Bronzino), 2nd edition, pp. 1–20, CRC Press, Boca Raton, 2000.

[141] Pedrizzetti, G., Perktold, K.: *Cardiovascular fluid mechanics*. Springer Verlag, Wien, 2003.

[142] Perkkiö, J., Keskinen, R.: Hematocrit reduction in bifurcations due to plasma skimming. *Bulletin of Mathematical Biology*, **45**(1), (1983), 41–50.

[143] Perktold, K., Leuprecht, A., Prosi, M., Berk, T., Czerny, M., Trubel, W., Schima, H.: Fluid dynamics, wall mechanics, and oxygen transfer in peripheral bypass anastomoses. *Annals of Biomedical Engineering*, **30**(4), (2002), 447–460.

[144] Perktold, K., Prosi, M.: Computational models of arterial flow and mass transport. In: *Cardiovascular fluid mechanics* (edit.: G. Pedrizzetti, K. Perktold), pp. 73–136, Springer Verlag, Wien, 2003.

[145] Picart, C., Piau, J.M., Galliard, H., Carpentier, P.: Blood low shear rate rheometry: Influence of fibrinogen level and hematocrit on slip and migrational effects. *Biorheology*, **35**(4-5), (1998), 335–353.

[146] Picart, C., Piau, J.M., Galliard, H., Carpentier, P.: Human blood shear yield stress and its hematocrit dependence. *Journal of Rheology*, **42**(1), (1998), 1–12.

[147] Popel, A.S., Johnson, P.C.: Microcirculation and hemorheology. *Annual Review of Fluid Mechanics*, **37**(1), (2005), 43–69.

[148] Pries, A.R., Secomb, T.W.: Blood flow in microvascular networks. *Comprehensive Physiology*, doi:10.1002/cphy.cp020401.

[149] Pries, A.R., Secomb, T.W., Gaehtgens, P.: Biophysical aspects of blood flow in the microvasculature. *Cardiovascular Research*, **32**(4), (1996), 654–667.

[150] Pries, A.R., Secomb, T.W., Gaehtgens, P., Gross, J.F.: Blood flow in microvascular networks. Experiments and simulation. *Circulation Research*, **67**(4), (1990), 826–834.

[151] Qiao, A.K., Liu, Y., Li, S., Zhao, H.: Numerical simulation of physiological blood flow in 2-way coronary artery bypass grafts. *Journal of Biological Physics*, **31**(2), (2005), 161–182.

[152] Qiao, A.K., Zeng, Y.J., Xu, X.H.: Numerical simulations of stenosed femoral artery with symmetric 2-way bypass graft. *Bio-Medical Materials and Engineering*, **14**(2), (2004), 167–174.

[153] Quarteroni, A., Rozza, G.: Optimal control and shape optimization of aorto-coronaric bypass anastomoses. *Mathematical Models and Methods in Applied Sciences*, **13**(12), (2003), 1801–1823.

[154] Quemada, D.: Rheology of concentrated disperse systems and minimum energy dissipation principle I. Viscosity-concentration relationship. *Rheologica Acta*, **16**(1), (1977), 82–94.

[155] Quemada, D.: Rheology of concentrated disperse systems II. A model for non-Newtonian shear viscosity in steady flows. *Rheologica Acta*, **17**(6), (1978), 632–642.

[156] Quemada, D.: Rheology of concentrated disperse systems III. General features of the proposed non-Newtonian model. Comparison with experimental data. *Rheologica Acta*, **17**(6), (1978), 643–653.

[157] Rachev, A., Manoach, E., Berry, J., Moore, J.E.: A model of stress-induced geometrical remodeling of vessel segments adjacent to stents and artery/graft anastomoses. *Journal of Theoretical Biology*, **206**(3), (2000), 429–443.

[158] Ramshaw, J.D., Mousseau, V.A.: Accelerated artificial compressibility method for steady-state incompressible flow calculations. *Computers & Fluids*, **18**(4), (1990), 361–367.

[159] Rhie, C.M., Chow, W.L.: Numerical study of the turbulent flow past an airfoil with trailing edge separation. *AIAA Journal*, **21**(11), (1983), 1525–1532.

[160] Rogers, S.E., Kwak, D., Kaul, U.: On the accuracy of the pseudocompressibility method in solving the incompressible Navier-Stokes equations. *Applied Mathematical Modelling*, **11**(1), (1987), 35–44.

[161] Rosencranz, R., Bogen, S.A.: Clinical laboratory measurement of serum, plasma, and blood viscosity. *American Journal of Clinical Pathology*, **125**, (2006), S78–S86.

[162] Sankaran, S., Moghadam, M.E., Kahn, A.M., Tseng, E.E., Guccione, J.M., Marsden, A.L.: Patient-specific multiscale modeling of blood flow for coronary artery bypass graft surgery. *Annals of Biomedical Engineering*, **40**(10), (2012), 2228–2242.

[163] Sankaranarayanan, M., Chua, L.P., Ghista, D.N., Tan, Y.S.: Computational model of blood flow in the aorto-coronary bypass graft. *Biomedical Engineering Online*, **4**, doi:10.1186/1475-925X-4-14.

[164] Sankaranarayanan, M., Ghista, D.N., Poh, C.L., Seng, T.Y., Kassab, G.S.: Analysis of blood flow in an out-of-plane CABG model. *American Journal of Physiology - Heart and Circulatory Physiology*, **291**(1), (2006), H283–H295.

[165] Sarkar, S., Salacinski, H.J., Hamilton, G., Seifaliani, A.M.: The mechanical properties of infrainguinal vascular bypass grafts: Their role in influencing patency. *European Journal of Vascular and Endovascular Surgery*, **31**(6), (2006), 627–636.

[166] Schramm, G.: *A practical approach to rheology and rheometry.* 2nd edition, Gebrueder HAAKE, Karlsruhe, 2000.

[167] Sequeira, A., Janela, J.: An overview of some mathematical models of blood rheology. In: *A portrait of state-of-the-art research at the Technical University of Lisbon* (edit.: M.S. Pereira), pp. 65–87, Springer Verlag, Amsterdam, 2007.

[168] Sheriff, J., Bluestein, D., Girdhar, G., Jesty, J.: High-shear stress sensitizes platelets to subsequent low-shear conditions. *Annals of Biomedical Engineering*, **38**(4), (2010), 1442–1450.

[169] Shi, Y., Lawford, P., Hose, R.: Review of zero-D and 1-D models of blood flow in the cardiovascular system. *Biomedical Engineering Online*, **10**, doi:10.1186/1475-925X-10-33.

[170] Somer, T., Meiselman, H.J.: Disorders of blood viscosity. *Annals of Medicine*, **25**(1), (1993), 31–39.

[171] Sottiurai, V.S.: Comparison of reversed, nonreversed translocated, and in situ vein grafts in arterial revascularization: Techniques, cumulative patency, versatility, and durability. *International Journal of Angiology*, **8**(4), (1999), 197–202.

[172] Staudacher, M.: Die erste autologe Venentransplantation von Erich Lexer (1907). *Gefässchirurgie*, **9**(1), (2004), 64–67, (in German).

[173] Stoltz, J.F., Singh, M., Riha, P.: *Hemorheology in practice*. 1st edition, IOS Press, Amsterdam, 1999.

[174] Špinar, J., Vítovec, J.: *Ischemická choroba srdeční*. Grada Publishing, Praha, 2003, (in Czech).

[175] Šrámek, B., Valenta, J., Klimeš, F.: *Biomechanics of the cardiovascular system*. Czech Technical University Press, Praha, 1995.

[176] Taggart, D.P.: Coronary artery bypass grafting is still the best treatment for multivessel and left main disease, but patients need to know. *The Annals of Thoracic Surgery*, **82**(6), (2006), 1966–1975.

[177] Tai, N.R., Salacinski, H.J., Edwards, A., Hamilton, G., Seifalian, A.M.: Compliance properties of conduits used in vascular reconstruction. *British Journal of Surgery*, **87**(11), (2000), 1516–1524.

[178] Tannehill, J.C., Anderson, D.A., Pletcher, R.H.: *Computational fluid mechanics and heat transfer*. 2nd edition, Taylor & Francis, London, 1997.

[179] Témam, R.: Sur l'approximation de la solution des équations de Navier-Stokes par la méthode des fractionnarires (II). *Archive for Rational Mechanics and Analysis*, **33**(5), (1969), 377–385, (in French).

[180] Texon, M.: A hemodynamic concept of atherosclerosis, with particular reference to coronary occlusion. *AMA Archives of Internal Medicine*, **99**(3), (1957), 418–427.

[181] Thubrikar, M.J.: *Vascular mechanics and pathology*. 1st edition, Springer Verlag, New York, 2007.

[182] Tiwari, A., Cheng, K.S., Salacinski, H., Hamilton, G., Seifalian, A.M.: Improving the patency of vascular bypass grafts: The role of suture materials and surgical techniques on reducing anastomotic compliance mismatch. *European Journal of Vascular and Endovascular Surgery*, **25**(4), (2003), 287–295.

[183] Toes, G.J.: *Intimal hyperplasia, the obstacle in bypass grafts*. Ph.D. thesis, University of Groningen, Netherlands, 2002.

[184] Toro, E.F.: *Riemann solvers and numerical methods for fluid dynamics – A practical introduction*. 2nd edition, Springer Verlag, Heidelberg, 1999.

[185] Tran-Son-Tay, R., Hwang, M., Garbey, M., Jiang, Z., Ozaki, C.K., Berceli, S.A.: An experiment-based model of vein graft remodeling induced by shear stress. *Annals of Biomedical Engineering*, **36**(7), (2008), 1083–1091.

[186] Turkel, E.: Preconditioned methods for solving the incompressible and low speed compressible equations. *Journal of Computational Physics*, **72**(2), (1987), 277–298.

[187] Ústav zdravotnických informací a statistiky ČR: *Zdravotnictví České republiky 2010 ve statistických údajích*. ÚZIS ČR, Praha, 2011, (in Czech).

[188] Van Tricht, I., De Wachter, D., Tordoir, J., Verdonck, P.: Hemodynamics and complications encountered with arteriovenous fistulas and grafts as vascular access for hemodialysis: A review. *Annals of Biomedical Engineering*, **33**(9), (2005), 1142–1157.

[189] Vara, D.S., Punshon, G., Sales, K.M., Hamilton, G., Seifalian, A.M.: Haemodynamic regulation of gene expression in vascular tissue engineering. *Current Vascular Pharmacology*, **9**(2), (2011), 167–187.

[190] Vimmr, J.: *Fluid flow modelling with applications in biomechanics and internal aerodynamics*. Habilitation thesis, University of West Bohemia, Pilsen, Czech Republic, 2008, (in Czech).

[191] Vural, K.M., Sener, E., Tasdemir, O.: Long-term patency of sequential and individual saphenous vein coronary bypass grafts. *European Journal of Cardio-Thoracic Surgery*, **19**(2), (2001), 140–144.

[192] Waite, L.: *Biofluid mechanics in cardiovascular systems*. 1st edition, McGraw-Hill, New York, 2006.

[193] Wells, R.E., Merrill, E.W.: Influence of flow properties of blood upon viscosity-hematocrit relationships. *Journal of Clinical Investigation*, **41**(8), (1962), 1591–1598.

[194] Wen, J., Zheng, T., Jiang, W., Deng, X., Fan, Y.: A comparative study of helical-type and traditional-type artery bypass grafts: Numerical simulation. *ASAIO Journal*, **57**(5), (2011), 399–406.

[195] Westerhof, N., Lankhaar, J., Westerhof, B.: The arterial Windkessel. *Medical & Biological Engineering & Computing*, **47**(2), (2009), 131–141.

[196] White, C.R., Haidekker, M., Bao, X., Frangos, J.A.: Temporal gradients in shear, but not spatial gradients, stimulate endothelial cell proliferation. *Circulation*, **103**(20), (2001), 2508–2513.

[197] WHO: World Health Organization – Cardiovascular diseases, 2011, URL `http://www.who.int/cardiovascular_diseases/`.

[198] Wootton, D.M., Ku, D.N.: Fluid mechanics of vascular systems, diseases, and thrombosis. *Annual Review of Biomedical Engineering*, **1**, (1999), 299–329.

[199] Xiong, F.L., Chong, C.K.: A parametric numerical investigation on haemodynamics in distal coronary anastomoses. *Medical Engineering & Physics*, **30**(3), (2008), 311–320.

[200] Yilmaz, F., Gundogdu, M.Y.: A critical review on blood flow in large arteries; relevance to blood rheology, viscosity models, and physiologic conditions. *Korea-Australia Rheology Journal*, **20**(4), (2008), 197–211.

[201] Yoo, S.S., Suh, S.H., Chang, N.I.: A comparative study on constitutive equations of human blood. *Korean Journal of Rheology*, **6**(2), (1994), 157–164.

[202] Zamir, M.: *The physics of coronary blood flow*. Springer Verlag, New York, 2005.

[203] Zang, Y., Street, R.L., Koseff, J.R.: A non-staggered grid, fractional step method for time-dependent incompressible Navier-Stokes equations in curvilinear coordinates. *Journal of Computational Physics*, **114**(1), (1994), 18–33.

[204] Zarins, C.K., Xu, C., Bassiouny, H.S., Glagov, S.: Intimal hyperplasia. In: *Haimovici's vascular surgery* (edit.: E. Ascher, H. Haimovici), 5^{th} edition, pp. 164–175, Wiley – Blackwell Publishing, Oxford, 2004.

[205] Zeng, D., Ding, Z., Friedman, M.H., Ethier, C.R.: Effects of cardiac motion on right coronary artery hemodynamics. *Annals of Biomedical Engineering*, **31**(4), (2003), 420–429.

[206] Zhang, J.B., Kuang, Z.B.: Study on blood constitutive parameters in different blood constitutive equations. *Journal of Biomechanics*, **33**(3), (2000), 355–360.

[207] Zhang, J.M., Chua, L.P., Ghista, D.N., Yu, S.C., Tan, Y.S.: Numerical investigation and identification of susceptible sites of atherosclerotic lesion formation in a complete coronary artery bypass model. *Medical & Biological Engineering & Computing*, **46**(7), (2008), 689–699.

Author's publications related to this Ph.D. thesis

A **Journal publications:**

A.1) Vimmr, J., Jonášová, A.: Analysis of blood flow through a three-dimensional bypass model. *Applied and Computational Mechanics*, **1**(2), (2007), 693-702.

A.2) Vimmr, J., Jonášová, A. : On the modelling of steady generalized Newtonian flows in a 3D coronary bypass. *Engineering Mechanics*, **15**(3), (2008), 193-203.

A.3) Vimmr, J., Jonášová, A.: Non-Newtonian effects of blood flow in complete coronary and femoral bypasses. *Mathematics and Computers in Simulation*, **80**(6), (2010), 1324-1336.

A.4) Jonášová, A., Vimmr, J., Bublík, O.: Numerical analysis of bypass model geometrical parameters influence on pulsatile blood flow. *Applied and Computational Mechanics*, **5**(1), (2011), 29-44.

A.5) Vimmr, J., Jonášová, A., Bublík, O.: Effects of three geometrical parameters on pulsatile blood flow in complete idealised coronary bypasses. *Computers & Fluids*, **69**(1), (2012), 147-171.

A.6) Jonášová, A., Vimmr, J., Bublík, O.: Pulsatile non-Newtonian blood flow modelling in realistic aorto-coronary bypass grafts. *Journal of Biomechanics*, **45**(S1), (2012), p. S135.

A.7) Vimmr, J., Jonášová, A., Bublík, O.: Numerical analysis of non-Newtonian blood flow and wall shear stress in realistic single, double and triple aorto-coronary bypasses. *International Journal for Numerical Methods in Biomedical Engineering*, **29**(10), (2013), 1057-1081.

B **Conference publications:**

B.1) Vimmr, J., Jonášová, A.: On modelling of steady flow in a bypass model. Proc. *Computational Mechanics 2006*, vol. 2, Hrad Nečtiny, 2006, pp. 689-696.

B.2) Jonášová, A., Vimmr, J.: Blood flow through a bypass model with stenotic artery. Proc. *Topical problems of fluid mechanics 2007*, Prague, 2007, pp. 81-84.

B.3) Vimmr, J., Jonášová, A.: Influence of junction angle on hemodynamics in a bypass model. *Modelling and optimization of physical systems*, vol. 6, Gliwice, 2007, pp. 153-156.

B.4) Jonášová, A., Vimmr, J.: The influence of geometry on blood flow in a bypass model. Proc. *1st IMACS International Conference on Computational Biomechanics and Biology*, Pilsen, 2007, pp. 1-2.

B.5) Vimmr, J., Jonášová, A.: Finite volume simulation of blood flow through complete bypass models. *PAMM – Proceedings in Applied Mathematics and Mechanics*, vol. 7(1), Zürich, 2007, pp. 4100005-4100006.

B.6) Jonášová, A., Vimmr, J.: Finite volume modelling of non-Newtonian blood flow in an occluded 3D bypass. Proc. *Topical problems of fluid mechanics 2008*, Prague, 2008, pp. 55-58.

B.7) Vimmr, J., Jonášová, A.: Computer simulation of non-Newtonian effects on blood flow in a complete 3D bypass model. Proc. *5th European Congress on Computational Methods in Applied Sciences and Engineering*, Venice, 2008, pp. 1-2.

B.8) Jonášová, A., Vimmr, J.: Numerical simulation of non-Newtonian blood flow in bypass models. *PAMM – Proceedings in Applied Mathematics and Mechanics*, vol. 8(1), Bremen, 2008, pp. 10179-10180.

B.9) Vimmr, J., Jonášová, A.: Numerical simulation of physiological pulsatile blood flow in complete bypass models. Proc. *X International Conference on Computational Plasticity – COMPLAS X*, Barcelona, 2009, pp. 1-4.

B.10) Jonášová, A., Vimmr, J., Bublík, O.: Finite volume modelling of unsteady blood flow using a fractional-step method. Proc. *Modelling 2009*, Rožnov pod Radhoštěm, 2009, p. 50.

B.11) Vimmr, J., Jonášová, A.: Modelling of hemodynamics in 3D bypass models. *Modelling and optimization of physical systems*, vol. 9, Gliwice, 2010, pp. 87-92.

B.12) Jonášová, A., Vimmr, J.: Physiological blood flow in a realistic bypass model. Proc. *Human Biomechanics 2010*, Sychrov, 2010, pp. 151-154.

B.13) Vimmr, J., Jonášová, A., Bublík, O.: A numerical study of pulsatile blood flow in a patient-specific coronary bypass model. Proc. *EUROMECH Colloquium 529 – Cardiovascular Fluid Mechanics: From theoretical aspects to diagnostic and therapeutic support*, Cagliari, 2011, pp. 70-73.

B.14) Vimmr, J., Jonášová, A., Bublík, O.: Numerical analysis of pulsatile blood flow in realistic coronary bypass models. Proc. *XI International Conference on Computational Plasticity – COMPLAS XI*, Barcelona, 2011, pp. 1-12.

B.15) Vimmr, J., Jonášová, A., Bublík, O.: Pulsatile blood flow modelling in realistic aorto-coronary bypass models. Proc. *4th International conference on Modelling of Mechanical and Mechatronical Systems*, Herĺany, 2011, pp. 1-11.

B.16) Vimmr, J., Jonášová, A., Bublík, O.: Non-Newtonian effects of pulsatile blood flow in a realistic bypass graft geometry. Proc. *Engineering Mechanics 2012*, Svratka, 2012, pp. 1-6.

B.17) Vimmr, J., Jonášová, A., Bublík: Modelling of blood's non-Newtonian behaviour in patient-specific aorto-coronary bypass grafts. Proc. *10th World Congress on Computational Mechanics*, São Paulo, 2012, pp. 1-20.

B.18) Vimmr, J., Jonášová, A., Bublík, O.: Pulsatile non-Newtonian blood flow in image-based models of carotid bifurcation. Proc. *XII International Conference on Computational Plasticity – COMPLAS XII*, Barcelona, 2013, pp. 884-895.

C **Other publications and research outputs:**

C.1) Jonášová, A., Vimmr, J., Bublík, O.: Software for simulation of laminar incompressible generalized Newtonian fluid flow. University of West Bohemia, Pilsen, Czech Republic, 2009, (ID code ZCU-KME-CFD-2-2009SW).

C.2) Vimmr, J., Jonášová, A.: *Modelování hemodynamiky v cévních náhradách.* Monograph, University of West Bohemia, Pilsen, Czech Republic, 2014. (in print)